frontiers | Research Topics

Women in cancer imaging and image-directed interventions vol II: 2022

Edited by
Samata Kakkad, Ellen Ackerstaff and Pilar López-Larrubia

Published in
Frontiers in Oncology

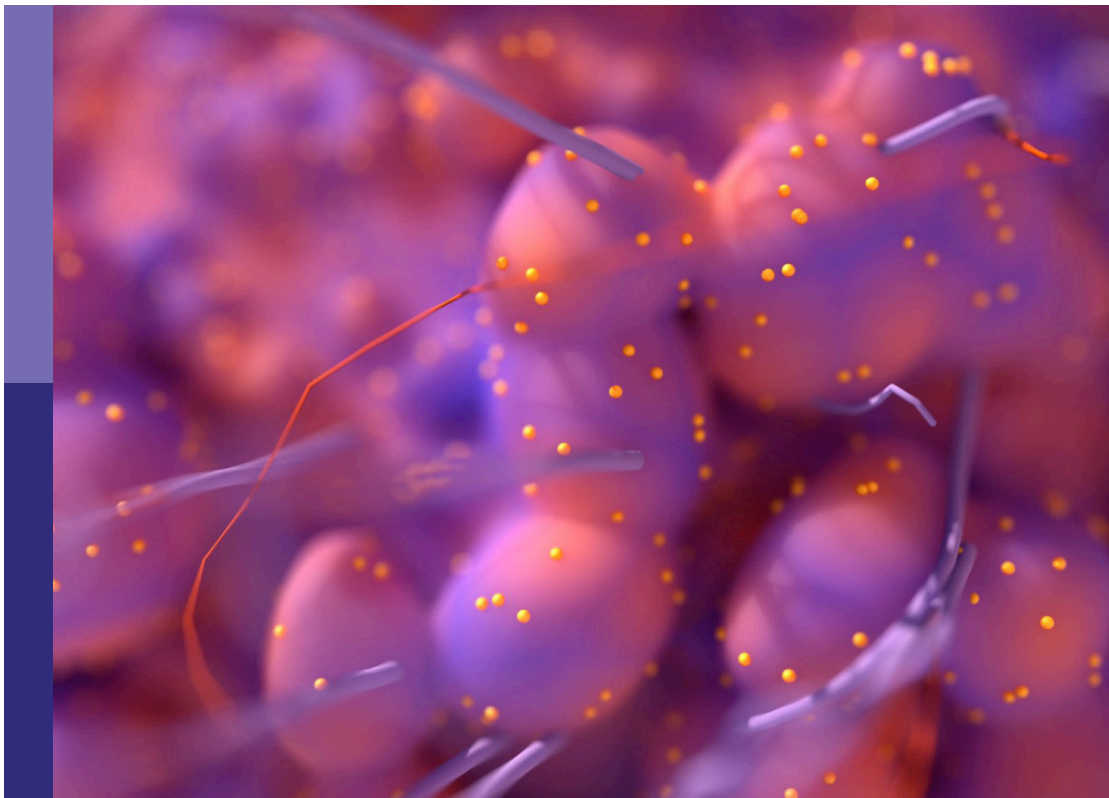

ISSN 1664-8714
ISBN 978-2-83251-844-1
DOI 10.3389/978-2-83251-844-1

About Frontiers

Frontiers is more than just an open access publisher of scholarly articles: it is a pioneering approach to the world of academia, radically improving the way scholarly research is managed. The grand vision of Frontiers is a world where all people have an equal opportunity to seek, share and generate knowledge. Frontiers provides immediate and permanent online open access to all its publications, but this alone is not enough to realize our grand goals.

Frontiers journal series

The Frontiers journal series is a multi-tier and interdisciplinary set of open-access, online journals, promising a paradigm shift from the current review, selection and dissemination processes in academic publishing. All Frontiers journals are driven by researchers for researchers; therefore, they constitute a service to the scholarly community. At the same time, the *Frontiers journal series* operates on a revolutionary invention, the tiered publishing system, initially addressing specific communities of scholars, and gradually climbing up to broader public understanding, thus serving the interests of the lay society, too.

Dedication to quality

Each Frontiers article is a landmark of the highest quality, thanks to genuinely collaborative interactions between authors and review editors, who include some of the world's best academicians. Research must be certified by peers before entering a stream of knowledge that may eventually reach the public - and shape society; therefore, Frontiers only applies the most rigorous and unbiased reviews. Frontiers revolutionizes research publishing by freely delivering the most outstanding research, evaluated with no bias from both the academic and social point of view. By applying the most advanced information technologies, Frontiers is catapulting scholarly publishing into a new generation.

What are Frontiers Research Topics?

Frontiers Research Topics are very popular trademarks of the *Frontiers journals series*: they are collections of at least ten articles, all centered on a particular subject. With their unique mix of varied contributions from Original Research to Review Articles, Frontiers Research Topics unify the most influential researchers, the latest key findings and historical advances in a hot research area.

Find out more on how to host your own Frontiers Research Topic or contribute to one as an author by contacting the Frontiers editorial office: frontiersin.org/about/contact

Women in cancer imaging and image-directed interventions vol II: 2022

Topic editors

Samata Kakkad — Merck, United States

Ellen Ackerstaff — Memorial Sloan Kettering Cancer Center, United States

Pilar López-Larrubia — Spanish National Research Council (CSIC), Spain

Citation

Kakkad, S., Ackerstaff, E., López-Larrubia, P., eds. (2023). *Women in cancer imaging and image-directed interventions vol II: 2022*. Lausanne: Frontiers Media SA.

doi: 10.3389/978-2-83251-844-1

Table of contents

frontiers in Oncology

ORIGINAL RESEARCH
published: 03 January 2022
doi: 10.3389/fonc.2021.797454

Multidisciplinary Tumor Board Smart Virtual Assistant in Locally Advanced Cervical Cancer: A Proof of Concept

Gabriella Macchia[1], Gabriella Ferrandina[2,3], Stefano Patarnello[4], Rosa Autorino[5], Carlotta Masciocchi[4], Vincenzo Pisapia[4], Cristina Calvani[4], Chiara Iacomini[4], Alfredo Cesario[6], Luca Boldrini[5], Benedetta Gui[7], Vittoria Rufini[7], Maria Antonietta Gambacorta[5], Giovanni Scambia[2,3] and Vincenzo Valentini[5]*

[1] Radiation Oncology Unit, Gemelli Molise Hospital - Università Cattolica del Sacro Cuore, Campobasso, Italy, [2] Department of Woman, Child and Public Health, Fondazione Policlinico Universitario A. Gemelli Istituto di Ricovero e Cura a Carattere Scientifico (IRCCS), Rome, Italy, [3] Department of Woman, Child and Public Health, Catholic University of the Sacred Heart, Rome, Italy, [4] Fondazione Policlinico Universitario A. Gemelli Istituto di Ricovero e Cura a Carattere Scientifico (IRCCS), Rome, Italy, [5] Radioterapia Oncologica, Dipartimento di Diagnostica per Immagini, Radioterapia Oncologica ed Ematologia, Fondazione Policlinico Universitario A. Gemelli, Istituto di Ricovero e Cura a Carattere Scientifico (IRCCS), Rome, Italy, [6] Scientific Directorate, Fondazione Policlinico Universitario A. Gemelli Istituto di Ricovero e Cura a Carattere Scientifico (IRCCS), Rome, Italy, [7] Dipartimento di Diagnostica per Immagini, Radioterapia Oncologica ed Ematologia, Fondazione Policlinico Universitario Agostino Gemelli, Istituto di Ricovero e Cura a Carattere Scientifico (IRCCS), Rome, Italy

OPEN ACCESS

Edited by:
Alessandro Stecco, University of Eastern Piedmont, Italy

Reviewed by:
Angelo Vanzulli, Niguarda Ca' Granda Hospital, Italy
Federica Tomao, European Institute of Oncology (IEO), Italy

***Correspondence:**
Rosa Autorino
rosa.autorino@policlinicogemelli.it

Specialty section:
This article was submitted to Cancer Imaging and Image-directed Interventions, a section of the journal Frontiers in Oncology

Received: *09 November 2021*
Accepted: *08 December 2021*
Published: *03 January 2022*

Citation:
Macchia G, Ferrandina G, Patarnello S, Autorino R, Masciocchi C, Pisapia V, Calvani C, Iacomini C, Cesario A, Boldrini L, Gui B, Rufini V, Gambacorta MA, Scambia G and Valentini V (2022) Multidisciplinary Tumor Board Smart Virtual Assistant in Locally Advanced Cervical Cancer: A Proof of Concept. Front. Oncol. 11:797454. doi: 10.3389/fonc.2021.797454

Aim: The first prototype of the "Multidisciplinary Tumor Board Smart Virtual Assistant" is presented, aimed to (i) Automated classification of clinical stage starting from different free-text diagnostic reports; (ii) Resolution of inconsistencies by identifying controversial cases drawing the clinician's attention to particular cases worthy for multi-disciplinary discussion; (iii) Support environment for education and knowledge transfer to junior staff; (iv) Integrated data-driven decision making and standardized language and interpretation.

Patients and Method: Data from patients affected by Locally Advanced Cervical Cancer (LACC), FIGO stage IB2-IVa, treated between 2015 and 2018 were extracted. Magnetic Resonance (MR), Gynecologic examination under general anesthesia (EAU), and Positron Emission Tomography–Computed Tomography (PET-CT) performed at the time of diagnosis were the items from the Electronic Health Records (eHRs) considered for analysis. An automated extraction of eHR that capture the patient's data before the diagnosis and then, through Natural Language Processing (NLP), analysis and categorization of all data to transform source information into structured data has been performed.

Results: In the first round, the system has been used to retrieve all the eHR for the 96 patients with LACC. The system has been able to classify all patients belonging to the training set and - through the NLP procedures - the clinical features were analyzed and classified for each patient. A second important result was the setup of a predictive model to evaluate the patient's staging (accuracy of 94%). Lastly, we created a user-oriented operational tool targeting the MTB who are confronted with the challenge of large volumes of patients to be diagnosed in the most accurate way.

Conclusion: This is the first proof of concept concerning the possibility of creating a smart virtual assistant for the MTB. A significant benefit could come from the integration of these automated methods in the collaborative, crucial decision stages.

Keywords: locally advanced cervical cancer, multidisciplinary tumor board smart virtual assistant, artificial intelligence, virtual medicine support, chemoradiation (CRT)

INTRODUCTION

Biological, radiological and clinical knowledge in the locally advanced cervical cancer (LACC) setting, as in all other fields of oncology, is growing on exponentially. Oncologists deal every day with many patients characterized by complex and heterogeneous phenotypes. The simultaneous elaboration of complex information is difficult even for experienced physicians and a significant amount of relevant information could be lost in the clinical decision process, as a direct consequence of the "information overload" (1).

The huge amount of data created in hospitals and populating complex data-lakes, stays largely unexploited and, in most of the circumstances, not organized at all. These general considerations make it clear that Artificial Intelligence (AI), a general term which covers the use of a computer algorithms to model intelligent processes (2, 3), is a field with potentially limitless applications in medicine and, more specifically, in oncology. Through Machine Learning methods, AI enables managing large amounts of data and allows smart data clustering for decision support in several knowledge areas.

The automated extraction and classification of actionable information from unstructured data (reports) represents a prerequisite for expanding "predictive" abilities and effectively tailoring patient treatments. Once unstructured and structured information are integrated and made consistent, and predictive methods are introduced to support diagnostic and therapeutic decisions, the most appropriate body where these data-driven methods can be exploited is the Multidisciplinary Tumor Board (MTB).

MTBs working groups have the main purpose in selecting the most appropriate and effective treatment for cancer patients, by taking into account staging of the tumor and its classification along with overall clinical characteristics. Several specialists often take part to the multidisciplinary meeting, such as radiation and medical oncologists, pathologists, radiologists, surgeons, nuclear medicine physicians and research nurses. Therefore, the point of views may be various and sometimes conflicting. Moreover, the discussion of each clinical case is often long and complex, especially if there are conflicting exams or if only the reports and not the images are available. Finally, there are not many cases that can be clearly discussed in a single MTB session.

AI and Machine Learning have already been used as a decision support tools in the framework of MTBs (4, 5) - yet many unmet needs are still voiced by MTB operators that may be addressed through such innovative approaches. The opportunities for more effective decision-making process can be summarized as follows:

- decision-making support by integrating different sources and information (as well as knowing which source is most reliable).
- decision-support systems that allow automated discrimination of simple vs. complex cases to help focusing efforts for the latter.
- reduce potential inconsistencies and lack of homogeneous criteria for diagnostic assessments by developing data-driven methods and common languages.
- enable increased teamwork and effective decision making across clinical expertise.
- leverage retrospective analyses from large data set to create methods and knowledge base that can be exported to other hospitals, thus creating a standardized approach for scalable methods and multicentric research efforts.

In our constant efforts to ameliorate the outcomes in the treatment of LACC, starting from the extensive work performed on chemo-radiation followed by surgery (5–10), we plan to implement a tailored AI-based decision support process. We blue-printed and implemented an automated system based on Natural Language Processing (NLP) (11, 12) to extract clinically relevant information from different free text reports of diagnostic exams and procedures that are commonly used in daily clinical activity, followed by a machine learning predictive method to support diagnostic decisions.

Therefore, to further develop and test the robustness of our automated system, we have performed a proof of concept by designing the first prototype of the "MTB Virtual Assistant" with the following goals:

i. Automated classification of clinical stage starting from different free-text diagnostic reports;
ii. Resolution of inconsistencies by identifying controversial cases drawing the clinician's attention to particular cases worthy for thorough multi-disciplinary discussion;
iii. Support environment for education and knowledge transfer to junior staff;
iv. Integrated data-driven decision making and standardized language and interpretation.

MATERIALS AND METHODS

Patients

Data from patients affected by LACC, FIGO stage IB2-IVa, treated between 2015 and 2018 were extracted from our institutional data-lake. The following Electronic Health Records (eHRs) items have been considered for analysis:

- Staging Magnetic Resonance (MR) report;
- Gynecologic examination under general anesthesia (EUA) report;

- Staging Positron Emission Tomography–Computed Tomography (PET-CT) report.

Other patient's relevant data (e.g., demographics, laboratory tests, body mass index, drugs, comorbidities etc.) were collected for further analysis.

Methods

A two steps model has been applied to allow the set-up of the MTB Virtual Assistant:

i. Automated extraction of the relevant eHR sets that capture the patient's data before the diagnosis and then, through Natural Language Processing (NLP), analysis and categorization of all information to transform source information into structured data,
ii. development of A.I. methods to support the clinical staff in the decision process with regards to tumor staging confirmation and to help in identifying the most complex cases, where more complex analyses and discussion are needed (e. g. due to conflicting information coming from different exams).

A first subset of patients with pre-validated staging and diagnosis was used as training set for steps one and two.

Once steps (i) and (ii) have been completed and successfully tested for patients' subsets with pre-validated staging and diagnosis (the 'training set'), we developed an integrated toolset to support the MTB diagnostic process. Each time a new patient is selected for staging and treatment decision-making and enters the workflow, her eHR are automatically processed to provide structured clinical features (e.g. presence/absence of specific disease features in the tumor region, tumor activity etc.).

The A.I. algorithm then delivers an assessment for the staging of the tumor with a certain degree of reliability, reported on the screen as percentage of accuracy. The MTB staff can proceed– if needed- to go deeper in the characterization of the information, performing further analyses of clinical data patterns from different sources and comparing the content from different eHRs. This process, characterized by such a depth and complexity of information, and the A.I. empowered multi-dimensional analyses allow a robust consensus on the clinical decision to be taken.

Step (i): Natural Language Processing: Extracting Clinical Data from Text-Based Medical Reports

The first step is represented by the extraction of clinically relevant information from MR, EUA, PET-CT reports and other eHRs. The challenge with these data sources was firstly to transform the unstructured information into discrete, categorical data able to define a clear, robust and actionable framework of clinical and pathological features related to the tumor loco-regional morphology.

The output of this transformation is therefore a pattern of structured clinical features that describe in detail the disease of the patient whose specific data constitute the source information of the integrated A.I. empowered analysis.

In terms of computer algorithm used, the NPL method to transform text into data is based on a hybrid approach using rules and annotations derived from medical guidelines, combined with A.I. (machine learning); in this experience, this was developed using the SAS Visual Text Analytics® environment (12, 13). Pre-processing steps as such as segmentation, boundary detection and tokenization, and word normalization (stemming, spelling correction, expansion of abbreviation) were performed to achieve a higher degree of accuracy. Thereafter, syntactic and semantic analysis were performed with the support of an algorithm that creates the network of words, showing the occurrence of links among two words and providing an enhanced approach to natural language understanding. Finally, the sequence of steps above gave us the relevant NLP features leading to data extraction from real life medical reports.

By using these NLP steps, the medical reports were processed and free-text diagnostic information were transformed into categorical or quantitative clinical data that classify the clinical features resulting from each of the three exams MR, EUA, PET-CT. The selection of the relevant clinical features that characterize the diagnosis – and most importantly tumor staging – was performed by the multidisciplinary clinical team and constitute the basis for the ontology of the study.

Therefore, the result of this data discovery process for each patient is a table showing how detailed clinical features in the tumor region are diagnosed for each of the three exams – as shown in **Table 1A**. Any clinical feature is then inspected and reported as being or not within the framework of the three types of exams. Categorical morphological variables (i. e. whether or not a specific region is involved) are mostly extracted from MR and EUA, while PET-CT clinical features provide additional levels of tumor (metabolic) activity.

Therefore, after the eHR automated reading and the subsequent NLP step, the patient's clinical features are collected in a summarized pattern, as shown in **Table 1B** (specific instance of the table for a patient case); this view shows, for each of the clinical features, whether this has been identified as positive (meaning whether that region is involved in the tumor progression) or not. Examples from **Table 1B** indicate bladder involvement, as detected both by MR and EUA, while rectovaginal septum appears as involved when analyzing the results from the EUA and not from the RM. This conflicting outcome may indicate uncertainty in the staging assessment, which is typically represented in the predictive model results, as explained in step (ii) below.

This transformation from unstructured to structured data is the mainstay of the input to the prediction and clustering then executed by A.I. (machine learning) models.

Step (ii): Assessment of Tumor Staging through Statistical Learning

To create a system that supports the MTB in disease staging, the first step is to use a supervised learning technique for the training

TABLE 1A | Clinical features included in the three diagnostic exams and data types.

	Data Type	Clinical Feature Included in diagnosis	Clinical Feature Included in diagnosis	Clinical Feature Included in diagnosis
		MR	EUA	PET-CT
Parametrium involvement	*Categorical*	o	o	
Vaginal lower third involvement	*Categorical*	o	o	
Vaginal middle third involvement	*Categorical*	o	o	
Vaginal upper third involvement	*Categorical*	o	o	
Bladder involvement	*Categorical*	o	o	
Rectum involvement	*Categorical*	o	o	
Vesico-vaginal septum involvement	*Categorical*	o	o	
Recto-vaginal septum involvement	*Categorical*	o	o	
Hydronephrosis	*Categorical*	o		
Lymph nodes involvement	*Categorical*	o		
Lymph nodes activity	*Quantitative*			o
Cervical lesion	*Categorical*	o	o	
Cervical activity	*Quantitative*			o
Fornix involvement	*Categorical*	o	o	
Stroma involvement	*Categorical*	o	o	
Methabolic activity	*Quantitative*			o
"Other" activity	*Quantitative*			o

MR: Magnetic resonance; EUA: Examination under anesthesia; PET-CT, Positron Emission Tomography–Computed Tomography.

set, where tumor stage was known *a priori* for each patient in this group. This was achieved by applying clustering methods to classify patients based on similarity in their clinical feature pattern (the summary view as in **Figure 1**) and in their diagnosed staging. When applying clustering algorithms for each of the 3 diagnostic methods separately (MR, EUA, PET-CT) seven groups for each of the three diagnoses were generated, with a good degree of discrimination. Once the clusters have been created in the training set, a machine learning algorithm has then been used to build a predictive model for the staging based on composition of the clusters. "Decision Tree" algorithms have been adopted, using the SAS Vyia ® analytics and modeling features.

Finally, a validation step has been performed on a new set of patients to predict their staging based on the trained Decision Tree model, testing the validity of the model.

RESULTS

The system has been firstly used to retrieve, with an automated extraction procedure, all the eHR for 96 patients with histological proven LACC. This represented and has been used as the training set of the study, with validated 2009 FIGO staging classification ranging from IB2 to IVA as output.

TABLE 1B | Example of a patient's pattern with convergent and conflicting features.

	Data Type	Clinical Feature Inspected (Y/N)	Clinical Feature Inspected (Y/N)	Clinical Feature Inspected (Y/N)
		MR	EUA	PET-CT
Parametrium involvement	*Categorical*	Y	Y	
Vaginal lower third involvement	*Categorical*	N	N	
Vaginal middle third involvement	*Categorical*	N	N	
Vaginal upper third involvement	*Categorical*	N	N	
Bladder involvement	*Categorical*	N	N	
Rectum involvement	*Categorical*	N	N	
Vesico-vaginal septum involvement	*Categorical*	N	N	
Recto-vaginal septum involvement	*Categorical*	Y	N	
Hydronephrosis	*Categorical*	N		
Lymph nodes involvement	*Categorical*	Y		
Lymph nodes activity	*Quantitative*			Y
Cervical lesion	*Categorical*	Y		
Cervical activity	*Quantitative*			Y
Fornix involvement	*Categorical*		Y	
Stroma involvement	*Categorical*	Y		
Methabolic activity	*Quantitative*			N
"Other" activity	*Quantitative*			N

MR: Magnetic resonance; EUA: Examination under anesthesia; PET-CT, Positron Emission Tomography–Computed Tomography; Y, yes; N, no.

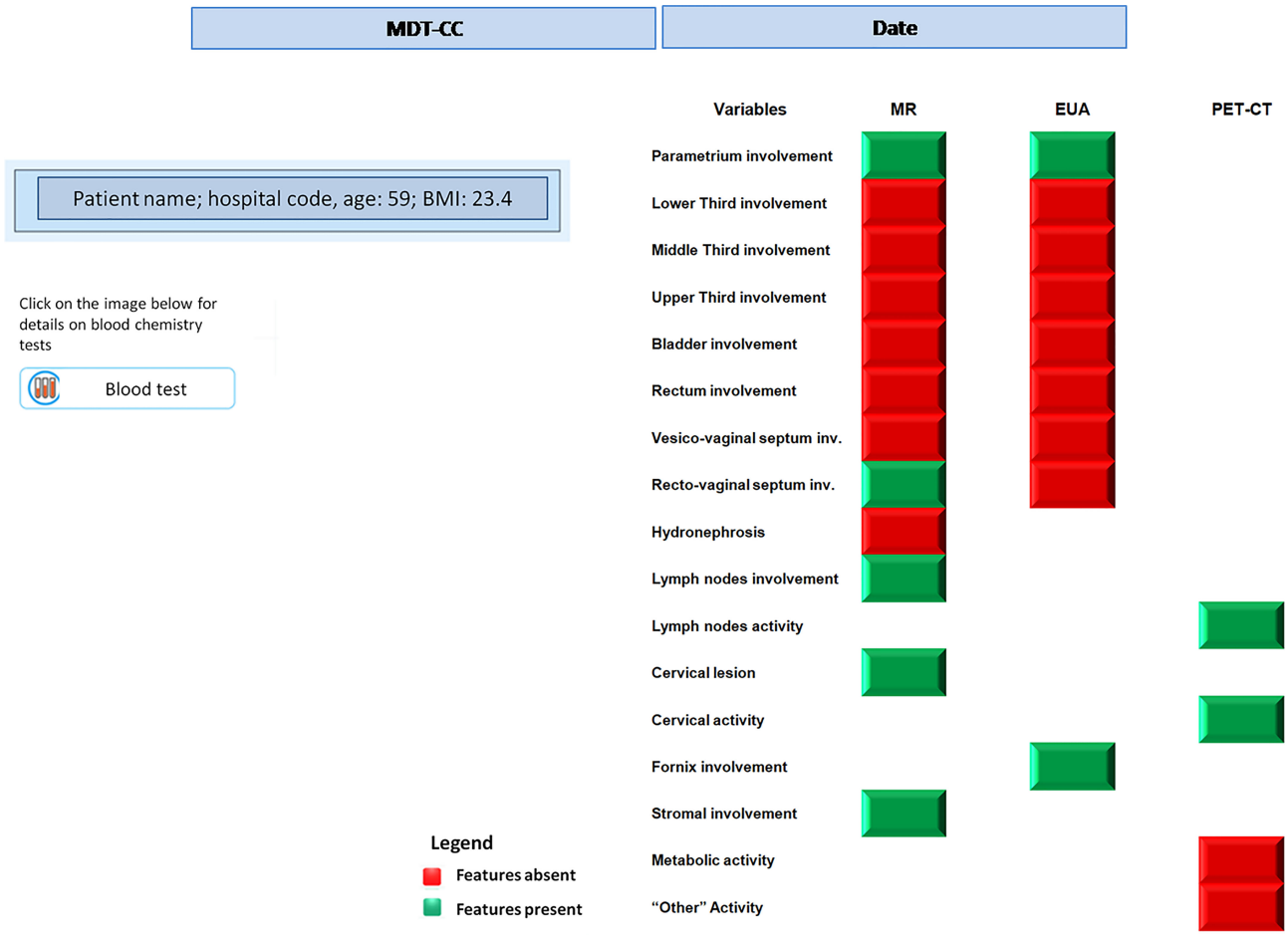

FIGURE 1 | Example of dashboard showing clinical features from three diagnoses.

The available eHR included MR, EUA, and PET-CT diagnostic reports for all these patients.

The system resulted to be able to classify all patients belonging to the training set and - through NLP procedures - the clinical features were analyzed and classified for each patient. This analysis provided the patient-specific summary dashboard shown in **Figure 1** (desktop MTB team dashboard, which corresponds to **Table 1B**). This highlights how the different diagnostic methods have identified which areas have been impacted by the tumor progression (i. e. presence/absence of the disease in different regions) and the main activity levels. Again, this 'clinical feature pattern' also highlights when two different diagnostic methods have provided different outcomes for a given area, which is critical to identify patients who require a more thorough analysis during the MTB meetings.

In addition, the clinical staff can retrieve other clinical parameters of interest directly from the system, such as laboratory exams, biomarkers, risk factors – and it is always possible to get the direct access to medical reports and compare them as shown in **Figure 2**.

Next, we focused on the development of predictive models for the 2009 FIGO staging classification based on the 96-patients worth training set and using a set of Decision Tree machine learning algorithms, obtaining a patient's staging prediction accuracy of 94%.

The model uses clinical features extracted and classified from the MR and the EUA reports. Even higher accuracy (98%) can be achieved integrating the input from the PET-CT.

However, we consider the staging prediction coming from MR and EUA combined as a more solid base for predictive methods, as these two exams evaluate the same morphological and anatomical indicators. In addition, they represent a consistent and replicable set of diagnosis that can be exported to other medical centers quite easily. Once the information dashboard and predictive model have been designed based on the training set, we have put focus in creating a user-oriented operational tool targeting the MTB and the clinical teams who

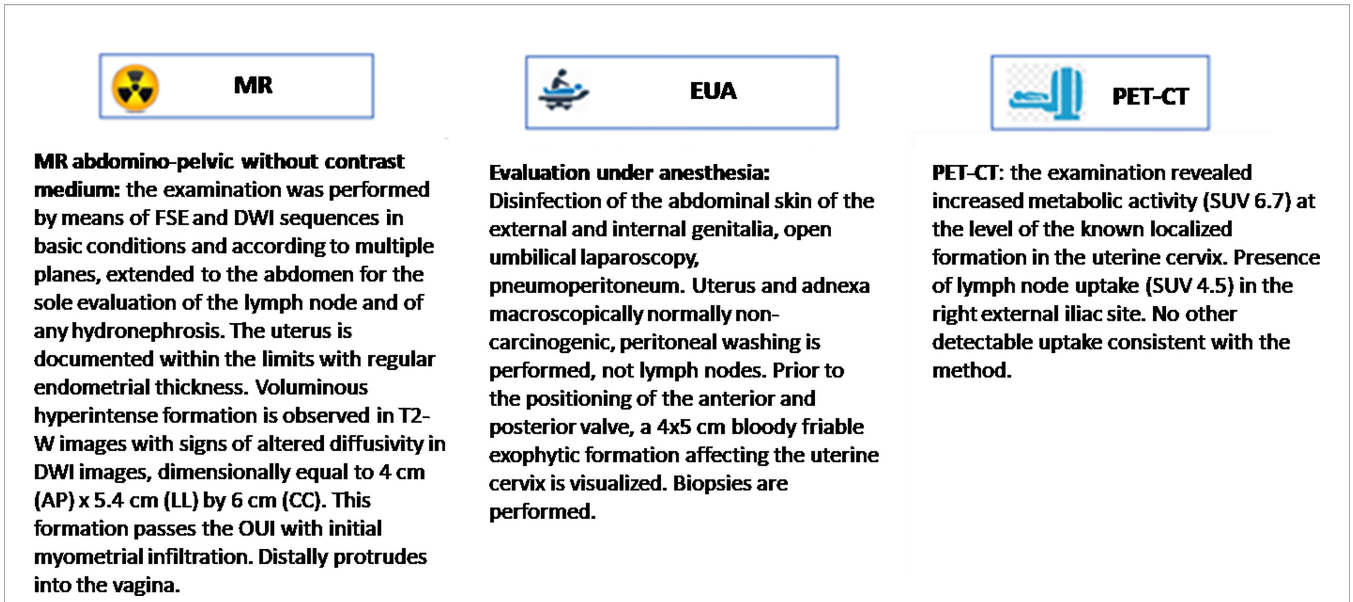

FIGURE 2 | Example of dashboard included in Virtual Assistant that compare medical reports.

are confronted with the challenge of large volumes of patients to be diagnosed in the most accurate way. The resulting decision support system is summarized in **Figure 3** in a logical diagram.

The flow to support the MTB is designed as follows:

- when a new patient is prepared for the discussion at the MTB, the system performs the following processing steps: (i) automatic retrieval of eHR and other clinical data; (ii) NLP based transformation of the free text reports into structured clinical features that characterize the single patient, on the basis of the three diagnostic exams (MR; EUA; PET-CT); (iii) clustering of patients according to the clinical features patterns; (iv) machine-learning based prediction of the pre-diagnostic FIGO staging;
- once the steps described above have been completed (in near-real time) for any new patient, the MTB staff will be able to consult the list of patients covered in the board discussion on

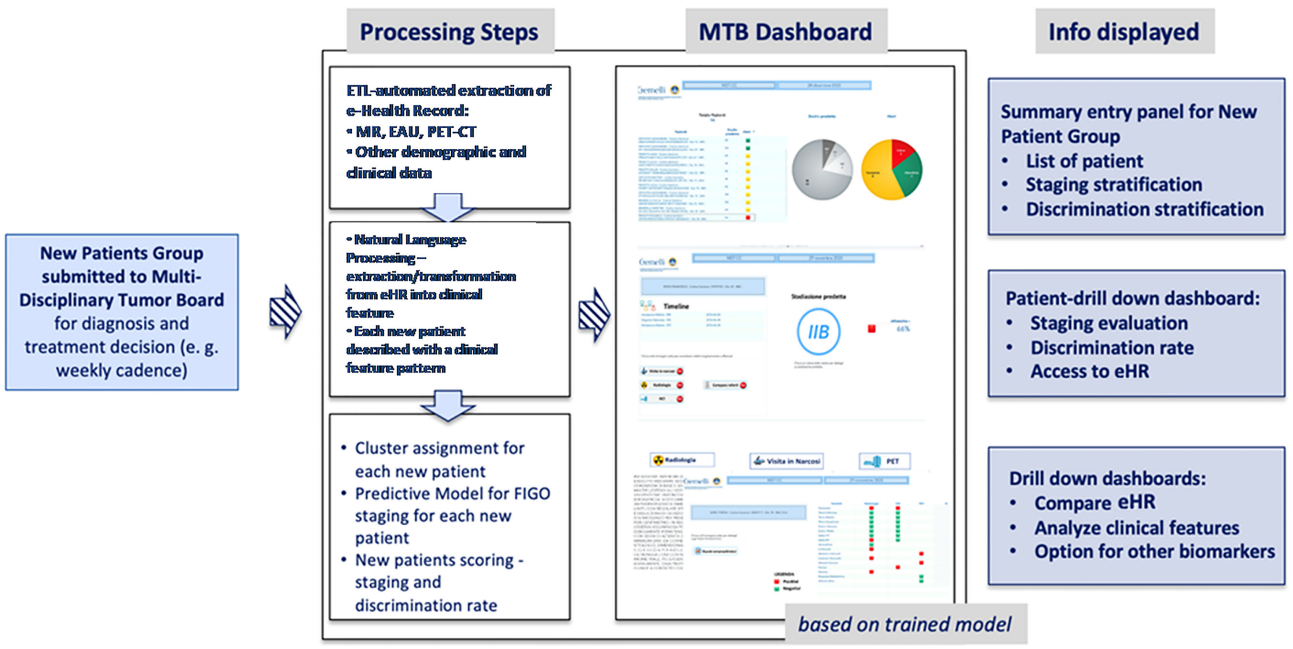

FIGURE 3 | Logical view of the Virtual Assistant dashboard and use in Multidisciplinary Tumor Board.

the system dashboard and the assessment of FIGO staging based on machine learning. The system provides also an alert that signals the degree of discrepancies in the diagnostic results which may impact the discrimination power (**Figure 4**) – the scoring in the dashboard will be low in case of controversial results. From there, the clinical team can navigate through the system, giving priority to the most critical patients (i.e., the patients where the model shows the lowest discrimination power, as in the example in **Figure 5**, where the A.I. model shows a low discrimination power, 66%, due to discrepancies in the different diagnostics);

- as already mentioned, from the single panel view of the critical patients, the MTB can get to a deeper view by analyzing the specific clinical features classification from the three exams (**Figure 1**). This drill-down may highlight clinical features where two exams have led to different interpretations from two specialists (e.g., radiologist and nuclear medicine physician), which in itself would trigger more discussion in the board.

Ultimately, the clinical team may want to compare the eHR items that originated the discrepancies, which would be immediately available in the system (**Figure 2**).

In order to test the effectiveness of the overall approach, the system has been tested with an independent group of 13 patients (whose features have not been used in the Training Set), confirming overall positive performances.

After all the medical reports were retrieved, the NLP system proceeded in classifying all patients in detail through their patterns of clinical features: the predictive model for FIGO staging has shown an accuracy of 93%, substantially confirming the performances observed in the training set.

DISCUSSION

A proof-of-concept for an integrated framework for automated classification of disease staging, and a Clinical Decision Support System in the multidisciplinary management of LACC is reported.

Using NLP, we have trained and validated a biomedical imaging report analyzer that performs a smart "automated classification" of the LACC stage. As a primary staging method, the algorithm trained using digital MR, PET-CT and EUA reports from the cohort used in the Training Set, achieved excellent accuracy when matched with the prediction of the stage.

The performance compared favorably to clinical staging and was confirmed to the same levels of accuracy when tested in the independent Validation Set. Notably, the reports were performed by different physicians without using a common template, so even though the task for the software was complex and prone to misinterpretation, it was successful.

To the best of our knowledge this is the first prototype aimed at supporting effectively a MTB in the prioritization and analysis of the most critical cases. The intuitive Graphical User Interface allows an easy detection of discrepancies among the imaging reports, so, rather than focusing on the clinical cases without diagnostic uncertainties whose treatment should be an easy skill, the software suggests the specialists to focus their attention on the most critical cases, optimizing both human and time resources, dedicating more quality time to deep discussion and achieving a more robust data-driven consensus.

In a large-volume scenario as well as in a low- resources setting, the implementation of an automatic tool as the one described could have a very relevant impact as supported by the promising results of this proof-of-concept.

Obviously, this tool is not intended to replace the tumor board's discussion of clinical situations, even in circumstances when the UAE and MR are in agreement. At truth, reports frequently underpin parts that aren't written, but are assessed in multidisciplinary meetings (e.g. some poor detection of the outer cervical stroma that is not a sure sign of parametrial invasion).It has to be considered as a facilitator of the decisional process and a tool to make MTD meetings go faster even if there are numerous clinical cases to be discussed.

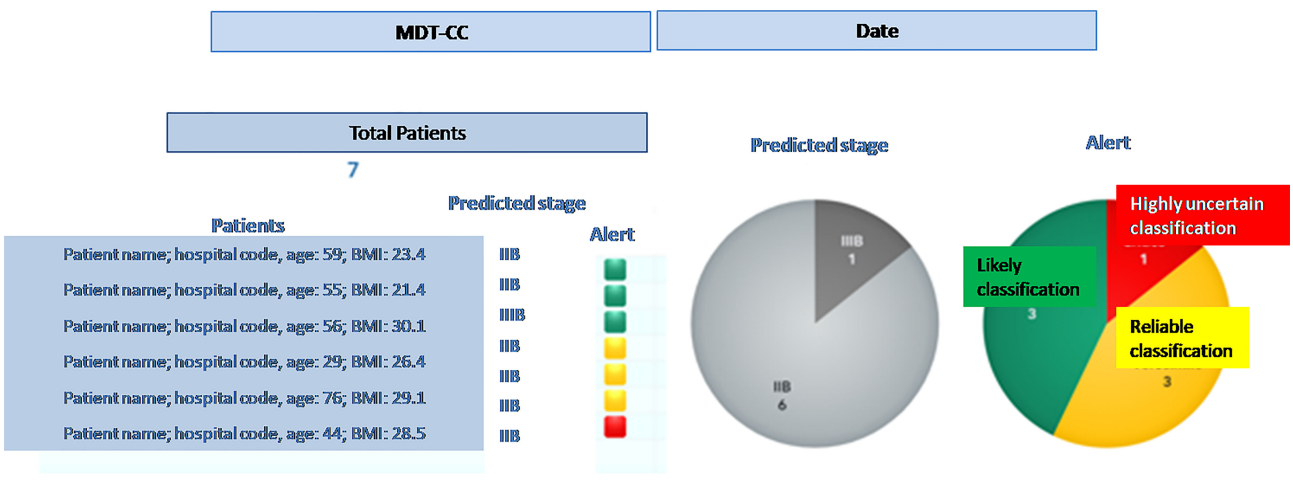

FIGURE 4 | Entry dashboard that classify incoming patients for the Multidisciplinary Tumor Board session.

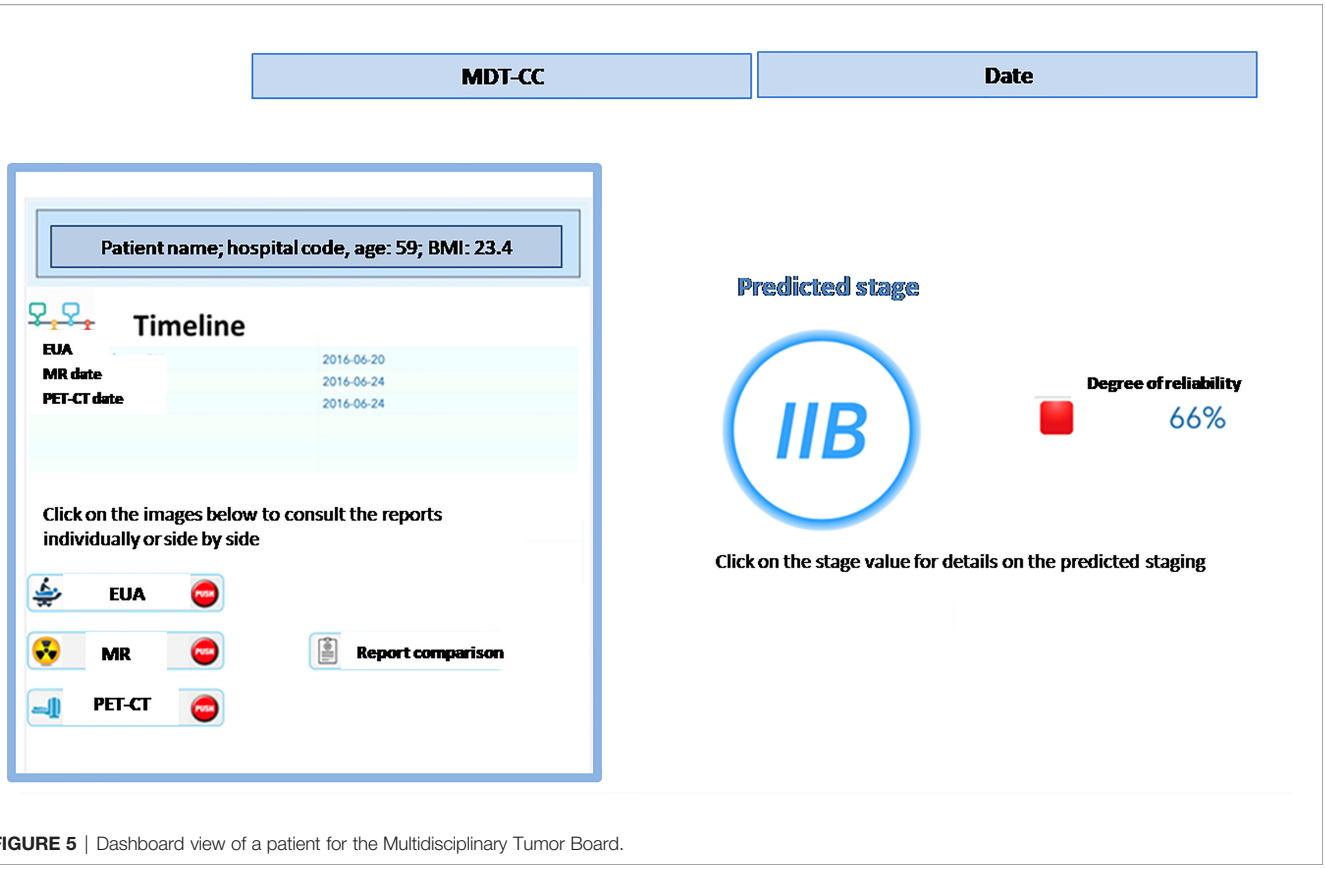

FIGURE 5 | Dashboard view of a patient for the Multidisciplinary Tumor Board.

The approach proposed in this paper is – to the best of our knowledge – quite novel and can complement other AI-based technologies experienced in other research projects (4, 14). As an example, radiology-focused applications aim to automate and streamline analytical tasks in order to improve the efficiency, accuracy, and consistency in the interpretation of the radiological imaging (e.g., computer aided detection and diagnosis software, i.e., CADe and CADx). Similarly, computer aided triage (CADt) software analyzes images to prioritize the review of images for patients with potentially time sensitive findings. Another promising area of growth is the use of AI to set up a Clinical Decision Support System for the treatment of cancer (e.g., IBM "Watson for Oncology" software). The latter stores and indexes literature, protocols, and patient charts, learning from test cases; thereafter, all the information input is verified by the experts from Memorial Sloan Kettering Cancer Center (15).

Albeit very focused and specific for LACC, this proof of concept could be easily adapted and extended to other cancer settings, demonstrating the favorable scalability of the provided structure. There is, in fact, much room for re-use of the many pivotal components:

- Extract/Transform/Load (ETL) automated extraction and following NLP clinical features classification;
- machine-learning based predictive model for FIGO staging, which can be trained on different patient set, classification system and endpoints;
- overall navigation and drill-down to different layers of information, to allow the MTB for a data-supported analysis and discussion (thus promoting collaborative methods and integration of skills).
- especially in the Covid 19 era where MTBs are performed increasingly in virtual/online mode, this system offers a remote collaborative platform into the hospital and among hospitals.

Furthermore, as already suggested by Bizzo et al. (16), A.I. can help drive the field toward more structured reporting from different specialists, which is critical for an effective MTB and serves as the basis for a "virtuous cycle" in creating additional data for A.I. to improve upon.

Moreover, a further strength of the proposed approach is represented by the machine-learning and clustering methods - used in connection with NLP and understanding of clinical features from diagnoses – that allowed us to identify patients' phenotypes which are not characterized only through the FIGO staging and can be especially useful for future prognostic models able to predict the complete pathological response, as well as other prognostic outcomes.

Lastly, new prospective clinical scenarios such as the possibility to introduce into the software other clinical tools that could be useful for early cervical cancer characterization can be speculated. For example, the addition of cervix clinical morphology and characterization by colposcopy images or

ultrasound measurements to the MTB Smart Virtual Assistant software could be quite useful in determining whether or not to employ conization in early cervical cancer. Some literature data are already available and could form the basis for a future integration project (17–20).

In terms of future developments starting from this proof of concept, we consider strategic the following key points:

- enlarge the training and validation cohort by recruiting patients coming from our center as well as other institutions: the increased cohort will allow to further improve the NLP effectiveness and predictive system accuracy;
- use of this setting as a base for an end-to-end model; covering also the re-staging and the pathological response definition; in this way, we could be able to provide further insights to the MTB not only at the diagnostics phase, but also along the treatment and the follow-up.
- extend to other languages (e.g., English), possibly integrating existing NLP system for eHR transformation and then connecting our clustering and predictive methodologies: this transformation could allow a widely dissemination.

In conclusion, while this prototype should still be considered as first proof of concept of the possibility of creating a Smart Virtual Assistant for MTB, we believe that this experience discloses a significant benefit in the integration of these automated methods in the collaborative, crucial decisional steps, giving clinicians the opportunity to save time by optimizing the duration of multidisciplinary meetings, to consolidate information and leverage data-driven evidence that would be not achievable in the more traditional settings and decisional workflows.

DATA AVAILABILITY STATEMENT

The raw data supporting the conclusions of this article will be made available by the authors, without undue reservation.

ETHICS STATEMENT

Ethical approval was not provided for this study on human participants because the project has received approval and has been reviewed by the Scientific Director of IRCCS Policlinico Gemelli. The patients/participants provided their written informed consent to participate in this study. Written informed consent was obtained from the individual(s) for the publication of any potentially identifiable images or data included in this article.

AUTHOR CONTRIBUTIONS

Conception and design, GM, SP, and VV. Revision of study design and protocol, GF, GM, AC, RA, LB, and CC. Study coordination, GM, SP, RA, and CM. Acquisition of data and patient recruitment, VP, CC, CI, BG, VR, MG, and VV. Radiotherapy quality check (of protocol), GM, RA, VV, and LB. Data management and statistical analysis, SP, VP, CI, CC, and CM. Revision of adaptation of and final approval of manuscript, all authors. Accountable for all aspects of the work, all authors. All authors contributed to the article and approved the submitted version.

REFERENCES

1. Abernethy AP, Etheredge LM, Ganz PA, Wallace P, German RR, Neti C, et al. Rapid-Learning System for Cancer Care. *J Clin Oncol* (2010) 28(27):4268–74. doi: 10.1200/JCO.2010.28.5478
2. Ahmed Z, Mohamed K, Zeeshan S, Dong X. Artificial Intelligence With Multi-Functional Machine Learning Platform Development for Better Healthcare and Precision Medicine. *Database (Oxford)* (2020) 2020: baaa010. doi: 10.1093/database/baaa010
3. Briganti G, Le Moine O. Artificial Intelligence in Medicine: Today and Tomorrow. *Front Med (Lausanne)* (2020) 7:27. doi: 10.3389/fmed.2020.00027
4. Kim MS, Park HY, Kho BG, Park CK, Oh IJ, Kim YC, et al. Artificial Intelligence and Lung Cancer Treatment Decision: Agreement With Recommendation of Multidisciplinary Tumor Board. *Transl Lung Cancer Res* (2020) 9(3):507–14. doi: 10.21037/tlcr.2020.04.11
5. Ferrandina G, Margariti PA, Smaniotto D, Petrillo M, Salerno MG, Fagotti A, et al. Long-Term Analysis of Clinical Outcome and Complications in Locally Advanced Cervical Cancer Patients Administered Concomitant Chemoradiation Followed by Radical Surgery. *Gynecol Oncol* (2010) 119:404–10. doi: 10.1016/j.ygyno.2010.08.004
6. Macchia G, Ferrandina G, Legge F, Deodato F, Ruggieri V, Lorusso D, et al. Prolonged Chemoradiation in Locally Advanced Carcinoma of the Uterine Cervix: Final Results of a Phase II Study (ESTER-1). *Am J Clin Oncol* (2010) 33:577–82. doi: 10.1097/COC.0b013e3181b9cf5c
7. Macchia G, Ferrandina G, Deodato F, Ruggieri V, Massaccesi M, Salutari V, et al. Concomitant Boost Dose Escalation Plus Large-Field Preoperative Chemoradiation in Locally Advanced Carcinoma of the Uterine Cervix: Results of a Phase I Study (LARA-CC- 1). *Gynecol Oncol* (2010) 118:128–33. doi: 10.1016/j.ygyno.2010.04.017
8. Macchia G, Morganti AG, Deodato F, Cilla S, Lucidi A, Massaccesi M, et al. Concomitant Boost Plus Large-Field Preoperative Chemoradiation in Locally Advanced Uterine Cervix Carcinoma: Phase II Clinical Trial Final Results (LARA-CC-1). *Gynecol Oncol* (2012) 125:594–9. doi: 10.1016/j.ygyno.2012.03.008
9. Macchia G, Cilla S, Deodato F, Legge F, Di Stefano A, Chiantera V, et al. Intensity-Modulated Extended-Field Chemoradiation Plus Simultaneous Integrated Boost in the Pre-Operative Treatment of Locally Advanced Cervical Cancer: A Dose-Escalation Study. *Br J Radiol* (2015) 88 (1055):20150385. doi: 10.1259/bjr.20150385
10. Ferrandina G, Palluzzi E, Gallotta V, Gambacorta MA, Autorino R, Turco LC, et al. Neo-Adjuvant Platinum-Based Chemotherapy Followed by Chemoradiation and Radical Surgery in Locally Advanced Cervical Cancer (LACC) Patients: A Phase II Study. *Eur J Surg Oncol* (2018) 44(7):1062–8. doi: 10.1016/j.ejso.2018.04.019
11. Pons E, Braun LM, Hunink MG, Kors JA. Natural Language Processing in Radiology: A Systematic Review. *Radiology* (2016) 279(2):329–43. doi: 10.1148/radiol.16142770
12. SAS Institute Inc. *SAS® Visual Text Analytics 8.4: User's Guide*. Cary, NC: SAS Institute Inc (2019).
13. Murri R, Lenkowicz J, Masciocchi C, Iacomini C, Fantoni M, Damiani A, et al. A Machine-Learning Parsimonious Multivariable Predictive Model of Mortality Risk in Patients With Covid-19. *Sci Rep* (2021) 11(1):21136. doi: 10.1038/s41598-021-99905-6
14. Zhou N, Zhang CT, Lv HY, Hao CX, Li TJ, Zhu JJ, et al. Concordance Study Between IBM Watson for Oncology and Clinical Practice for Patients With

Cancer in China. *Oncologist* (2019) 24(6):812–9. doi: 10.1634/theoncologist.2018-0255
15. Somashekhar SP, Sepúlveda MJ, Puglielli S, Norden AD, Shortliffe EH, Rohit Kumar C, et al. Watson for Oncology and Breast Cancer Treatment Recommendations: Agreement With an Expert Multidisciplinary Tumor Board. *Ann Oncol* (2018) 29:418–23. doi: 10.1093/annonc/mdx781
16. Bizzo BC, Almeida RR, Michalski MH, Alkasab TK. Artificial Intelligence and Clinical Decision Support for Radiologists and Referring Providers. *J Am Coll Radiol* (2019) 16(9 Pt B):1351–6. doi: 10.1016/j.jacr.2019.06.010
17. Chandran V, Sumithra MG, Karthick A. Diagnosis of Cervical Cancer Based on Ensemble Deep Learning Network Using Colposcopy Images. *BioMed Res Int* (2021) 2021:5584004. doi: 10.1155/2021/5584004
18. Hu L, Bell D, Antani S. An Observational Study of Deep Learning and Automated Evaluation of Cervical Images for Cancer Screening. *J Natl Cancer Inst* (2019) 111(9):923–32. doi: 10.1093/jnci/djy225
19. Shao J, Zhang Z, Liu H. DCE-MRI Pharmacokinetic Parameter Maps for Cervical Carcinoma Prediction. *Comput Biol Med* (2020) 118:103634. doi: 10.1016/j.compbiomed.2020.103634
20. Tomao F, Maruccio M, Preti EP, Boveri S, Ricciardi E, Zanagnolo V, et al. Conization in Early Stage Cervical Cancer: Pattern of Recurrence in a 10-Year Single-Institution Experience. *Int J Gynecol Cancer* (2017) 27(5):1001–8. doi: 10.1097/IGC.0000000000000991

Conflict of Interest: The authors declare that the research was conducted in the absence of any commercial or financial relationships that could be construed as a potential conflict of interest.

Publisher's Note: All claims expressed in this article are solely those of the authors and do not necessarily represent those of their affiliated organizations, or those of the publisher, the editors and the reviewers. Any product that may be evaluated in this article, or claim that may be made by its manufacturer, is not guaranteed or endorsed by the publisher.

frontiers in Oncology

ORIGINAL RESEARCH
published: 13 January 2022
doi: 10.3389/fonc.2021.796317

The Role of MRI Pancreatic Protocol in Assessing Response to Neoadjuvant Therapy for Patients With Borderline Resectable Pancreatic Cancer

Nervana Hussien[1†], Rasha S. Hussien[2†], Darine Helmy Amin Saad[3‡], Mohamed El Kassas[4†], Walid F. Elkhatib[5,6†] and Mai Ezz El Din[7†]*

[1] Department of Clinical Oncology, Faculty of Medicine, Helwan University, Cairo, Egypt, [2] Department of Radiology, Faculty of Medicine, Ain Shams University, Cairo, Egypt, [3] Department of Biological Anthropology, National Research Centre, Cairo, Egypt, [4] Department of Endemic Medicine, Faculty of Medicine, Helwan University, Cairo, Egypt, [5] Department of Microbiology and Immunology, Faculty of Pharmacy, Ain Shams University, Cairo, Egypt, [6] Department of Microbiology & Immunology, Faculty of Pharmacy, Galala University, Suez, Egypt, [7] Department of Clinical Oncology, Faculty of Medicine, Ain Shams University, Cairo, Egypt

Background: Borderline Resectable Pancreatic Cancer (BRPC) remains a unique entity that is difficult to categorize due to variance in definitions and the small number of patients. The ultimate goal is to achieve a free resection (R0) after a favorable response to neoadjuvant therapy that is somewhat difficult to assess by current radiological parameters.

Aim: To evaluate the role of Magnetic Resonance Imaging (MRI) pancreatic protocol, including Diffusion-Weighted Imaging (DWI), in patients with BRPC receiving neoadjuvant therapy, and further compare it to RECIST criteria and outcome.

Methods: Histologically confirmed BRPC patients were prospectively included. DWI-MRI was performed pre- and post-therapy. Clinical characteristics with ensuing operability were recorded and correlated to radiological RECIST/apparent diffusion coefficient (ADC) change, preoperative therapy administrated, surgical resection status, and survival.

Results: Out of 30 BRPC cases, only 11 (36.7%) ultimately underwent pancreaticoduodenectomy. Attaining a stationary or stable disease *via* ADC/RECIST was achieved in the majority of cases (60%/53.3% respectively). Of the 12 patients (40%) who achieved a regression by ADC, 11 underwent surgery with an R0 status. These surgical cases showed variable RECIST responses (PR=5, SD=4, PD=3). Responders by ADC to neoadjuvant therapy were significantly associated to presenting with abdominal pain ($p = 0.07$), a decline in post-therapy CA19-9 ($p<0.001$), going through surgery ($p<0.001$), and even achieving better survival ($p<0.001$ *vs.* 0.66).

Conclusion: DWI-MRI ADC picked up patients most likely to undergo a successful operative procedure better than traditional RECIST criteria. An algorithm incorporating novel radiological advances with CA19-9 deserves further assessment in future studies.

Keywords: borderline resectable pancreatic cancer, ADC, radiological assessment, RECIST criteria, DWI-MRI

OPEN ACCESS

Edited by:
Fu Wang,
Xi'an Jiaotong University, China

Reviewed by:
Stefano Francesco Crinò,
University of Verona, Italy
Matteo De Pastena,
University of Verona, Italy

****Correspondence:***
Nervana Hussien
nervana.hussien@med.helwan.edu.eg

†ORCID:
Nervana Hussien
orcid.org/0000-0002-4238-583X
Rasha S. Hussien
orcid.org/000-0001-6599-1237
Mohamed El Kassas
orcid.org/0000-0002-3396-6894
Walid F. Elkhatib
orcid.org/0000-0001-5815-3200
Mai Ezz El Din
orcid.org/0000-0002-2109-606X

‡Scopus ID:
Darine Helmy Amin
Scopus ID: 57215047304

Specialty section:
This article was submitted to Cancer Imaging and Image-directed Interventions, a section of the journal Frontiers in Oncology

Received: *18 October 2021*
Accepted: *06 December 2021*
Published: *13 January 2022*

Citation:
Hussien N, Hussien RS, Saad DHA, El Kassas M, Elkhatib WF and Ezz El Din M (2022) The Role of MRI Pancreatic Protocol in Assessing Response to Neoadjuvant Therapy for Patients With Borderline Resectable Pancreatic Cancer. Front. Oncol. 11:796317. doi: 10.3389/fonc.2021.796317

INTRODUCTION

Renowned for its grim outlook, pancreatic malignancies herald a dismal prognosis, with the surgical option serving as the only potential niche for this grave malignancy (1). The emergence of the concept of borderline pancreatic ductal adenocarcinoma (BPDAC) is a small subset of patients that deserves recognition, and many have set out to define this category mainly based on the imaging acquired. Nevertheless, the operating theater acts as the real test if these patients may undergo an actual curative resection or not (2). Because of its excellent accuracy and low complication rate, endoscopic ultrasound-guided fine needle aspiration (EUS-FNA) (or biopsy) is a first-line technique for conclusive tissue diagnosis of pancreatic cancer (3, 4). However, EUS-FNA has some limitations in its diagnostic abilities especially in relatively small tumors, in addition to its limited availability and practice difficulty issues in some resource limited health care settings (5). As radiological diagnostic advances have continued to detect and set the scene for this potentially curative procedure, it remains yet challenging to select those operable cases correctly (6).

A notable quality improvement in detecting and characterization of pancreatic ailments is diffusion-weighted (DW) magnetic resonance (MR). This technique has the added advantage of the relatively quick performance, minus the need for gadolinium-based contrast agents, and offers a measure for tissue diffusion (diffusion coefficients). DW MR imaging utilizes the motion of water molecules in biologic tissues; thus, a restricted signal intensity (or impeded) results in a low apparent diffusion coefficient (ADC) on ADC maps and high signal intensity on DW MR images, and *vice versa* (4).

Therefore, having impeded free water diffusion due to high cell density and fibrosis, a feature of malignancy such as pancreatic carcinoma presents with low ADC compared to healthy pancreatic tissue (7, 8). On the other hand, when water molecules are agile, for example, in necrotic tissue post-treatment, this is reflected by higher ADC values (9). Pancreatic adenocarcinoma has a mean ADC 1.33×10^{-3} mm^2/s with a range of 0.78 $\times 10^{-3}$ to 2.32 $\times$ 10^{-3} mm^2/s reflecting the different amounts of cellular density admixed with necrosis and fibrosis (9).

This study aimed to evaluate the role of MRI pancreatic protocol, including Diffusion-Weighted Imaging (DWI) in patients with borderline resectable pancreatic adenocarcinoma after neoadjuvant therapy, to identify responders by MRI with surgical, histopathological, and outcome data.

PATIENTS AND METHODS

A prospective study of subjects with BRPC who received their treatment at Helwan and Ain Shams University Hospitals was performed. The study was granted ethical Institutional Review Board approval. The NCCN criteria were used to define Borderline resectable pancreatic cancer as any tumor radiologically in contact with major peripancreatic vasculature as the portal vein (PV) or superior mesenteric vein (SMV) that was deemed resectable (+/− reconstruction) or <180° involvement of the common hepatic artery (CHA) or superior mesenteric artery (SMA) without any tumor extension reaching the celiac axis (CA) or hepatic artery bifurcation (10). Metastatic, resectable, and locally advanced cases were excluded. Treatment naïve patients lacking severe comorbidities with an Eastern Cooperative Oncology Group (ECOG) performance status 0–2 were included. Neoadjuvant chemotherapy (gemcitabine-based or FOLFIRINOX) was administered for six cycles.

EUS-FNA was conducted under deep sedation with intravenous midazolam, propofol, and fentanyl administration, by highly experienced endsonographers in the study centers. Pentax linear echoendoscope EG-3870UTK (PENTAX Medical, Tokyo, Japan, insertion tube of 12.8 mm, biopsy channel of 3.8 mm), with a Hitachi–Aloka Avius processor (Hitachi, Tokyo, Japan), was used for obtaining EUS-FNA. Under EUS guidance, and with the assistance of Color Doppler to exclude interfering vasculature, tissue acquisition was performed using specific EUS needles. The gained material was processed by preserving in 10% neutral-buffered formalin fixative for the creation of a tissue block. The remnant of the aspirated sample was to be smeared on a glass slide and fixed immediately in 95% ethyl alcohol for subsequent staining. All samples were examined by an experienced cytopathologist.

All patients underwent dedicated pancreatic MRI before and after treatment by the fourth week. ADC maps were acquired, and the mean ADC value of the mass was calculated before and after treatment. Also, the longest dimension was measured on T2WI before and after treatment. Vascular relations were assessed on the dynamic study.

MR Imaging Protocol

The study was performed on a 3.0-T MRI system (MAGNETOM Skyra; Siemens Healthcare, Erlangen, Germany) with an 18-element body phased array coil and a 32-element spine array coil. Before contrast injection, anatomical MRI was performed, including axial T2-weighted (T2W) HASTE (half-Fourier acquisition single-shot turbo spin-echo) with controlled respiration, without and with fat suppression (FS); coronal T2-weighted HASTE without FS; coronal and axial T2/T1TrueFISP; axial 3D T1-weighted Volumetric Interpolated Breath-hold Examination (VIBE) with Dixon reconstruction D (in-phase, out-of-phase, fat-only, and water only images) in breath-holding.

Gadolinium-based contrast was given intravenously using a power injector (Ulrich Medical® Tennessee TM, Germany) at an infusion rate of 1 ml/s. Then, T1-weighted breath-hold VIBE images with SPAIR fat suppression in the arterial, venous, and delayed phases were obtained. Subtracted images were computed as well. Details of sequence parameters are reported in **Table 1**.

Diffusion-Weighted Imaging

DWI was performed using a single-shot echo-planar imaging (EPI) pulse sequence during free breathing. A parallel imaging technique was used to reduce the echo train length. Monopolar gradients were utilized to perform a 3D diagonal encoding with the following b-value(s): 0, 400, and 800 s/mm^2.

TABLE 1 | Sequence parameters for MRI pancreatic protocol.

Sequence	TR/TE	Matrix	FOX	Slice thickness	Intersection gap	Acquisition time
T2-HASTE	2200/95	320 × 259 mm	350 × 317 mm	5.0 mm	0.1 mm	1.46 s
T2/T1TrueFISP	426/1.68	256 × 256 mm	377 × 303.5 mm	5.0 mm	0	0.21 s
3D T1-VIBE	4.0/1.31	320 × 182 × 160 mm	400 × 325 mm	3.0 mm	0.6 mm	0.17
DWI	7,100/56	128 × 128 mm	380 × 308 mm	4.0 mm	0.08 mm	3.35 s

Multidisciplinary consultation was done to assess response and resectability accordingly. Response Evaluation Criteria in Solid Tumors (RECIST) version 1.1 (11) was utilized to measure neoadjuvant therapy effect coupled with MRI ADC value, all through pancreatic protocol MRIs pre- and post-therapy. The pathological completeness of margins (R status) was reported in patients who underwent the procedure.

Data on treatment, response to neoadjuvant chemotherapy by RECIST 1.1, degree of resection (R status), outcome, and survival were collected.

The primary objective was to assess the response rate by RECIST and ADC values utilizing MRI pre- and post-neoadjuvant chemotherapy and then correlate this to the resection margin outcome. The secondary objectives were overall survival (OS) and relapse-free survival (RFS) assessment and their relation to the response parameters (RECIST and ADC value) as well as their relation to the various baseline characteristics.

Overall survival was defined as the time interval between the date of diagnosis and the date of death. The definition of RFS was from the date of diagnosis till the date of cancer recurrence (surgical cases; disease-free survival—DFS)/progression (non-surgical cases; progression-free survival—PFS).

A sample size of 30 patients was selected to achieve an 80% power to detect a mean of paired differences of 0.2 (pre and post mean ADC values) with an estimated standard deviation difference of 0.03 and with a significance value (alpha) of 0.05 based on the work by Dalah et al. (12).

Data analysis and interpretation were conducted using SPSS (Statistical Package for the Social Science; SPSS Inc., Chicago, IL, USA) version 22 for Microsoft Windows. Quantitative data were described as mean ± standard deviation (± SD) or median (interquartile range [IQR]) according to data normality, while qualitative data were expressed as frequencies and percentages. According to the data type, the association between data was tested using the Chi-square test with Fisher's exact, Mann-Whitney test, or one-way ANOVA. Survival data were recorded and tabulated using Kaplan Meier, and the log-rank test evaluated the differences in survival. Variables with a p-value of less than 5% were considered statistically significant.

RESULTS

A total of 30 patients with histopathologically proven PDAC were recruited, and all received neoadjuvant chemotherapy (gemcitabine-based or FOLFIRINOX). Pre- and post-chemotherapy MRI scans were compared, and after multidisciplinary assessment, 11 patients were deemed operable. Patient baseline characteristics are displayed in **Table 2**.

After a median follow-up of 14 months (IQR 10.75–22), 19 patients were alive (63.3%), resulting in a mean survival of 13.679 months (SE 1.009; 95% CI 11.702–15.656), while median OS that was not reached (NR) as seen in **Figure 1A**. When comparing survival for the surgical and non-surgical patients, 10 deaths were in the inoperable group, and only one died in the surgical series. The mean OS for the non-surgical cases was 8.51months (SE 0.377; 95% CI 7.77–9.25) and then for the surgical cases, 17.7 months (SE 0.285; 95% CI 17.14–18.25) as also seen in **Figure 1B**. The median OS for the surgical group was NR, and for the non-surgical group, it was 9 months (SE 0.459; 95% CI 8.101–9.899)

RFS in the whole cohort was set at a mean RFS of 10.16 months (SE 1.137; 95% CI 7.934–12.389) and a median of 9 months (SE

TABLE 2 | General characteristics of the study group (n=30).

Variable		Patients (n = 30)
Age in years, mean± SD (median; range)		52.5 ± 6.6 (53.5; 40–62)
Gender, No. (%)	Male	22 (73.3)
	Female	8 (26.7)
Presentation, No. (%)	Weight loss	26 (86.7)
	Abdominal pain	28 (93.3)
	Jaundice	14 (46.7)
ECOG performance, No. (%)	0	11 (36.7%)
	1	19 (63.3%)
CA19-9 U/ml median (range)	**Pre-treatment**	250 (100–400)
	Post-treatment	170 (20–285)
Site, No. (%)	Body	12 (40.0)
	Head	7 (23.3)
	Neck	5 (16.7)
	Tail	6 (20.0)
Neoadjuvant chemotherapy, No. (%)	Gemcitabine/cisplatin	11 (36.7)
	FOLFIRINOX	19 (63.3)
MRI involvement, No. (%)	Celiac, SMA	1 (3.3)
	Celiac, SMV	3 (10)
	Portal/SMA	10 (33.3)
	Portal/SMV	1 (3.3)
	SMA	5 (16.7)
	SMA, celiac, SMV/PV	1 (3.3)
	SMV/PV, SMA	9 (30)
ADC × 10^{-3} mm^2/s, median (range)	**Pre-treatment**	1.3 (1.1–1.4)
	Post-treatment	1.4 (1.3–1.7)
ADC response, No. (%)	Stationary	18 (60)
	Regressive	12 (40)
RECIST, No. (%)	SD	16 (53.3)
	PD	9 (30)
	PR	5 (16.7)
Surgery, No. (%)		11 (36.7)
R0 (n =11), No. (%)		11 (100)

PV, portal vein; SMA, superior mesenteric artery; SMV, superior mesenteric vein.

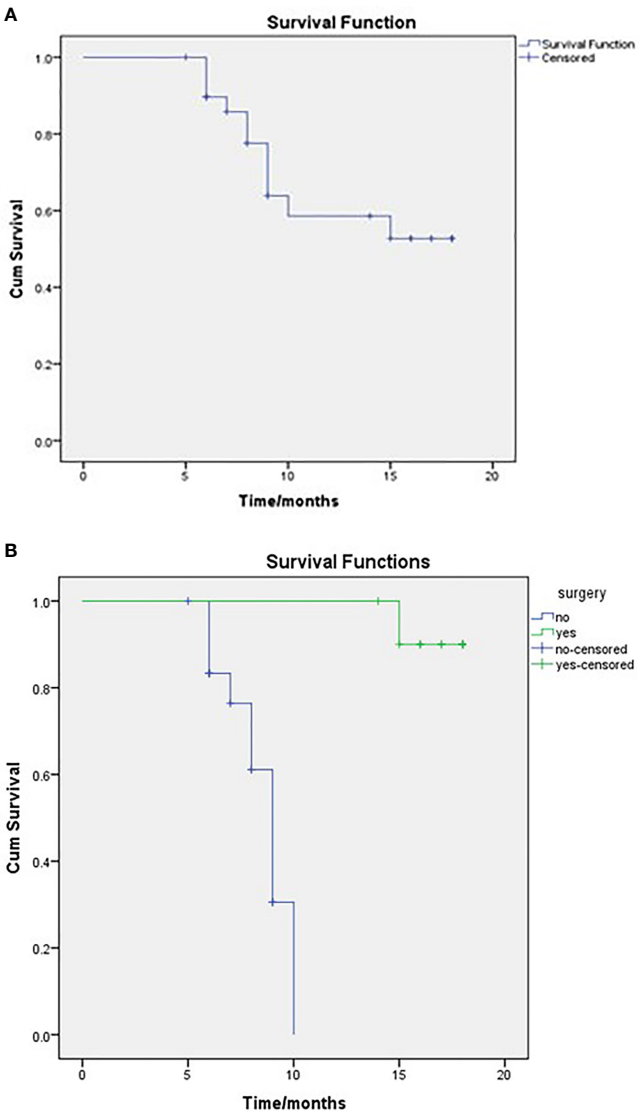

FIGURE 1 | OS of the entire study population **(A)** and comparison between surgical and non-surgical groups **(B)**, as regards to the mean OS for the non-surgical cases was 8.51 months and for the surgical cases 17.7 months. Log-rank, P = <0.001.

1.167; 95% CI 6.713–11.287). The non-surgical series had a mean PFS of 5.88 months (SE 0.576; 95% CI 4.751–7.008) and a median PFS of 5 months (SE 0.483; 95% CI 4.053–5.947).

Mean DFS for the surgical cases was 15.73 months (SE 1.21; 95% CI 13.529–17.925), and with three cases exhibiting recurrence (27.3%), median DFS was not reached, as evident in **Figure 2**.

Assessment for a response *via* RECIST and ADC values is depicted in **Table 3** and **Figure 3**, and it displayed a significant association (p= 0.007). However, it is of poor magnitude based on a kappa statistic of 0.29. The specific ADC value for the resected and non-resected cases is seen in **Table 3**, similarly displaying a significant difference. Discordant response between ADC and RECIST is further depicted in **Figures 4**, **5**.

When examining the median ADC values for all cases pre- and post-NACT, the main driver of a positive correlation overall (P-value 0.001) was more apparent in the surgical cases (P-value 0.003 *vs.* 0.29), as seen in **Table 4**. CA19-9 had a positive statistical significance for all cases, surgical or not, hence did not differentiate the two groups.

Attaining a regressive response (or response) to neoadjuvant therapy *via* ADC parameters was significantly associated with abdominal pain as a presenting symptom, a decline in post-therapy CA19-9, and the performance of surgery (**Table 5**). Moreover, ADC displayed significance compared to RECIST criteria when correlated to the outcome, as demonstrated in **Table 5** and **Figure 6**.

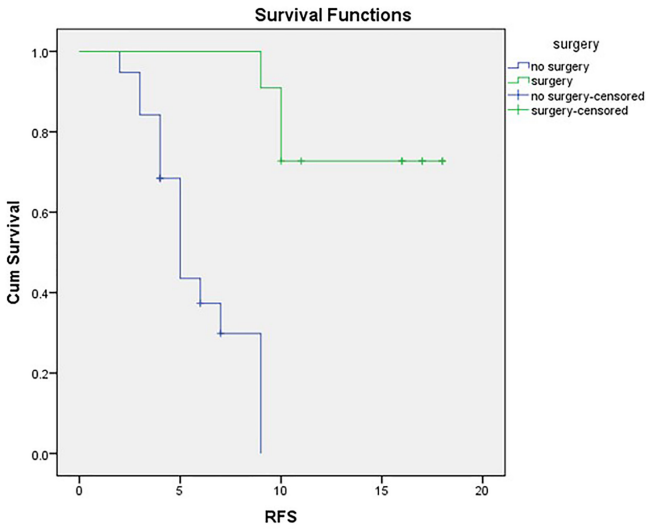

FIGURE 2 | RFS in surgical and non-surgical series.

On further analysis for the association between the reduction in CA19-9 after NACT and its correlation with the ADC response, it was apparent that regressive patients had a significantly more significant reduction in CA19-90 (p <0.001) than stationary patients, while RECIST responders lacked this association (p=0.203) (**Table 6**).

Upon addressing the discordance in response, further analysis was performed on the 12 responding patients *via* ADC criteria. They were further categorized into their relevant RECIST subgroup, and CA19-9 normalization values were analyzed. A significant relation was observed for all categories of response by size, thus rendering RECIST criteria inconclusive in response assessment of response even if coupled with the tumor marker (**Table 7**).

DISCUSSION

The ultimate goal of BRPC is the potentiality of achieving an R0 surgery *via* neoadjuvant therapy. Preoperative therapy has the added advantage of treating micrometastasis at an earlier stage

TABLE 3 | Association between ADC response and RECIST.

Variable		RECIST				
		SD (n =16)	PD (n =9)	PR (n =5)	Kappa	P-value
ADC, No. (%)	**Stationary (n =18)**	12	6	0	0.293	0.007
	Regressive (n =12)	4	3	5		

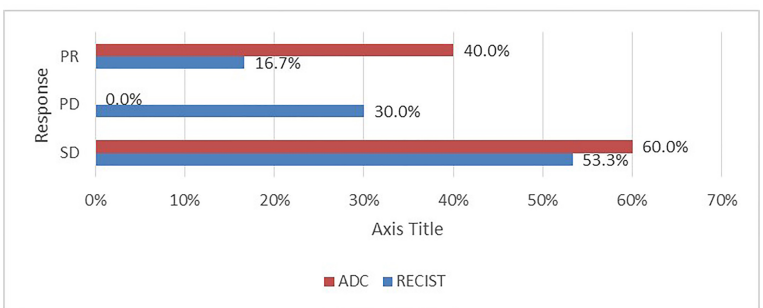

FIGURE 3 | Distribution of response according to ADC and RECIST.

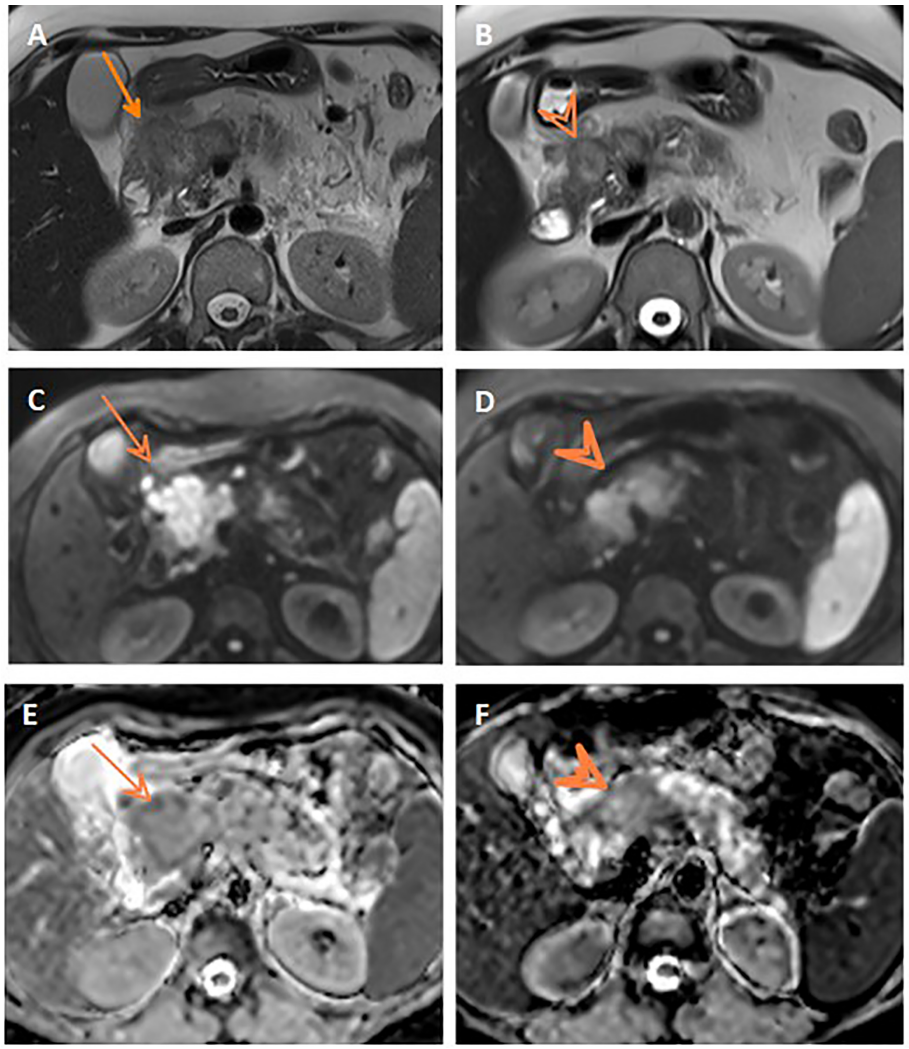

FIGURE 4 | Discordant response between ADC and RECIST. Axial T2WI **(A)** shows progression of the pancreatic mass after neoadjuvant therapy compared to initial axial T2WI **(B)**. Post-treatment and initial DWIs (**C**, **D,** respectively) show corresponding restricted DWI of the mass. Post-treatment and initial ADC maps (**E, F,** respectively) show comparable ADC values of the mass on both studies.

and offers an observation period to exclude rapid progressors exhibiting a poor response to treatment (13).

This study demonstrated the enhanced utility of ADC *via* MRI DWI as a predictor of achieving a favorable pathologic response with clear resection margins paving the way to better survival. This favorable response concurred to achieving normalization in CA19-9 levels as well. Traditional RECIST criteria did not perform well in identifying cases that exhibited response *via* these two metrics.

Further analysis into responding patients by ADC and subclassifying them further by RECIST criteria deemed inconclusive even when CA19-9 response was accounted for with significant p values for all PD, SD, and PR universally expressed.

In the current series, approximately one-third of the BRPC were ultimately resected, 36.6% to be precise, corresponding similarly to the rate reported by two meta-analyses that additionally demonstrated favorable survival rate over 20% at 5-years (14, 15).

The radiologist's incremental role in selecting neoadjuvant therapy responders has remained difficult to determine despite technological advances firmly. MD Anderson Cancer Center reported that among 122 BRPC patients, the documented CR as assessed by CT was in only one patient (0.8%), PR in 12%, with SD in 69%. Nevertheless, 66% underwent the surgical procedure with a 95% R0 resection plus a 33-month mOS (95% confidence interval, 25.4–40.6 months) compared to a mOS of 12 months (95% confidence interval, 9.5–14.5 months) in those patients that did not undergo the excision. They concluded RECIST criteria 1.1 was not associated with OS and failed to predict resectability (16). Using CT imaging, other studies reported a low response rate that did not signify an abandonment of pancreatectomy (17, 18).

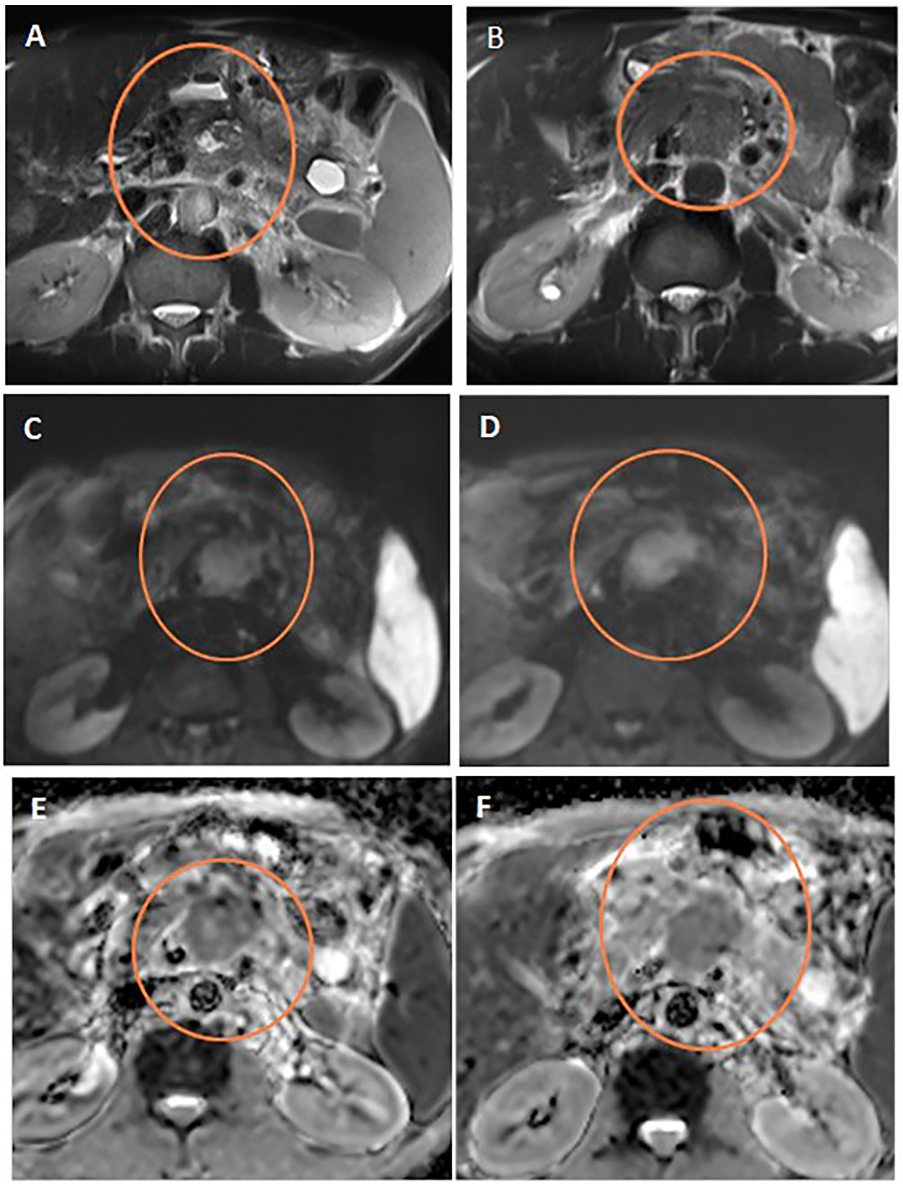

FIGURE 5 | Discordant response between ADC and RECIST. Axial T2WI **(A)** shows stationary size of the pancreatic mass after neoadjuvant therapy compared to initial axial T2WI **(B)**. Note the central cystic change of the mass of necrosis. Post-treatment and initial DWIs (**C, D**, respectively) show corresponding restricted DWI of the mass. Post-treatment and initial ADC maps (**E, F**, respectively) show regression of the ADC values of the mass on post-treatment study compared to initial one.

TABLE 4 | Pre- and post-neoadjuvant ADC and CA19-9 values for the study population.

Variables	Median (range)	Pre-treatment	Post-treatment	P-value
ADC	All cases (30)	1.3 (1.0–1.4)	1.4 (1.1–1.7)	0.001
	Surgical cases (11)	1 (1–1.3)	1.4 (1.3–1.7)	0.003
	Non-surgical cases (19)	1.4 (1–1.4)	1.3 (1–1.7)	0.29
CA19-9 (U/mL)	All cases (30)	250 (100–400)	170 (20-285)	0.001
	Surgical cases (11)	250 (100–380)	35 (20–48)	0.003
	Non-surgical cases (19)	300 (130–400)	280 (25–380)	0.023

TABLE 5 | Association between ADC response and characteristics of the study population (n =30).

Variable		ADC Response		
		Stationary (n =18)	Regressive (n =12)	P-value
Age in years, mean± SD		53.1 ± 6.9	51.7 ± 6.4	0.58
Male, No. (%)		13 (72.2)	9 (75)	0.86
Presentation, No. (%)	Weight loss	17 (94.4)	9 (75)	0.13
	Abdominal pain	18 (100)	10 (83.3)	0.07
	Jaundice	8 (44.4)	6 (50)	0.76
ECOG performance, No. (%)	0	5(45.5)	6 (54.5)	0.11
	1	7 (36.8)	12 (63.2)	
CA19-9 in U/ml, median (Range)	Pre-treatment	280 (130–400)	250 (100–380)	0.36
	Post-treatment	280 (25–380)	35 (20–48)	<0.001
Site, No. (%)	Body	7 (38.9)	5 (41.7)	0.98
	Head	4 (22.2)	3 (25)	
	Neck	3 (16.7)	2 (16.7)	
	Tail	4 (22.2)	2 (16.7)	
Neoadjuvant chemotherapy, No. (%)	Gemcitabine/cisplatin	8 (44.4)	3 (25)	0.43
	FOLFIRINOX	10 (55.5)	9 (75)	
MRI involvement, No. (%)	Celiac, SMA	0	1 (8.3)	0.59
	Celiac, SMV	2 (11.1)	1 (8.3)	
	Portal/SMA	7 (38.9)	3 (33.3)	
	Portal/SMV	1 (5.6)	0	
	SMA	3 (16.7)	2 (16.7)	
	SMA, celiac, SMV/PV	1 (5.5)	0	
	SMV/PV, SMA	4 (22.2)	5 (41.7)	
Surgery, No. (%)		0	11 (100)	<0.001

Novel imaging parameters associated with diffusion and perfusion were entered to improve the predictive potential for the operative procedure, pathologic response, and ensuing outcome. A small retrospective study found that tumor delineation by DWI provided the best estimate of tumor size (19). Okada et al. (20) prospectively reviewed 28 patients with BRPC who underwent DWI before neoadjuvant chemotherapy and surgery and found post-treatment whole-tumor ADC value a predictor of R0 resectability; however, the cutoff value of ADC at the location of vascular contact did not discriminate R0 resectability.

Pre- and post-neoadjuvant chemoradiation (nCR) mean ADC values in pancreatic tumors were retrospectively compared and correlated to pathological treatment response in a group of 25 (of which 22 were BRPC) patients by Dalah et al. (12). Significantly higher post-nCR ($1.667 \pm 0.161\times10^{-3}$) compared with pre-nCR ADC values ($1.395 \pm 0.136\times10^{-3}$ mm^2/s) were reported. Additionally, mean ADC after neoadjuvant treatment was significantly associated with the pathological response attained ($r=-0.5172$; $P=0.02$) demonstrably higher values in favorably responding tumors. Despite the different methodology demonstrated in their radiotherapy usage and histopathological grading assessment for the response, these results are congruent to ours, whereas we used R0 as a parameter for successful resection.

In another prospective trial, 60 consecutive pancreatic cancer patients were enrolled, and imaging biomarkers as DWI, magnetic resonance spectroscopy (MRS), and PET/MRI correlated stage and PFS (21). This work concluded that these modalities gave complementary data describing the disease characteristics, and a ratio incorporating ADC min served as the most potent biomarker for tumor aggressiveness, stage, and PFS.

Contrastingly, a retrospective observation of 36 pancreatic cancer cases concluded that relying on ADC parameters in response assessment may be misleading and warned against abandoning traditional RECIST criteria. They reported size reduction solely predicted pathologic response with 92% sensitivity and 27% specificity compared to increased ADCs, 48% sensitivity but a better specificity of 73% (22).

Not being devoid of limitations, this study had a small number of patients, and in the end those that were able to undergo the surgical procedure were yet even smaller, as is the case in this borderline subtype. Also, pathologic examination of tissue was not collected, and comment on resection margin sufficed for this parameter, making inter-trial comparisons difficult. However, it is worth noting that R0 alone in our study did provide excellent relevance to improved survival. Finally, ADC has been a subject of interobserver variability according to the region of interest volume and site, not to mention technical factors related to the MRI system (23).

Coming to address this final drawback, radiologists with expertise in abdominal MRI imaging along with rigorous reporting and revision reviewed all scans. Other strengths included the analysis of all recruited cases in intent-to-treat fashion, even though some didn't undergo the operation. Finally, the majority of cases received FOLFIRINOX, which is considered to have favorable mOS and R0 resection in BRPC, making it a temporally relevant treatment.

CONCLUSION

The current study displayed the value of incorporating functional domains to traditional criteria to better elucidate

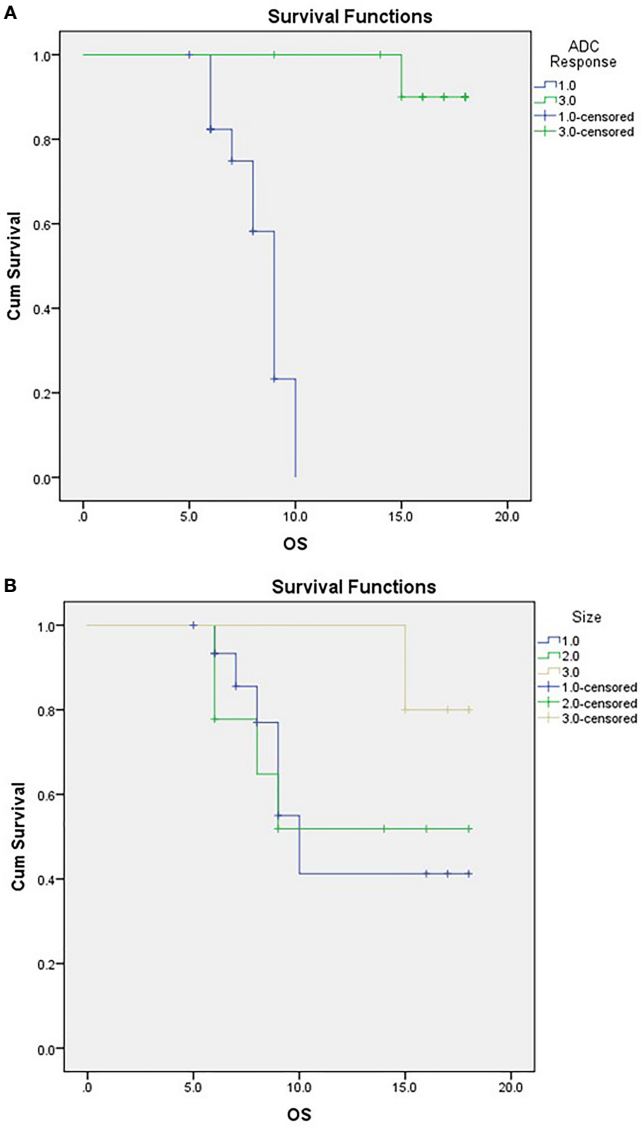

FIGURE 6 | Kaplan-Meier Curve of OS according to ADC response **(A)** and RECIST classification **(B)**. For **(A)** ;1/green=responder, 3/blue=non-responder. For **(B)** 1/blue=PD,2/green:SD, 3/beige: PR.

TABLE 6 | Association between ADC response/RECIST and OS of the study population and CA19-9 (n =30).

Variable		ADC Response			RECIST			
		Stationary (n =18)	Regressive (n =12)	P-value	SD (n =16)	PD (n =9)	PR (n =5)	P-value
Outcomes, No. (%)	Alive	8 (44.4)	11 (91.7)	<0.001	10 (62.5)	5 (55.6)	4 (80)	0.66
	Dead	10 (66.6)	1 (8.3)		6 (37.5)	4 (44.4)	1 (20)	
OS, mean (95% CI)		8.39 (87.64–9.14)	17.7 (17.14–18.26)	<0.001	12.41 (9.3–15.45)	12.88 (9.19–16.55)	17.4 (16.35–18.45)	0.35
CA-19-9 in U/ml	Pre-treatment	280 (130–400)	250 (100–380)	0.36	270 (100–400)	250 (150–370)	250 (100–380)	0.91
	Post-treatment	280 (25–380)	35 (20–48)	<0.001	225 (30–380)	220 (25–380)	33 (20–40)	0.022
	Mean change[a]	14.4 (–1.33–30.8)	210.8 (153.0–267.8)	<0.001	63.4 (3.4–123.5)	78.6 (10.8 146.3)	214.4 (88.9 339.9)	0.203

[a]*Data are presented as mean (95% CI).*

TABLE 7 | Association between RECIST and CA19-9 in ADC responders.

Variable		ADC Response			P-value
		Regressive (n =12)			
CA19-9		Mean reduction	Pretreatment median (range)	Post-treatment median (range)	
RECIST	SD (n =4)	−136.3 (154)	290 (100–380)	35 (30–45)	<0.001
	PD (n =3)	−195.7 (153)	220 (200–250)	45 (35–48)	0.004
	PR (n =5)	−112 (134.1)	250 (100–380)	33 (20–40)	<0.001

candidates of surgical potential and hence favorable outcome. The simultaneity of response in both assessed imaging reporting modalities in this study was observed in five cases only. Furthermore, in the 12 responders *via* ADC, all attained an R0 operation, and 11 remained alive, indicating that the ADC could be used to assess treatment response for PDAC. Radiomics continues to solve challenging questions in therapy assessment, and relying on old parameters needs to be updated into approved modern evidence-based algorithms and pathways.

DATA AVAILABILITY STATEMENT

The data that support the findings of this study are available from the corresponding author, upon reasonable request.

ETHICS STATEMENT

The studies involving human participants were reviewed and approved by Helwan IRB. The patients/participants provided their written informed consent to participate in this study.

AUTHOR CONTRIBUTIONS

NH was responsible for the conception, design, and quality control of this study. NH, RH, DA, and ME performed the study selection and data extraction, and contributed to the writing of the manuscript. NH and ME collected statistical output and were major contributors in writing the manuscript. MK and WE participated in study selection, editing, and statistical analyses. All authors contributed to the article and approved the submitted version.

REFERENCES

1. Ducreux M, Cuhna AS, Caramella C, Hollebecque A, Burtin P, Goéré D, et al. Cancer of the Pancreas: ESMO Clinical Practice Guidelines for Diagnosis, Treatment and Follow-Up. *Ann Oncol* (2015) 26:v56–68. doi: 10.1093/annonc/mdv295
2. Bockhorn M, Uzunoglu FG, Adham M, Imrie C, Milicevic M, Sandberg AA, et al. Borderline Resectable Pancreatic Cancer: A Consensus Statement by the International Study Group of Pancreatic Surgery (ISGPS). *Surgery* (2014) 155 (6):977–88. doi: 10.1016/j.surg.2014.02.001
3. Crinò SF, Larghi A, Bernardoni L, Parisi A, Frulloni L, Gabbrielli A, et al. Touch Imprint Cytology on Endoscopic Ultrasound Fine-Needle Biopsy Provides Comparable Sample Quality and Diagnostic Yield to Standard Endoscopic Ultrasound Fine-Needle Aspiration Specimens in the Evaluation of Solid Pancreatic Lesions. *Cytopathology* (2019) 30(2):179–86. doi: 10.1111/cyt.12662
4. Crinò SF, Ammendola S, Meneghetti A, Bernardoni L, Conti Bellocchi MC, Gabbrielli A, et al. Comparison Between EUS-Guided Fine-Needle Aspiration Cytology and EUS-Guided Fine-Needle Biopsy Histology for the Evaluation of Pancreatic Neuroendocrine Tumors. *Pancreatology* (2021) 21(2):443–50. doi: 10.1016/j.pan.2020.12.015
5. Kitano M, Minaga K, Hatamaru K, Ashida R. Clinical Dilemma of Endoscopic Ultrasound-Guided Fine Needle Aspiration for Resectable Pancreatic Body and Tail Cancer. *Dig Endosc* (2021). doi: 10.1111/den.14120
6. Michelakos T, Pergolini I, Castillo CF, Honselmann KC, Cai L, Deshpande V, et al. Predictors of Resectability and Survival in Patients With Borderline and Locally Advanced Pancreatic Cancer Who Underwent Neoadjuvant Treatment With FOLFIRINOX. *Ann Surg* (2019) 269(4):733–40. doi: 10.1097/SLA.0000000000002600
7. Wang Y, Chen ZE, Nikolaidis P, McCarthy RJ, Merrick L, Sternick LA, et al. Diffusion-Weighted Magnetic Resonance Imaging of Pancreatic Adenocarcinomas: Association With Histopathology and Tumor Grade. *J Magn Reson Imaging* (2011) 33(1):136–42. doi: 10.1002/jmri.22414
8. Koh D-M, Lee J-M, Bittencourt LK, Blackledge M, Collins DJ. Body Diffusion-Weighted MR Imaging in Oncology. *Magn Reson Imaging Clin N Am* (2016) 24(1):31–44. doi: 10.1016/j.mric.2015.08.007
9. Wagner M, Doblas S, Daire J-L, Paradis V, Haddad N, Leitão H, et al. Diffusion-Weighted MR Imaging for the Regional Characterization of Liver Tumors. *Radiology* (2012) 264(2):464–72. doi: 10.1148/radiol.12111530
10. Al-Hawary MM, Francis IR, Chari ST, Fishman EK, Hough DM, Lu DS, et al. Pancreatic Ductal Adenocarcinoma Radiology Reporting Template: Consensus Statement of the Society of Abdominal Radiology and the American Pancreatic Association. *Radiology* (2014) 270(1):248–60. doi: 10.1148/radiol.13131184
11. Eisenhauer EA, Therasse P, Bogaerts J, Schwartz LH, Sargent D, Ford R, et al. New Response Evaluation Criteria in Solid Tumours: Revised RECIST Guideline (Version 1.1). *Eur J Cancer* (2009) 45(2):228–47. doi: 10.1016/j.ejca.2008.10.026
12. Dalah E, Erickson B, Oshima K, Schott D, Hall WA, Paulson E, et al. Correlation of ADC With Pathological Treatment Response for Radiation Therapy of Pancreatic Cancer. *Transl Oncol* (2018) 11(2):391–8. doi: 10.1016/j.tranon.2018.01.018
13. Javed AA, Wright MJ, Siddique A, Blair AB, Ding D, Burkhart RA, et al. Outcome of Patients With Borderline Resectable Pancreatic Cancer in the Contemporary Era of Neoadjuvant Chemotherapy. *J Gastrointest Surg* (2019) 23(1):112–21. doi: 10.1007/s11605-018-3966-8
14. Gillen S, Schuster T, Meyer zum Büschenfelde C, Friess H, Kleeff J. Preoperative/Neoadjuvant Therapy in Pancreatic Cancer: A Systematic Review and Meta-Analysis of Response and Resection Percentages. Seiler C, Editor. *PloS Med* (2010) 7(4):e1000267. doi: 10.1371/journal.pmed.1000267
15. Assifi MM, Lu X, Eibl G, Reber HA, Li G, Hines OJ. Neoadjuvant Therapy in Pancreatic Adenocarcinoma: A Meta-Analysis of Phase II Trials. *Surgery* (2011) 150(3):466–73. doi: 10.1016/j.surg.2011.07.006
16. Katz MHG, Fleming JB, Bhosale P, Varadhachary G, Lee JE, Wolff R, et al. Response of Borderline Resectable Pancreatic Cancer to Neoadjuvant Therapy

Is Not Reflected by Radiographic Indicators. *Cancer* (2012) 118(23):5749–56. doi: 10.1002/cncr.27636
17. Ferrone CR, Marchegiani G, Hong TS, Ryan DP, Deshpande V, McDonnell EI, et al. Radiological and Surgical Implications of Neoadjuvant Treatment With FOLFIRINOX for Locally Advanced and Borderline Resectable Pancreatic Cancer. *Ann Surg* (2015) 261(1):12–7. doi: 10.1097/SLA.0000000000000867
18. Hussien N, Sallam K, Abdel-Kawi M, Ezz El Din M. The Role of Radiological Parameters in Assessing Response to Neoadjuvant Therapy in Borderline Resectable Pancreatic Cancer. *Res Oncol* (2020) 16(1):1–5. doi: 10.21608/resoncol.2020.18938.1088
19. Legrand L, Duchatelle V, Molinié V, Boulay-Coletta I, Sibileau E, Zins M. Pancreatic Adenocarcinoma: MRI Conspicuity and Pathologic Correlations. *Abdom Imaging* (2015) 40(1):85–94. doi: 10.1007/s00261-014-0196-8
20. Okada K, Kawai M, Hirono S, Kojima F, Tanioka K, Terada M, et al. Diffusion-Weighted MRI Predicts the Histologic Response for Neoadjuvant Therapy in Patients With Pancreatic Cancer: A Prospective Study (DIFFERENT Trial). *Langenbeck's Arch Surg* (2020) 405(1):23–33. doi: 10.1007/s00423-020-01857-4
21. Chen BB, Tien YW, Chang MC, Cheng MF, Chang YT, Wu CH, et al. PET/MRI in Pancreatic and Periampullary Cancer: Correlating Diffusion-Weighted Imaging, MR Spectroscopy and Glucose Metabolic Activity With Clinical Stage and Prognosis. *Eur J Nucl Med Mol Imaging* (2016) 43 (10):1753–64. doi: 10.1007/s00259-016-3356-y
22. Jajja M, Ferez-Pinzon A, Maxwell D, Krasinskas A, Pardeep Mittal PS. Diffusion Weighted Magnetic Resonance Sequences do Not Improve Pathologic Response Prediction After Neoadjuvant Therapy for Pancreatic Cancer. *J Pancreas* (2020) 21(6):139–45.
23. Ma C, Guo X, Liu L, Zhan Q, Li J, Zhu C, et al. Effect of Region of Interest Size on ADC Measurements in Pancreatic Adenocarcinoma. *Cancer Imaging* (2017) 17(1):13–9. doi: 10.1186/s40644-017-0116-6

Conflict of Interest: The authors declare that the research was conducted in the absence of any commercial or financial relationships that could be construed as a potential conflict of interest.

frontiers | Frontiers in Oncology

CASE REPORT
published: 04 May 2022
doi: 10.3389/fonc.2022.894421

Case Report: Inguinal Myxofibrosarcoma Arising From the Surgical Site of Resected Squamous Cell Carcinoma

Hongyu Hu[1†], *Xianwen Hu*[1†], *Dandan Li*[2], *Jiong Cai*[1*] *and Pan Wang*[1*]

[1] Department of Nuclear Medicine, Affiliated Hospital of Zunyi Medical University, Zunyi, China, [2] Department of Obstetrics, Zunyi Hospital of Traditional Chinese Medicine, Zunyi, China

OPEN ACCESS

Edited by:
Pilar López-Larrubia,
Spanish National Research Council (CSIC), Spain

Reviewed by:
Ismaheel Lawal,
University of Pretoria, South Africa
Simona Maria Fragomeni,
Agostino Gemelli University Polyclinic (IRCCS), Italy
Wang Shijiang,
Shandong First Medical University, China

***Correspondence:**
Jiong Cai
jiong_cai@163.com
Pan Wang
1298178828@qq.com

[†]These authors have contributed equally to the work

Specialty section:
This article was submitted to Cancer Imaging and Image-directed Interventions, a section of the journal Frontiers in Oncology

Received: 11 March 2022
Accepted: 04 April 2022
Published: 04 May 2022

Citation:
Hu H, Hu X, Li D, Cai J and Wang P (2022) Case Report: Inguinal Myxofibrosarcoma Arising From the Surgical Site of Resected Squamous Cell Carcinoma. Front. Oncol. 12:894421. doi: 10.3389/fonc.2022.894421

Myxofibrosarcoma (MFS) is a rare soft tissue sarcoma that originates in the mesenchymal tissue and occurs mainly in the limbs of elderly patients. Herein, we present the case of a 64-year-old woman who underwent extensive left vulvar resection and bilateral lymphadenectomy for vulvar squamous cell carcinoma 6 months previously. A mass was found again at the original surgical site of the left groin 3 months prior, and its size had increased significantly in the past 1 month, with ulceration and pus. Magnetic resonance imaging (MRI) showed a 10-cm mass in the left groin area; fluoro18-labeled deoxyglucose positron emission tomography/computed tomography (^{18}F-FDG PET/CT) showed a marked increase in mass metabolism in the left groin area, which was highly suspected to be a recurrence of squamous cell carcinoma. Subsequently, the patient underwent surgery and the postoperative pathology and immunohistochemistry confirmed MFS. In conclusion, MFS has rarely been reported to arise from the surgical site of squamous cell carcinoma. Our case study demonstrates that MFS should be included in the differential diagnosis of superficial masses in patients with a prior surgical history who present with a soft tissue mass at the surgical site, especially for recently developed rapidly increasing masses. This study aimed to systematically review the clinical features, diagnosis, differential diagnosis, treatment, and prognosis of this disease based on our case and related published literature and to provide clinicians with a broader perspective on the differential diagnosis of soft tissue tumors.

Keywords: myxofibrosarcoma, squamous cell carcinoma, magnetic resonance imaging, positron emission computed tomography, case report

CASE DESCRIPTION

A 64-year-old woman was admitted to a local county hospital 6 months previously because of the discovery of a left vulvar mass. CT revealed a mass of approximately 3.5 cm × 2.0 cm (vertical diameter × horizontal diameter) in her left vulva, and multiple enlarged lymph nodes were seen in the left groin area (**Supplementary Figure S1**). The clinician suspected that she had a malignant tumor and lymph node metastasis in the left inguinal region; therefore, extensive excision of the left vulvar

mass and repair of the vulva followed by bilateral lymph node dissection were undertaken. Postoperative pathology revealed keratinized squamous cell carcinoma of the vulva, with a tumor invasion depth of 5 mm, no tumor invasion at the resection margin, metastasis in the left inguinal lymph node (3/7), and no metastasis in the right inguinal lymph node (0/3). The patient did not undergo further postoperative chemoradiotherapy. She complained that a painful lump had reappeared in the original surgical incision area of her left groin area 3 months previously; in the past month, the lump had rapidly increased in size, ruptured, and ulcerated; thus, she visited our hospital for treatment. Physical examination revealed a cauliflower-like protruding skin mass in the left groin with superficial ulceration and bleeding. Moreover, a 2-cm mass was observed in the right inguinal area, and the skin surface was red without ulceration or exudation. She had no other positive signs, and her routine blood and tumor marker values were within the normal range. She then underwent imaging examinations; computed tomography (CT) demonstrated a soft tissue-dense mass in the left groin area, which presented as low T1 and high T2 signals on magnetic resonance imaging (MRI), and contrast-enhanced scan showed tumor infiltration into the fascia as "fascial tail sign." In addition, an unevenly enhanced nodular abnormal signal shadow was observed in the right inguinal region, as shown in **Figure 1**. Fluoro18-labeled deoxyglucose positron emission tomography/computed tomography (^{18}F-FDG PET/CT) showed a high FDG concentration in the left groin mass, with a maximum standard uptake value (SUVmax) of 31.38, and increased FDG uptake in the right nodule, with an SUVmax of 28, as shown in **Figure 2**. According to the patient's history of vulvar squamous cell carcinoma and the above imaging findings, the radiologist first considered that the left mass was a recurrence of squamous cell carcinoma, while the right inguinal nodule was a lymph node metastasis. Therefore, the patient underwent enlarged resection of the tumor in the left inguinal region with local pedicled flap transfer and repair and bilateral inguinal lymph node dissection. During the operation, the scalpel moved the skin and subcutaneous tissue along a 2-cm incision at the edge of the tumor to the tumor base, and the tumor base was found to be adherent to the femoral artery and femoral vein. The transverse diameter of the tumor after resection was approximately 20.0 cm, and no tumor involvement was observed at the upper, lower, left, or right margins of the tumor under a microscope. Hematoxylin–eosin staining showed that the tumor cells in the left mass were spindle-shaped, the blood vessels were curvilinear, the interstitium was myxoid, and the right groin lesion showed an irregular squamous cell composition and visible horn strains. Immunohistochemistry showed positive expression of vimentin, CD68, and partial smooth muscle actin (SMA) and negative expression of β-catenin, CD, Cluster of differentiation (CD34), desmin, S100, and Signal transducer and activator of transcription (STAT6) in left groin tumor cells, as shown in **Figure 3**. Based on these pathological and immunohistochemical findings, the patient was diagnosed with myxofibrosarcoma (grade II) in the left groin region and keratinized squamous cell carcinoma in the right inguinal lymph node. The patient refused chemotherapy and radiotherapy after surgery; thus, we suggested a follow-up review. The patient was still alive after a 1-year follow-up, and the latest MRI results showed no tumor recurrence or local metastasis.

DISCUSSION

Myxofibrosarcoma is a mesenchymal tumor that most commonly occurs in the extremities of elderly patients aged 60–70 years, especially in the lower extremities. It rarely affects the trunk, head,

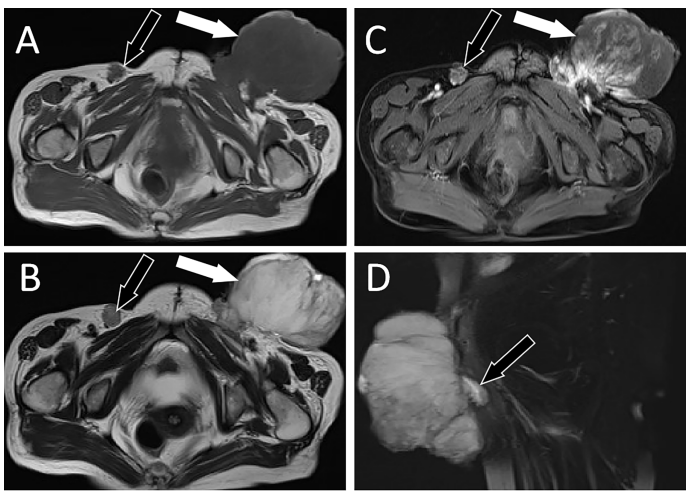

FIGURE 1 | MRI examination; **(A)** Axial T1WI shows hypointense signal of left groin mass (white arrow) and right inguinal lymph nodes (black arrow). **(B)** Axial T2WI imaging demonstrates slightly high signal intensity in the left groin area (white arrow) and low signal intensity in the right inguinal lymph nodes (black arrow). **(C)** Contrast-enhanced T1WI with fat suppression: the left groin mass showed uneven enhancement (white arrow), while the right inguinal lymph nodes showed marginal enhancement (black arrow). **(D)** Sagittal contrast-enhanced T1WI clearly shows the "tail fascial sign" (black arrow). T1WI, T1-weighted images; T2WI, T2-weighted images

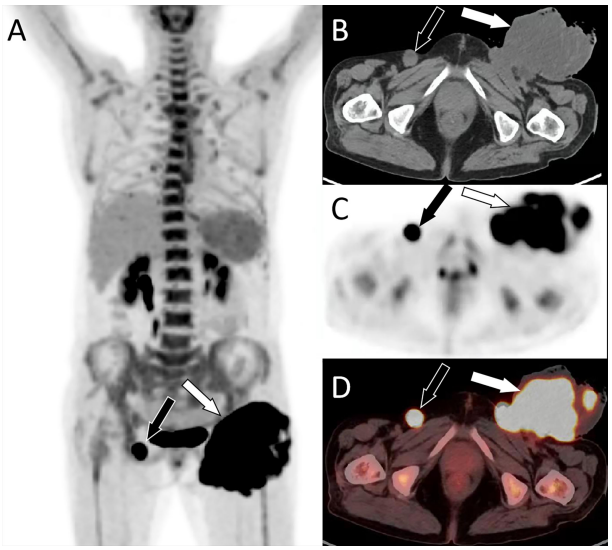

FIGURE 2 | PET/CT examination. **(A)** Whole-body MIP images showed a lumpy hypermetabolic lesion in the left groin (white arrow) and increased nodular uptake of FDG in the right groin (black arrow). **(B)** Axial CT shows an uneven low-density mass in the left groin (white arrow) and a rounded soft tissue density nodule in the right inguinal region (black arrow). **(C)** PET and **(D)** PET/CT fusion images show a hypermetabolic mass in the left groin area with SUVmax of 31.38 (white arrow) and nodules in the right groin area with radioactive uptake with SUVmax of 28.0 (black arrow). MIP, maximum intensity projection; FDG, fluorodeoxyglucose; PET, positron emission tomography; CT, computed tomography; SUVmax, maximum standard uptake.

neck, hands, or feet (1). Myxofibrosarcoma in the groin has rarely been reported in the literature. Clinically, compared with other types of sarcomas, MFS has a higher local recurrence rate and lower distant metastasis rate (2). Pathological examination usually classifies tumors into four grades of malignancy based on their cell abundance, cytopleomorphism, and prevalence of mitotic images (3). MFS has obvious atypia, and grade I and II tumors are dominated by fibroblast-like cells, while grade III and IV tumors are mainly characterized by histiocytic cells (4). Histologically, MFS is characterized by alternating hypocellular and myxoid areas, multicellular fibrous areas, long curvy blood vessels in various mucinous stroma, and a polynodular growth pattern (5). Tumors can be either shallow or deep and usually occur under or in the context of the skin, accounting for 20%–70% of the cases (6). The etiology of the disease is not clear at present, but the association between acute trauma and the development of soft tissue sarcoma was first reported in the literature in 1901, as well as in surgical scars, burn scars, and sites of repeated trauma (7). Ineffective wound repair by dysfunctional fibroblasts is thought to play a key role in accelerating the formation of malignant tumors in genetically predisposed individuals (8). It has also been reported that acute tissue injury activates satellite cells and promotes sarcoma formation through the HGF, Hepatocyte growtll factor (HGF)/C-MET signaling pathway (9). Clinically, cases of myxofibrosarcoma secondary to soft tissue injury have been reported (10–12). In the present case, the patient was tumor-susceptible, and the tumor occurred at the surgical site. Therefore, it was speculated that the occurrence of the tumor might be related to previous surgical trauma; however, a larger number of cases is necessary to confirm this hypothesis. Tumors are abundant in the myxoid matrix. Weiss and Enzinger, in their initial description of Malignant Fibrous Histiocytoma (MFH) myxoid variants, required that at least 50% of tumors should consist of myxoid regions in order for it to be classified as MFS (13). As the imaging presentation of this disease is not specific, it is difficult to make a specific diagnosis. Therefore, we lack a typical understanding of this disease, increasing the chances for misdiagnosis. However, imaging examination also has important clinical significance for fibrosarcoma, and common imaging examinations include CT, MRI, and PET-CT. MRI has a good resolution that can not only clearly show the location, size, shape, and invasion range of the

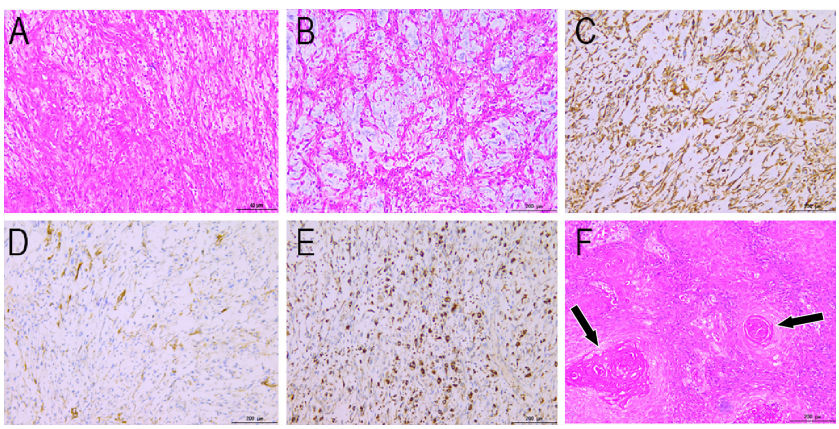

FIGURE 3 | Histopathological findings (HE staining: **A**, ×40; **B**, ×200) show fusiform tumor cells, curving vessels, and myxoid alterations in the stroma. Immunohistochemical staining showing vimentin **(C)**, SMA **(D)**, and CD68 **(E)** positivity. **(F)** Histopathological view of the right inguinal lymphadenopathy. HE staining shows irregular squamous cells and horn strains (arrows). HE, hematoxylin and eosin.

tumor but also reveal the pathological components of the tumor; thus, it is considered to be an indispensable examination method for the diagnosis of soft tissue tumors, including myxofibrosarcoma (1). Depending on the components of the lesion, there are different manifestations on imaging. Due to the presence of the myxoid matrix in tumors, myxoid changes are relativistic on MRI. On T1-weighted imaging (T1WI), myxoid substrates with low cell density have less signal intensity than muscle, but areas with high cell density are similar to the intensity of muscle on MRI. The myxoma matrix has signal intensity on T2WI/Short Time Inversion Recovery (STIR), whereas areas with high cell density show low signal intensity, and myxoid matrix enhancement is poor (14). MFS is classified into two types, solid and "tail-like", based on T2-weighted MRI. In the "tail-like" type, there is extensive spread along the fascial planes that extended away from the primary site of tumor (15). This type of tumor often infiltrates and extends along the fascia plane, showing a specific "tail fascia sign" on MRI, which is consistent with myxoid fibrosarcoma; however, not all cases of this histotype show this feature (14). PET/CT also has high value in revealing details on tumor metabolism and distant metastasis and has high sensitivity for the detection of primary sites and metastases. PET/CT is a new imaging method that plays a significant role in the detection, staging, and treatment of many sarcomas and cancers. However, the small sample size has not proven its effectiveness (16). The radioactive uptake of myxoid tumors is linked to the proportion of mucous components in the tumors. Generally, tumors with a higher proportion of mucus have a lower radioactive uptake, which is related to the fact that the mucous components of tumors cannot capture FDG (17). There are few reports on the ^{18}F-FDG PET/CT findings of myxosarcoma, with a maximum standard value range of 10.1 to 16.8 (18–20). In this case, myxofibrosarcoma showed hypermetabolism on PET-CT, which may be related to the fact that our patient had grade II myxofibrosarcoma with more spindle cells and less myxoid matrix (approximately 60%). The clinical, pathological, and imaging features of the disease overlap with different histotypes, and an accurate diagnosis can be challenging. It is often necessary to distinguish it from other mucinous tumors such as intramuscular myxoma and myxoid liposarcoma. Intramuscular myxoma is a common benign myxoid soft-tissue tumor. On MRI, there is a feathery T2 hyperintensity around the lesion, often in a mildly diffuse or thick peripheral and septal pattern (21). Myxoid liposarcoma usually appears in younger patients and is characterized by its lipid content (22). Extraskeletal myxoid chondrosarcomas are distinguished by their characteristic cartilage matrix on MRI (23). The diagnosis of this disease relies mainly on histopathological examination, which is the gold standard. Surgical resection is the standard treatment for local disease. Generally, when surgery is performed, extensive resection should include a soft tissue edge of 2 cm around the tumor and tumor cells should not be left at the edge (24). Postoperative radiotherapy is essential when an adequate margin cannot be obtained (25). Patients with this disease have an overall 5-year survival rate of approximately 60%–70%, and good disease-specific survival compared to that seen in other sarcomas (26). Due to the high recurrence rate of this tumor, all patients require close observation and follow-up after treatment. Our patient was still alive after a 1-year follow-up by imaging examination, and the latest MRI results showed no tumor recurrence or local metastasis (**Supplementary Figure S2**).

In conclusion, myxofibrosarcoma rarely develops in the surgical region after squamous cell carcinoma. The presence of "tail fascial sign" on MRI suggests the possibility of the disease, and the radioactive uptake of tumors on PET-CT images is related to the composition of mucous in tumors. More mucus in tumors leads to low metabolism, while less mucus leads to high metabolism. Second, our case suggests that myxofibrosarcoma may be associated with surgical trauma; however, this needs to be confirmed in a large number of cases in the future. In addition, our patient had an incidental association of left groin myofibrosarcoma and right inguinal lymph node squamous cell carcinoma metastasis, suggesting that non-monism should be considered in the diagnosis of tumors in future studies.

DATA AVAILABILITY STATEMENT

The data involved in the article can be obtained through the corresponding author under reasonable conditions.

ETHICS STATEMENT

The present study was approved by the Ethics Committee of Affiliated Hospital of Zunyi Medical University, Zunyi, Guizhou, China.

AUTHOR CONTRIBUTIONS

JC and PW: funding acquisition; DL: investigation; XH: methodology; HH: writing -original draft; HH and JC: writing—review and editing.

FUNDING

This study was funded by the National Natural Science Foundation of the People's Republic of China, NSFC (grant numbers: 81571712), Zunyi Medical College Research Start Fund 2018ZYFY03, and QianKeHe platform talents [2017] (grant numbers:5733-035).

SUPPLEMENTARY MATERIAL

The Supplementary Material for this article can be found online at: https://www.frontiersin.org/articles/10.3389/fonc.2022.894421/full#supplementary-material

REFERENCES

1. Mentzel T, Calonje E, Wadden C, Camplejohn RS, Beham A, Smith MA, et al. Myxofibrosarcoma. Clinicopathologic Analysis of 75 Cases With Emphasis on the Low-Grade Variant. *Am J Surg Pathol* (1996) 20(4):391–405. doi: 10.1097/00000478-199604000-00001
2. Haglund KE, Raut CP, Nascimento AF, Wang Q, George S, Baldini EH. Recurrence Patterns and Survival for Patients With Intermediate- and High-Grade Myxofibrosarcoma. *Int J Radiat Oncol Biol Phys* (2012) 82(1):361–7. doi: 10.1016/j.ijrobp.2010.08.042
3. Angervall L, Kindblom LG, Merck C. Myxofibrosarcoma. A Study of 30 Cases. *Acta Pathologica Microbiologica Scandinavica Section A Pathol* (1977) 85a (2):127–40. doi: 10.1111/j.1699-0463.1977.tb00410.x
4. Denschlag D, Kontny U, Tempfer C, Orlowska-Volk M, Niemeyer C, Gitsch G. Low-Grade Myxofibrosarcoma of the Vulva in a 15-Year-Old Adolescent: A Case Report. *Int J Surg Pathol* (2005) 13(1):117–9. doi: 10.1177/106689690501300118
5. Look Hong NJ, Hornicek FJ, Raskin KA, Yoon SS, Szymonifka J, Yeap B, et al. Prognostic Factors and Outcomes of Patients With Myxofibrosarcoma. *Ann Surg Oncol* (2013) 20(1):80–6. doi: 10.1245/s10434-012-2572-3
6. Haglund KE, Raut CP, Nascimento AF, Wang Q, George S, Baldini EH. Recurrence Patterns and Survival for Patients With Intermediate- and High-Grade Myxofibrosarcoma. *Int J Radiat Oncol* Biol* Phys* (2012) 82(1):361–7. doi: 10.1016/j.ijrobp.2010.08.042
7. Klingbeil KD, Vangara SS, Fertig RM, Radick JL. Acute Trauma Precipitating the Onset of Chest Wall Myxofibrosarcoma. *Indian J Surg Oncol* (2018) 9 (3):411–3. doi: 10.1007/s13193-018-0768-0
8. Nakanishi H, Tomita Y, Yoshikawa H, Sato N, Ochi T, Aozasa K. Frequent P53 Gene Mutations in Soft Tissue Sarcomas Arising in Burn Scar. *Jpn J Cancer Res: Gann* (1999) 90(3):276–9. doi: 10.1111/j.1349-7006.1999.tb00744.x
9. Van Mater D, Añó L, Blum JM, Webster MT, Huang W, Williams N, et al. Acute Tissue Injury Activates Satellite Cells and Promotes Sarcoma Formation via the HGF/c-MET Signaling Pathway. *Cancer Res* (2015) 75 (3):605–14. doi: 10.1158/0008-5472.CAN-14-2527
10. Hong H, Keum DI, Lee JH, Roh MR. Myxofibrosarcoma Arising in a Burn Scar. *J Dermatol* (2014) 41(1):113–5. doi: 10.1111/1346-8138.12338
11. Kanno S, Asai J, Nakamura N, Komori S, Iida S, Hanada K, et al. Myxofibrosarcoma Arising in a Burn Scar. *J Dermatol* (2014) 41(1):279–80. doi: 10.1111/1346-8138.12409
12. Picardo NE, Mann B, Whittingham-Jones P, Shaerf D, Skinner JA, Saifuddin A, et al. Bilateral Symmetrical Metachronous myxofibrosarcoma: A Case Report and Review of the Literature. *Skeletal Radiol* (2011) 40(8):1085–8. doi: 10.1007/s00256-011-1123-5
13. Weiss SW, Enzinger FM. Myxoid Variant of Malignant Fibrous Histiocytoma. *Cancer* (1977) 39(4):1672–85. doi: 10.1002/1097-0142(197704)39:4<1672::AID-CNCR2820390442>3.0.CO;2-C
14. Lefkowitz RA, Landa J, Hwang S, Zabor EC, Moskowitz CS, Agaram NP, et al. Myxofibrosarcoma: Prevalence and Diagnostic Value of the "Tail Sign" on Magnetic Resonance Imaging. *Skeletal Radiol* (2013) 42(6):809–18. doi: 10.1007/s00256-012-1563-6
15. Manoso MW, Pratt J, Healey JH, Boland PJ, Athanasian EA. Infiltrative MRI Pattern and Incomplete Initial Surgery Compromise Local Control of Myxofibrosarcoma. *Clin Orthopaedics Related Res* (2006) 450:89–94. doi: 10.1097/01.blo.0000229292.98850.14
16. Tewfik JN, Greene GS. Fluorine-18-Deoxyglucose-Positron Emission Tomography Imaging With Magnetic Resonance and Computed Tomographic Correlation in the Evaluation of Bone and Soft-Tissue Sarcomas: A Pictorial Essay. *Curr Probl Diagn Radiol* (2008) 37(4):178–88. doi: 10.1067/j.cpradiol.2007.10.005
17. Benz MR, Dry SM, Eilber FC, Allen-Auerbach MS, Tap WD, Elashoff D, et al. Correlation Between Glycolytic Phenotype and Tumor Grade in Soft-Tissue Sarcomas by ^{18}F-FDG PET. *J Nucl Med Off Publication Soc Nucl Med* (2010) 51(8):1174–81. doi: 10.2967/jnumed.109.074229
18. Erdoğan EB, Asa S, Aksoy SY, Ozhan M, Halac M. Appearance of Recurrent Cardiac Myxofibrosarcoma on FDG PET/CT. *Clin Nucl Med* (2014) 39 (6):559–60. doi: 10.1097/RLU.0000000000000420
19. Yi C, Wang X, Shi X, Zhang X, Chen Z. 18F-FDG PET/CT Imaging of Multiple Myxofibrosarcoma in Left Upper Abdomen and Chest Wall. *Nuklearmedizin* (2012) 51(6):N53–4. doi: 10.3413/PDF-5236-19157
20. Ito K, Masuda-Miyata Y, Wada S, Morooka M, Yamasawa K, Hashimoto M. F-18 FDG PET/CT Imaging of Bulky Myxofibrosarcoma in Chest Wall. *Clin Nucl Med* (2011) 36(3):212–3. doi: 10.1097/RLU.0B013E318208F2E0
21. Baheti AD, Tirumani SH, Rosenthal MH, Howard SA, Shinagare AB, Ramaiya NH, et al. Myxoid Soft-Tissue Neoplasms: Comprehensive Update of the Taxonomy and MRI Features. *AJR Am J Roentgenology* (2015) 204(2):374–85. doi: 10.2214/AJR.14.12888
22. Petscavage-Thomas JM, Walker EA, Logie CI, Clarke LE, Duryea DM, Murphey MD. Soft-Tissue Myxomatous Lesions: Review of Salient Imaging Features With Pathologic Comparison. *Radiographics Rev Publ Radiol Soc North America Inc* (2014) 34(4):964–80. doi: 10.1148/rg.344130110
23. Zhang GW, Wang AJ, Zhang GH, Zhao SN, Qu JL. Extraskeletal Myxoid Chondrosarcoma: A Report of Two Cases. *Oncol Lett* (2014) 7(4):1289–91. doi: 10.3892/ol.2014.1884
24. Roland CL, Wang WL, Lazar AJ, Torres KE. Myxofibrosarcoma. *Surg Oncol Clinics North America* (2016) 25(4):775–88. doi: 10.1016/j.soc.2016.05.008
25. Peterson AC, Porter M, Porter J. Adult Testicular Sarcoma: Presentation, Evaluation, and Treatment. *Urology* (2002) 59(2):294–5. doi: 10.1016/S0090-4295(01)01524-2
26. Sanfilippo R, Miceli R, Grosso F, Fiore M, Puma E, Pennacchioli E, et al. Myxofibrosarcoma: Prognostic Factors and Survival in a Series of Patients Treated at a Single Institution. *Ann Surg Oncol* (2011) 18(3):720–5. doi: 10.1245/s10434-010-1341-4

Conflict of Interest: The authors declare that the research was conducted in the absence of any commercial or financial relationships that could be construed as a potential conflict of interest.

frontiers | Frontiers in Oncology

ORIGINAL RESEARCH
published: 18 May 2022
doi: 10.3389/fonc.2022.884554

Evaluation of a CD13 and Integrin $\alpha_v\beta_3$ Dual-Receptor Targeted Tracer ^{68}Ga-NGR-RGD for Ovarian Tumor Imaging: Comparison With ^{18}F-FDG

Yu Long[1,2], Fuqiang Shao[1,2], Hao Ji[1,2], Xiangming Song[1,2], Xiaoying Lv[1,2], Xiaotian Xia[1,2], Qingyao Liu[1,2], Yongxue Zhang[1,2], Dexing Zeng[3], Xiaoli Lan[1,2] and Yongkang Gai[1,2]**

[1] Department of Nuclear Medicine, Union Hospital, Tongji Medical College, Huazhong University of Science and Technology, Wuhan, China, [2] Hubei Province Key Laboratory of Molecular Imaging, Wuhan, China, [3] Department of Radiology, University of Pittsburgh, Pittsburgh, PA, United States

OPEN ACCESS

Edited by:
Samata Kakkad,
Merck, United States

Reviewed by:
Domenico Albano,
University of Brescia, Italy
Fang Xie,
Fudan University, China

***Correspondence:**
Xiaoli Lan
LXL730724@hotmail.com
Yongkang Gai
gykmail@hust.edu.cn

Specialty section:
This article was submitted to Cancer Imaging and Image-directed Interventions, a section of the journal Frontiers in Oncology

Received: 26 February 2022
Accepted: 08 April 2022
Published: 18 May 2022

Citation:
Long Y, Shao F, Ji H, Song X, Lv X, Xia X, Liu Q, Zhang Y, Zeng D, Lan X and Gai Y (2022) Evaluation of a CD13 and Integrin $\alpha_v\beta_3$ Dual-Receptor Targeted Tracer ^{68}Ga-NGR-RGD for Ovarian Tumor Imaging: Comparison With ^{18}F-FDG. Front. Oncol. 12:884554. doi: 10.3389/fonc.2022.884554

Ovarian cancer has the highest mortality rate of gynecologic malignancy. ^{18}F-FDG positron emission tomography (PET) adds an important superiority over traditional anatomic imaging modalities in oncological imaging but has drawbacks including false negative results at the early stage of ovarian cancer, and false positives when inflammatory comorbidities are present. Aminopeptidase N (APN, also known as CD13) and integrin $\alpha_v\beta_3$ are two important targets overexpressed on tumor neo-vessels and frequently on ovarian cancerous cells. In this study, we used subcutaneous and metastatic models of ovarian cancer and muscular inflammation models to identify ^{68}Ga-NGR-RGD, a heterodimeric tracer consisting of NGR and RGD peptides targeting CD13 and integrin $\alpha_v\beta_3$, respectively, and compared it with ^{18}F-FDG. We found that ^{68}Ga-NGR-RGD showed greater contrast in SKOV3 and ES-2 tumors than ^{18}F-FDG. Low accumulation of ^{68}Ga-NGR-RGD but avid uptake of ^{18}F-FDG were observed in inflammatory muscle. In abdominal metastasis models, PET imaging with ^{68}Ga-NGR-RGD allowed for rapid and clear delineation of both peritoneal and liver metastases (3-6 mm), whereas, ^{18}F-FDG could not distinguish the metastasis lesions due to the relatively low metabolic activity in tumors and the interference of intestinal physiological ^{18}F-FDG uptake. Due to the high tumor-targeting efficacy, low inflammatory uptake, and higher tumor-to-background ratios compared to that of ^{18}F-FDG, ^{68}Ga-NGR-RGD presents a promising imaging agent for diagnosis, staging, and follow-up of ovarian tumors.

Keywords: positron emission tomography (PET), ovarian cancer, CD13, integrin $\alpha_v\beta_3$, dual-receptor targeted

INTRODUCTION

Ovarian cancer has the highest mortality rate of all gynecologic malignant cancers, with more than 80% of patients presenting with advanced disease (1). Due to their silent nature of the disease, patients often present with advanced stages at first diagnosis, which will result in 29-75% of patients succumbing to ovarian cancer within 5 years. However, if diagnosed at stage I (ovary defined), the

5-year survival rate exceeds 90% (1, 2). Therefore, it's a research priority to improve early detection and prevention, as a better prognosis correlated with early stage at diagnosis.

Functional imaging plays an essential role in the management of ovarian cancers. In particular, with the development and promotion of PET/MRI (3, 4) with excellent soft tissue contrast and digital PET scanner (5, 6) with higher sensitivity and diagnostic performance than analog PET, functional imaging will reduce radiation dose, enhance the diagnostic confidence and ensure the better strategies for patient management and personalized treatment, showing a wider clinical application prospect. ^{18}F-FDG positron emission tomography/computed tomography (PET/CT) imaging, as the most frequently used functional imaging method in oncological imaging, adds an important superiority over traditional anatomic imaging modalities by providing functional information about cellular glucose metabolism. However, ^{18}F-FDG PET is not recommended for the primary detection of ovarian cancers with a relatively low level of sensitivity (52-58%) and specificity (76-78%) (1, 7, 8), which might be due to tumor size and cystic or mucinous histological features with no/low metabolic activity in tumors (9, 10). Besides, it is limited by several pitfalls, such as higher ovarian glucose metabolism during menstruation and midcycle, physiologic accumulation in several benign diseases, as well as its imprecise distinction between cancerous growths and acute inflammation lesions (11–14). Novel PET agents targeting biological tumor features, including cell proliferation, angiogenesis, hypoxia, metabolism, and receptor overexpression, are pursued in preclinical researches to better detect early malignant lesions, evaluate the heterogeneity of biological features, and monitoring treatment response more accurately (10, 15–19).

Angiogenesis plays a prominent role in tumor growth, invasion and metastasis by providing abundant oxygen, nutrients, and metastatic conduits (20). aminopeptidase N (APN, also known as CD13) and integrin $\alpha_v\beta_3$ are two key regulators involved in tumor angiogenesis and tumor progression. They are overexpressed on the tumoral neo-endothelial cells during angiogenesis as well as cancerous cells, regarded as two important hallmarks of tumor angiogenesis (21–24). There are several studies have focused on the imaging and/or treatment of ovarian tumors by targeting CD13 (25, 26) or integrin $\alpha_v\beta_3$ (27, 28). However, these angiogenesis-related factors, including CD13 and integrin $\alpha_v\beta_3$, are usually differentially expressed in ovarian tumor tissues and cell lines due to the heterogeneity and genetically instability of the disease (29, 30), making it a very challenging approach to find "the optimal target", and may also be one of the reasons for drug resistance of cancer to monotherapy. Therefore, an alternative approach is to develop a complementary receptor-targeting agent for the detection and treatment of tumors.

Previously, we developed a CD13 and integrin $\alpha_v\beta_3$ dual-receptor targeted radiotracer, ^{68}Ga-NGR-RGD, which demonstrated promising results in PET imaging of breast cancers with superior imaging efficacy than monomeric ^{68}Ga-NGR and ^{68}Ga-RGD (31). Furthermore, the physiological uptake of ^{68}Ga-NGR-RGD is low in most normal organs, except kidneys, which may make this dual-receptor targeted tracer supplement or even be superior to ^{18}F-FDG PET/CT in the early diagnosis and staging of ovarian tumors. In this study, we aim to evaluate the value of ^{68}Ga-NGR-RGD in PET/CT imaging of ovarian tumors. In addition, we also investigated its potential application in distinguishing tumors and inflammation. Routine ^{18}F-FDG imaging was also conducted as a control group in all prepared mice models.

MATERIALS AND METHODS

Synthesis of NGR-RGD and Radiolabeling

NGR-RGD was synthesized and radiolabeled using our previously developed method (31). Briefly, 150 μL sodium acetate buffer (0.25 M, pH 6.8) and 2 μL NGR-RGD (2 mM) were added to the tube containing 500 μL $^{68}GaCl_3$ in 0.05 M HCl (150-200 MBq) and mixed. The final pH of the radiolabeling solution was approximately 4.0. Then, the mixture was heated at 95°C for 5 min. The radiolabeling field of the product ^{68}Ga-NGR-RGD was determined by radio-HPLC. ^{68}Ga was produced with a ^{68}Ge/^{68}Ga generator (Isotope Technologies Garching GmbH, Garching, Germany). Peptides were obtained commercially from Chinapeptide (Shanghai, China) or Gl Biochem (Shanghai, China).

Cell Culture

Human ovarian cancer cells, SKOV3, ES-2, and OVCAR4 were derived from our own laboratory preservation and cultured in GibcoDulbecco's Modified Eagle Medium/Nutrient mixture F-12 (DMEM/F12; Gibco, Carlsbad CA, USA), supplemented with 10% fetal bovine serum (FBS; Sciencell, Carlsbad CA, USA), 100 mg/mL streptomycin and 100 mg/mL penicillin (Solarbio, Shanghai, China) at 37°C in a humidified incubator with 5% CO_2.

Western Blot Analysis

Cancer cells were harvested, and total protein concentration was measured with the BCA protein assay kit (Aidlab, Beijing, China). After denaturation and separation by SDS-PAGE, proteins were transferred to a polyvinylidenefluoride (PVDF) membrane. Next, the blots were incubated with primary antibodies (1:500 anti-CD13, 1:1000 anti-Integrin alpha V, and 1:1000 anti-Integrin beta 3; Abcam, Cambridge MA, USA), and Glyceraldehyde-3-phosphate dehydrogenase (1:10000 GAPDH; Sungene, Tianjin, China). Next, the membrane was incubated with goat anti-rabbit IgG/HRP (diluted 1:20000; Sungene, Tianjin, China). The membrane was scanned by enhanced chemiluminescence (ECL kit, Beyotime) and analyzed using Quantity One software (Bio-Rad, Hercules CA, USA).

In Vitro Cell Uptake and Blocking Studies

Cells in logarithmic phase were harvested and counted using a cytometer (Cellmeter Mini, Nexcelom Bioscience LLC, Lawrence MA, USA). Cells were seeded in a 24-well plate at 2×10^5 cells per well 24 h in advance. 74 kBq ^{68}Ga-NGR-RGD in 50 μL PBS were added to each well and incubated at 37°C for 30 min, 1 h and 2 h. For blocking study, cells were pretreated with one hundred times

excess of non-radioactive NGR-RGD or NGR + RGD 15 min in advance. At the end of each time point, supernatant was collected, and cells were washed twice with pre-cooled PBS (wash 1) before lysed with 1 N sodium hydroxide; then each well was washed twice with pre-cooled PBS (wash 2). Cells, supernatant and wash solutions were subjected to radioactivity analysis using an automatic gamma counter (2470 WIZARD; PerkinElmer, Waltham MA, USA). The percentage of radioactivity taken up by the cells was calculated according to Equation 1, wherein Cpm represents decay-corrected radioactivity counts per minute.

$$\%\ radioactivity\ uptake = [Cpm(Cells) + Cpm(Wash\ 2)]/[Cpm(Cells) + Cpm(Supernatant) + Cpm(Wash\ 1) + Cpm(Wash\ 2)] \times 100 \quad \text{(Equation 1)}$$

Animal Models

All animal studies were carried out according to the regulations and standards of the Institutional Animal Care and Use Committee of Tongji Medical College of Huazhong University of Science and Technology. Subcutaneous SKOV3 or ES-2 tumors were engrafted into 4-6 weeks-old female BALB/C nude mice obtained from Beijing HFK Bioscience Co. Ltd (Beijing, China). For implantation, 5×10^6 cancer cells in 100 μL PBS were subcutaneously injected into the right shoulder of each mouse. The mice were subjected to the following experiments when tumor size reached 8-10 mm. For mouse muscular inflammation models, 20 μL turpentine oil (Aladdin, China) was injected into the right thigh muscle of each mouse using a 29-gauge hypodermic needle. Turpentine oil caused visible redness and swelling within 3 h after injection and the inflammation mice were subjected to PET/CT scans at 24 h after injection of turpentine oil.

For abdominal metastasis models, SKOV3 or ES-2 cells were harvested and resuspended in a mixed solution (50% Matrigel, Corning and 50% PBS). Next, 5×10^6 tumor cells in 200 μL were injected into intra-peritoneal cavity (1, 32, 33). About 20 days later, the mice underwent PET/CT imaging.

Animal PET/CT Imaging and Biodistribution

PET/CT imaging was performed on the lnliView-3000B small animal PET/SPECT/CT (Novel Medical, Beijing, China). Overnight fasted tumor-bearing and inflammation mice received intravenous (i.v.) injection of 2.4-3 MBq ^{18}F-FDG. Animals were then returned to anesthesia induction box and subsequently anesthetized with 2.0% isoflurane delivered in 100% air. PET/CT scans were performed at 1 h after injection. The day after ^{18}F-FDG imaging, the PET/CT-based protocol for ^{68}Ga-NGR-RGD imaging were conducted, including intravenous injection of the ^{68}Ga-NGR-RGD solution (4-5.5 MBq) and identical procedures. For abdominal metastasis groups, PET/CT were performed at 1 h p.i. of ^{18}F-FDG or ^{68}Ga-NGR-RGD. Images were quantified *via* region-of-interest (ROI) analysis.

Following the terminal PET/CT scan, mice were sacrificed, and organs of interest were harvested, weighed, and γ-counted (2470 WIZARD; PerkinElmer, Waltham MA, USA) to validate the imaging data. The tracer accumulation of tissues and organs were noted by the percentage of injected dose per gram of tissue and corrected for radioactive decay (%ID/g).

Immunohistochemistry Analysis

Tumors were extracted, fixed in 4% paraformaldehyde, and then dehydrated and embedded in paraffin. Fixed tumor tissue sections (5 μm) were deparaffinized, rehydrated and permeabilized in EDTA buffer (pH 9.0). The sections were blocked for nonspecific binding by adding 3% hydrogen peroxide and 10% normal goat serum. Sections were incubated with primary antibodies at 4°C overnight (anti-$\alpha_v\beta_3$, 1:100; anti-CD13, 1:100; anti-CD31, 1:2000, Abcam, Cambridge MA, USA). Then sections were further stained with secondary antibody (HRP-labeled goat anti-rabbit IgG, diluted 1:50) at room temperature for 25 min, and then incubated with 3,3'-diaminobenzidine (DAB, Beyotime, Hangzhou, China) for 5 min. Last, slides were counterstained with hematoxylin (Beyotime), dehydrated, covered, and observed under light microscopy.

Statistical Analysis

Quantitative data were described as the mean ± standard deviation (SD). Statistical analysis was performed using student *t*-test and p-values < 0.05 were considered statistically significant.

RESULTS

CD13 and Integrin $\alpha_v\beta_3$ Expression in Ovarian Tumor Cell Lines

Expression levels of CD13 and integrin $\alpha_v\beta_3$ in three ovarian tumor cell lines were determined *via* Western blot, with GAPDH used as an internal control (**Figures 1A, B**). Strong integrin $\alpha_v\beta_3$ band intensity was observed in SKOV3 and OVCAR4 cell lines and strong CD13 staining was found in ES-2 cell line, indicating the high expression of CD13 and/or integrin $\alpha_v\beta_3$ in ovarian tumor cell lines.

Uptake Profile of ^{68}Ga-NGR-RGD in Ovarian Tumor Cells

To demonstrate the specificity of NGR-RGD for ovarian tumor cells, we conducted the cell uptake and blocking studies of ^{68}Ga-NGR-RGD in SKOV3, OVCAR4, and ES-2 ovarian tumor cells. High uptake of ^{68}Ga-NGR-RGD was observed in these three ovarian tumor cells with a gradually increasing trend over time (**Figure 1C**). On the contrary, minimal uptake of ^{68}Ga-NGR-RGD by SKOV3 and ES-2 cells was detected when pretreated with excess amounts of non-radiolabeled NGR-RGD or NGR+RGD (**Figure 1D**).

PET/CT Imaging and Biodistribution of ^{68}Ga-NGR-RGD in Subcutaneous Tumors

Next, we performed the PET/CT scan in SKOV3 and ES-2 tumor-bearing mice and turpentine oil-induced muscular inflammation mice using ^{18}F-FDG and ^{68}Ga-NGR-RGD. As

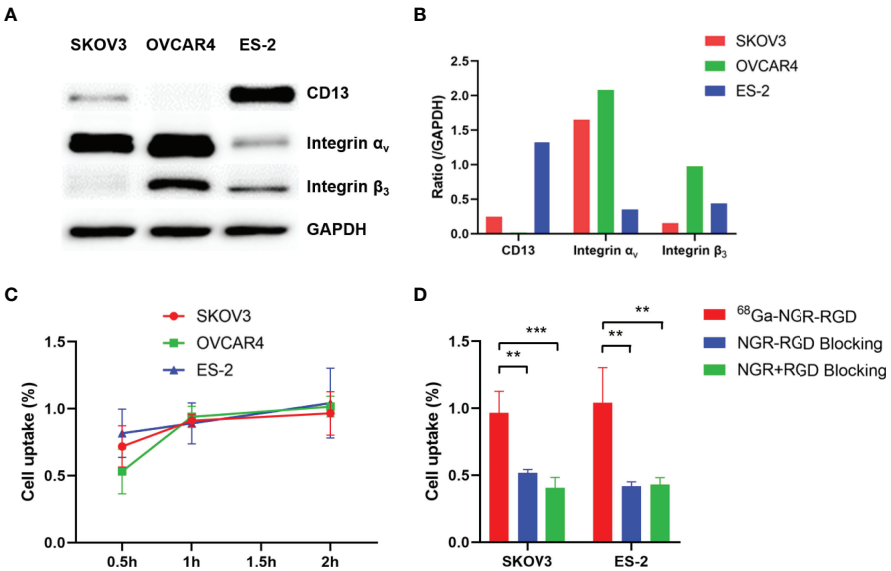

FIGURE 1 | Evaluation of binding affinity of ^{68}Ga-NGR-RGD to ovarian tumor cells. **(A)** Western blot analysis of expression of CD13, integrin α_v and integrin β_3 in three ovarian tumor cell lines, with GAPDH used as internal control. **(B)** The semi-quantitative analysis was conducted through the integrated optical density ratio of CD13, integrin α_v and integrin β_3 to GAPDH. **(C)** Uptake of ^{68}Ga-NGR-RGD in SKOV3, OVCAR4 and ES-2 ovarian tumor cell lines at 0.5 h, 1 h, 2 h. **(D)** Uptake of ^{68}Ga-NGR-RGD in SKOV3 and ES-2 cells with or without blocking dose of NGR-RGD or NRG + RGD at 2 h. Cell uptake and blocking assays showed the ^{68}Ga-NGR-RGD displayed specific binding to ovarian tumor cell lines. **p < 0.01, ***p < 0.001. Data are expressed as mean ± SD (n = 4).

shown in **Figure 2A**, ^{68}Ga-NGR-RGD clearly delineated both SKOV3 and ES-2 ovarian tumors, and the tumor contrast of ^{68}Ga-NGR-RGD PET imaging was greater than that of ^{18}F-FDG. On the contrary, the uptake of ^{68}Ga-NGR-RGD in inflammatory muscle was minimal, while avid uptake of ^{18}F-FDG in them was observed.

The quantitative data were obtained from the region-of-interest (ROI) analysis. Consistent with the PET images, ^{68}Ga-NGR-RGD showed significantly higher tumor-to-muscle (T/M) and tumor-to-liver (T/L) ratios, with values of 2.71 ± 0.21 and 1.05 ± 0.04 for SKOV3-bearing mice and 2.78 ± 0.34 and 1.43 ± 0.16 for ES-2-bearing mice (n=4; all $p<0.05$), as compared to low T/M and T/L ratios of ^{18}F-FDG (0.92 ± 0.22 and 0.92 ± 0.04 for SKOV3, 1.03 ± 0.47 and 0.97 ± 0.26 for ES-2) (**Figures 2B, C**). We also quantified the tracer uptakes in inflammatory muscles and compared them with tumors. The uptakes of ^{68}Ga-NGR-RGD in inflammatory muscles were much lower than tumors; however, their ^{18}F-FDG uptakes were much higher (**Figure 2D**). And as expected, the tumor-to-inflammatory muscle ratios of ^{68}Ga-NGR-RGD in SKOV3 and ES-2 were significantly higher than that of ^{18}F-FDG (all $p<0.001$) (**Figure 2E**).

Biodistribution studies of ^{68}Ga-NGR-RGD were conducted at 1 h post injection to validate the PET analysis. ^{68}Ga-NGR-RGD uptake in SKOV3 and ES-2 xenografts were 0.68 ± 0.03%ID/g and 0.70 ± 0.17%ID/g, respectively (**Figure 3A**). And high tumor-to-muscle and tumor-to-liver ratios were recorded in both ovarian tumors (**Figure 3B**), consistent with PET imaging studies, further indicating the utility of ^{68}Ga-NGR-RGD in the diagnosis of ovarian cancer.

Immunohistochemistry Staining in Tumor Tissues

SKOV3 tumor sections showed high expression of integrin $\alpha_v\beta_3$ and moderate CD13, and ES-2 tumor sections showed abundant CD13 and moderate integrin $\alpha_v\beta_3$ (**Figure 3C**). The staining of endothelial marker CD31 (cluster of differentiation 31) was also conducted to evaluate the angiogenesis of tumors. Both SKOV3 and ES-2 tumors displayed neovascularity. Immunohistochemical results of tumor tissues were consistent with western blot results.

PET Imaging and Biodistribution in Metastatic Models

To further investigate the potential application of ^{68}Ga-NGR-RGD in detecting metastases, SKOV3 and ES-2 abdominal metastatic models were established by injecting tumor cells intraperitoneally to simulate peritoneum implantation metastasis of ovarian cancers. As shown in **Figure 4**, peritoneal metastases could be easily delineated from ^{68}Ga-NGR-RGD PET/CT imaging in both ovarian tumor models. However, ^{18}F-FDG PET showed limited value in detecting these metastatic lesions, which was limited by the relatively low uptake in tumors and high background signals. In the images of ^{68}Ga-NGR-RGD (**Figures 4A, C**), several focal uptakes were found in the abdominal space of both SKOV3 and ES-2 group mice, suspected to be the peritoneal implantations; while in the images of ^{18}F-FDG (**Figures 4B, D**), several strips with high signal were observed in abdomen. Surgical explorations were done on the same mice after scanning, finding reddish-white

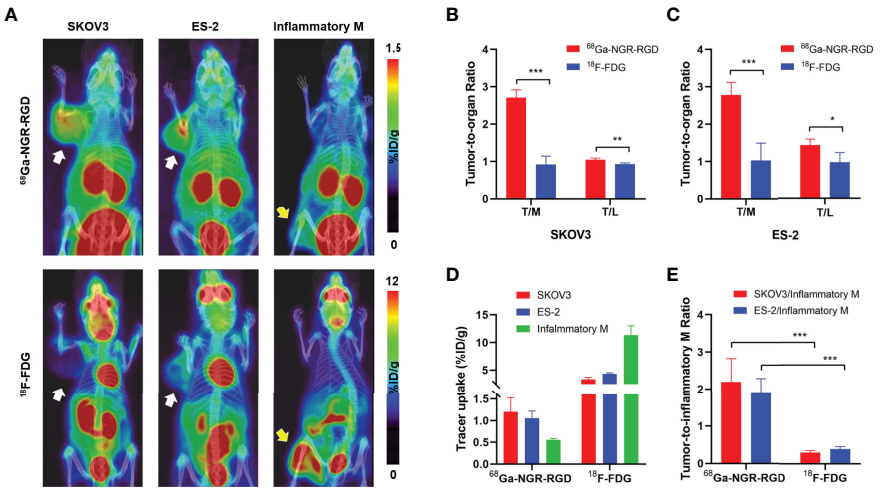

FIGURE 2 | PET/CT imaging and quantitative analysis of ^{68}Ga-NGR-RGD and ^{18}F-FDG in subcutaneous ovarian cancer models and inflammation models. **(A)** Representative static small PET/CT images of ^{68}Ga-NGR-RGD and ^{18}F-FDG in SKOV3 and ES-2 xenograft mice and turpentine oil-induced muscular inflammation mice at 1 h post radiotracer injection. White arrows indicated tumors and yellow arrows indicate the inflammatory muscles. **(B, C)** Tumor-to-muscle (T/M) and tumor-to-liver (T/L) ratios among ^{68}Ga-NGR-RGD and ^{18}F-FDG imaging in SKOV3 **(B)** and ES-2 **(C)** xenograft mice. **(D)** Quantification of ^{68}Ga-NGR-RGD and ^{18}F-FDG uptake in SKOV3 and ES-2 tumors and inflammatory muscle. **(E)** Tumor-to-inflammatory muscle (Tumor/Inflammatory M) ratios. *p < 0.05, **p < 0.01, ***p < 0.001. Data are expressed as mean ± SD (n = 4).

nodules with a slightly firm texture in all these groups (**Supplementary Figure 2**). The nodules were extracted for further evaluation, along with muscle, large intestine, small intestine, spleen, and kidney. The nodular tissues (3-6 mm) were confirmed to be ^{68}Ga-NGR-RGD-avid but ^{18}F-FDG-nonavid by ex-vivo PET imaging. High radioactivity accumulation was found in kidney, indicating that the tracer was mainly excreted *via* kidney. Other tissues in the abdominal cavity such as intestines and spleens showed low signals, indicating that the high signal focuses in PET images were the tumor metastases; whereas, uptake of ^{18}F-FDG was high in large intestine, suggesting the high signal regions in the image were not metastases but intestinal physiological uptake. Additionally, there were some liver metastases found in ES-2 abdominal models (**Figure 4E**). The liver metastases of ovarian tumor showed a strong uptake of ^{68}Ga-NGR-RGD but a similar low uptake of ^{18}F-FDG as healthy liver, which further demonstrated that ^{68}Ga-NGR-RGD has excellent metastasis detection efficiency of small peritoneal implants and liver metastases over ^{18}F-FDG. The hematoxylin-eosin (HE) staining confirmed that the lesions on the liver were metastatic tumors (**Figure 4F**).

Ex-vivo biodistribution studies showed 2.11 ± 0.67%ID/g and 0.97 ± 0.23%ID/g tumor uptake of ^{68}Ga-NGR-RGD in the SKOV3 and ES-2 abdominal metastasis models, respectively (**Figure 5** and **Supplementary Table 1**). Tumor uptakes of SKOV3 metastases were higher than SKOV3 subcutaneous tumors, which might be attributed to a better blood supply and the smaller metastasis size (34). Higher tumor-to-muscle (T/M) and tumor-to-liver (T/L) ratios were recorded in ^{68}Ga-NGR-RGD group, consistent with the results of s.c. tumor models (**Supplementary Figure 3**). More specifically, tumor-to-small intestine (T/SI) and tumor-to-large intestine (T/LI) ratios of ^{68}Ga-NGR-RGD in abdominal metastasis models were significantly higher than that of ^{18}F-FDG ($p<0.01$), which was consistent with PET imaging (**Figure 5C**).

DISCUSSION

CD13 and integrin $\alpha_v\beta_3$ are two important angiogenic factors involved in the regulation of tumor angiogenesis and tumor progression and several related targeted tracers were developed for the detection of ovarian cancers, with proven specific and sensitive targeting ability to ovarian cancers (22–25). However, due to the high heterogeneity, and genetical instability of ovarian cancer leading to a progressive increase in the number of different angiogenic factors as the cancer progress to advanced stages (20, 29, 30, 35, 36), the single-receptor targeted imaging strategies may only cover a limited subset of the patients. Owing to the dual-receptor binding property, improved *in vivo* kinetics, and increased circulation half-life, heterodimer tracers are expected to be more sensitive than single receptor-targeted tracers, especially when only one receptor type is overexpressed in a tumor model (31, 37, 38). In this study, we investigated the ability and potential of our recently developed dual CD13 and integrin $\alpha_v\beta_3$ targeted tracer ^{68}Ga-NGR-RGD, as a tumor-specific PET imaging agent, for the early diagnosis and staging of ovarian tumors. ^{68}Ga-NGR-RGD exhibited sharp contrasts in subcutaneous ovarian xenografts and metastases, higher tumor-to-background ratios, and in addition, high capability for distinguishing tumor from inflammatory tissue which is

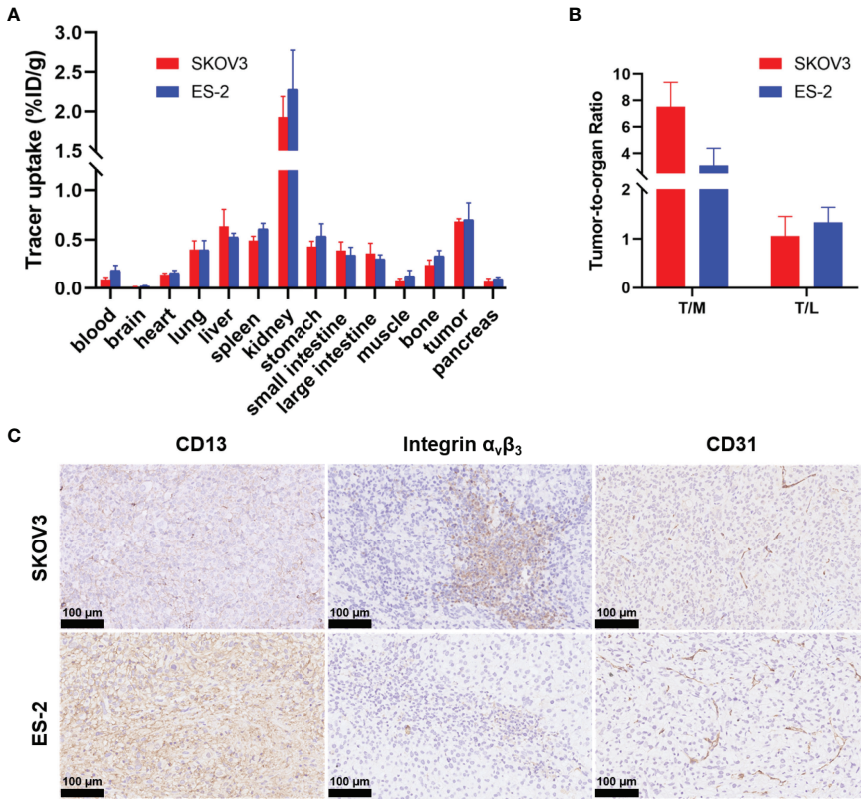

FIGURE 3 | Biodistribution data of ^{68}Ga-NGR-RGD in ovarian xenograft mice and immunohistochemistry analysis of tumor tissue sections. **(A)** Biodistribution of ^{68}Ga-NGR-RGD in SKOV3 and ES-2 subcutaneous ovarian tumor models at 1 h after injection (n = 4). **(B)** Tumor-to-muscle (T/M) and tumor-to-liver (T/L) ratios of ^{68}Ga-NGR-RGD in SKOV3 and ES-2 xenograft mice. **(C)** Immunohistochemistry staining of CD13, integrin $\alpha_v\beta_3$ and CD31 in SKOV3 and ES-2 tumor sections. Scale bar = 50 μm.

superior to ^{18}F-FDG, suggesting it has great potential to provide an enhancement to the standard diagnostic imaging of ovarian cancer.

Here, three ovarian tumor cell lines were selected and confirmed to express high level of integrin $\alpha_v\beta_3$ and/or CD13, indicating the possibility of dual-receptor targeted tracer for the detection of ovarian tumors. *In vitro* studies showed high uptake of ^{68}Ga-NGR-RGD in three ovarian cancer cell lines, and blocking studies showed significant decrease tracer uptake, validating the specific binding of our radio-tracer towards integrin $\alpha_v\beta_3$ and CD13 on ovarian tumor cells. Both SKOV3 and ES-2 subcutaneous metastatic tumors were clearly visualized by ^{68}Ga-NGR-RGD PET imaging at 1 h post tracer injection, although SKOV3 cells expressed a high level of integrin $\alpha_v\beta_3$ but relatively low level of CD13, and ES-2 expressed a high level of CD13 but low integrin $\alpha_v\beta_3$. These PET imaging results suggested a broad application of ^{68}Ga-NGR-RGD in the detection of ovarian tumors with improved tumor-targeting efficacy and sensitivity. Specifically, we could readily identify the location of small peritoneal implants and liver metastases (3-6 mm) in SKOV3 and ES-2 abdominal metastatic models. These results demonstrated the utility of ^{68}Ga-NGR-RGD for the sensitive detection of integrin $\alpha_v\beta_3$ and/or CD13 positive ovarian tumors.

When compared with ^{18}F-FDG, greater contrast of subcutaneous and metastatic tumors was observed in ^{68}Ga-NGR-RGD PET imaging of SKOV3 and ES-2 ovarian tumor models with significantly higher tumor-to-background ratios (T/M and T/L). In addition, the overall abdominal background uptake of ^{68}Ga-NGR-RGD with exception of urinary system was relatively low, so small metastases could be clearly delineated and easily differentiated from background uptake of surrounding tissues. However, ^{18}F-FDG accumulated heavily in the large intestine due to physiological intestinal uptake, which often makes it difficult to distinguish between normal intestinal uptake with adjacent abdominal or pelvic tumor or nodal uptake (39–42). Moreover, in turpentine oil-induced muscular inflammatory lesions (**Supplementary Figure 1**), high uptake of ^{18}F-FDG was observed in inflammatory cells (neutrophils and macrophages) and granulation tissues, which showed similar histology and FDG-avid features to the reported studies (43–45), mimicking a false-positive lesion of ^{18}F-FDG PET. In contrast to ^{18}F-FDG, ^{68}Ga-NGR-RGD showed low accumulation in inflammatory muscles. Therefore, the false-positive results in physical uptake of surrounding tissues and inflammatory changes detected by ^{18}F-FDG can potentially be avoided using ^{68}Ga-NGR-RGD as a more tumor-specific imaging agent.

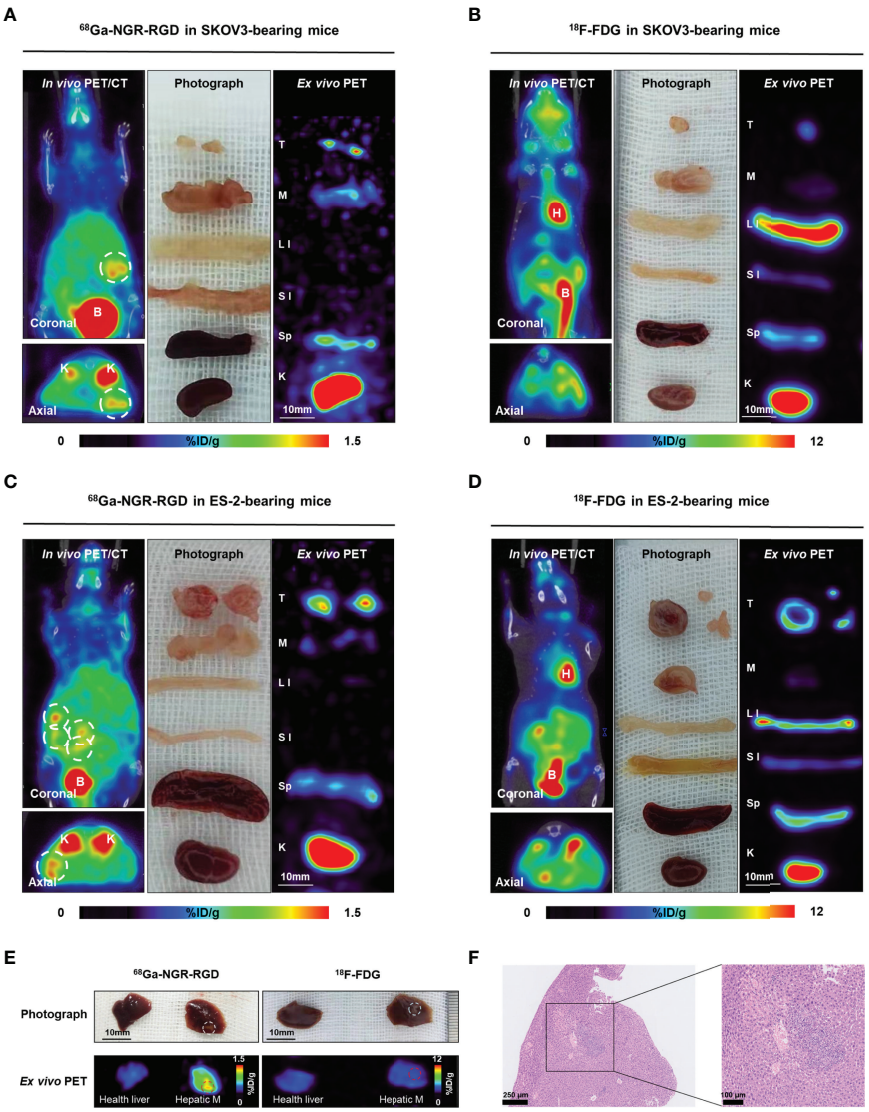

FIGURE 4 | Radiological-surgical correlation of abdominal metastatic models. **(A–D)** Representative static PET/CT images of ^{68}Ga-NGR-RGD and ^{18}F-FDG in SKOV3 and ES-2 abdominal ovarian metastasis models at 1 h post injection. In ^{68}Ga-NGR-RGD PET/CT imaging, several metastatic lesions with strong uptake were found in the peritoneal space [**(A, C)**, white circle]. In ^{18}F-FDG PET/CT imaging, there were several stripe high uptake foci **(B, D)**. Surgical exploration was done in the same animal after PET/CT imaging. Diffuse reddish-white nodules with a slightly firm texture were seen in the peritoneal space. Ex vivo PET imaging of excised tissues was performed. The small metastases showed relatively high ^{68}Ga-NGR-RGD uptake and low ^{18}F-FDG uptake. H, heart; B, bladder; T, tumor; M, muscle; LI, large intestine; SI, small intestine; Sp, spleen; K, kidney. Scale bar = 10 mm **(E)** ES-2 hepatic metastases (Hepatic M) showed strong uptake of ^{68}Ga-NGR-RGD, but a similar low uptake of ^{18}F-FDG as healthy liver. **(F)** HE staining confirmed that the lesion on liver was tumor tissue. Scale bar = 250 μm or 100 μm.

There are many potential applications that probably profit from PET imaging targeting CD13 and integrin $\alpha_v\beta_3$. With the great contrast of small tumors and higher tumor-to-background ratios than ^{18}F-FDG, ^{68}Ga-NGR-RGD could provide significant additional information, such as the relationship between tumor lesions with adjacent tissues and distant metastases, for determining TNM staging and optimal treatment options, so it suggests that ^{68}Ga-NGR-RGD is a potential candidate to be added to the workup and treatment planning of patients with ovarian tumors. In addition, anti-angiogenesis therapy has been regarded as a new era for tumor treatment in recent years, and targeting the tumor neovascularization, including CD13 and integrin $\alpha_v\beta_3$, has become a widely accepted therapeutic strategy in clinic (46, 47). The heterodimer strategy may also help with the development of therapy molecules, allowing for selection of responders and treatment response monitoring during and after therapy.

One limitation of this study is that only two types of tumor models were used, while ovarian tumors are highly heterogeneous with complex tumor components (48). Future work will evaluate tumor uptake of ^{68}Ga-NGR-RGD in other types of tumor models,

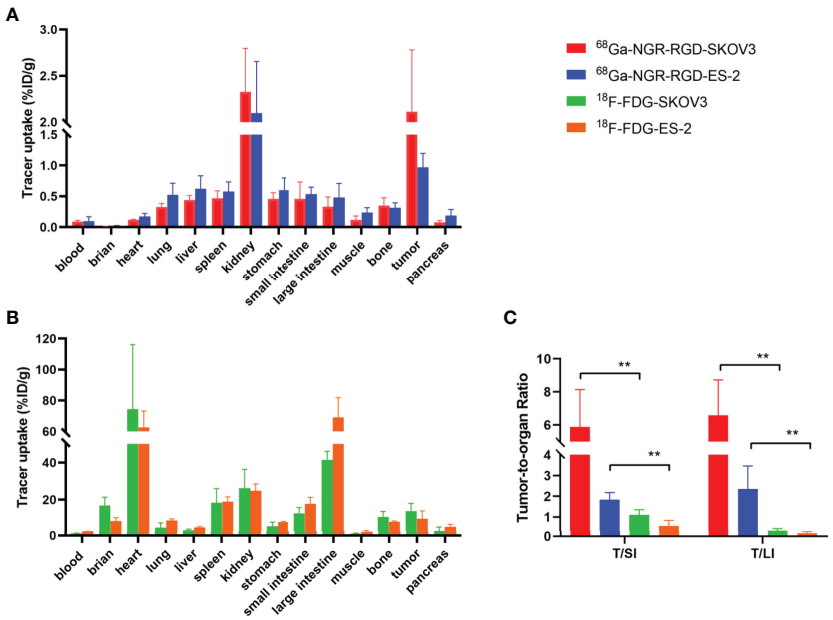

FIGURE 5 | Biodistribution for the validation of PET/CT results. Biodistribution of ^{68}Ga-NGR-RGD in SKOV3 and ES-2 **(A)** abdominal metastatic ovarian tumor models and ^{18}F-FDG in SKOV3 and ES-2 **(B)** metastatic models at 1 h after tracer injection. **(C)** Metastatic tumor lesions showed avid ^{68}Ga-NGR-RGD uptake with a significantly higher tumor-to-small intestine (T/SI) and tumor-to-large intestine (T/LI) comparing to ^{18}F-FDG. **p < 0.01. Data are expressed as mean ± SD (n = 4).

especially patient-derived xenograft models, with a various expression of CD13 and integrin $\alpha_v\beta_3$. Currently, ^{68}Ga is usually produced by an in-house ^{68}Ge/^{68}Ga generator, and one elution could provide a dose enough for 2-5 patients based on the specification of the generator. Therefore, we believe the final cost of a ^{68}Ga-tracer scan will be acceptable and should be close to routine ^{18}F-FDG PET scans (after considering the cyclotron and its maintenance). Clinical studies evaluating the safety and efficacy of the dual-receptor targeted tracer in humans are ongoing, which will be free of charge for the patients enrolled, and we will report relevant data in the future.

In conclusion, ^{68}Ga-NGR-RGD demonstrated a promising application for early diagnosis, staging, and follow-up of ovarian cancer, as it showed high tracer uptake, sharp contrasts in subcutaneous xenograft and metastases, and higher tumor-to-background ratios in ovarian tumor models with different expression levels of CD13 and integrin $\alpha_v\beta_3$, demonstrating superior diagnostic values than ^{18}F-FDG PET/CT. Meanwhile, *in vivo* PET imaging studies showed significantly lower accumulation of ^{68}Ga-NGR-RGD in inflammatory lesions as compared to ^{18}F-FDG, suggesting the potential of ^{68}Ga-NGR-RGD for differentiating between tumor and non-tumor inflammation.

DATA AVAILABILITY STATEMENT

The original contributions presented in the study are included in the article/**Supplementary Material**. Further inquiries can be directed to the corresponding authors.

ETHICS STATEMENT

The animal study was reviewed and approved by the Institutional Animal Care and Use Committee of Tongji Medical College of Huazhong University of Science and Technology.

AUTHOR CONTRIBUTIONS

YL wrote the majority of the manuscript. YL, FS, and HJ performed the canine operations. XS and XYL assisted in PET imaging and biodistribution studies. XX, QL, and YZ provided specific experimental advice and technique support. YG and DZ was the primary developer of NGR-RGD and provided guidance for dosing and imaging decisions. YL, XLL, and YG designed the experiments, analyzed the data, and edited the manuscript. All authors contributed to the article and approved the submitted version.

FUNDING

This work was supported by the National Natural Science Foundation of China (81801738, 81630049).

SUPPLEMENTARY MATERIAL

The Supplementary Material for this article can be found online at: https://www.frontiersin.org/articles/10.3389/fonc.2022.884554/full#supplementary-material

REFERENCES

1. Siegel RL, Miller KD, Jemal A. Cancer Statistics, 2019. *CA Cancer J Clin* (2019) 69:7–34. doi: 10.3322/caac.21551
2. Iyer VR, Lee SI. MRI, CT, and PET/CT for Ovarian Cancer Detection and Adnexal Lesion Characterization. *AJR Am J Roentgenol* (2010) 194:311–21. doi: 10.2214/AJR.09.3522
3. Beiderwellen K, Grueneisen J, Ruhlmann V, Buderath P, Aktas B, Heusch P, et al. [(18)F]Fdg PET/MRI vs. PET/CT for Whole-Body Staging in Patients With Recurrent Malignancies of the Female Pelvis: Initial Results. *Eur J Nucl Med Mol Imaging* (2015) 42:56–65. doi: 10.1007/s00259-014-2902-8
4. Khiewvan B, Torigian DA, Emamzadehfard S, Paydary K, Salavati A, Houshmand S, et al. An Update on the Role of PET/CT and PET/MRI in Ovarian Cancer. *Eur J Nucl Med Mol Imaging* (2017) 44:1079–91. doi: 10.1007/s00259-017-3638-z
5. López-Mora DA, Carrió I, Flotats A. Digital PET vs Analog Pet: Clinical Implications. *Semin Nucl Med* (2021) 52:302–11. doi: 10.1053/j.semnuclmed.2021.10.004
6. Alberts I, Prenosil G, Sachpekidis C, Weitzel T, Shi K, Rominger A, et al. Digital Versus Analogue PET in [(68)Ga]Ga-PSMA-11 PET/CT for Recurrent Prostate Cancer: A Matched-Pair Comparison. *Eur J Nucl Med Mol Imagl* (2020) 47:614–23. doi: 10.1007/s00259-019-04630-y
7. Fenchel S, Grab D, Nuessle K, Kotzerke J, Rieber A, Kreienberg R, et al. Asymptomatic Adnexal Masses: Correlation of FDG PET and Histopathologic Findings. *Radiology* (2002) 223:780–8. doi: 10.1148/radiol.2233001850
8. Rieber A, Nüssle K, Stöhr I, Grab D, Fenchel S, Kreienberg R, et al. Preoperative Diagnosis of Ovarian Tumors With MR Imaging: Comparison With Transvaginal Sonography, Positron Emission Tomography, and Histologic Findings. *AJR Am J Roentgenol* (2001) 177:123–9. doi: 10.2214/ajr.177.1.1770123
9. Rockall AG, Cross S, Flanagan S, Moore E, Avril N. The Role of FDG-PET/CT in Gynaecological Cancers. *Cancer Imaging* (2012) 12:49–65. doi: 10.1102/1470-7330.2012.0007
10. Ponisio MR, Dehdashti F. A Role of PET Agents Beyond FDG in Gynecology. *Semin Nucl Med* (2019) 49:501–11. doi: 10.1053/j.semnuclmed.2019.06.008
11. Lerman H, Metser U, Grisaru D, Fishman A, Lievshitz G, Even-Sapir E. Normal and Abnormal 18f-FDG Endometrial and Ovarian Uptake in Pre- and Postmenopausal Patients: Assessment by PET/Ct. *J Nucl Med* (2004) 45:266–71.
12. Rahman WT, Wale DJ, Viglianti BL, Townsend DM, Manganaro MS, Gross MD, et al. The Impact of Infection and Inflammation in Oncologic (18)F-FDG PET/CT Imaging. *BioMed Pharmacot* (2019) 117:109168. doi: 10.1016/j.biopha.2019.109168
13. Almuhaideb A, Papathanasiou N, Bomanji J. 18f-Fdg PET/CT Imaging in Oncology. *Ann Saudi Med* (2011) 31:3–13. doi: 10.4103/0256-4947.75771
14. Boré P, Descourt R, Ollivier L, Le Roux PY, Abgral R. False Positive 18f-Fdg Positron Emission Tomography Findings in Schwannoma-A Caution for Reporting Physicians. *Front Med (Lausanne)* (2018) 5:275. doi: 10.3389/fmed.2018.00275
15. Boyle AJ, Tong J, Zoghbi SS, Pike VW, Innis RB, Vasdev N. Repurposing (11) C-PS13 for PET Imaging of Cyclooxygenase-1 in Ovarian Cancer Xenograft Mouse Models. *J Nucl Med* (2021) 62:665–8. doi: 10.2967/jnumed.120.249367
16. Sanduleanu S, Wiel A, Lieverse R, Marcus D, Ibrahim A, Primakov S, et al. Hypoxia PET Imaging With [18f]-HX4-A Promising Next-Generation Tracer. *Cancers (Basel)* (2020) 12:1322. doi: 10.3390/cancers12051322
17. Trencsényi G, Márián T, Lajtos I, Krasznai Z, Balkay L, Emri M, et al. 18fdg, [18f] FLT, [18f]FAZA, and 11C-Methionine Are Suitable Tracers for the Diagnosis and *In Vivo* Follow-Up of the Efficacy of Chemotherapy by miniPET in Both Multidrug Resistant and Sensitive Human Gynecologic Tumor Xenografts. *BioMed Res Int* (2014) 2014:787365. doi: 10.1155/2014/787365
18. Makvandi M, Pantel A, Schwartz L, Schubert E, Xu K, Hsieh CJ, et al. A PET Imaging Agent for Evaluating PARP-1 Expression in Ovarian Cancer. *J Clin Invest* (2018) 128:2116–26. doi: 10.1172/JCI97992
19. Matsumoto H, Watabe T, Igarashi C, Tachibana T, Hihara F, Waki A, et al. Evaluation of (64)Cu-Labeled New Anti-Egfr Antibody NCAB001 With Intraperitoneal Injection for Early Pet Diagnosis of Pancreatic Cancer in Orthotopic Tumor-Xenografted Mice and Nonhuman Primates. *Pharmaceut (Basel)* (2021) 14:950. doi: 10.3390/ph14100950
20. Lugano R, Ramachandran M, Dimberg A. Tumor Angiogenesis: Causes, Consequences, Challenges and Opportunities. *Cell Mol Life Sci* (2020) 77:1745–70. doi: 10.1007/s00018-019-03351-7
21. Luan Y, Xu W. The Structure and Main Functions of Aminopeptidase N. *Curr Med Chem* (2007) 14:639–47. doi: 10.2174/092986707780059571
22. Hashida H, Takabayashi A, Kanai M, Adachi M, Kondo K, Kohno N, et al. Aminopeptidase N Is Involved in Cell Motility and Angiogenesis: Its Clinical Significance in Human Colon Cancer. *Gastroenterology* (2002) 122:376–86. doi: 10.1053/gast.2002.31095
23. Danhier F, Le Breton A, Préat V. RGD-Based Strategies to Target Alpha(V) Beta(3) Integrin in Cancer Therapy and Diagnosis. *Mol Pharm* (2012) 9:2961–73. doi: 10.1021/mp3002733
24. Kumar CC. Integrin Alpha V Beta 3 as a Therapeutic Target for Blocking Tumor-Induced Angiogenesis. *Curr Drug Targets* (2003) 4:123–31. doi: 10.2174/1389450033346830
25. Cui SX, Qu XJ, Gao ZH, Zhang YS, Zhang XF, Zhao CR, et al. Targeting Aminopeptidase N (APN/CD13) With Cyclic-Imide Peptidomimetics Derivative CIP-13f Inhibits the Growth of Human Ovarian Carcinoma Cells. *Cancer Lett* (2010) 292:153–62. doi: 10.1016/j.canlet.2009.11.021
26. Yang Y, Zhang J, Zou H, Shen Y, Deng S, Wu Y. Synthesis and Evaluation of (68) Ga-Labeled Dimeric cNGR Peptide for PET Imaging of CD13 Expression With Ovarian Cancer Xenograft. *J Cancer* (2021) 12:244–52. doi: 10.7150/jca.49628
27. Jin ZH, Tsuji AB, Degardin M, Sugyo A, Obara S, Wakizaka H, et al. Radiotheranostic Agent (64)Cu-Cyclam-RAFT-C(-RGDfK-)(4) for Management of Peritoneal Metastasis in Ovarian Cancer. *Clin Cancer Res* (2020) 26:6230–41. doi: 10.1158/1078-0432.CCR-20-1205
28. Minamimoto R, Karam A, Jamali M, Barkhodari A, Gambhir SS, Dorigo O, et al. Pilot Prospective Evaluation of (18)F-FPPRGD2 PET/CT in Patients With Cervical and Ovarian Cancer. *Eur J Nucl Med Mol Imaging* (2016) 43:1047–55. doi: 10.1007/s00259-015-3263-7
29. Kobayashi M, Sawada K, Kimura T. Potential of Integrin Inhibitors for Treating Ovarian Cancer: A Literature Review. *Cancers (Basel)* (2017) 9:83. doi: 10.3390/cancers9070083
30. Friedman R. Drug Resistance in Cancer: Molecular Evolution and Compensatory Proliferation. *Oncotarget* (2016) 7:11746–55. doi: 10.18632/oncotarget.7459
31. Gai Y, Jiang Y, Long Y, Sun L, Liu Q, Qin C, et al. Evaluation of an Integrin α(V)β(3) and Aminopeptidase N Dual-Receptor Targeting Tracer for Breast Cancer Imaging. *Mol Pharm* (2020) 17:349–58. doi: 10.1021/acs.molpharmaceut.9b01134
32. Wu GJ, Zeng GF. METCAM/MUC18 is a Novel Tumor and Metastasis Suppressor for the Human Ovarian Cancer SKOV3 Cells. *BMC Cancer* (2016) 16:136. doi: 10.1186/s12885-016-2181-9
33. Wen W, Liang W, Wu J, Kowolik CM, Buettner R, Scuto A, et al. Targeting JAK1/STAT3 Signaling Suppresses Tumor Progression and Metastasis in a Peritoneal Model of Human Ovarian Cancer. *Mol Cancer Ther* (2014) 13:3037–48. doi: 10.1158/1535-7163.MCT-14-0077
34. Soret M, Bacharach SL, Buvat I. Partial-Volume Effect in PET Tumor Imaging. *J Nucl Med* (2007) 48:932–45. doi: 10.2967/jnumed.106.035774
35. Wang Z, Dabrosin C, Yin X, Fuster MM, Arreola A, Rathmell WK, et al. Broad Targeting of Angiogenesis for Cancer Prevention and Therapy. *Semin Cancer Biol* (2015) 35 Suppl:S224–224S243. doi: 10.1016/j.semcancer.2015.01.001
36. Kroeger PT Jr, Drapkin R. Pathogenesis and Heterogeneity of Ovarian Cancer. *Curr Opin Obstet Gynecol* (2017) 29:26–34. doi: 10.1097/GCO.0000000000000340
37. Liu Z, Niu G, Wang F, Chen X. (68)Ga-Labeled NOTA-RGD-BBN Peptide for Dual Integrin and GRPR-Targeted Tumor Imaging. *Eur J Nucl Med Mol Imaging* (2009) 36:1483–94. doi: 10.1007/s00259-009-1123-z
38. Judmann B, Braun D, Wängler B, Schirrmacher R, Fricker G, Wängler C. Current State of Radiolabeled Heterobivalent Peptidic Ligands in Tumor Imaging and Therapy. *Pharmaceut (Basel)* (2020) 13:173. doi: 10.3390/ph13080173
39. Franquet E, Palmer MR, Gifford AE, Selen DJ, Chen YC, Sedora-Roman N, et al. Rifaximin Suppresses Background Intestinal 18f-FDG Uptake on PET/CT Scans. *Nucl Med Commun* (2014) 35:1026–31. doi: 10.1097/MNM.0000000000000170
40. Gutman F, Alberini JL, Wartski M, Vilain D, Le Stanc E, Sarandi F, et al. Incidental Colonic Focal Lesions Detected by FDG Pet/Ct. *AJR Am J Roentgenol* (2005) 185:495–500. doi: 10.2214/ajr.185.2.01850495

41. Heusner TA, Hahn S, Hamami ME, Kim UH, Baumeister R, Forsting M, et al. Gastrointestinal 18f-FDG Accumulation on PET Without a Corresponding CT Abnormality Is Not an Early Indicator of Cancer Development. *Eur Radiol* (2009) 19:2171–9. doi: 10.1007/s00330-009-1405-7
42. Tatlidil R, Jadvar H, Bading JR, Conti PS. Incidental Colonic Fluorodeoxyglucose Uptake: Correlation With Colonoscopic and Histopathologic Findings. *Radiology* (2002) 224:783–7. doi: 10.1148/radiol.2243011214
43. Watabe T, Ikeda H, Nagamori S, Wiriyasermkul P, Tanaka Y, Naka S, et al. (18)F-FBPA as a Tumor-Specific Probe of L-Type Amino Acid Transporter 1 (LAT1): A Comparison Study With (18)F-FDG and (11)C-Methionine Pet. *Eur J Nucl Med Mol Imaging* (2017) 44:321–31. doi: 10.1007/s00259-016-3487-1
44. Lee SJ, Thien Quach CH, Jung KH, Paik JY, Lee JH, Park JW, et al. Oxidized Low-Density Lipoprotein Stimulates Macrophage 18f-FDG Uptake *Via* Hypoxia-Inducible Factor-1α Activation Through Nox2-Dependent Reactive Oxygen Species Generation. *J Nucl Med* (2014) 55:1699–705. doi: 10.2967/jnumed.114.139428
45. Takeshita N, Tohma T, Miyauchi H, Suzuki K, Nishimori T, Ohira G, et al. Suture Granuloma With False-Positive Findings on FDG-PET/CT Resected *Via* Laparoscopic Surgery. *Int Surg* (2015) 100:604–7. doi: 10.9738/INTSURG-D-14-00140.1
46. He L, Zhu W, Chen Q, Yuan Y, Wang Y, Wang J, et al. Ovarian Cancer Cell-Secreted Exosomal miR-205 Promotes Metastasis by Inducing Angiogenesis. *Theranostics* (2019) 9:8206–20. doi: 10.7150/thno.37455
47. Ferrara N, Kerbel RS. Angiogenesis as a Therapeutic Target. *Nature* (2005) 438:967–74. doi: 10.1038/nature04483
48. Torre LA, Trabert B, DeSantis CE, Miller KD, Samimi G, Runowicz CD, et al. Ovarian Cancer Statistics, 2018. *CA Cancer J Clin* (2018) 68:284–96. doi: 10.3322/caac.21456

Conflict of Interest: The authors declare that the research was conducted in the absence of any commercial or financial relationships that could be construed as a potential conflict of interest.

Publisher's Note: All claims expressed in this article are solely those of the authors and do not necessarily represent those of their affiliated organizations, or those of the publisher, the editors and the reviewers. Any product that may be evaluated in this article, or claim that may be made by its manufacturer, is not guaranteed or endorsed by the publisher.

frontiers | Frontiers in Oncology

CASE REPORT
published: 12 July 2022
doi: 10.3389/fonc.2022.925382

Case Report: Lung Adenocarcinoma Initially Presenting With Cutaneous and Subcutaneous Metastases

Jingjing Wang[1,2,3], *Ruolin Wu*[1,2,3], *Fang Liu*[1,2,3], *Liu Yang*[4], *Fan Hu*[1,2,3], *Zhijian Wu*[1,2,3], *Zairong Gao*[1,2,3*] *and Xiaotian Xia*[1,5*]

[1] Department of Nuclear Medicine, Union Hospital, Tongji Medical College, Huazhong University of Science and Technology, Wuhan, China, [2] Hubei Province Key Laboratory of Molecular Imaging, Wuhan, China, [3] Key Laboratory of Biological Targeted Therapy, the Ministry of Education, Wuhan, China, [4] Department of Dermatology, Union Hospital, Tongji Medical College, Huazhong University of Science and Technology, Wuhan, China, [5] Department of Nuclear Medicine, The People's Hospital of Honghu, Honghu, China

Cutaneous and subcutaneous soft tissue metastases are rare in lung adenocarcinoma and suggest poor prognosis. We report a patient with lung adenocarcinoma who initially presented with cutaneous and subcutaneous metastases to the abdomen that were initially presumed to be herpes zoster and an occult subcutaneous soft tissue mass. Because the lesions progressed over 3 weeks despite routine herpes zoster treatment, magnetic resonance imaging was performed and showed a presumed sarcoma; however, ^{18}F-fluourodeoxyglucose positron emission tomography/computed tomography demonstrated pulmonary lesions. Biopsy of the abdominal lesion confirmed poorly differentiated lung adenocarcinoma. Early diagnosis of soft tissue metastasis can be difficult. Clinicians should suspect internal organ malignancy when a progressive cutaneous or subcutaneous soft tissue lesion is encountered.

Keywords: lung adenocarcinoma, soft tissue, skin rashes, metastasis, ^{18}F-FDG, PET/CT

OPEN ACCESS

Edited by:
Pilar López-Larrubia, Spanish National Research Council (CSIC), Spain

Reviewed by:
Murat Fani BOZKURT, Hacettepe University, Turkey
Deguan Lv, University of Pittsburgh Medical Center, United States

***Correspondence:**
Zairong Gao, gaobonn@hust.edu.cn
Xiaotian Xia, Xiaxiaotian_xia@hust.edu.cn

Specialty section:
This article was submitted to Cancer Imaging and Image-directed Interventions, a section of the journal Frontiers in Oncology

Received: *21 April 2022*
Accepted: *23 June 2022*
Published: *12 July 2022*

Citation:
Wang J, Wu R, Liu F, Yang L, Hu F, Wu Z, Gao Z and Xia X (2022) Case Report: Lung Adenocarcinoma Initially Presenting With Cutaneous and Subcutaneous Metastases. Front. Oncol. 12:925382. doi: 10.3389/fonc.2022.925382

INTRODUCTION

Lung cancer is a frequently encountered malignancy that can metastasize to almost all organs and is associated with high mortality (1, 2). Lung adenocarcinoma commonly metastasizes to the liver, adrenal glands, brain, and bone (3). Soft tissue metastases from lung adenocarcinoma are rare and occur predominantly in men (4). They may be apparent before the primary tumor and typically herald a poor prognosis. Reported mean survival in patients with skin metastases is 2.9 months (5), so early diagnosis and treatment are important. However, the diagnosis of skin metastases may be delayed or missed. A high index of suspicion is required.

CASE DESCRIPTION

A 52-year-old woman presented with a 3-week history of painful rash and subcutaneous soft tissue mass overlying the right abdomen at the waistline. She denied constitutional symptoms such as fever, chills, night sweats, and unintentional weight loss. There was no history of major trauma, surgery, smoking, alcohol use, or drug or food allergy. Notably, the patient was exposed to

secondhand smoke from nicotine cigarettes due to her husband's smoking. In addition, her father died of esophageal cancer. Herpes zoster was initially suspected but appropriate treatment did not result in clinical improvement. In fact, progression had occurred. Therefore, she was hospitalized for further investigation and treatment. Physical examination showed a raised skin mass surrounded by swelling and erythema on the right abdomen (**Figure 1A**). Serum erythrocyte sedimentation rate, C-reactive protein, white blood cell count, and multiple tumor markers were elevated. Ultrasonography revealed a solid mass underneath the rash. On magnetic resonance imaging (MRI), the mass was 10 cm in diameter and inhomogeneous on T2-weighted sequences (**Figures 1B, C**) and exhibited markedly restricted diffusion on diffusion-weighted sequences (**Figure 1D**). The mass was suspected to be a sarcoma. To investigate potential distant metastases, ^{18}F-fluourodeoxyglucose (FDG) positron emission tomography (PET)/computed tomography (CT) was performed, which showed the previously demonstrated large abdominal mass was hypermetabolic in the periphery and hypometabolic in the center (**Figure 2A**); other hypermetabolic lesions were shown in the right lung and the posterior pleural wall (**Figure 2B–E**). Lung cancer with metastases was suspected and the patient underwent ultrasound-guided biopsy of the subcutaneous soft tissue mass. Examination of hematoxylin and eosin-stained specimen (**Figure 3A**) revealed abundant oval and plump cells with enlarged nuclei and red, broad cytoplasm. Immunohistochemical examination showed staining was positive for CK7 (**Figure 3B**), TTF-1 (**Figure 3C**), and PCK but negative for P63, CK20, Villin, ER, CDX2, HER2, P16, GATA-3, and VT-1. This suggested a diagnosis of primary pulmonary adenocarcinoma with metastasis. Because PDL-1 was expressed (**Figure 3D**) and EGFR mutation was not detected, the patient was placed on bevacizumab plus pemetrexed–platinum doublet chemotherapy. After six cycles, the primary pulmonary lesions shrunk but the cutaneous lesions did not. Molecular testing revealed mutation in the BRAF 15 exon and targeted therapy was proposed, but the patient refused for financial reasons. For relieving the patient's pain, palliative radiotherapy was initiated.

DISCUSSION

Lung cancer morbidity and mortality is highest of all cancers (1, 2) and lung adenocarcinoma accounts for approximately 40% of all lung cancers (6). Although lung carcinoma can metastasize to all organs, the liver, adrenal glands, bone, kidney, and brain are the most common sites (3). Metastasis to cutaneous and subcutaneous soft tissues is rare, with reported incidence rates ranging between 1% and 12% (5, 7–9). Soft tissue metastasis can be challenging to diagnose when it is the initial cancer manifestation, as in our patient, who presented with a painful rash in the absence of typical lung adenocarcinoma symptoms (10). Soft tissue metastases may rapidly progress when the initial diagnosis is missed.

To evaluate soft tissue metastases, MRI is the most sensitive and specific imaging modality and enables assessment of tissue characteristics, tumor extent, and areas of reactivity (11, 12). In our patient, MRI was highly suspicious for sarcoma but ^{18}F-FDG PET/CT suggested a lung primary, which was confirmed by biopsy. Although MRI can distinguish between benign and malignant tumors, it cannot further distinguish malignancy. Compared with sarcoma, soft tissue metastases from organ malignancies are rare. They are easily missed, especially when symptoms of the primary are absent or atypical. Therefore, ^{18}F-FDG PET/CT before biopsy is essential to improve diagnostic accuracy and distinguish soft tissue masses.

Optimal management requires accurate diagnosis, which requires biopsy in most cases (13, 14). In our patient, histopathological and immunohistochemical examinations resulted in a diagnosis of poorly differentiated pulmonary adenocarcinoma (15, 16). In this disease, the appearance of metastatic soft tissue masses indicates an advanced stage and poor prognosis. Chemotherapy, immunotherapy, targeted therapy, and radiotherapy are the mainstay treatments for soft tissue metastasis; surgery is not typically recommended (17–19). Unfortunately, six cycles of bevacizumab plus pemetrexed–platinum doublet chemotherapy were not as effective as we had hoped. The targeted therapy has been shown to decrease tumor burden, decrease symptoms, and dramatically improve survival outcomes in advanced lung cancers (19, 20). However, our patient

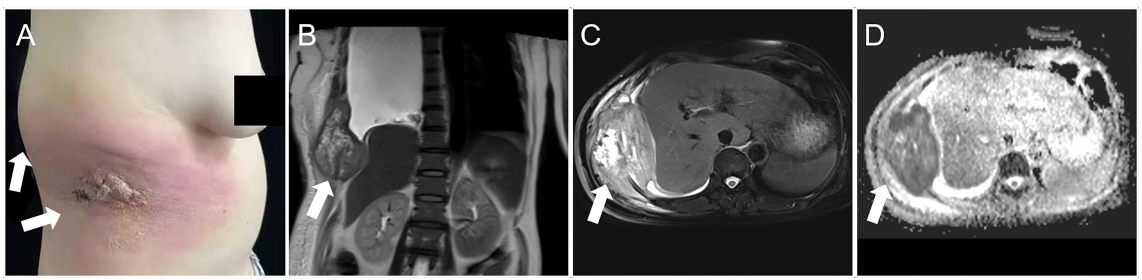

FIGURE 1 | Physical examination showed an erythematous rash and swelling surrounding a skin mass on the right abdomen (**A**, arrows). Magnetic resonance imaging shoed an inhomogeneous soft tissue mass approximately 10 cm in diameter (**B**, coronal T2-weighted image; **C**, axial fat saturation T2-weighted image). The lesion also showed markedly restricted diffusion on diffusion-weighted sequences (**D**, arrow).

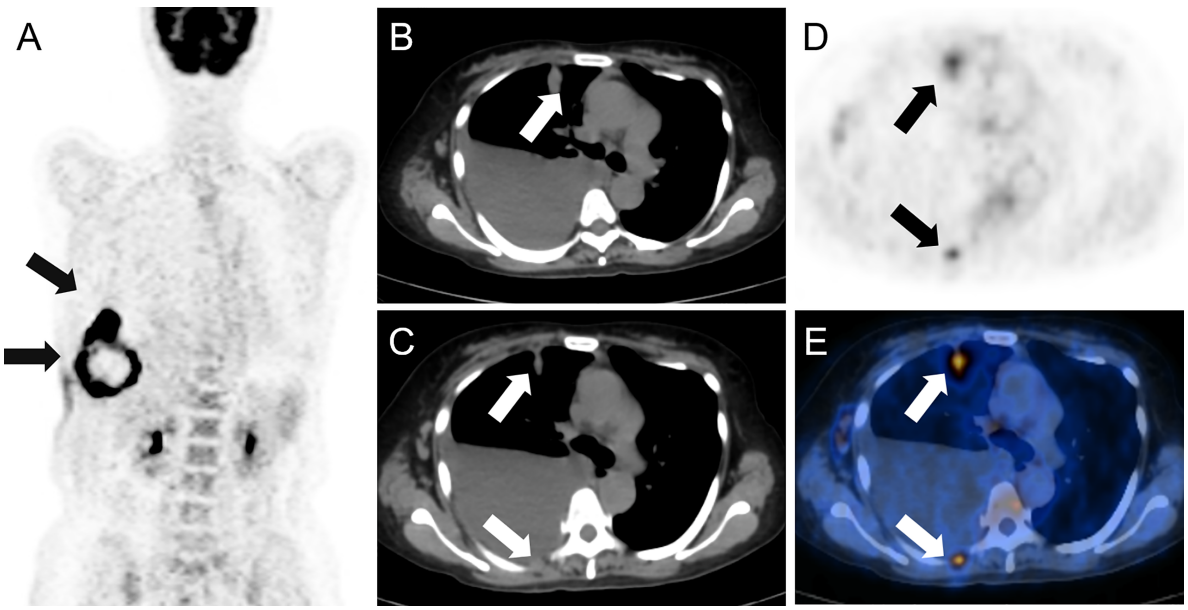

FIGURE 2 | A large mass showing hypermetabolism peripherally and hypometabolism centrally was found on 18F-fluorodeoxyglucose positron emission tomography/computed tomography **(A)**, arrows. Hypermetabolic lesions were imaged in the right lung and the posterior pleural wall (arrows) on axial computed tomography **(B, C)**, positron emission tomography **(D)** and fusion imaging **(E)**.

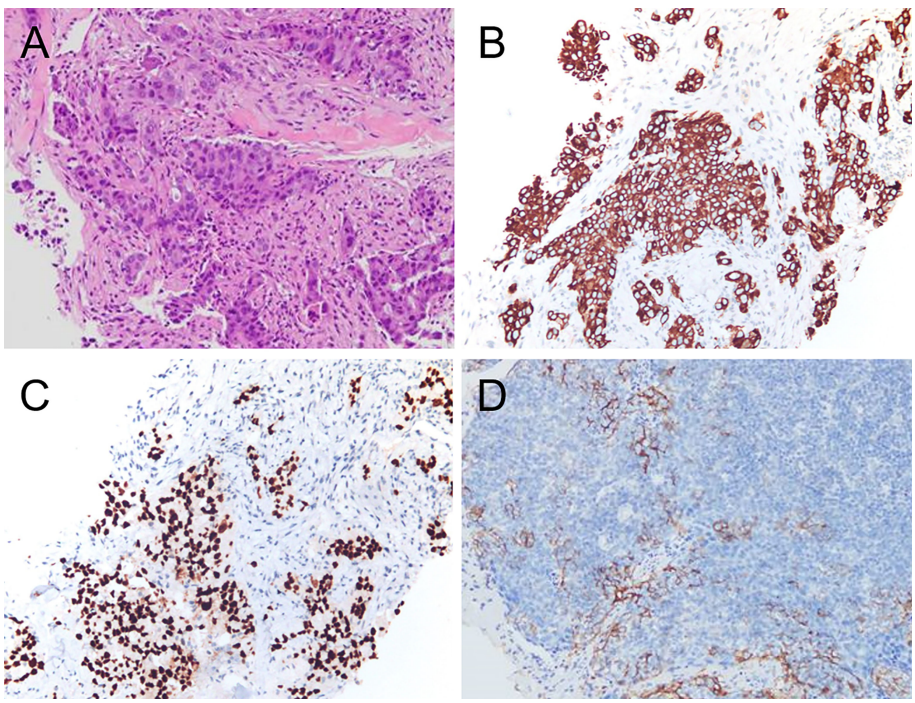

FIGURE 3 | Hematoxylin and eosin staining revealed the tumor was composed of abundant oval and plump cells with enlarged nuclei and red, broad cytoplasm **(A)**. Immunohistochemical staining for CK 7 **(B)** showed a strong and diffuse brown cytoplasmic reaction. TTF-1 staining **(C)** Showed strong nuclear staining of tumor cells. Immunohistochemical analysis showed PDL-1 expression **(D)**.

refused the targeted therapy for financial reasons. Then palliative radiotherapy was initiated and proved effective for pain relief. To date, the patient's general condition has remained stable.

Early diagnosis of soft tissue metastasis can be difficult. Clinicians should suspect internal organ malignancy when a progressive cutaneous or subcutaneous soft tissue lesion is encountered. A thorough examination should be performed and ^{18}F-FDG PET/CT should be considered for further evaluation.

DATA AVAILABILITY STATEMENT

The raw data supporting the conclusions of this article will be made available by the authors, without undue reservation.

ETHICS STATEMENT

The studies involving human participants were reviewed and approved by Ethical Committee of Union Hospital, Tongji Medical College. The patients/participants provided their written informed consent to participate in this study.

AUTHOR CONTRIBUTIONS

JW, RW, LY, ZW and XX obtained and analyzed the clinical data. JW and XX wrote the manuscript. FL and FH designed and constructed the figures. XX and ZG designed the study. All authors contributed to patient care and writing and revising the manuscript and figures. All authors contributed to the article and approved the submitted version.

FUNDING

This research was supported by the National Natural Science Foundation of China (Grant Numbers 81801737, 81771866).

ACKNOWLEDGMENTS

We thank Dr. Ranran Ding for providing and analyzing the immunohistochemical data of CK7 and TTF-1. We thank Liwen Bianji (Edanz) (https://www.liwenbianji.cn) for editing the language of a draft of this manuscript.

REFERENCES

1. Siegel RL, Miller KD, Fuchs HE, Jemal A. Cancer Statistics, 2021. *CA Cancer J Clin* (2021) 71(1):7–33. doi: 10.3322/caac.21654
2. Allemani C, Matsuda T, Di Carlo V, Harewood R, Matz M, Nikšić M, et al. Global Surveillance of Trends in Cancer Survival 2000–14 (Concord-3): Analysis of Individual Records for 37 513 025 Patients Diagnosed With One of 18 Cancers From 322 Population-Based Registries in 71 Countries. *Lancet* (2018) 391(10125):1023–75. doi: 10.1016/s0140-6736(17)33326-3
3. Tamura T, Kurishima K, Nakazawa K, Kagohashi K, Ishikawa H, Satoh H, et al. Specific Organ Metastases and Survival in Metastatic Non-Small-Cell Lung Cancer. *Mol Clin Oncol* (2015) 3(1):217–21. doi: 10.3892/mco.2014.410
4. Alcaraz I, Cerroni L, Rütten A, Kutzner H, Requena L. Cutaneous Metastases From Internal Malignancies: A Clinicopathologic and Immunohistochemical Review. *Am J Dermatopathol* (2012) 34(4):347–93. doi: 10.1097/DAD.0b013e31823069cf
5. Song Z, Lin B, Shao L, Zhang Y. Cutaneous Metastasis as a Initial Presentation in Advanced Non-Small Cell Lung Cancer and Its Poor Survival Prognosis. *J Cancer Res Clin Oncol* (2012) 138(10):1613–7. doi: 10.1007/s00432-012-1239-6
6. Tvedten E, Deak Z, Schwartz B, Rice A. An Atypical Presentation of Soft Tissue Metastasis in a Patient With Lung Cancer. *Cureus* (2021) 13(7):e16294. doi: 10.7759/cureus.16294
7. Gül U, Kiliç A, Gönül M, Külcü Cakmak S, Erinçkan C. Spectrum of Cutaneous Metastases in 1287 Cases of Internal Malignancies: A Study From Turkey. *Acta dermato-venereol* (2007) 87(2):160–2. doi: 10.2340/00015555-0199
8. Dhambri S, Zendah I, Ayadi-Kaddour A, Adouni O, El Mezni F. Cutaneous Metastasis of Lung Carcinoma: A Retrospective Study of 12 Cases. *J Eur Acad Dermatol Venereol JEADV* (2011) 25(6):722–6. doi: 10.1111/j.1468-3083.2010.03818.x
9. Hidaka T, Ishii Y, Kitamura S. Clinical Features of Skin Metastasis From Lung Cancer. *Internal Med* (1996) 35(6):459–62. doi: 10.2169/internalmedicine.35.459
10. Kocher F, Hilbe W, Seeber A, Pircher A, Schmid T, Greil R, et al. Longitudinal Analysis of 2293 Nsclc Patients: A Comprehensive Study From the Tyrol Registry. *Lung Cancer* (2015) 87(2):193–200. doi: 10.1016/j.lungcan.2014.12.006
11. Mayerson JL, Scharschmidt TJ, Lewis VO, Morris CD. Diagnosis and Management of Soft-Tissue Masses. *J Am Acad Orthop Surg* (2014) 22(11):742–50. doi: 10.5435/jaaos-22-11-742
12. Miwa S, Otsuka T. Practical Use of Imaging Technique for Management of Bone and Soft Tissue Tumors. *J Orthopaedic Sci* (2017) 22(3):391–400. doi: 10.1016/j.jos.2017.01.006
13. Khoo M, Pressney I, Hargunani R, Saifuddin A. Small, Superficial, Indeterminate Soft-Tissue Lesions as Suspected Sarcomas: Is Primary Excision Biopsy Suitable? *Skeletal Radiol* (2017) 46(7):919–24. doi: 10.1007/s00256-017-2635-4
14. Fenzl L, Bubel K, Mehrmann M, Schneider G. Bildgebung Und Biopsie Von Weichteiltumoren. *Der Radiologe* (2018) 58(1):79–92. doi: 10.1007/s00117-017-0331-y
15. Kummar S, Fogarasi M, Canova A, Mota A, Ciesielski T. Cytokeratin 7 and 20 Staining for the Diagnosis of Lung and Colorectal Adenocarcinoma. *Br J Cancer* (2002) 86(12):1884–7. doi: 10.1038/sj.bjc.6600326
16. Ordóñez NG. Value of Thyroid Transcription Factor-1, E-Cadherin, Bg8, Wt1, and Cd44s Immunostaining in Distinguishing Epithelial Pleural Mesothelioma From Pulmonary and Nonpulmonary Adenocarcinoma. *Am J Surg Pathol* (2000) 24(4):598–606. doi: 10.1097/00000478-200004000-00016
17. Damron TA, Heiner J. Distant Soft Tissue Metastases: A Series of 30 New Patients and 91 Cases From the Literature. *Ann Surg Oncol* (2000) 7(7):526–34. doi: 10.1007/s10434-000-0526-7
18. Hashimoto K, Nishimura S, Akagi M. Lung Adenocarcinoma Presenting as a Soft Tissue Metastasis to the Shoulder: A Case Report. *Medicina (Kaunas Lithuania)* (2021) 57(2):181. doi: 10.3390/medicina57020181
19. Ettinger DS, Wood DE, Aisner DL, Akerley W, Bauman J, Chirieac LR, et al. Non-Small Cell Lung Cancer, Version 5.2017, Nccn Clinical Practice Guidelines in Oncology. *J Natl Compr Cancer Network JNCCN* (2017) 15(4):504–35. doi: 10.6004/jnccn.2017.0050
20. Tan AC, Tan DSW. Targeted Therapies for Lung Cancer Patients With Oncogenic Driver Molecular Alterations. *J Clin Oncol* (2022) 40(6):611–25. doi: 10.1200/JCO.21.01626

Conflict of Interest: The authors declare that the research was conducted in the absence of any commercial or financial relationships that could be construed as a potential conflict of interest.

this article, or claim that may be made by its manufacturer, is not guaranteed or endorsed by the publisher.

frontiers | Frontiers in Oncology

ORIGINAL RESEARCH
published: 13 July 2022
doi: 10.3389/fonc.2022.902991

Development and Validation of a Clinical-Image Model for Quantitatively Distinguishing Uncertain Lipid-Poor Adrenal Adenomas From Nonadenomas

Wenting Pan[1†], Huangqi Zhang[1†], Shengze Jin[2], Xin Li[1], Jiawen Yang[1], Binhao Zhang[1], Xue Dong[3], Ling Ma[4] and Wenbin Ji[1*]*

[1] Department of Radiology, Taizhou Hospital of Zhejiang Province Affiliated to Wenzhou Medical University, Taizhou, China, [2] Department of Radiology, Taizhou Hospital of Zhejiang Province, Shaoxing University, Taizhou, China, [3] Department of Radiology, Taizhou Hospital, Zhejiang University, Taizhou, China, [4] He Kang Corporate Management (Shanghai) Co.Ltd, Shanghai, China

OPEN ACCESS

Edited by:
Lei Hu,
Shanghai Jiao Tong University, China

Reviewed by:
Xuehan Hu,
Peking University, China
Shaofeng Duan,
GE Healthcare, China

***Correspondence:**
Huangqi Zhang
1224190004@qq.com
Wenbin Ji
wb.j@163.com

[†]These authors have contributed equally to this work and share first authorship

Specialty section:
This article was submitted to Cancer Imaging and Image-directed Interventions, a section of the journal Frontiers in Oncology

Received: 23 March 2022
Accepted: 13 June 2022
Published: 13 July 2022

Citation:
Pan W, Zhang H, Jin S, Li X, Yang J, Zhang B, Dong X, Ma L and Ji W (2022) Development and Validation of a Clinical-Image Model for Quantitatively Distinguishing Uncertain Lipid-Poor Adrenal Adenomas From Nonadenomas. Front. Oncol. 12:902991. doi: 10.3389/fonc.2022.902991

Background: There remains a demand for a practical method of identifying lipid-poor adrenal lesions.

Purpose: To explore the predictive value of computed tomography (CT) features combined with demographic characteristics for lipid-poor adrenal adenomas and nonadenomas.

Materials and Methods: We retrospectively recruited patients with lipid-poor adrenal lesions between January 2015 and August 2021 from two independent institutions as follows: Institution 1 for the training set and the internal validation set and Institution 2 for the external validation set. Two radiologists reviewed CT images for the three sets. We performed a least absolute shrinkage and selection operator (LASSO) algorithm to select variables; subsequently, multivariate analysis was used to develop a generalized linear model. The probability threshold of the model was set to 0.5 in the external validation set. We calculated the sensitivity, specificity, accuracy, and area under the receiver operating characteristic curve (AUC) for the model and radiologists. The model was validated and tested in the internal validation and external validation sets; moreover, the accuracy between the model and both radiologists were compared using the McNemar test in the external validation set.

Results: In total, 253 patients (median age, 55 years [interquartile range, 47–64 years]; 135 men) with 121 lipid-poor adrenal adenomas and 132 nonadenomas were included in Institution 1, whereas another 55 patients were included in Institution 2. The multivariable analysis showed that age, male, lesion size, necrosis, unenhanced attenuation, and portal venous phase attenuation were independently associated with adrenal adenomas. The clinical-image model showed AUCs of 0.96 (95% confidence interval [CI]: 0.91, 0.98), 0.93 (95% CI: 0.84, 0.97), and 0.86 (95% CI: 0.74, 0.94) in the training set, internal

validation set, and external validation set, respectively. In the external validation set, the model showed a significantly and non-significantly higher accuracy than reader 1 (84% vs. 65%, P = 0.031) and reader 2 (84% vs. 69%, P = 0.057), respectively.

Conclusions: Our clinical-image model displayed good utility in differentiating lipid-poor adrenal adenomas. Further, it showed better diagnostic ability than experienced radiologists in the external validation set.

Keywords: adrenal adenoma, computed tomography, model, clinic, distinguish

INTRODUCTION

Over the last decades, there has been an epidemic increase in the detection of adrenal incidentalomas (1). Adrenal adenomas account for most adrenal lesions and do not require further treatment or only need regular follow-up (2). Adrenal adenomas that contain large amounts of fat could be reliably diagnosed through conventional imaging methods (3). However, 30% of adenomas having an attenuation value of >10 HU (i.e., lipid-poor adenomas) cannot be correctly differentiated from nonadenomas (1). For adrenal lesions suspected to be metastatic tumors or pheochromocytoma, further clinical examination and intervention are needed to avoid adverse events, such as life-threatening hypertension crises during operation. Therefore, it is important to distinguish adrenal lipid-poor adenoma from nonadenoma.

Chemical shift magnetic resonance imaging and energy spectrum computed tomography (CT) are slightly more sensitive for detection (4–7). However, their general use is limited by the high price and relatively limited accessibility. Thus, lipid-poor adrenal lesions usually need a dedicated adrenal washout CT protocol for further characterization (8–11). Nevertheless, the delayed phase and additional radiation exposure may limit the utility of the washout CT protocol (12). However, the relative percentage wash-in ratio of adrenal lesions from the unenhanced to the portal venous phase can remedy the above defects (12, 13). To our knowledge, only a few studies including a large number of lipid-rich adenomas have simultaneously assessed unenhanced attenuation and contrast wash-in features on CT (12, 14). There is currently no combined model established on easily available demographic information and CT characteristics for distinguishing lipid-poor adenomas and nonadenomas. Therefore, we aimed to develop a practical clinical-image model for identifying lipid-poor adrenal lesions.

MATERIALS AND METHODS

Our study was approved by the Institutional Review Committee, and the requirement of written informed consent was waived. We followed the TRIPOD Statement (15) and completed the checklist (**Supplementary Table S1**).

The Training Set and the Internal Validation Set

We conducted a retrospective study on patients with adrenal lesions who were continuously treated in Institution 1 from January 2015 to August 2021. The inclusion criteria were as follows: adult patients with adrenal lesions who underwent adrenal or abdominal unenhanced and contrast-enhanced CT scans.

The exclusion criteria were as follows: (a) lesions with an HU ≤ 10 on unenhanced CT and visible lipid-rich lesions (lipid-rich adrenal adenoma or myelolipoma); (b) missing solid components in the lesion: the change of CT attenuation between the portal venous phase and unenhanced phase is ≤ 10 HU; (c) lesions showing an increase of 10%–30% in the maximum diameter of the adrenal gland during the follow-up period; (d) the scheme of the adrenal or abdominal CT did not meet the standards; (e) lesions with a history of systematic or local treatment; and (f) lesions with a maximum diameter < 10 mm, which was determined to avoid the partial volume effect caused by a thickness of 5 mm (8). For patients with multiple adrenal lesions, only the maximum diameter was included in the analysis to reduce the aggregation effect. The flowchart of the patient selection is summarized in **Figure 1**. Patients from Institution 1 were randomly split into the training set and the internal validation set according to a ratio of 7:3. Some data in this study had been used in prior research (16) on radiomics conducted by our team.

Reference Standard

For all lesions, the final diagnosis was based on pathology or widely accepted imaging standards (8). The diagnostic criteria for lipid-poor adrenal adenomas and nonadenomas are summarized in **Supplementary Material S1**.

The External Validation Set

Institution 2 analyzed patients with adrenal lesions continuously treated from January 2015 to August 2021, constructed an independent external validation set, and tested the model. Patients in Institution 1 and Institution 2 were selected based on the same inclusion and exclusion criteria (**Figure 1**). Moreover, the scanning equipment, protocol, and contrast agent concentration were consistent for patients in both institutions.

Abbreviations: CT, computed tomography; AUC, area under the receiver operating characteristic curve; CI, confidence interval; IQR, Interquartile range; BMI, Body Mass Index; HU, Hounsfield unit.

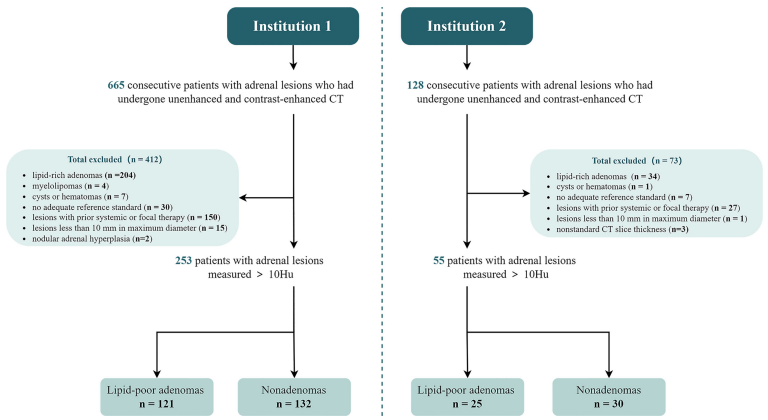

FIGURE 1 | Flowchart of the study sample.

Image Acquisition

All unenhanced and contrast-enhanced CT images were obtained using multi-slice spiral CT scanners (uCT 530; United Imaging, Shanghai, China; Discovery CT750HD; GE Healthcare, Chicago, IL, USA). The images were displayed and stored in the image archiving and communication system (PACS). The CT protocols are provided in **Supplementary Material S2**.

Image Analysis

The region of interest was manually drawn in the lesion layer with the maximum diameter. Additionally, the obvious cystic, calcified, and necrotic areas were avoided. All regions of interest were determined on contrast-enhanced images. Subsequently, they were copied to the unenhanced images. Placements were corrected if necessary.

Two radiologists (ZHQ, reader 1, a radiologist with 3 years of experience; LX, reader 2, a radiologist with 20 years of experience), who were blinded to the clinical data and final diagnosis, independently reviewed the CT images and recorded information regarding shape, boundary, and necrosis. Moreover, they measured the maximum diameter and the unenhanced and portal venous phase CT attenuations which was also called contrast-enhanced attenuation.

Absolute enhancement was calculated by subtracting unenhanced from contrast-enhanced attenuation. The absolute enhancement rate was calculated as follows: contrast-enhanced attenuation/unenhanced attenuation × 100%. Based on established guidelines (8): 1 ~ 2 cm, 2 ~ 4 cm, and ≥ 4 cm were defined as small, medium, and large nodules, respectively.

To assess inter-reader agreement, all analyses were performed independently by a third radiologist (PWT, a radiologist with 2 years of experience), who was also unaware of any clinical data and final diagnosis. The consistency of quantitative variables between the two readers was compared using intraclass correlation coefficients (ICC). Inter-reader agreement was evaluated using the kappa statistics for qualitative variables. Between-reader differences were shown in the Bland Altman plots based on the mean of the measurement (17). After the consistency test, the variables with ICC or kappa statistics > 0.8 was included. The average values of the quantitative variables were used for subsequent analysis. Between-reader disagreements in qualitative data were resolved through a consensus between the two readers.

Statistical Analysis

Normally distributed continuous variables were analyzed using Student's t-test and presented as means and standard deviations. Non-normally distributed continuous variables were examined using the Mann-Whitney U test and presented as medians and interquartile range (IQR). Categorical variables were analyzed using the chi-square or Fisher's exact test and expressed as the frequency and percentage.

We conducted a least absolute shrinkage and selection operator (LASSO) algorithm to select demographic variables and CT features in the training set. We established a generalized linear model (logistic regression) through multivariate analysis of statistically significant variables to predict the probability of lipid-poor adrenal adenoma. Identification and calibration are crucial attributes with respect to the performance evaluation of multivariable models (18). Clinical effectiveness was evaluated using decision curve analysis. The constructed model was used to predict the probability of lipid-poor adenoma in the internal validation set and external validation set.

The sensitivity, specificity, accuracy, and receiver operating characteristic curve (AUC) of the model, and two readers were calculated. AUCs between the combined model, unenhanced attenuation, and absolute enhancement rate was compared using the Delong test in the training set and internal validation set. The accuracy between the model and both readers were compared through the McNemar test in the external validation set. MedCalc (version 19.4.1, MedCalc Software) and R software (version 4.1.1, http://www.r-project.org) (rms, glmnet, rmda, ggDCA, Hmisc, DynNom, rsconnect) were used to perform the statistical analyses. Statistical significance was set at two sided. $P<0.05$.

RESULTS

Study Participants

We included 665 patients with adrenal lesions who underwent adrenal or abdominal unenhanced and contrast-enhanced CT. We excluded 412 patients and included 253 in Institution 1 (median age, 55 years [IQR, 47-64 years]; 135 men). Among the included patients, 121 (48%) showed lipid-poor adrenal adenomas, while 132 (52%) showed nonadenomas, including 68 (27%) metastases and 64 (25%) other nonadenomas (**Figure 1**).

The 121 lipid-poor adrenal adenomas were identified based on pathological diagnosis (n = 109); size stability (n = 11), and abnormal ^{18}F-FDG uptake, fulfilling the criteria for adenoma (n = 1).

The primary lesions and the diagnostic approaches of metastases, and pathological types of other nonadenomas are presented in **Supplementary Material S3**.

Using the same inclusion and exclusion criteria, 55 patients (median age, 61 years [IQR, 50-70 years]; 29 men) with adrenal lesions from Institution 2 were included in the external validation set. Among them, 25 (45%) had adrenal adenomas and 30 (55%) had nonadenomas, including 13 metastases and 17 others (**Figure 1**).

Characteristics of the Patients From Institution 1 and Institution 2

Table 1 summarizes the clinical and CT characteristics of the patients from Institution 1 and Institution 2. Patients with adrenal adenomas were significantly younger and more of the female sex than those with nonadenomas (median age, 52 years [IQR, 44–57 years] vs. 60 years [IQR, 52–67 years], [P < 0.001]; women: 64% [77/121] vs. 31% [41/132], [P < 0.001]). Moreover, patients with adrenal adenomas showed a higher BMI than patients with nonadenomas (median BMI, 24.6 kg/m^2 [IQR, 22.4–26.7 kg/m^2] vs. 23.1 kg/m^2 [IQR, 20.8–25.9 kg/m^2], [P < 0.001]).

Regarding the CT signs, patients with lipid-poor adrenal adenomas showed lower unenhanced attenuation than patients with nonadenomas (median, 23 HU [IQR, 16–32 HU] vs. 37 HU [IQR, 34–43 HU], [P < 0.001]), with no significant between-group difference in contrast-enhanced attenuation (median, 65 HU [IQR, 54–76 HU] vs. 67 HU [IQR, 57–79 HU], [P = 0.317]). However, patients with adrenal adenomas showed higher absolute enhancement attenuation than patients with nonadenomas (median, 35 HU [IQR, 25–52 HU] vs. 26 HU [IQR, 19–42 HU], [P < 0.001]). Similarly, the absolute enhancement rate was higher in adenomas than in nonadenomas (296% [IQR, 233–353%] vs. 175% [IQR, 157–197%], [P < 0.001]).

Unilateral lesions were more frequent in patients with adenomas than in those with nonadenomas (102 of 121 patients [84%] vs. 96 of 132 patients [73%]; P = 0.026). Lipid-poor adrenal adenomas were smaller in diameter and were less prone to necrosis than nonadenomas (P < 0.001). There were no significant between-group differences in the other demographic and CT characteristics (P > 0.05).

Characteristics of the Training Set and Internal Validation Set

Supplementary Table S2 summarizes the clinical and CT characteristics of the training set and internal validation set. Except for the distribution of lesions and contrast-enhanced attenuation, other clinical and CT features were statistically different between patients with adenoma and those with

TABLE 1 | Characteristics of Institution 1 and Institution 2.

Variables	Institution 1			Comparison with Institution 2		
	Lipid-poor Adenoma (n = 121)	Nonadenoma* (n = 132)	*P*	Institution 1 (n = 253)	Institution 2 (n = 55)	*P*
Age (years), median (IQR)	52 (44-57)	60 (52-67)	**<0.001**	55 (47-64)	61 (50-70)	0.048
Sex, n (%)			**<0.001**			0.932
Male	44 (36)	91 (69)		135 (53)	29 (47)	
Female	77 (64)	41 (31)		118 (47)	26 (53)	
BMI (kg/m^2), median (IQR)	24.6 (22.4-26.7)	23.1 (20.8-25.9)	**<0.001**	23.5 (21.5-26.2)	23.4 (20.85-25.8)	0.259
Distribution of lesions, n (%)			**0.026**			0.550
Unilateral	102 (84)	96 (73)		198 (78)	41 (75)	
Bilateral	19 (16)	36 (27)		55 (22)	14 (25)	
Necrosis, n (%)	9 (7)	63 (48)	**<0.001**	72 (28)	18 (33)	0.529
Diameter (cm), n (%)			**<0.001**			0.443
1-2	63 (52)	25 (19)		88 (35)	15 (27)	
2-4	54 (45)	62 (47)		116 (46)	29 (53)	
≥4	4 (3)	45 (34)		49 (19)	11 (20)	
Unenhanced attenuation (HU), median (IQR)	23 (16-32)	37 (34-43)	**<0.001**	34 (22-40)	33 (25-37)	0.772
Contrast-enhanced attenuation (HU), median (IQR)	65 (54-76)	67 (57-79)	0.317	66 (57-78)	64 (55-80)	0.691
Absolute enhancement (HU), median (IQR)	35 (25-52)	26 (19-42)	**<0.001**	35 (26-46)	34 (23-50)	0.709
Absolute enhancement ratio (%), median (IQR)	296 (233-353)	175 (157-197)	**<0.001**	214 (173-300)	199 (170-277)	0.679

There were 132 patients with nonadenoma in the Institution 1, the complete information of them is summarized in **Supplementary Material S3.*

BMI, Body Mass Index; IQR, Interquartile range; kg, kilogram; m, meter. P: categorical variables—Chi-Squared Test or Fisher's exact test; continuous variables—Mann–Whitney U test. The bold value means statistical significance.

nonadenoma in the training set (P < 0.05). No statistically significant difference was observed in all variables between the training set and the internal validation set.

Feature Selection

The inter-reader agreement was moderate for shape and boundary (κ = 0.53–0.56) and almost perfect for necrosis (κ = 0.86), size, unenhanced attenuation, and contrast-enhanced attenuation (ICC = 0.98–0.99). More details are shown in **Supplementary Figure S1**. After LASSO, except for body mass index (BMI) and distribution of lesions, the other variables were included (**Supplementary Figure S2**).

Multivariable Analysis and Model Construction

Multivariate analysis showed that age (odds ratio [OR], 0.94; 95% confidence interval [CI]: 0.90, 0.98; P = 0.015), male sex (OR, 0.26; 95% CI: 0.08, 0.74; P = 0.015), lesion size (2-4cm: OR, 0.51; 95% CI: 0.14, 1.75; P = 0.289; ≥ 4 cm: OR, 0.09; 95% CI: 0.01, 0.57; P = 0.014), necrosis (OR, 0.19; 95% CI: 0.04, 0.78; P = 0.027), unenhanced attenuation (OR, 0.79; 95% CI: 0.72, 0.85; P < 0.001), and contrast-enhanced attenuation (OR, 1.07; 95% CI: 1.04, 1.11; P < 0.001) were independently associated with adrenal adenomas (**Table 2**). The formula of the combined model is as follows:

$$\ln\left(\frac{p}{1-p}\right) = 7.4743 - 1.3572 \times (Sex = male) - 0.0593 \times age - 0.6636 \times (Tumor\ size = Middle) - 2.4000 \times (Tumor\ size = Lager) - 1.6424 \times (Necrosis = Yes) - 0.2361 \times Unenhanced\ attenuation + 0.0700 \times Contrast\ enhanced\ attenuation$$

Prognostic Performance of the Model

In the training set, the AUCs were 0.96 (95% CI: 0.91, 0.98), 0.87 (95% CI: 0.81, 0.91), and 0.92 (95% CI: 0.87, 0.96) for the model, unenhanced attenuation, and absolute enhancement rate, respectively. Additionally, the diagnostic performance of the model was higher than that of the unenhanced attenuation or absolute enhancement rate (P < 0.001 and P = 0.002, respectively). The AUC of the model was 0.93 (95% CI: 0.84, 0.97) in the internal validation set, which was superior to that of the unenhanced attenuation and absolute enhancement rate (AUC: 0.83 [95% CI: 0.73, 0.91; P = 0.040] and 0.88 [95% CI: 0.78, 0.94; P = 0.060], respectively). **Figure 2** shows the nomogram and the receiver operating characteristic (ROC) curves in the training set and internal validation set. Moreover, the calibration curve of the model in the training set is shown in **Supplementary Figure S3**. The online tool is available at https://zhanghuangqi.shinyapps.io/dynnomapp/. Examples of the nomogram's clinical use are displayed in **Figures 3**, **4**. The decision curve and clinical impact curves are shown in **Supplementary Figures S4, S5**. This study revealed that the model achieved a seemingly better net benefit than unenhanced attenuation or relative enhancement rate.

External Validation Set

In the external validation set (n = 55), the AUC of the model was 0.86 (95% CI: 0.74, 0.94). The model (84%; 95% CI: 71%, 92%) showed a significantly and non-significantly higher accuracy than reader 1 (65%; 95%CI: 51%, 78%; P = 0.031) and reader 2 (69%; 95% CI: 55%, 81%; P = 0.057), respectively (**Table 3**).

DISCUSSION

It is desirable to develop a practical and convenient method for identifying lipid-poor adrenal lesions. To our knowledge, this is the first study to establish a combined model based on easily available demographic information and CT characteristics for differentiating lipid-poor adrenal adenomas from nonadenomas. Our model was validated and tested using the internal validation set and independent external data and showed good diagnostic efficiency. Further, it displayed better diagnostic ability than inexperienced radiologists in the external validation set.

TABLE 2 | Results of multivariate analysis for features selected by LASSO algorithm.

Variable	Multivariable Analysis	
	OR (95% CI)	P
Age (per 1 year)	0.94 (0.90, 0.98)	0.015
Sex		
Female	Ref.	
Male	0.26 (0.08, 0.74)	0.015
Diameter (cm)		
1-2	Ref.	
2-4	0.51 (0.14, 1.75)	0.289
≥4	0.09 (0.01, 0.57)	0.014
Necrosis		
No	Ref.	
Yes	0.19 (0.04, 0.78)	0.027
Unenhanced attenuation (per 1 HU)	0.79 (0.72, 0.85)	<0.001
Contrast-enhanced attenuation (per 1 HU)	1.07 (1.04, 1.11)	<0.001

OR, odds ratio; CI, confidence interval; cm, centimeter; HU, Hounsfield Unit; Ref., reference. Data in parentheses are 95% CIs.

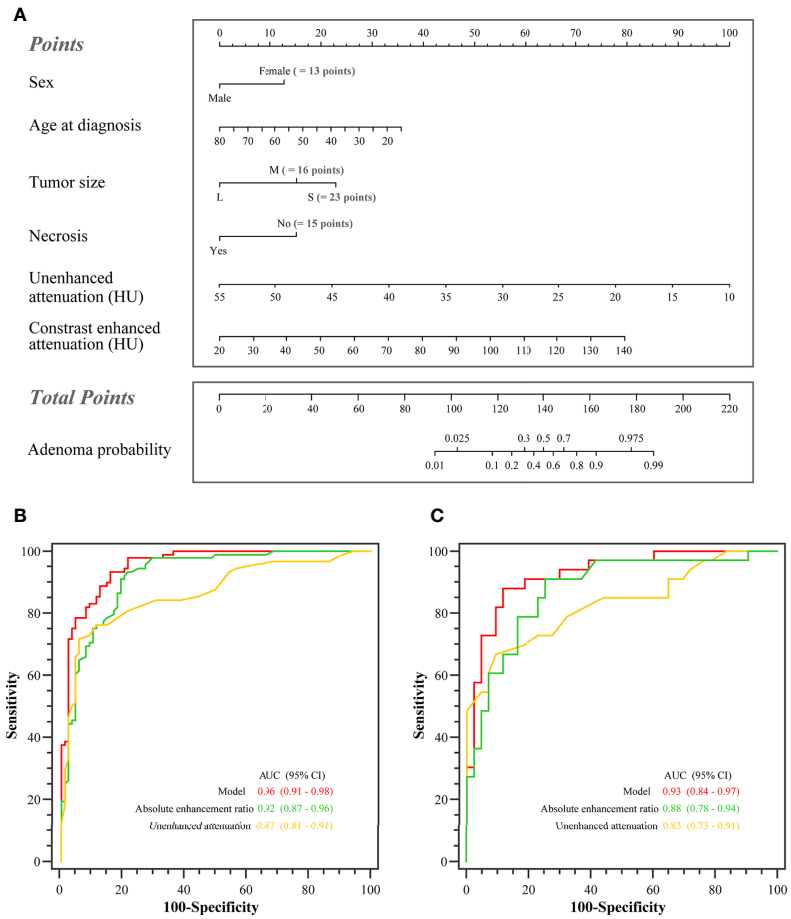

FIGURE 2 | The nomogram and the receiver operating characteristic (ROC) curves in the training set and the internal validation set. **(A)** Nomogram of lipid-poor adrenal adenoma prediction based on clinical-image model. Added up the scores of each variable to get the total score. Based on it, the probability of lipid-poor adrenal adenoma was showed by projecting the score to the risk axis. Online tool is available at https://zhanghuangqi.shinyapps.io/dynnomapp/. **(B)** The ROC curves for differentiating lipid-poor adenomas and nonadenomas in the training set. The highest area under the curve was obtained with the combined model (0.96 [95% CI: 0.91, 0.98]), followed by absolute enhancement rate (0.92 [95% CI: 0.87, 0.96]), and unenhanced attenuation (0.87 [95% CI: 0.81, 0.91]). **(C)** The combined model displayed the best diagnostic performance for prediction of lipid-poor adenomas in the internal validation set (AUC, 0.93 [95% CI: 0.84, 0.97]).

To facilitate the clinical use of this model, we have transformed it into online software for use.

Previous studies have tried to identify lipid-poor adrenal adenoma. Several studies found that CT attenuation displayed potential usefulness in distinguishing adrenal adenoma (13, 14, 19). Our clinical-image model showed higher diagnostic efficiency than simple unenhanced CT attenuation and absolute enhancement rates. In previous studies, the diagnosis of adenomas was confirmed by long-term radiological follow-up; there was a relatively low proportion of adenomas confirmed by surgery or puncture (20, 21). However, in our study, 90% (109 of 121 patients) of the adenomas were confirmed by pathology. Yi et al. developed radiomic nomograms to distinguish subclinical pheochromocytoma from lipid-poor adenoma through CT images with an AUC of 0.904 (22). Our model was based on easily available demographic information and CT features and also achieved good performance; moreover, our study covered a wider etiology of adrenal nonadenoma.

Multivariable analysis revealed that the main demographics for predicting lipid-poor adrenal adenoma were age and sex, consistent with previous studies (23–25). Many nonadenomas were metastases, which tend to occur in the elderly (8). The presence or absence of necrosis and lesion size were independently associated with the diagnosis of lipid-poor adrenal adenoma. According to relevant guidelines (8), we used the lesion size as a categorical variable since it is clinically significant. Given the high possibility of benign lesions, follow-up should be conducted for lesions with a size of 1–2 cm. For lesions with a size > 2 cm and < 4 cm, the next plan is determined in combination with unenhanced attenuation. Finally, for lesions larger than 4 cm, surgical resection is decided based on the malignancy history.

Patients with adenomas showed lower unenhanced attenuation than patients with nonadenomas. Several studies

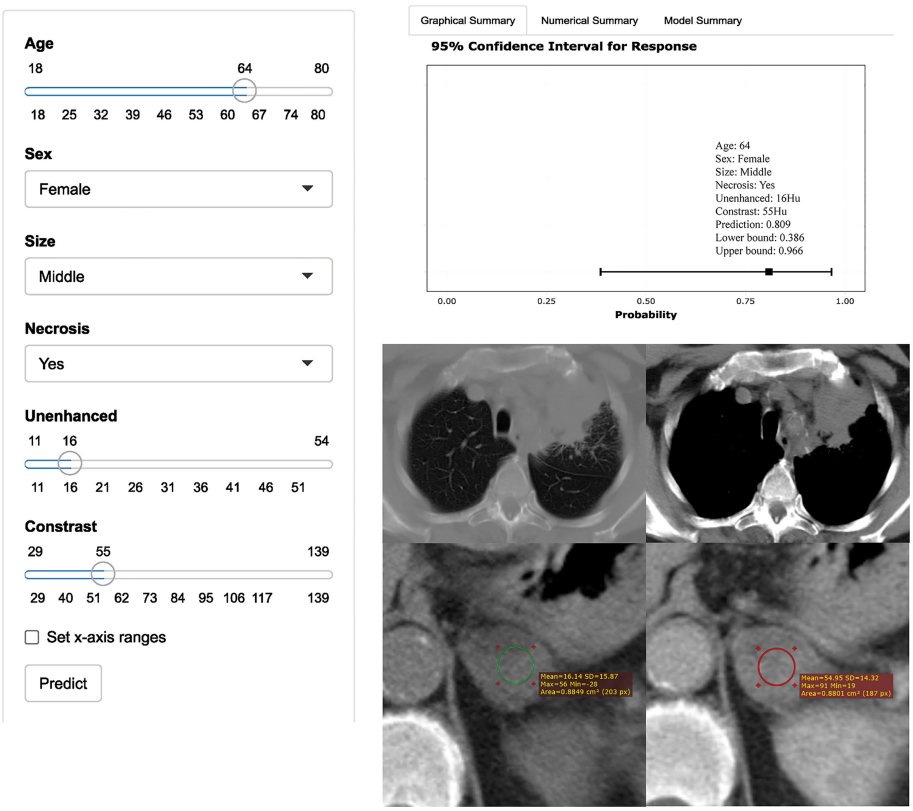

FIGURE 3 | Axial unenhanced and contrast-enhanced adrenal CT images in a 64-year-old woman with cough and expectoration. The woman was accidentally found having left adrenal lesions due to chest CT findings of left upper lung mass and multiple lymph nodes in the left hilar and mediastinum. CT features were analyzed as follows: lesion location = "left", size = " middle (2.7cm×2.1cm)", shape ="quasi-circular", unenhanced attenuation = 16 HU, contrast-enhanced attenuation = 55 HU, and necrosis= "yes". Both radiologists evaluated that the possibility of nonadenoma (metastasis) was high, while the possibility of adenoma judged by the model was up to 81% (95% CI: 39%, 97%). The result of pathological diagnosis was adrenal adenoma.

have demonstrated that adrenal adenomas have lower unenhanced attenuation than pheochromocytomas or malignant adrenal lesions (26). Pathologically, adrenal adenoma, whether rich in or lacking lipids, is a benign neoplasm of adrenocortical cells. The adrenal cortex consists of zona glomerulosa, zona fasciculata, and zona reticularis. The zona fasciculata constitutes three-fourths of the cortex comprising lipid-laden cells (1).

Although adenomas have been reported to show rapid wash in the portal vein phase (13, 27), they often showed no statistically significant difference in univariate analysis. A recent study (12) indicated that the ratio of portal venous phase attenuation to unenhanced attenuation allowed sufficient identification of lipid-poor adenomas and nonadenomas. Therefore, we attempted to incorporate the portal vein phase attenuation into the combined model, which was an independent risk factor in multivariate analysis. The above may be attributed to the correlations between independent variables; the influence of independent variables on dependent variables reflects their own role and the mixed roles of other variables.

In the external validation set, there were 13 cases of adrenal metastases, which were accurately identified by our combined model. A total of five nonadenomas were misjudged as adenomas, including four pheochromocytomas and one spindle cell tumor. Only one pheochromocytoma among these five patients was correctly identified by reader 2. Previous studies have indicated that some pheochromocytomas are misdiagnosed as adenomas on adrenal enhanced CT (20, 28). Furthermore, these pheochromocytomas were rich in blood vessels and displayed rapid washout similar to adenomas, which cannot be accurately characterized in the delayed phase (20, 28).

Our study has some limitations. First, we did not collect the full clinical history or laboratory examination. However, this was consistent with our study objective, which was an early, rapid, and noninvasive diagnosis of lipid-poor adenoma and effective stratification of patients to avoid some unnecessary examination. Second, we used a total iodine dose of 400 mgI/kg, which is lower than previously reported values (10, 20, 29) and might limit the application of our model. This could be attributed to our participants weighing less than those in previous studies due to race differences. Simultaneously, an excessively high iodine dose adversely affects patients, causing fever, pain, and contrast medium nephropathy (30, 31). Third, the diagnostic efficiency of the combined model in the external validation set was not as

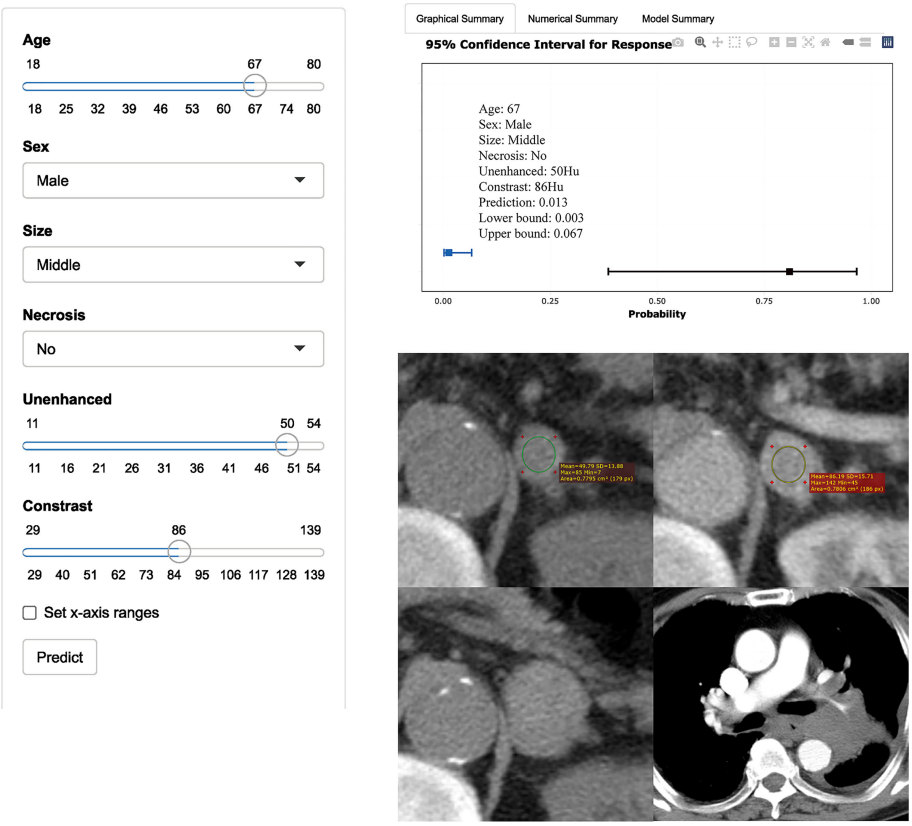

FIGURE 4 | Axial unenhanced and contrast-enhanced adrenal CT images in a 67-year-old man with dizziness and unstable walking. The man was accidentally found having left adrenal lesions due to abdominal CT findings of right kidney occupied. Meanwhile, the boundary of the mass was clear, and no obvious enlarged lymph nodes were found around. CT features were analyzed as follows: lesion location = "left", size = "middle (2.7cm×2.1cm)", shape ="quasi-circular", unenhanced attenuation = 50 HU, and contrast-enhanced attenuation = 86 HU. The renal lesion was considered to be a malignancy. Reader 1 thought that it was more likely to be nonadenoma, while reader 2 thought that it was more likely to be adenoma. The possibility of adenoma judged by the model was only 1% (95% CI: 0%, 7%). One year later, the patient went to see a doctor again due to repeated cough, expectoration, and chest tightness. CT showed that left hilar was occupied by mass with bronchial and pulmonary artery stenosis. It was confirmed as small cell lung cancer pathologically. The left adrenal gland was significantly larger than before, with maximum diameter of 3.3cm. Metastasis was considered first, but it cannot be determined whether the metastasis was from lung cancer or renal cancer.

high as we expected. Moreover, the diagnostic accuracy of the two readers in the external validation set was lower than that in the training set, which could partly explain the reduced diagnostic efficiency of the model. Specifically, this might be attributed to differences in the types of patients treated in both sets.

CONCLUSION

This study shows that the combined model, which is based on accessible demographic characteristics and CT features, can facilitate the identification of lipid-poor adrenal adenoma. In the training set, the combined model had better diagnostic

TABLE 3 | Sensitivity, Specificity, and Accuracy for Differentiating Lipid-Poor Adenomas from Nonadenomas by Two Readers and the Model.

	External Validation Set		
	Sensitivity (%)	**Specificity (%)**	**Accuracy (%)**
Reader1	80 (20/25) [59, 93]	53 (16/30) [34, 72]	65 (36/55) [51, 78]
Reader2	56 (14/25) [35, 76]	80 (24/30) [61, 82]	69 (38/55) [55, 81]
Model	84 (21/25) [64, 96]	83 (25/30) [65, 94]	84 (46/55) [71, 92]

Data in parentheses are numbers of lesions, with 95% CIs in brackets.

efficiency than unenhanced attenuation or the absolute enhancement rate. In the external validation set, the model showed higher accuracy than an inexperienced radiologist.

DATA AVAILABILITY STATEMENT

The original contributions presented in the study are included in the article/**Supplementary Material**. Further inquiries can be directed to the corresponding authors.

AUTHOR CONTRIBUTIONS

WP, HZ, and WJ: conception and design. HZ, XL, SJ, and JY: collection and assembly of data. HZ, WP, and LM: data analysis and interpretation. WP, XD, BZ, and JY: manuscript writing. All authors contributed to the article and approved the submitted version.

ACKNOWLEDGMENTS

We would like to thank Editage (www.editage.com) for English language editing.

SUPPLEMENTARY MATERIAL

The Supplementary Material for this article can be found online at: https://www.frontiersin.org/articles/10.3389/fonc.2022.902991/full#supplementary-material

REFERENCES

1. Sherlock M, Scarsbrook A, Abbas A, Fraser S, Limumpornpetch P, Dineen R, et al. Adrenal Incidentaloma. *Endocr Rev* (2020) 41:775–820. doi: 10.1210/endrev/bnaa008
2. Fassnacht M, Arlt W, Bancos I, Dralle H, Newell-Price J, Sahdev A, et al. Management of Adrenal Incidentalomas: European Society of Endocrinology Clinical Practice Guideline in Collaboration With the European Network for the Study of Adrenal Tumors. *Eur J Endocrinol* (2016) 175:G1–1G34. doi: 10.1530/EJE-16-0467
3. Maurea S, Mainolfi C, Bazzicalupo L, Panico MR, Imparato C, Alfano B, et al. Imaging of Adrenal Tumors Using FDG PET: Comparison of Benign and Malignant Lesions. *AJR Am J Roentgenol* (1999) 173:25–9. doi: 10.2214/ajr.173.1.10397094
4. Platzek I, Sieron D, Plodeck V, Borkowetz A, Laniado M, Hoffmann RT. Chemical Shift Imaging for Evaluation of Adrenal Masses: A Systematic Review and Meta-Analysis. *Eur Radiol* (2019) 29:806–17. doi: 10.1007/s00330-018-5626-5
5. Nagayama Y, Inoue T, Oda S, Tanoue S, Nakaura T, Morinaga J, et al. Unenhanced Dual-Layer Spectral-Detector CT for Characterizing Indeterminate Adrenal Lesions. *Radiology* (2021) 301:369–78. doi: 10.1148/radiol.2021202435
6. Connolly MJ, McInnes M, El-Khodary M, McGrath TA, Schieda N. Diagnostic Accuracy of Virtual non-Contrast Enhanced Dual-Energy CT for Diagnosis of Adrenal Adenoma: A Systematic Review and Meta-Analysis. *Eur Radiol* (2017) 27:4324–35. doi: 10.1007/s00330-017-4785-0
7. Nagayama Y, Inoue T, Oda S, Tanoue S, Nakaura T, Ikeda O, et al. Adrenal Adenomas Versus Metastases: Diagnostic Performance of Dual-Energy Spectral CT Virtual Noncontrast Imaging and Iodine Maps. *Radiology* (2020) 296:324–32. doi: 10.1148/radiol.2020192227
8. Mayo-Smith WW, Song JH, Boland GL, Francis IR, Israel GM, Mazzaglia PJ, et al. Management of Incidental Adrenal Masses: A White Paper of the ACR Incidental Findings Committee. *J Am Coll Radiol* (2017) 14:1038–44. doi: 10.1016/j.jacr.2017.05.001
9. Szolar DH, Kammerhuber F. Quantitative CT Evaluation of Adrenal Gland Masses: A Step Forward in the Differentiation Between Adenomas and Nonadenomas. *Radiology* (1997) 202:517–21. doi: 10.1148/radiology.202.2.9015083
10. Kebapci M, Kaya T, Gurbuz E, Adapinar B, Kebapci N, Demirustu C. Differentiation of Adrenal Adenomas (Lipid Rich and Lipid Poor) From Nonadenomas by Use of Washout Characteristics on Delayed Enhanced CT. *Abdom Imaging* (2003) 28:709–15. doi: 10.1007/s00261-003-0015-0
11. Foti G, Malleo G, Faccioli N, Guerriero A, Furlani L, Carbognin G. Characterization of Adrenal Lesions Using MDCT Wash-Out Parameters: Diagnostic Accuracy of Several Combinations of Intermediate and Delayed Phases. *Radiol Med* (2018) 123:833–40. doi: 10.1007/s11547-018-0911-6
12. Nagayama Y, Inoue T, Kato Y, Tanoue S, Kidoh M, Oda S, et al. Relative Enhancement Ratio of Portal Venous Phase to Unenhanced CT in the Diagnosis of Lipid-Poor Adrenal Adenomas. *Radiology* (2021) 301:360–8. doi: 10.1148/radiol.2021210231
13. Foti G, Faccioli N, Manfredi R, Mantovani W, Mucelli RP. Evaluation of Relative Wash-in Ratio of Adrenal Lesions at Early Biphasic CT. *AJR Am J Roentgenol* (2010) 194:1484–91. doi: 10.2214/AJR.09.3636
14. Szolar DH, Kammerhuber FH. Adrenal Adenomas and Nonadenomas: Assessment of Washout at Delayed Contrast-Enhanced CT. *Radiology* (1998) 207:369–75. doi: 10.1148/radiology.207.2.9577483
15. Moons KG, Altman DG, Reitsma JB, Ioannidis JP, Macaskill P, Steyerberg EW, et al. Transparent Reporting of a Multivariable Prediction Model for Individual Prognosis or Diagnosis (TRIPOD): Explanation and Elaboration. *Ann Intern Med* (2015) 162:W1–73. doi: 10.7326/M14-0698
16. Zhang B, Zhang H, Li X, Jin S, Yang J, Pan W, et al. Can Radiomics Provide Additional Diagnostic Value for Identifying Adrenal Lipid-Poor Adenomas From Non-Adenomas on Unenhanced Ct. *Front Oncol* (2022) 12:888778. doi: 10.3389/fonc.2022.888778
17. Abu-Arafeh A, Jordan H, Drummond G. Reporting of Method Comparison Studies: A Review of Advice, an Assessment of Current Practice, and Specific Suggestions for Future Reports. *Br J Anaesth* (2016) 117:569–75. doi: 10.1093/bja/aew320
18. Alba AC, Agoritsas T, Walsh M, Hanna S, Iorio A, Devereaux PJ, et al. Discrimination and Calibration of Clinical Prediction Models: Users Guides to the Medical Literature. *JAMA* (2017) 318:1377–84. doi: 10.1001/jama.2017.12126
19. Ng CS, Wei W, Altinmakas E, Li X, Ghosh P, Perrier NA, et al. Differentiation of Malignant and Benign Adrenal Lesions With Delayed CT: Multivariate Analysis and Predictive Models. *AJR Am J Roentgenol* (2018) 210:W156–156W163. doi: 10.2214/AJR.17.18428
20. Caoili EM, Korobkin M, Francis IR, Cohan RH, Platt JF, Dunnick NR, et al. Adrenal Masses: Characterization With Combined Unenhanced and Delayed Enhanced CT. *Radiology* (2002) 222:629–33. doi: 10.1148/radiol.2223010766
21. Caoili EM, Korobkin M, Francis IR, Cohan RH, Dunnick NR. Delayed Enhanced CT of Lipid-Poor Adrenal Adenomas. *AJR Am J Roentgenol* (2000) 175:1411–5. doi: 10.2214/ajr.175.5.1751411
22. Yi X, Guan X, Zhang Y, Liu L, Long X, Yin H, et al. Radiomics Improves Efficiency for Differentiating Subclinical Pheochromocytoma From Lipid-Poor Adenoma: A Predictive, Preventive and Personalized Medical Approach in Adrenal Incidentalomas. *EPMA J* (2018) 9:421–9. doi: 10.1007/s13167-018-0149-3
23. Mosconi C, Vicennati V, Papadopoulos D, Dalmazi GD, Morselli-Labate AM, Golfieri R, et al. Can Imaging Predict Subclinical Cortisol Secretion in Patients

With Adrenal Adenomas? A CT Predictive Score. *AJR Am J Roentgenol* (2017) 209:122–9. doi: 10.2214/AJR.16.16965
24. Northcutt BG, Trakhtenbroit MA, Gomez EN, Fishman EK, Johnson PT. Adrenal Adenoma and Pheochromocytoma: Comparison of Multidetector CT Venous Enhancement Levels and Washout Characteristics. *J Comput Assist Tomogr* (2016) 40:194–200. doi: 10.1097/RCT.0000000000000343
25. Pennanen M, Raade M, Louhimo J, Sane T, Heiskanen I, Arola J, et al. Adrenocortical Tumours: High CT Attenuation Value Correlates With Eosinophilia But Does Not Discriminate Lipid-Poor Adenomas From Malignancy. *J Clin Pathol* (2013) 66:1076–80. doi: 10.1136/jclinpath-2013-201513
26. Akbulut S, Erten O, Kahramangil B, Gokceimam M, Kim YS, Li P, et al. A Critical Analysis of Computed Tomography Washout in Lipid-Poor Adrenal Incidentalomas. *Ann Surg Oncol* (2021) 28:2756–62. doi: 10.1245/s10434-020-09329-1
27. Inan N, Arslan A, Akansel G, Anik Y, Balci NC, Demirci A. Dynamic Contrast Enhanced MRI in the Differential Diagnosis of Adrenal Adenomas and Malignant Adrenal Masses. *Eur J Radiol* (2008) 65:154–62. doi: 10.1016/j.ejrad.2007.03.012
28. Park BK, Kim B, Ko K, Jeong SY, Kwon GY. Adrenal Masses Falsely Diagnosed as Adenomas on Unenhanced and Delayed Contrast-Enhanced Computed Tomography: Pathological Correlation. *Eur Radiol* (2006) 16:642–7. doi: 10.1007/s00330-005-0017-0
29. Park SW, Kim TN, Yoon JH, Kim TH, Chung JM, Jeon UB, et al. The Washout Rate on the Delayed CT Image as a Diagnostic Tool for Adrenal Adenoma Verified by Pathology: A Multicenter Study. *Int Urol Nephrol* (2012) 44:1397–402. doi: 10.1007/s11255-012-0202-4
30. Li Z, Li Q, Shen Y, Li A, Li H, Liang L, et al. Adrenal and Nephrogenic Hypertension: An Image Quality Study of Low Tube Voltage, Low-Concentration Contrast Media Combined With Adaptive Statistical Iterative Reconstruction. *Int J Clin Pract* (2016) 70 Suppl 9B:B29–36. doi: 10.1111/ijcp.12860
31. Romano G, Briguori C, Quintavalle C, Zanca C, Rivera NV, Colombo A, et al. Contrast agents and renal cell apoptosis. *Eur Heart J* (2008) 29:2569–76. doi: 10.1093/eurheartj/ehn197

Conflict of Interest: Author LM is employed by He Kang Corporate Management (SH).

The remaining authors declare that the research was conducted in the absence of any commercial or financial relationships that could be construed as a potential conflict of interest.

Publisher's Note: All claims expressed in this article are solely those of the authors and do not necessarily represent those of their affiliated organizations, or those of the publisher, the editors and the reviewers. Any product that may be evaluated in this article, or claim that may be made by its manufacturer, is not guaranteed or endorsed by the publisher.

frontiers | Frontiers in Oncology

TYPE Original Research
PUBLISHED 25 July 2022
DOI 10.3389/fonc.2022.943960

OPEN ACCESS

EDITED BY
Pilar López-Larrubia,
Spanish National Research Council (CSIC), Spain

REVIEWED BY
Emily Chang,
University of North Carolina at Chapel Hill, United States
Hongli Cao,
Fudan University, China

*CORRESPONDENCE
Wei Zhou
Zw11468@126.com

SPECIALTY SECTION
This article was submitted to Cancer Imaging and Image-directed Interventions, a section of the journal Frontiers in Oncology

RECEIVED 14 May 2022
ACCEPTED 28 June 2022
PUBLISHED 25 July 2022

CITATION
Tao L, Fan J, Zhan W, Li W, Lu J, Yang N, Ma B and Zhou W (2022) Contrast-enhanced ultrasound manifestations of renal masses undetectable on conventional ultrasound.
Front. Oncol. 12:943960.
doi: 10.3389/fonc.2022.943960

Contrast-enhanced ultrasound manifestations of renal masses undetectable on conventional ultrasound

Lingling Tao[1], Jinfang Fan[1], Weiwei Zhan[2], Weiwei Li[1], Jian Lu[3], Nanan Yang[3], Binbin Ma[4] and Wei Zhou[2*]

[1]Department of Ultrasound, Ruijin Hospital LuWan Branch, Shanghai Jiaotong University School of Medicine, Shanghai, China, [2]Department of Ultrasound, Ruijin Hospital, Shanghai Jiaotong University School of Medicine, Shanghai, China, [3]Department of Interventional Radiology, Ruijin Hospital LuWan Branch, Shanghai Jiaotong University School of Medicine, Shanghai, China, [4]Department of Urology, Ruijin Hospital LuWan Branch, Shanghai Jiaotong University School of Medicine, Shanghai, China

This study aimed to retrospectively analyze the features of contrast-enhanced ultrasound (CEUS) of renal masses that cannot be detected by conventional ultrasound (CUS). The data of 264 patients who underwent CEUS for renal lesions from January 2016 to December 2019 were retrieved. Of these, 16 patients with renal masses which were not detected by CUS were included in the final analysis. The corresponding characteristics of CEUS were evaluated, including intensity of enhancement, homogeneity, wash-in and wash-out patterns, and perilesional rim-like enhancement. Of the 16 patients, 10 patients had clear cell renal cell carcinoma (ccRCC) and 6 patients had urothelial carcinoma of the renal pelvis (UCRP). Compared with the location on non-enhanced computed tomography (CT) scan, all tumors were detected on CEUS. Most (7/10) of the ccRCCs appeared as hyperenhancement, homogeneous enhancement, synchronous-in, and no perilesional rim-like enhancement. Most (4/6) of the UCRPs appeared as isoenhancement, slow-in, fast-out, and no perilesional rim-like enhancement. CEUS may be helpful in the diagnosis and differential diagnosis of renal tumors which were not observed on CUS, and it might be an alternative method for some patients when contrast-enhanced computed tomography (CECT) or magnetic resonance imaging (MRI) cannot be performed.

KEYWORDS

conventional ultrasound, non-enhanced computed tomography, renal mass, undetectable, contrast-enhanced ultrasound, clear cell renal cell carcinoma, urothelial carcinoma of the renal pelvis

Introduction

The differential diagnosis of renal tumor histotypes is vital for clinical treatment decision-making and prognosis evaluation. Imaging examination is the main basis for clinical differentiation of renal tumor histotypes, which is of great significance (1). Most of the patients with renal masses are asymptomatic in the early stage, and 70%–80% of renal tumors can be detected by ultrasound (US) in routine physical examination (2). Although conventional ultrasound (CUS), including B mode and color Doppler, has an important role in the diagnosis of renal tumors, it also has some limitations. Factors such as obesity, growth pattern, echo, and location may interfere with the CUS examination, leading to misdiagnosis or missed diagnosis, which often requires further examinations (3, 4).

Contrast-enhanced ultrasound (CEUS) was recently introduced as a promising technique for the evaluation of renal tumors (5). CEUS is performed by using a microbubble contrast agent. As the size of the microbubbles is similar to red cells (ranging from 1 to 10 μm), the microbubbles remain completely in the intravascular space with no nephrotoxicity and discharge through the respiratory system. The European Federation of Societies for Ultrasound in Medicine and Biology Guidelines and Recommendations on the Clinical Practice of CEUS have suggested indications for CEUS of renal diseases (6). CEUS is helpful in evaluating atypical cysts and uncertain masses detected by computed tomography (CT) or magnetic resonance imaging (MRI) (7). In addition to the role in the differential diagnosis of renal masses, CEUS can also detect masses that cannot be observed on CUS; however, there were very few related studies (8). In our daily work, we also found some cases with renal masses which were not detected by CUS. These patients had a single suspicious renal mass on non-enhanced CT scan. However, they were unable to undergo contrast-enhanced computed tomography (CECT) or MRI for their own reasons, so CEUS was then performed at the ultrasound department, which clearly showed the masses. This study aimed to analyze CEUS features of renal masses that were undetectable by CUS.

Materials and methods

Patients

This retrospective study was approved and supervised by the institutional review committee of our hospital, and informed consent was obtained from each patient prior to the CEUS examination. The data of 264 patients from January 2017 to December 2020 were retrieved. Of these, 16 patients with renal masses were included in the final analysis. Histopathological evaluation was performed on the specimens obtained from surgically resected lesions. The inclusion criteria were as follows: 1) no renal mass was found on CUS; 2) a single suspicious renal mass was observed on CT; 3) CEUS was performed after CT examination; and 4) patients had not undergone any invasive treatments before. The exclusion criteria were as follows: 1) a renal mass that can be easily identified by CUS; 2) cases that were confirmed by CECT or MRI; 3) cases who had incomplete imaging data; and 4) patients who were pregnant, had a history of cardiac failure, or had respiratory disorders.

Imaging technology and technical characteristics

US examination was performed by using an ultrasonic diagnostic instrument (Aplio 500, Canon Medical Systems, Tokyo, Japan), equipped with a probe 6C1 (frequency of 3.5–5.0 MHz) for CUS and CEUS with a mechanical index of 0.07. Compared with the location of the renal mass shown on the non-enhanced CT scan, CUS was used to identify the renal mass. At the same time, CUS was used to observe whether the renal pelvis was separated. If the mass was still not found, CEUS was performed on the area suspected by non-enhanced CT scan.

The area suspected by non-enhanced CT scan was then targeted, and imaging settings such as depth, gain, and focal zone were optimized to ensure adequate image quality. CEUS was administered by injecting 1.2–2.4 ml of SonoVue (Bracco, Italy) through an antecubital vein followed by flushing with 5.0 ml of normal saline. All dynamic images were observed for 3 min and stored on a hard disk for further analysis. All CEUS examinations were evaluated by two radiologists with more than 10 years of experience in CEUS. Differences in opinions and findings were discussed and resolved by the same two radiologists.

Analysis of CEUS

The enhancement pattern and characteristics of CEUS were evaluated according to the literature (9). A) Enhancement intensity at peak: the enhancement degree of the lesion was compared with that of the renal cortex, and it was classified as hyper-, iso-, or hypoenhancement. B) Enhanced homogeneity: the homogeneity was divided into homogeneous and heterogeneous. C) Wash-in pattern was classified as “fast-in,” “synchronous-in,” or “slow-in,” indicating that the contrast agent entered the mass faster than, the same as, and more slowly than the adjacent renal cortex, respectively. D) Wash-out pattern was divided into “fast-out,” “synchronous-out,” or “slow-out,” indicating that the contrast agent discharged from the mass faster than, the same as, and more slowly than the

adjacent cortex, respectively. E) Perilesional rim-like enhancement was divided into present or absent.

Analysis of CUS after CEUS

In the simultaneous display mode of both CUS and CEUS images, the mass displayed on CEUS was delineated, and the corresponding position of the mass on CUS was also automatically delineated. The CUS features of the suspicious area were analyzed. CUS features included echogenicity, homogeneity, and blood flow signal. The echogenicity was classified as hypoechoic, isoechoic, or hyperechoic when compared with that of the adjacent renal cortex. Homogeneity was classified as homogeneous and heterogeneous. The blood flow signal inside the tumor was divided into yes or no.

Results

A total of 6 women and 10 men were recruited, with a mean age of 62.2 ± 12.2 years (range, 38–83 years). There were a total of 16 masses, with a mean maximum diameter of 2.2 ± 0.7 cm (range, 1.2–3.8 cm). Of the 16 tumors, 9 (56.3%) were on the left, and the remaining 7 (43.7%) were on the right. All the masses were diagnosed by postoperative pathology. The pathological results were clear cell renal cell carcinoma (ccRCC) in 10 patients (62.5%), with a mean maximum diameter of 2.0 ± 0.4 cm (range, 1.5–2.9 cm), and urothelial carcinoma of the renal pelvis (UCRP) in 6 patients (37.5%), with a mean maximum diameter of 2.6 ± 0.9 cm (range, 1.2–3.8 cm) (Table 1).

Of the 10 cases with ccRCC, 10 (100.0%) showed hyperenhancement on CEUS. Six cases (60.0%) showed homogeneous enhancement, and seven cases (70.0%) showed a synchronous-in pattern (Figure 1). Of the six patients with UCRP, five (83.3%) showed a slow-in pattern, four (66.7%) showed a fast-out pattern, and the enhancement intensity was isoenhancement in four cases (66.7%) (Figure 2). In one case of UCRP with renal pelvis stones, CEUS showed an isoenhancement lesion next to the stones, while it was suspicious for a thrombus or a mass on CT (Figure 3). Perilesional rim-like enhancement was not observed in all the cases.

All the cases were performed in the simultaneous display mode of both CUS and CEUS images. Of the 10 cases with ccRCC, 7 cases (70.0%) were isoechoic, and the other 3 cases (30.0%) were hypoechoic on CUS. No renal pelvis separation was observed in the 10 cases of ccRCC. The largest ccRCC was not clearly demarcated from the renal pelvis and surrounding blood vessels on CT, and it was mistaken for a tumor of the renal pelvis (Figure 4); however, it was not observed on CUS. Of the six cases with UCRP, all the lesions were hypoechoic on CUS.

TABLE 1 Clinical characteristics of the 16 patients with renal masses.

Case	Gender	Age	Location	Size (cm)	Clinical presentation	Reasons why CECT or MRI was not performed	Surgical methods	Pathology
1	Female	83	Right	1.9 × 1.6	Asymptomatic	Chronic renal failure	PN	ccRCC
2	Female	52	Left	1.5 × 1.3	Pain and discomfort in the left waist	Allergy to contrast media	PN	ccRCC
3	Male	38	Left	1.8 × 1.6	Asymptomatic	Allergy to contrast media	PN	ccRCC
4	Male	43	Right	1.6 × 1.5	Asymptomatic	Unwilling	PN	ccRCC
5	Male	71	Right	2.1 × 1.9	Pain and discomfort in the right waist	Allergy to contrast media	PN	ccRCC
6	Male	69	Left	2.9 × 2.1	Asymptomatic	Unwilling	RN	ccRCC
7	Female	57	Right	2.7 × 1.8	Asymptomatic	Unwilling	RN	ccRCC
8	Male	65	Right	1.5 × 1.2	Pain and discomfort in the right waist	Renal dysfunction	PN	ccRCC
9	Male	58	Left	1.7 × 1.6	Asymptomatic	Unwilling	PN	ccRCC
10	Male	71	Left	2.3 × 2.1	Asymptomatic	Unwilling	PN	ccRCC
11	Female	56	Right	2.4 × 1.8	Pain and discomfort in the right waist, gross hematuria	Allergy to contrast media	RN with excision of bladder cuff	UCRP
12	Female	69	Right	2.2 × 1.6	Gross hematuria	Renal dysfunction	RN	UCRP
13	Male	66	Left	1.2 × 7.8	Pain and discomfort in the left waist	Allergy to contrast media	RN with excision of bladder cuff	UCRP
14	Male	74	Left	3.8 × 3.3	Pain and discomfort in the left waist, gross hematuria	Unwilling	RN with excision of bladder cuff	UCRP
15	Male	73	Left	3.4 × 1.9	Gross hematuria	Renal dysfunction	RN	UCRP
16	Male	50	Left	2.4 × 2.1	Gross hematuria	Allergy to contrast media	RN	UCRP

ccRCC, clear cell renal cell carcinoma; UCRP, urothelial carcinoma of the renal pelvis; RN, radical nephrectomy; PN, partial nephrectomy.

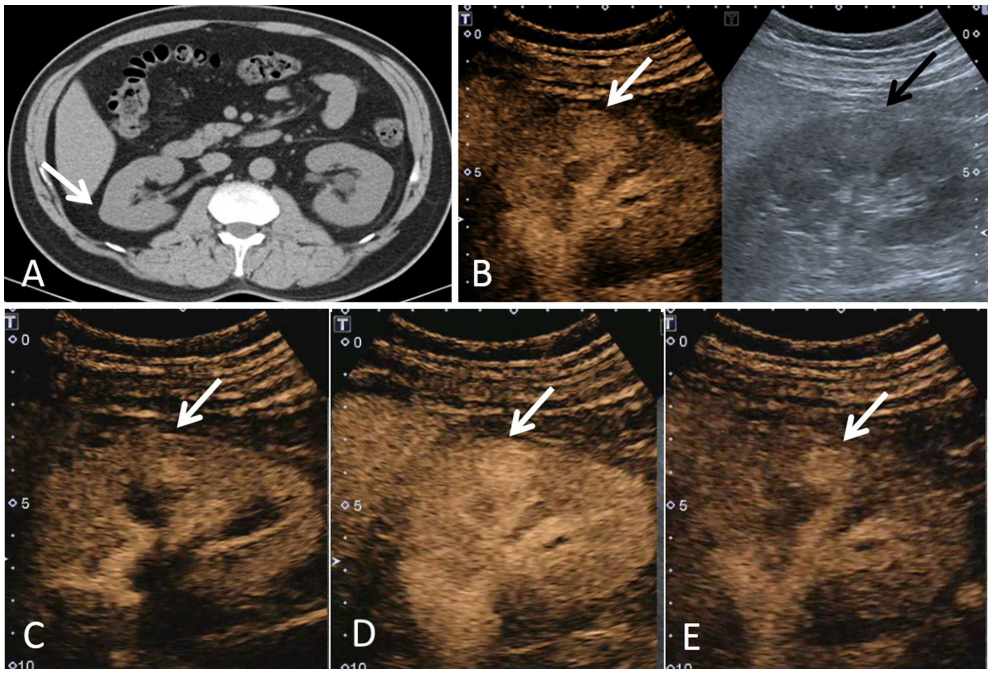

FIGURE 1
A 43-year-old man had a ccRCC in the right kidney with the size of 1.6 × 1.5 cm. **(A)** Non-enhanced CT showed a suspicious lesion in the middle of the right kidney (white arrow). **(B)** According to the position displayed on CT, the simultaneous display mode of conventional ultrasound (CUS, right) and contrast-enhanced ultrasound (CEUS, left) was performed, and CEUS showed a lesion with hyperenhancement (white arrow), but it was not detected on CUS (black arrow). **(C)** On CEUS imaging, it showed that the contrast agent entered the mass synchronously with the adjacent renal cortex (white arrow). **(D)** At the peak of enhancement intensity, it showed homogeneous hyperenhancement compared with that of the renal cortex (white arrow). **(E)** When the contrast agent discharged from the mass, it showed a slow-out pattern compared to the adjacent cortex (white arrow).

Slight renal pelvis separation was observed in three cases (**Table 2**).

Discussion

The European Association of Urology Guidelines on Renal Cell Carcinoma suggested that CECT and MRI were the preferred imaging modalities for the characterization and diagnosis of renal cell carcinoma (RCC), and CEUS can be used as a supplementary method for patients with chronic renal failure or known allergy to iodide or gadolinium-containing contrast agents (10). Among all the diagnosis methods, CEUS has the advantages of minimal invasiveness, no radiation, real time, and no burden on renal metabolism, which may be helpful for tumor diagnosis, especially for early differential diagnosis (1).

In recent years, with the development of medical imaging technology, more and more small renal tumors have been detected, and the sonographic characteristics have been summarized (11). However, for some tumors with atypical sonographic appearances, misdiagnosis and missed diagnosis may occur. Although great advances had been achieved in imaging techniques, the detection of small renal tumors remained a challenge for CUS. These lesions commonly showed blurred margins, which were confused with the surrounding renal cortex. Moreover, the sensitivity of CUS was fundamentally correlated to the size of the tumor. The smaller the tumor size, the more difficult it can be detected by CUS; however, CEUS was less affected by these factors.

Of the 16 patients in our study, 10 patients (62.5%) had ccRCCs. The incidence of ccRCC is 70% of renal carcinoma (12). Most of the ccRCCs are asymptomatic and detected by incidental radiological examination (13). In our series, seven cases were asymptomatic, and three cases had pain and discomfort in the waist. On CUS, seven (70.0%) cases were isoechoic, which were indistinguishable from the surrounding renal cortex, and the lesions did not protrude from the renal capsule either. The other three cases (30.0%) were hypoechoic on CUS, which was similar to the echogenicity of the renal cone nearby. Therefore, these lesions were easily missed on CUS. However, the 10 cases with ccRCCs showed high enhancement on CEUS, which was easily distinguished from the adjacent renal parenchyma. Li et al. also reported that 26.3% of small tumors could not be detected by CUS, while all the tumors could be distinguished from the adjacent renal cortex on CEUS, by showing a sharper margin and high enhancement (8).

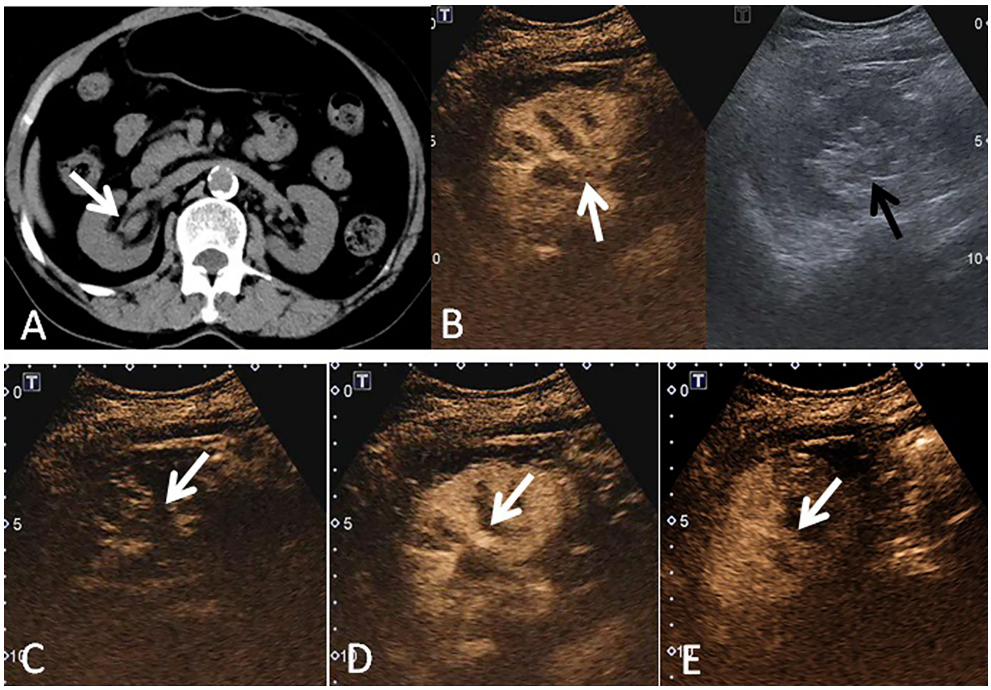

FIGURE 2
A 69-year-old woman had a UCRP in the right kidney with the size of 2.2 × 1.6 cm. **(A)** A suspicious renal pelvis mass (white arrow) was observed on non-enhanced CT scan. **(B)** According to the position displayed on CT, the simultaneous display mode of CUS (right) and CEUS (left) was performed, and CEUS demonstrated local contrast enhancement in the renal pelvis (white arrow). CUS showed a slight separation of the renal pelvis, but no lesion was observed (black arrow). **(C)** On CEUS imaging, it showed a slow-in pattern compared to the renal cortex (white arrow). **(D)** The enhancement intensity of the tumor was similar to that of the adjacent renal cortex (white arrow). **(E)** Compared to the renal cortex, the tumor showed a fast-out pattern (white arrow) on CEUS.

In the past, many studies have focused on the value of CEUS in the differential diagnosis between benign and malignant renal neoplasms. In addition to high enhancement, heterogeneous enhancement and perilesional rim-like enhancement were also highly suggestive of ccRCC (1, 14–17). Perilesional rim-like enhancement may represent the tumor's pseudocapsule which was caused by the compression of the adjacent normal parenchyma, leading to ischemia, necrosis, and then deposition of fibrous tissue (18). However, it was not observed in all the ccRCCs. The main reason might be that the mass size in our study was smaller (mean, 2.0 ± 0.4 cm) than that of previous studies (14, 19). Intratumoral hemorrhage, necrosis, and compression might not be obvious in small tumors. Because of this, the rate (40.0%) of heterogeneous enhancement in the present study was lower than that in previous studies (19, 20). In addition, most ccRCCs showed a synchronous-in pattern, and it was consistent with the results reported by Li et al. (8). This characteristic might be related to the pathologic features of RCC, which was characterized by numerous thin-walled vessels with a rich blood flow (8). Our results showed that CEUS was helpful in detecting tumors in renal parenchyma that were undetectable on CUS; however, only some features appeared on CEUS, which could be helpful in the differential diagnosis. Therefore, the final diagnosis still depends on pathology findings.

In this study, there were six cases with UCRP which were not detected by CUS. The urothelial tumor originating from the renal pelvis accounts for about 10%–15% of all renal neoplasms, mainly including urothelial carcinoma (90%), squamous cell carcinoma (9%), and mucinous adenocarcinoma (1%) (21). Urothelial carcinoma was usually seen in elderly men with the most common symptom of gross or microscopic hematuria (22). Some patients might also have low back pain; however, 10%–15% of patients may be asymptomatic (23). In this study, gross hematuria was observed in three patients, and back pain was observed in four patients.

The main components of the renal sinus, including the collecting duct, lymphatic channels, adipose tissue, fibrous tissue, and nerve fibers, contribute to the hyperechogenicity of renal sinus on CUS, which might easily cover up iso- or hypoechoic lesions (24). When the renal pelvis separation is eccentric in shape, only the lateral margins are visible, and when the renal pelvis separation is lentil-like in shape, the lesion can be missed. The malignant tumors of the renal pelvis may be detected by showing neoplastic angiogenesis; however, color or power Doppler has limited sensitivity in detecting small vessels and low-speed blood flow. CEUS has a high sensitivity in detecting microvasculature, and renal pelvis tumors show local contrast enhancement on CEUS, which can clearly depict the

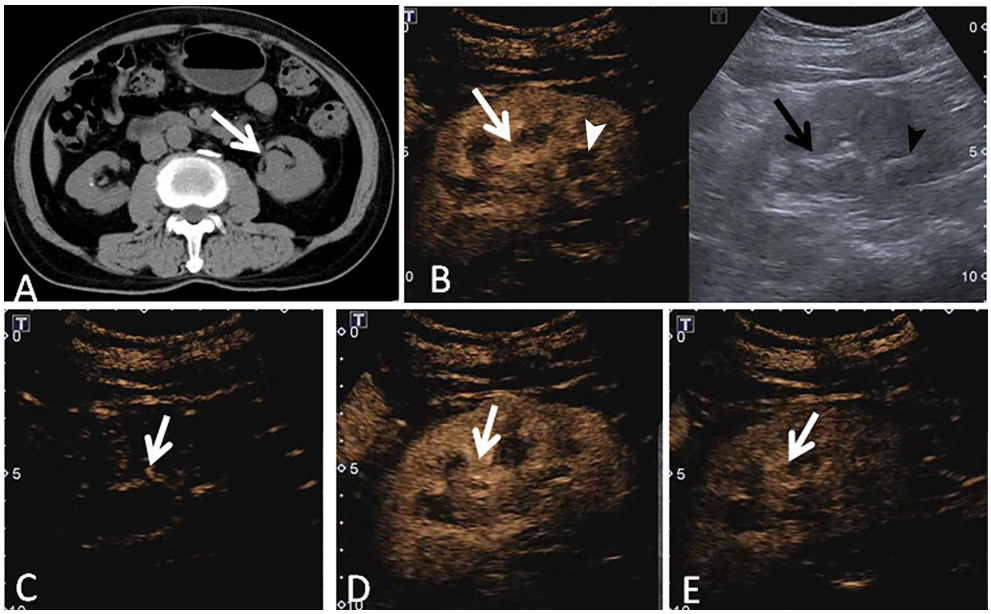

FIGURE 3
A 73-year-old man had a UCRP in the left kidney with the size of 3.4 × 1.9 cm. **(A)** Non-enhanced CT scan showed that there may be blood clots in the renal pelvis (white arrow). **(B)** According to the position displayed on CT, the simultaneous display mode of CUS (right) and CEUS (left) was performed. No obvious lesion (black arrow) was detected on CUS, but it showed a slight separation of the renal pelvis and a stone (black arrowhead) in the lower part of the renal pelvis. On CEUS, a lesion with enhancement was observed (white arrow), and the stone showed no enhancement (white arrowhead). **(C)** The contrast agent entered the lesion more slowly than that of the adjacent renal cortex (white arrow). **(D)** The tumor showed heterogeneous enhancement, and the enhancement intensity of the tumor (white arrow) was similar to that of the adjacent renal cortex. **(E)** The contrast agent discharged from the mass quickly, and the tumor (white arrow) showed a fast-out pattern compared to the renal cortex.

outline of the tumor; thus, a definite diagnosis can be obtained (25). In this study, six cases of UCRP were indistinguishable from the hypoechoic renal pelvis, but they showed isoenhancement or hypoenhancement on CEUS. Therefore, they can be recognized by CEUS because the renal pelvis was not enhanced.

Of the six cases with UCRP, five cases (83.3%) showed a slow-in pattern, and four cases (66.7%) showed a fast-out pattern on CEUS. These findings were consistent with a previous study. Xue et al. (26) reported that slow-in, fast-out, and hypoenhancement were associated with renal urothelial carcinoma, and the enhancement intensity at peak was lower than that of the renal parenchyma. Compared with the renal cortex, the contrast agent in the tumor discharges earlier and faster, making the edge of the tumor easy to identify. Therefore, the renal urothelial tumor might be detected more easily by CEUS.

Sometimes, blood clots in the collecting system are difficult to distinguish from the renal pelvis tumor by CUS due to a similar sonographic appearance; however, on CEUS, tumors could show slight enhancement, which might be distinguished from blood clots with no contrast enhancement. In the case of UCRP combined with renal pelvis stones in our study, CT showed that there may be blood clots in the renal pelvis. No abnormalities were observed on CUS; however, CEUS showed an isoenhancement zone, indicating that there might be a tumor rather than blood clots. Our results showed that CEUS was helpful in detecting tumors in the renal pelvis that were undetectable on CUS, and it was also useful in the differential diagnosis. If a suspicious mass is observed on CT, and CECT is not available, CEUS can be recommended. However, the value of CEUS and CECT in the differential diagnosis of renal pelvis lesions needs to be further compared with a large sample.

The study has some limitations. First, the retrospective nature of this study might lead to potential bias in data collection. Second, the sample size of this study was limited, and no statistical analysis was performed. A further study with a large sample size should be performed. Furthermore, because the kidneys are located in the posterior peritoneum, it may be difficult to demonstrate blood flow in renal masses on color Doppler.

In conclusion, CEUS may be helpful in the diagnosis and differential diagnosis of renal tumors which were not observed on CUS, and it could increase confidence in clinical decision-making. CEUS might be an alternative method for some patients when CECT or MRI cannot be performed.

10.3389/fonc.2022.943960

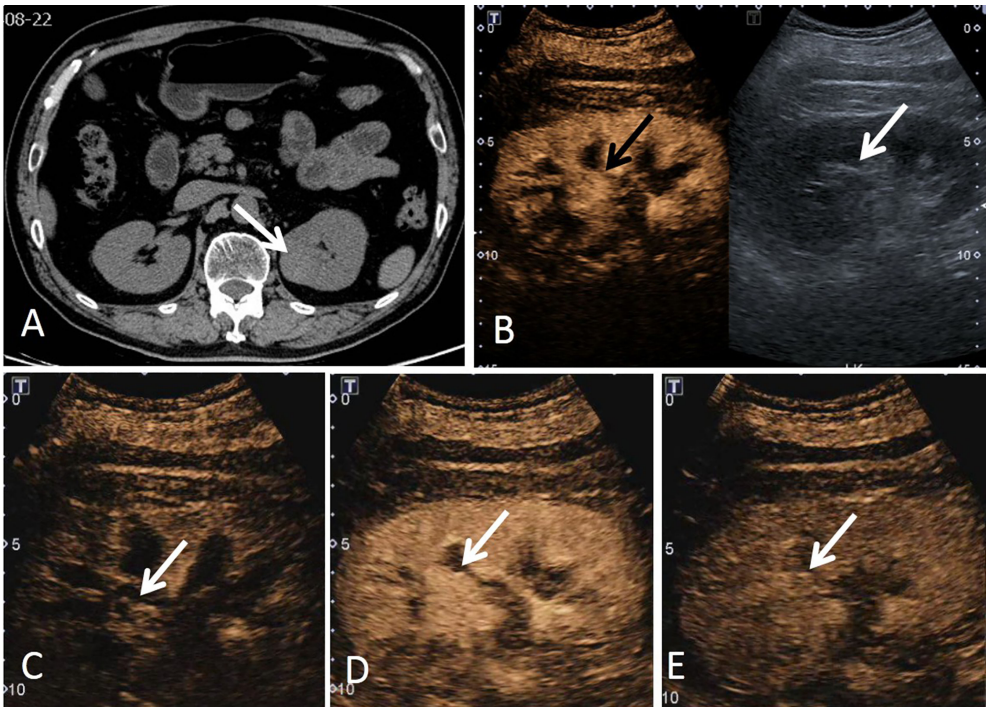

FIGURE 4
A 69-year-old man had a ccRCC in the left kidney with the size of 2.9 × 2.1 cm. **(A)** Non-enhanced CT scan showed a mass (white arrow) that was poorly demarcated from the renal pelvis and surrounding vessels. **(B)** According to the position displayed on CT, the simultaneous display mode of CUS (right) and CEUS (left) was performed, CEUS showed a suspicious mass with hyperenhancement (black arrow), but it was not clear on CUS (white arrow). **(C)** On CEUS imaging, the contrast agent entered the mass (white arrow) synchronously with the adjacent renal cortex. **(D)** The tumor showed homogeneous enhancement, and the enhancement intensity was slightly higher than that of the adjacent renal cortex (white arrow). **(E)** CEUS imaging showed that the tumor had a slow-out pattern (white arrow) compared to the renal cortex.

TABLE 2 CEUS and CUS characteristics of the 16 renal masses.

Case	Enhancement intensity	Homogeneity (CEUS)	Wash-in pattern	Wash-out pattern	Perilesional rim-like enhancement	Echogenicity	Homogeneity (CUS)	Blood flow signal
1	Hyperintense	Heterogeneous	Synchronous	Synchronous	Absent	Hypoechoic	Heterogeneous	Yes
2	Hyperintense	Heterogeneous	Synchronous	Fast	Absent	Isoechoic	Heterogeneous	Yes
3	Hyperintense	Heterogeneous	Slow	Synchronous	Absent	Isoechoic	Heterogeneous	No
4	Hyperintense	Homogeneous	Synchronous	Slow	Absent	Isoechoic	Homogeneous	Yes
5	Hyperintense	Homogeneous	Synchronous	Slow	Absent	Isoechoic	Homogeneous	Yes
6	Hyperintense	Homogeneous	Synchronous	Slow	Absent	Hypoechoic	Heterogeneous	No
7	Hyperintense	Heterogeneous	Synchronous	Synchronous	Absent	Isoechoic	Homogeneous	No
8	Hyperintense	Homogeneous	Synchronous	Fast	Absent	Isoechoic	Homogeneous	No
9	Hyperintense	Homogeneous	Fast	Synchronous	Absent	Hypoechoic	Homogeneous	No
10	Hyperintense	Homogeneous	Fast	Slow	Absent	Isoechoic	Homogeneous	No
11	Isointense	Homogeneous	Slow	Fast	Absent	Hypoechoic	Heterogeneous	No
12	Hypointense	Homogeneous	Slow	Fast	Absent	Hypoechoic	Heterogeneous	No
13	Hypointense	Homogeneous	Slow	Fast	Absent	Hypoechoic	Homogeneous	No
14	Isointense	Heterogeneous	Fast	Slow	Absent	Hypoechoic	Heterogeneous	No
15	Isointense	Heterogeneous	Slow	Fast	Absent	Hypoechoic	Heterogeneous	No
16	Isointense	Heterogeneous	Slow	Synchronous	Absent	Hypoechoic	Heterogeneous	No

CEUS, contrast-enhanced ultrasound; CUS, conventional ultrasound.

Data availability statement

The original contributions presented in the study are included in the article/supplementary material. Further inquiries can be directed to the corresponding author.

Ethics statment

The studies involving human participants were reviewed and approved by the ethical committee of Ruijin Hospital LuWan Branch, Shanghai Jiaotong University School of Medicine. Written informed consent for participation was not required for this study in accordance with the national legislation and the institutional requirements.

Author contributions

Study concept and design: WZ, WWZ, and LT. Acquisition of data: LT, JF, WL, NY, and BM. Resources: LT, JF, WL, NY, and BM. Analysis and interpretation of data: WZ, LT, and JL. Drafting of the manuscript: LT. Critical revision of the manuscript for important intellectual content: WZ and JL. Technical or material support: WZ, WWZ, and JL. Study supervision: WWZ. All authors read and approved the final manuscript.

Conflict of interest

The authors declare that the research was conducted in the absence of any commercial or financial relationships that could be construed as a potential conflict of interest.

Publisher's note

References

1. Sun D, Wei C, Li Y, Lu Q, Zhang W, Hu B. Contrast-enhanced ultrasonography with quantitative analysis allows differentiation of renal tumor histotypes. *Sci Rep* (2016) 6:35081. doi: 10.1038/srep35081

2. Tian W, Lu J, Jiao D, Cong Z. An evaluation of the clinical diagnostic value of contrast-enhanced ultrasound combined with contrast-enhanced computed tomography in space-occupying lesions of the kidney. *Onco Targets Ther* (2017) 10:3493–9. doi: 10.2147/ott.S135500

3. Granata A, Zanoli L, Insalaco M, Valentino M, Pavlica P, Di Nicolò PP, et al. Contrast-enhanced ultrasound (Ceus) in nephrology: Has the time come for its widespread use? *Clin Exp Nephrol* (2015) 19(4):606–15. doi: 10.1007/s10157-014-1040-8

4. Putz FJ, Erlmeier A, Wiesinger I, Verloh N, Stroszczynski C, Banas B, et al. Contrast-enhanced ultrasound (ceus) in renal imaging at an interdisciplinary ultrasound centre: possibilities of dynamic microvascularisation and perfusion. *Clin Hemorheol Microcirc* (2017) 66(4):293–302. doi: 10.3233/ch-179103

5. Setola SV, Catalano O, Sandomenico F, Siani A. Contrast-enhanced sonography of the kidney. *Abdom Imaging* (2007) 32(1):21–8. doi: 10.1007/s00261-006-9001-7

6. Piscaglia F, Nolsøe C, Dietrich CF, Cosgrove DO, Gilja OH, Bachmann Nielsen M, et al. The efsumb guidelines and recommendations on the clinical practice of contrast enhanced ultrasound (ceus): update 2011 on non-hepatic applications. *Ultraschall Med* (2012) 33(1):33–59. doi: 10.1055/s-0031-1281676

7. Nilsson A. Contrast-enhanced ultrasound of the kidneys. *Eur Radiol* (2004) 14 Suppl 8:P104–9.

8. Li CX, Lu Q, Huang BJ, Xue LY, Yan LX, Wen JX, et al. The value of contrast-enhanced ultrasound (ceus) in detecting minute renal cell carcinoma. *Discovery Med* (2014) 18(99):179–88.

9. Lu Q, Xue LY, Huang BJ, Wang WP, Li CX. Histotype differentiation of hypo-echoic renal tumors on ceus: usefulness of enhancement homogeneity and intensity. *Abdom Imaging* (2015) 40(6):1675–83. doi: 10.1007/s00261-014-0340-5

10. Ljungberg B, Bensalah K, Canfield S, Dabestani S, Hofmann F, Hora M, et al. Eau guidelines on renal cell carcinoma: 2014 update. *Eur Urol* (2015) 67(5):913–24. doi: 10.1016/j.eururo.2015.01.005

11. Wei SP, Xu CL, Zhang Q, Zhang QR, Zhao YE, Huang PF, et al. Contrast-enhanced ultrasound for differentiating benign from malignant solid small renal masses: comparison with contrast-enhanced ct. *Abdom Radiol (NY)* (2017) 42 (8):2135–45. doi: 10.1007/s00261-017-1111-x

12. Tamai H, Takiguchi Y, Oka M, Shingaki N, Enomoto S, Shiraki T, et al. Contrast-enhanced ultrasonography in the diagnosis of solid renal tumors. *J Ultrasound Med* (2005) 24(12):1635–40. doi: 10.7863/jum.2005.24.12.1635

13. Valera VA, Merino MJ. Misdiagnosis of clear cell renal cell carcinoma. *Nat Rev Urol* (2011) 8(6):321–33. doi: 10.1038/nrurol.2011.64

14. Xu ZF, Xu HX, Xie XY, Liu GJ, Zheng YL, Lu MD. Renal cell carcinoma and renal angiomyolipoma: differential diagnosis with real-time contrast-enhanced ultrasonography. *J Ultrasound Med* (2010) 29(5):709–17. doi: 10.7863/jum.2010.29.5.709

15. Zhang S, Lin L, Li JH, Qiu L, Han P. [Characteristics of renal occupying lesions in contrast-enhanced ultrasonography]. *Sichuan Da Xue Xue Bao Yi Xue Ban* (2014) 45(6):984–7.

16. Xue LY, Lu Q, Huang BJ, Li CX, Yan LX, Wang WP. Differentiation of subtypes of renal cell carcinoma with contrast-enhanced ultrasonography. *Clin Hemorheol Microcirc* (2016) 63(4):361–71. doi: 10.3233/ch-152024

17. Zhang D, Xin XJ, Mu J, Mao YR, Zhang S. [Comparative analysis of superb microvascular imaging and contrast-enhanced ultrasound in diagnosis of small renal masses]. *Zhonghua Yi Xue Za Zhi* (2019) 99(23):1778–81. doi: 10.3760/cma.j.issn.0376-2491.2019.23.005

18. Pickhardt PJ, Lonergan GJ, Davis CJJr., Kashitani N, Wagner BJ. From the archives of the afip. infiltrative renal lesions: Radiologic-pathologic correlation. armed forces institute of pathology. *Radiographics* (2000) 20(1):215–43. doi: 10.1148/radiographics.20.1.g00ja08215

19. Jiang J, Chen Y, Zhou Y, Zhang H. Clear cell renal cell carcinoma: contrast-enhanced ultrasound features relation to tumor size. *Eur J Radiol* (2010) 73(1):162–7. doi: 10.1016/j.ejrad.2008.09.030

20. Rübenthaler J, Negrão de Figueiredo G, Mueller-Peltzer K, Clevert DA. Evaluation of renal lesions using contrast-enhanced ultrasound (ceus); a 10-year retrospective european single-centre analysis. *Eur Radiol* (2018) 28(11):4542–9. doi: 10.1007/s00330-018-5504-1

21. Prando A, Prando P, Prando D. Urothelial cancer of the renal pelvicaliceal system: unusual imaging manifestations. *Radiographics* (2010) 30(6):1553–66. doi: 10.1148/rg.306105501

22. Wong-You-Cheong JJ, Wagner BJ, Davis CJJr. Transitional cell carcinoma of the urinary tract: Radiologic-pathologic correlation. *Radiographics* (1998) 18 (1):123–42. doi: 10.1148/radiographics.18.1.9460113

23. Kirkali Z, Tuzel E. Transitional cell carcinoma of the ureter and renal pelvis. *Crit Rev Oncol Hematol* (2003) 47(2):155–69. doi: 10.1016/s1040-8428(03)00079-9

24. Rha SE, Byun JY, Jung SE, Oh SN, Choi YJ, Lee A, et al. The renal sinus: pathologic spectrum and multimodality imaging approach. *Radiographics* (2004) 24 Suppl 1:S117–31. doi: 10.1148/rg.24si045503

25. Li F, Bai M, Wu Y, He Y, Gu J, Xing J, et al. Comparative +. *Ultrasound Med Biol* (2015) 41(12):3109–19. doi: 10.1016/j.ultrasmedbio.2015.07.034

26. Xue LY, Lu Q, Huang BJ, Li CL, Yan CJ, Wen JX, et al. Evaluation of renal urothelial carcinoma by contrast-enhanced ultrasonography. *Eur J Radiol* (2013) 82(4):e151–7. doi: 10.1016/j.ejrad.2012.11.001

frontiers | Frontiers in Oncology

TYPE Original Research
PUBLISHED 05 August 2022
DOI 10.3389/fonc.2022.908265

OPEN ACCESS

EDITED BY
Dakai Jin,
Alibaba DAMO Academy, United States

REVIEWED BY
Alessandro Gonfiotti,
University of Florence, Italy
Francesco Guerrera,
University of Turin, Italy
Ke Yan,
Alibaba DAMO Academy, China

*CORRESPONDENCE
Jiayuan Sun
xkyyjysun@163.com
Wenhui Xie
xknuclear888@163.com

†These authors have contributed equally to this work

SPECIALTY SECTION
This article was submitted to Cancer Imaging and Image-directed Interventions, a section of the journal Frontiers in Oncology

RECEIVED 30 March 2022
ACCEPTED 27 June 2022
PUBLISHED 05 August 2022

CITATION
Zhi X, Sun X, Chen J, Wang L, Ye L, Li Y, Xie W and Sun J (2022) Combination of ^{18}F-FDG PET/CT and convex probe endobronchial ultrasound elastography for intrathoracic malignant and benign lymph nodes prediction. *Front. Oncol.* 12:908265. doi: 10.3389/fonc.2022.908265

Combination of ^{18}F-FDG PET/CT and convex probe endobronchial ultrasound elastography for intrathoracic malignant and benign lymph nodes prediction

Xinxin Zhi[1,2,3†], Xiaoyan Sun[4,5†], Junxiang Chen[1,2,3], Lei Wang[6], Lin Ye[1,2,3], Ying Li[1,2,3], Wenhui Xie[5*] and Jiayuan Sun[1,2,3*]

[1]Department of Respiratory Endoscopy, Shanghai Jiao Tong University, Shanghai, China, [2]Department of Respiratory and Critical Care Medicine, Shanghai Chest Hospital, Shanghai Jiao Tong University, Shanghai, China, [3]Shanghai Engineering Research Center of Respiratory Endoscopy, Shanghai, China, [4]Department of Nuclear Medicine, The Fifth People's Hospital of Shanghai Fu Dan University, Shanghai, China, [5]Department of Nuclear Medicine, Shanghai Chest Hospital, Shanghai Jiao Tong University, Shanghai, China, [6]Department of Ultrasound, Shanghai Chest Hospital, Shanghai Jiao Tong University, Shanghai, China

Background: Positron emission tomography–computed tomography (PET/CT) and convex probe endobronchial ultrasound (CP-EBUS) elastography are important diagnostic methods in predicting intrathoracic lymph nodes (LNs) metastasis, but a joint analysis of the two examinations is still lacking. This study aimed to compare the diagnostic efficiency of the two methods and explore whether the combination can improve the diagnostic efficiency in differentiating intrathoracic benign LNs from malignant LNs.

Materials and Methods: LNs examined by EBUS-guided transbronchial needle aspiration (EBUS-TBNA) and PET/CT from March 2018 to June 2019 in Shanghai Chest Hospital were retrospectively analyzed as the model group. Four PET/CT parameters, namely, maximal standardized uptake value mean standardized uptake value (SUVmean), SUVmean, metabolic tumor volume (MTV), and tumor lesion glycolysis (TLG); four quantitative elastography indicators (stiff area ratio, mean hue value, RGB, and mean gray value); and the elastography grading score of targeted LNs were analyzed. A prediction model was constructed subsequently and the dataset from July to November 2019 was used to validate the diagnostic capability of the model.

Results: A total of 154 LNs from 135 patients and 53 LNs from 47 patients were enrolled in the model and validation groups, respectively. Mean hue value and grading score were independent malignancy predictors of elastography, as well as SUVmax and TLG of PET/CT. In model and validation groups, the combination of PET/CT and elastography demonstrated sensitivity, specificity, positive and negative predictive values, and accuracy for

malignant LNs diagnosis of 85.87%, 88.71%, 91.86%, 80.88%, and 87.01%, and 94.44%, 76.47%, 89.47%, 86.67%, and 88.68%, respectively. Moreover, elastography had better diagnostic accuracies than PET/CT in both model and validation groups (85.71% *vs*. 79.22%, 86.79% *vs*. 75.47%).

Conclusion: EBUS elastography demonstrated better efficiency than PET/CT and the combination of the two methods had the best diagnostic efficacy in differentiating intrathoracic benign from malignant LNs, which may be helpful for clinical application.

KEYWORDS

PET/CT, endobronchial ultrasound, elastography, lymph nodes, diagnosis

Introduction

Positron emission tomography–computed tomography (PET/CT) plays a great role in the staging of mediastinal lymph nodes (LNs) of non-small cell lung cancer, with a sensitivity and specificity of 77% and 86%, respectively, for predicting LNs metastasis (1–3). However, PET/CT can only reflect the uptake value of contrast agent. Inflammatory changes in lymphoid follicles and histiocytes can increase ^{18}F-fluorodeoxyglucose (^{18}F-FDG) uptake, leading to the existence of false-positive results (4, 5). LNs with tuberculosis infection can also have a false-positive result because glucose metabolism increases with the accumulation of FDG in inflammatory phagocytes of granulomatous tissue (6). With the development of PET/CT technology and the increasing clinical demand for sensitivity of malignant LN prediction, the diagnostic false-positive rate (FPR) increased, leading to a very important pathological biopsy (7).

Endobronchial ultrasound-guided transbronchial needle aspiration (EBUS-TBNA) is an essential minimally invasive examination, and it can be used to diagnose mediastinal enlarged LNs with significantly high FDG uptake caused by anthracosis (8). For malignant diseases, due to the limited sampling of puncture needle, tumor micrometastasis may lead to the presence of false-negative results (9). Therefore, EBUS-TBNA has a false-negative rate (FNR) of 20% for lung cancer (10). Relevant guidelines indicate that sonographic features can be used to predict malignant and benign LNs during EBUS-TBNA operation, and may prevent the need for repeat EBUS procedures when initial biopsy results are inconclusive (11, 12). Elastography can quantify the degree of tissue deformation in grayscale mode and relative stiffness of tissues can be imaged as a color image to reflect the benign and malignant tissues indirectly (13). Generally, tumor tissue has a harder texture relative to normal tissue. Research found that elastography had a better diagnostic efficiency compared with single grayscale or blood flow Doppler feature (14, 15).

PET/CT and elastography are useful tools in the diagnosis of intrathoracic LNs, which can help the selection of LNs with the greatest likelihood of malignancy during EBUS-TBNA and reduce unnecessary puncture (16, 17). For LNs with negative TBNA results, PET/CT and elastography may have a good supplementary role to reduce FNR. The two methods can reflect the benign and malignant LNs from different aspects, such as elastography, which mainly reflects the degree of stiffness of LNs, while PET/CT mainly reflects the degree of FDG metabolism of LNs. However, there has been no related research about the comparison of PET/CT and elastography, as well as the combination of the two methods in predicting intrathoracic malignant LNs. This study aimed to analyze PET/CT and EBUS elastography indicators in the model group to compare the diagnostic efficiency of the two methods for intrathoracic LNs. Then, a prediction model will be established based on the model group and the diagnostic efficiency will be validated in another dataset.

Materials and methods

Patients

This study was conducted in Shanghai Chest Hospital. EBUS-TBNA examination was performed on patients who met the following criteria: (1) enlarged mediastinal/hilar LNs (at least 1 node >10 mm in the short axis) based on CT or positive intrathoracic LNs detected (SUV ≥ 2.5) by PET/CT; (2) pathological confirmation by EBUS-TBNA was clinically required and feasible to confirm the nature of the LN; and (3) no contraindication to the procedure. Patients who underwent EBUS-TBNA examination and PET/CT from March 2018 to November 2019 were consecutively enrolled and LNs meeting the following criteria were analyzed: The time interval between PET/CT and EBUS-TBNA was less than 1 month; LNs had not

been diagnosed before EBUS-TBNA examination and no antitumor therapy had been performed for target LNs before EBUS-TBNA or PET/CT. LNs without elastography videos were excluded. LNs from March 2018 to June 2019 were assigned into the model group and LNs from July 2019 to November 2019 were assigned into the validation group. This study was approved by the local Ethics Committee of Shanghai Chest Hospital (No. KS-1947). The final diagnosis of LNs depended on pathological results of EBUS-TBNA, thoracoscopy, mediastinoscopy, microbiological examination, or clinical follow-up for at least 1 year.

^{18}F-FDG PET/CT image acquisition

All patients were intravenously injected with 0.10–0.15 mCi/kg (3.7–5.6 Mbq/kg) of ^{18}F-FDG after fasting for 6 h with a blood glucose level of less than 10.0 mmol/L (180 mg/dl). A combined PET/CT scanner Biograph 64, Siemens, Germany was used 45–60 min later after ^{18}F-FDG injection. Patients were subjected to CT positioning scanning from the skull base to one-third of the upper femur and then the scanned area was selected for spiral CT scanning. Scanning conditions were as follows: tube voltage was 120 kV, tube current was automatically adjusted according to CARE Dose 4D technology, and layer thickness was 5.0 mm. Subsequently, 5–6 beds were used for whole-body PET image acquisition, and the acquisition time was 2 min/bed. CT scan data were used to correct the attenuation of PET images, and the TrueX + TOF method was used to reconstruct the images to obtain PET images, CT images, and transverse, sagittal, and coronal fusion images (18).

Elastography

Elastography videos of LNs were recorded with an ultrasound host (EU-ME2, Olympus) and an ultrasound bronchoscope (BF-UC260FW, Olympus) in accordance with standard operation. A scanning frequency of 10 MHz for the ultrasound probe was set for all LNs. After grayscale and Doppler mode were examined, a bronchoscopist switched to elastography mode. The sampling frame should include the target LN and surrounding tissue. When the EBUS probe touched the airway, internal compression of targeted LN from fluctuation of adjacent vessels and the breathing movement can exert a pressurization effect to form elastography. If the image is not ideal, the operator can gently press the screw part of the bronchoscopy handle to pressurize the airway at a frequency of 3–5 times per second to achieve ideal images. After the elastography became stable, two 20-s videos were recorded and stored (14).

Measurement of PET/CT and elastography parameters

All PET/CT parameters were firstly measured by a nuclear medicine physician with more than 3,000 cases of PCT/CT imaging diagnostic experience and then reviewed by another nuclear medicine physician with a similar experience. Short axis was measured at the maximum cross-section of the targeted LN on the CT image (1). Functional images of the maximal standardized uptake value (SUVmax) and mean standardized uptake value (SUVmean) were obtained using attenuation-corrected transaxial images, the ^{18}F-FDG injected dose, the patient's body weight, and the cross-calibration factor between PET and the dose calibrator. SUV was defined as follows: SUV = tissue concentration (MBq/g)/[injected dose (MBq)/body weight (g)]. Siemens syngo *via* software was used to automatically calculate the metabolic tumor volume (MTV) and tumor lesion glycolysis (TLG) (TLG = SUVmean * MTV). The measurement of all parameters was based on the delineation of target LN (19).

The qualitative grading score method was used: 1 (scattered soft, mixed green–yellow–red); 2 (homogeneous soft, predominantly green); 3 (intermediate, mixed blue–green yellow–red); 4 (scattered hard, mixed blue–green); and 5 (homogeneous hard, predominantly blue). A score of 1–3 denotes benign and a score of 4–5 indicates malignant (14, 20). Three experienced doctors (LW, JC, and XZ) with EBUS imaging observation of more than 500 LNs reviewed elastography videos twice independently blind to the final diagnosis of LNs, and determined the final qualitative evaluation result of each expert subsequently. For grading score of disagreement, three experts reached a consensus to decide on the final assessment result. In order to reduce subjectivity and quantify tissue elasticity, the above three doctors selected the representative images of LNs from videos together according to the final grading score previously determined. Software developed by MatlabTM was used by two doctors (JC and XZ) together to draw the region of interest (ROI), and stiff area ratio (SAR), RGB, mean hue value, and mean gray value methods were used as the quantitative indicators (14, 21–23).

Statistical analysis

Receiver operating characteristic analysis was used to determine the optimum cutoff values of continuous variables, and the best cutoff values were taken at the maximal Youden index. Chi-squared test or Fisher's exact test was used for categorical variables. $p < 0.05$ was considered statistically significant. Significant PET/CT and elastography variables of the univariate analysis or those deemed clinically important were then entered into a multivariable logistic regression model to

assess the factors independently associated with predict malignancy. Cohen's kappa method was used to analyze the intra- and interobserver agreement of real-time elastography grading score (24). SPSS version 25.0 (IBM Corp., Armonk, NY, USA) was used for statistical analyses.

Results

Patients and LNs

A total of 154 LNs, namely, 92 malignant LNs and 62 benign LNs, from 135 patients were analyzed in the model group (Table 1). Adenocarcinoma accounted for the largest proportion of malignant LNs (27.27%), as well as nonspecific lymphadenitis of benign LNs (33.77%). There were 53 LNs from 47 patients in the validation group, namely, 36 malignant LNs (18 adenocarcinoma, 6 squamous carcinoma, 1 non-small cell lung cancer not otherwise specified, 5 small cell lung cancer, 3 neuroendocrine tumor not otherwise specified, 2 unknown type of lung cancer, and 1 lymphoma) and 17 benign LNs (12 nonspecific lymphadenitis, 3 sarcoidosis, and 2 tuberculosis). Perfect agreement was reached for intra- and interobserver agreement of the elastography grading score, which were 0.883 and 0.913, respectively.

Diagnostic value of PET/CT and elastography parameters

Receiver operating characteristic curves of PET/CT and elastography variables derived from the model group according to the final diagnosis were shown in Figure 1. The cutoff values and area under the curve (AUC) values of PET/CT and elastography variables were presented in Table 2. SUVmax and TLG were two PET/CT parameters with the highest AUC

TABLE 1 Patients and LNs in the model group.

Number of patients	**135**
Sex, male/female	94/41
Age, years, mean (range)	62.08 (35–83)
Total LNs	154
Station	**No. of LNs (%)**
2R	1 (0.65)
3P	1 (0.65)
4L	12 (7.79)
4R	47 (30.52)
7	51 (33.12)
10L	3 (1.95)
10R	6 (3.90)
11L	16 (10.39)
11Ri	9 (5.814)
11Rs	8 (5.19)
Diagnosis	
Malignant	92 (59.74)
Adenocarcinoma	42 (27.27)
Squamous carcinoma	18 (11.69)
Non-small cell lung cancer not otherwise specified	6 (3.90)
Small cell lung cancer	16 (10.39)
Neuroendocrine tumor not otherwise specified	3 (1.95)
Lymphoepithelioma-like carcinoma	1 (0.65)
Unknown type of lung cancer	2 (1.30)
Metastatic tumors (non-lung primary malignancy)	4 (2.60)
Benign	62 (40.26)
Nonspecific lymphadenitis	52 (33.77)
Sarcoidosis	7 (4.55)
Tuberculosis	2 (1.30)
Non-tuberculous mycobacterium infection	1 (0.65)

LNs, lymph nodes.

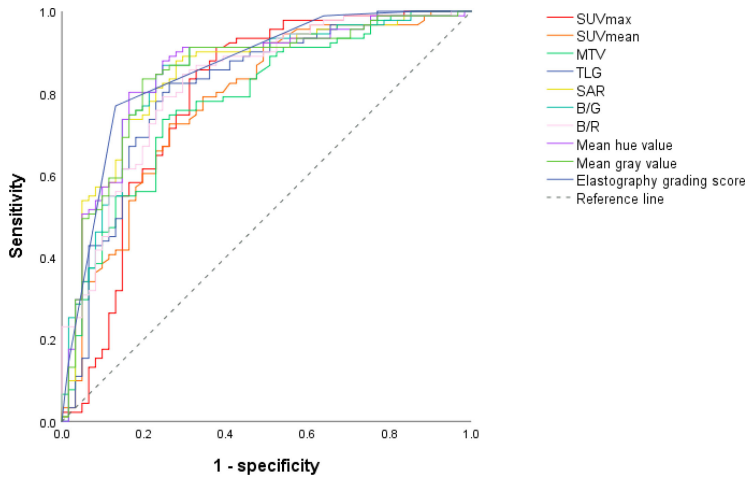

FIGURE 1
ROC curves of PET/CT and elastography parameters in the model group. Through the ROC curves, the best cutoff value reflecting the best diagnostic performance and the AUC value reflecting the overall diagnostic performance of each variable can be obtained. ROC, receiver operating characteristic; AUC, area under the curve; SUVmax, maximal standardized uptake value; SUVmean, mean standardized uptake value; MTV, metabolic tumor volume; TLG, tumor lesion glycolysis; SAR, stiff area ratio; B/G, blue versus green; B/R, blue versus red.

values of 0.788 and 0.813, respectively. Mean hue value and grading score were two elastography quantitative indicators with the highest AUC values of 0.854 and 0.860, respectively. As shown in Table 3, SUVmax, TLG, mean hue value, and grading score were independent predictive indexes for malignant LNs.

Comparison and combined diagnostic value of PET/CT and elastography

In the model group, for PET/CT parameters, SUVmax and TLG had the highest sensitivity of 91.30% and 81.52% and the lowest FNR of 8.70% and 18.48%, respectively (Table 4). When SUVmax or TLG positive (SUVmax > 7.02 or TLG > 12.53) was diagnosed PET/CT positive, both SUVmax and TLG negative (SUVmax ≤ 7.02 and TLG ≤ 12.53) were diagnosed as PET/CT negative, and the sensitivity, FNR, and diagnostic accuracy of PET/CT were 93.48%, 6.52%, and 79.22%, respectively (Table 5). For elastography indicators, mean hue value and grading score had the highest specificity of 83.87% and 87.10%, and the lowest FPR of 16.13% and 12.90%, respectively (Table 4). When mean hue value or grading score positive (mean hue value > 132.73 or grading score > 3) was diagnosed as elastography positive, that is, both mean hue value and grading score negative (mean hue value ≤ 132.73 or grading score ≤ 3) were justified as elastography negative, the diagnostic accuracy of elastography

TABLE 2 Cutoff values and corresponding AUC of PET/CT and elastography variables for malignant LN prediction in the model group.

Index	Cutoff	*p*-value	AUC	95% confidence interval
SUVmax	7.02	1.77E-09	0.788	0.706–0.871
SUVmean	4.59	5.01E-09	0.780	0.703–0.857
MTV	3.47	4.68E-09	0.781	0.706–0.856
TLG	12.53	6.37E-11	0.813	0.740–0.886
SAR	0.33	4.44E-13	0.847	0.782–0.912
B/G	1.05	7.50E-13	0.844	0.777–0.910
B/R	1.47	8.84E-12	0.827	0.760–0.894
Mean hue value	132.73	1.62E-13	0.854	0.789–0.918
Mean gray value	193.39	4.44E-13	0.847	0.781–0.913
Elastography grading score	3.5	6.16E-14	0.860	0.798–0.922

AUC, area under the curve; LNs, lymph nodes; SUVmax, maximal standardized uptake value; MTV, metabolic tumor volume; SUVmean, mean standardized uptake value; TLG, tumor lesion glycolysis; SAR, stiff area ratio; B/G, blue versus green; B/R, blue versus red.

TABLE 3 Univariate and multivariate analyses of PET/CT and elastography parameters in the model group.

Index	Univariate analysis	Multivariate analysis
SUVmax > 7.02	7.82E-13	3.54E-02
SUVmean > 4.59	2.11E-08	
MTV > 3.47	2.99E-09	
TLG > 12.53	5.33E-12	3.63E-02
SAR > 0.33	1.72E-14	
B/G > 1.05	6.17E-14	
B/R > 1.47	7.74E-12	
Mean hue value > 132.73	3.85E-15	1.81E-02
Mean gray value > 193.39	7.31E-15	
Short axis > 1 cm	1.25E-03	
Elastography grading score > 3	5.40E-17	1.49E-03

SUVmax, maximal standardized uptake value; SUVmean, mean standardized uptake value; MTV, metabolic tumor volume; TLG, tumor lesion glycolysis; SAR, stiff area ratio; B/G, blue versus green; B/R, blue versus red.

was 85.71% (Table 5). Figure 2 displays the false-positive representative images of PET/CT in LNs with tuberculosis, sarcoidosis, and nonspecific lymphadenitis, as well as the false-negative representative image of elastography in LNs with neuroendocrine tumor not otherwise specified. The combination of PET/CT with elastography can achieve the highest diagnostic accuracy of 87.01% in the model group; only when both the two methods (PET/CT and elastography) were positive was the combined method justified as positive. That is, either PET/CT or elastography negative was the combined method justified as negative. Similar results can be seen at the validation group, PET/CT combined with elastography had the best diagnostic performance with an accuracy of 88.68% (Table 5). The detailed diagnostic results of PET/CT, elastography, and the combined method in the validation group were displayed in Figure 3.

Discussion

This study explored the diagnostic capacity of PET/CT and EBUS elastography on intrathoracic LNs. SUVmax ≥ 2.5 was commonly used as a positive criterion, and sensitivity and specificity estimates for the SUVmax ≥ 2.5 were 81.3% and 79.4%, respectively (25). The sensitivity of SUVmax was 91.30% in this study. However, the high SUVmax values of sarcoidosis and tuberculosis, which were 13.53 ± 8.37 and 17.57 ± 10.89, respectively, led to a low specificity of 62.90%. FDG uptake is related to the size of LNs, and a false-negative result could be caused by the small size of LNs (26). In the model group, SUVmax for short axis ≤ 1 cm and >1 cm is 6.01 ± 3.53 and 11.00 ± 5.36, respectively, with significant statistical difference ($p < 0.001$). It was suggested that SUVmax is more reproducible than SUVmean (27). In our study, SUVmean had the lowest

TABLE 4 Diagnostic efficiency of PET/CT and elastography variables for malignant lymph nodes prediction in the model group.

Index	Sensitivity	Specificity	PPV	NPV	Accuracy	FPR	FNR
SUVmax	91.30%	62.90%	78.50%	82.98%	79.87%	37.10%	8.70%
SUVmean	71.74%	74.19%	80.49%	63.89%	72.73%	25.81%	28.26%
MTV	72.83%	75.81%	81.71%	65.28%	74.03%	24.19%	27.17%
TLG	81.52%	74.19%	82.42%	73.02%	78.57%	25.81%	18.48%
SAR	88.04%	72.58%	82.65%	80.36%	81.82%	27.42%	11.96%
B/G	86.96%	72.58%	82.47%	78.95%	81.17%	27.42%	13.04%
B/R	83.70%	70.97%	81.05%	74.58%	78.57%	29.03%	16.30%
Mean hue value	80.43%	83.87%	88.10%	74.29%	81.82%	16.13%	19.57%
Mean gray value	82.61%	80.65%	86.36%	75.76%	81.82%	19.35%	17.39%
Short axis > 1 cm	95.65%	20.97%	64.23%	76.47%	65.58%	79.03%	4.35%
Elastography grading score	81.52%	87.10%	90.36%	76.06%	83.77%	12.90%	18.48%

LNs, lymph nodes; SUVmax, maximal standardized uptake value; SUVmean, mean standardized uptake value; MTV, metabolic tumor volume; TLG, tumor lesion glycolysis; SAR, stiff area ratio; B/G, blue versus green; B/R, blue versus red; PPV, positive predictive value; NPV, negative predictive value; FPR, false-positive rate; FNR, false-negative rate.

TABLE 5 The diagnostic efficiency of PET/CT, elastography, and combination model in the model and validation groups.

Index	Sensitivity	Specificity	PPV	NPV	Accuracy	FPR	FNR
Model group							
PET/CT	93.48%	58.06%	76.79%	85.71%	79.22%	41.94%	6.52%
Elastography	89.13%	80.65%	87.23%	83.33%	85.71%	19.35%	10.87%
PET/CT+ Elastography	85.87%	88.71%	91.86%	80.88%	87.01%	11.29%	14.13%
Validation group							
PET/CT	100.00%	23.53%	73.47%	100.00%	75.47%	76.47%	0.00%
Elastography	94.44%	70.59%	87.18%	85.71%	86.79%	29.41%	5.56%
PET/CT+ Elastography	94.44%	76.47%	89.47%	86.67%	88.68%	23.53%	5.56%

PPV, positive predictive value; NPV, negative predictive value; FPR, false-positive rate; FNR, false-negative rate.

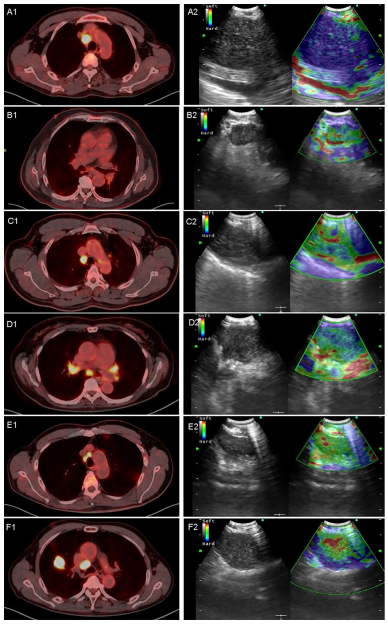

FIGURE 2
Representative images of PET/CT and elastography in a variety of diseases. A1 and A2 are representative true-positive images of malignant LNs examined by PET/CT and elastography, which showed a 4R LN with adenocarcinoma; B1 and B2 show a 7 LN with nonspecific lymphadenitis, true-negative results in both elastography and PET/CT; C1 and C2 show a 4R LN with tuberculosis, and PET/CT showed high metabolism with an SUVmax of 7.85 and a TLG of 39.09. In contrast, elastography showed a grading score of 3 and a mean hue value of 117.74; D1 and D2 showed a 7 LN with sarcoidosis, in which PET/CT showed a high metabolism while elastography showed soft tissue. SUVmax, TLG, grading score, and mean hue value were 5.5, 22.06, 3, and 105.84, respectively; E1 and E2 showed a 4R LN with nonspecific lymphadenitis, false positive by PET/CT but true negative by elastography, and SUVmax, TLG, grading score, and mean hue value were 7.84, 11.33, 1, and 89.37, respectively; F1 and F2 show a 4R LN with neuroendocrine tumor not otherwise specified, and PET/CT showed high metabolism with an SUVmax of 13.29 and a TLG of 42.19. However, elastography shows false-negative results with grading score of 3 and mean hue value of 124.42. LN, lymph node; SUVmax, maximal standardized uptake value; TLG, tumor lesion glycolysis.

accuracy among PET/CT parameters. Volumetric parameter MTV could be used to predict LN metastasis in lung cancer, and it is an important prognostic indicator for NSCLC (28). MTV in our study showed statistically significant differences in benign and malignant LNs, but had the lowest AUC value among the four PET/CT parameters. TLG is calculated by multiplying SUVmean to MTV in an ROI, which can represent both metabolic and volumetric information (19). TLG is an independent parameter for differentiating benign and malignant LNs with the highest AUC among PET/CT parameters in this study. In both model and validation groups, the combination of SUVmax and TLG provided better diagnostic efficiency than any single parameter.

CP-EBUS sonographic features can be used to predict malignant and benign diagnoses during EBUS-TBNA (12). By measuring the compressibility of the tissue, elastography can reflect the different relative stiffness between normal and malignant LNs, and it has been extensively studied using qualitative and quantitative methods. The elastography grading score divides an image into 5 grades, which is convenient for clinical application. For quantitative elastography indicators, SAR is a good predictor of malignant LNs, with an accuracy of 81.82% in this study and 83% and 82.35% in other studies (22, 29). The RGB color model defines a color density of 0–49 as blue pixels. In the model group, blue versus green (B/G) and blue versus red (B/R) had accuracies of 81.17% and 78.57%, respectively, but with the lowest AUC among quantitative elastography indicators. The HSV color model defines a pixel value range from 145 to 180 as blue pixels. Mao et al. found that the AUC of mean hue value was 0.814, and when the cutoff value was 126.28, the corresponding accuracy was 80.88% (22). Mean hue values were 145.00 ± 16.16 and 119.66 ± 17.74 for malignant and benign LNs, and it was the only independent predictor among quantitative indicators. Mean gray values for malignant and benign LNs in the model group were 197.36 ± 14.06 and 182.55 ± 29.61. The AUC of mean gray value was lower than that of mean hue value in this study. In terms of diagnostic methods, the combination of qualitative score with mean hue value had a better diagnostic performance in both groups relative to PET/CT.

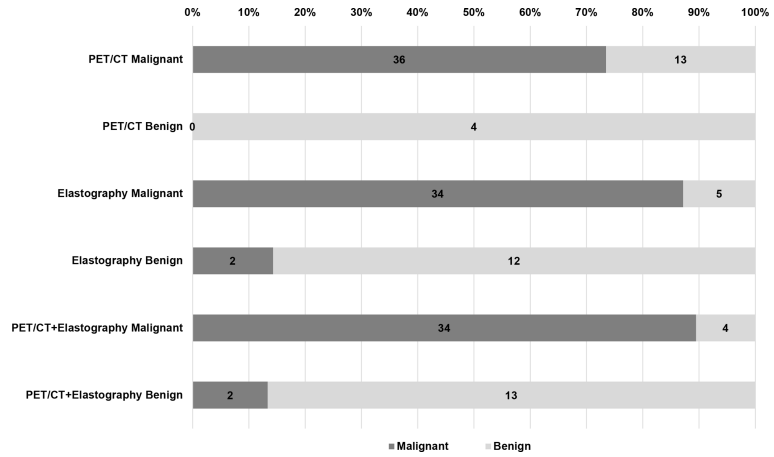

FIGURE 3
Diagnostic efficiency of PET/CT, elastography, and combination method in the validation group. Of the 53 LNs in the validation group, there were 13 false positive and 0 false negative LNs in PET/CT, 5 false positive and 2 false negative LNs in elastography, but only 4 false positive and 2 false negative LNs in the combined method. LN, lymph node.

^{18}F-FDG is not specific for tumor, which can be taken up by various physiologic variants and benign pathologic lesions, leading to false-positive results (30, 31). In the model group, the FPR of PET/CT (SUVmax combined with TLG) was 41.94% (26/62), and 73.08% (19/26) were diagnosed as true negative by elastography among the 26 false-positive cases by PET/CT (19 nonspecific lymphadenitis, 4 sarcoidosis, 2 tuberculosis, and 1 non-tuberculous mycobacterium infection). Inflammation was a well-known factor associated with FPR of PET scan. For nonspecific lymphadenitis, 36.54% (19/52) in the model group and 66.67% (8/12) in the validation group were diagnosed as false positive by PET/CT, and the proportions for sarcoidosis were 57.14% (4/7) in the model group and 100% (3/3) in the validation group. For tuberculosis, a total of 4 cases in model and validation groups had a positive SUVmax. Studies had shown that tuberculosis is prone to lead to false-positive results, because along with the accumulation of FDG in inflammatory phagocytes and macrophages, glucose metabolism increased, and staging accuracy using PET/CT was low in lung cancer patients with parenchymal tuberculosis sequelae (6, 32). In the validation group, there were 13 cases of false-positive diagnosis by PET/CT, among which 9 cases were diagnosed as negative by elastography. This result suggested that elastography could reduce the FPR of PET/CT. Besides, 2 cases of false negative results diagnosed by elastography (1 neuroendocrine tumor not otherwise specified and 1 adenocarcinoma) showed high FDG uptake of SUVmax, suggesting that PET/CT may reduce FNR of elastography. However, only when PET/CT and elastography all positive in this study were considered as malignant, so the combined method did not decrease the FNR.

This study still had some limitations. Although the diagnostic model constructed in this study has been validated, the validation part was still a retrospective study, and further prospective validation is needed. Moreover, all LNs in this study were from a specialized thoracic hospital with a limited category of diseases and the dataset was not large enough. Therefore, a multicenter study with a larger dataset may acquire better results because of different case compositions in different research centers. Moreover, the subjects of this study were mainly patients undergoing LN diagnosis rather than lung cancer staging, such as sarcoidosis and tuberculosis in benign diseases, which may be the reason why the diagnostic specificity and accuracy of PET/CT were slightly lower than those of elastography.

In conclusion, the non-invasive diagnostic model combining PET/CT and EBUS elastography constructed in this study had a higher diagnostic accuracy than any single method for intrathoracic benign and malignant LN differentiation. Furthermore, the diagnostic performance of elastography was superior to PET/CT when the two methods were compared separately. This study may optimize the clinical diagnostic methods of intrathoracic benign and malignant LNs.

Data availability statement

The original contributions presented in the study are included in the article/supplementary material. Further inquiries can be directed to the corresponding authors.

Ethics statement

This study was reviewed and approved by Ethics Committee of Shanghai Chest Hospital. Written informed consent for

participation was not required for this study in accordance with the national legislation and the institutional requirements.

Author contributions

XZ processed elastography videos, analyzed elastography sonographic features collected statistics, and drafted and revised the manuscript. XS collected and analyzed PET/CT data and drafted the manuscript. JC performed EBUS-TBNA examination, analyzed elastography indicators. LW analyzed the elastography indicators. LY assisted in the final diagnostic of lymph nodes. YL revised the paper. WX designed the conception of the study and revised the work. JS designed the conception of the study, revised the manuscript, and supported this study. All authors contributed to the article and approved the submitted version.

Funding

This work was supported by the National Natural Science Foundation of China [grant number 81870078], the Shanghai Municipal Health and Medical Talents Training Program [grant number 2018BR09], and the Shanghai Municipal Education Commission-Gaofeng Clinical Medicine Grant Support [grant number 20181815].

Acknowledgments

The authors acknowledge the doctors in the Department of Respiratory and Critical Care Medicine for the collection of elastography videos and the doctors in the Nuclear Department for the acquisition of PET/CT imaging at Shanghai Chest Hospital.

Conflict of interest

All authors in this study declare that the research was conducted in the absence of any commercial or financial relationships that could be construed as a potential conflict of interest.

Publisher's note

References

1. Toloza EM, Harpole L, McCrory DC. Noninvasive staging of non-small cell lung cancer: A review of the current evidence. *Chest* (2003) 123(1 Suppl):137S–46S. doi: 10.1378/chest.123.1_suppl.137S

2. Gupta NC, Tamim WJ, Graeber GG, Bishop HA, Hobbs GR. Mediastinal lymph node sampling following positron emission tomography with fluorodeoxyglucose imaging in lung cancer staging. *Chest* (2001) 120(2):521–7. doi: 10.1378/chest.120.2.521

3. Silvestri GA, Gonzalez AV, Jantz MA, Margolis ML, Gould MK, Tanoue LT, et al. Methods for staging non-small cell lung cancer: Diagnosis and management of lung cancer, 3rd Ed: American college of chest physicians evidence-based clinical practice guidelines. *Chest* (2013) 143(5 Suppl):e211S–50S. doi: 10.1378/chest.12-2355

4. Lee JW, Kim BS, Lee DS, Chung JK, Lee MC, Kim S, et al. 18f-FDG PET/CT in mediastinal lymph node staging of non-Small-Cell lung cancer in a tuberculosis-endemic country: Consideration of lymph node calcification and distribution pattern to improve specificity. *Eur J Nucl Med Mol Imaging* (2009) 36(11):1794–802. doi: 10.1007/s00259-009-1155-4

5. Kwon SY, Min JJ, Song HC, Choi C, Na KJ, Bom HS. Impact of lymphoid follicles and histiocytes on the false-positive FDG uptake of lymph nodes in non-small cell lung cancer. *Nucl Med Mol Imaging* (2011) 45(3):185–91. doi: 10.1007/s13139-011-0085-9

6. Kubota R, Yamada S, Kubota K, Ishiwata K, Tamahashi N, Ido T. Intratumoral distribution of fluorine-18-Fluorodeoxyglucose *In vivo*: High accumulation in macrophages and granulation tissues studied by microautoradiography. *J Nucl Med* (1992) 33(11):1972–80.

7. Lee BE, von Haag D, Lown T, Lau D, Calhoun R, Follette D. Advances in positron emission tomography technology have increased the need for surgical staging in non-small cell lung cancer. *J Thorac Cardiovasc Surg* (2007) 133(3):746–52. doi: 10.1016/j.jtcvs.2006.10.043

8. Hewitt RJ, Wright C, Adeboyeku D, Ornadel D, Berry M, Wickremasinghe M, et al. Primary nodal anthracosis identified by EBUS-TBNA as a cause of FDG PET/CT positive mediastinal lymphadenopathy. *Respir Med Case Rep* (2013) 10:48–52. doi: 10.1016/j.rmcr.2013.09.005

9. Lee JE, Kim HY, Lim KY, Lee SH, Lee GK, Lee HS, et al. Endobronchial ultrasound-guided transbronchial needle aspiration in the diagnosis of lung cancer. *Lung Cancer* (2010) 70(1):51–6. doi: 10.1016/j.lungcan.2010.01.008

10. Anantham D, Koh MS, Ernst A. Endobronchial ultrasound. *Respir Med* (2009) 103(10):1406–14. doi: 10.1016/j.rmed.2009.04.010

11. Hylton DA, Turner J, Shargall Y, Finley C, Agzarian J, Yasufuku K, et al. Ultrasonographic characteristics of lymph nodes as predictors of malignancy during endobronchial ultrasound (EBUS): A systematic review. *Lung Cancer* (2018) 126:97–105. doi: 10.1016/j.lungcan.2018.10.020

12. Wahidi MM, Herth F, Yasufuku K, Shepherd RW, Yarmus L, Chawla M, et al. Technical aspects of endobronchial ultrasound-guided transbronchial needle aspiration: CHEST guideline and expert panel report. *Chest* (2016) 149(3):816–35. doi: 10.1378/chest.15-1216

13. Dietrich CF, Jenssen C, Herth FJ. Endobronchial ultrasound elastography. *Endosc Ultrasound* (2016) 5(4):233–8. doi: 10.4103/2303-9027.187866

14. Sun J, Zheng X, Mao X, Wang L, Xiong H, Herth FJF, et al. Endobronchial ultrasound elastography for evaluation of intrathoracic lymph nodes: A pilot study. *Respiration* (2017) 93(5):327–38. doi: 10.1159/000464253

15. Rozman A, Malovrh MM, Adamic K, Subic T, Kovac V, Flezar M. Endobronchial ultrasound elastography strain ratio for mediastinal lymph node diagnosis. *Radiol Oncol* (2015) 49(4):334–40. doi: 10.1515/raon-2015-0020

16. Gao SJ, Kim AW, Puchalski JT, Bramley K, Detterbeck FC, Boffa DJ, et al. Indications for invasive mediastinal staging in patients with early non-small cell lung cancer staged with PET-ct. *Lung Cancer* (2017) 109:36–41. doi: 10.1016/j.lungcan.2017.04.018

17. Zhi X, Chen J, Xie F, Sun J, Herth FJF. Diagnostic value of endobronchial ultrasound image features: A specialized review. *Endosc Ultrasound* (2021) 10(1):3–18. doi: 10.4103/eus.eus_43_20

18. Sun XY, Chen TX, Chang C, Teng HH, Xie C, Ruan MM, et al. SUVmax of 18FDG PET/CT predicts histological grade of lung adenocarcinoma. *Acad Radiol* (2021) 28(1):49–57. doi: 10.1016/j.acra.2020.01.030

19. Ruan M, Liu L, Wang L, Lei B, Sun X, Chang C, et al. Correlation between combining 18F-FDG PET/CT metabolic parameters and other clinical features and ALK or ROS1 fusion in patients with non-Small-Cell lung cancer. *Eur J Nucl Med Mol Imaging* (2020) 47(5):1183–97. doi: 10.1007/s00259-019-04652-6

20. Zhi X, Chen J, Wang L, Xie F, Zheng X, Li Y, et al. Endobronchial Ultrasound Multimodal Imaging for the Diagnosis of Intrathoracic Lymph Nodes. *Respiration* (2021) 100(9):898–908. doi: 10.1159/000515664

21. Landoni V, Francione V, Marzi S, Pasciuti K, Ferrante F, Saracca E, et al. Quantitative analysis of elastography images in the detection of breast cancer. *Eur J Radiol* (2012) 81(7):1527–31. doi: 10.1016/j.ejrad.2011.04.012

22. Mao XW, Yang JY, Zheng XX, Wang L, Zhu L, Li Y, et al. Comparison of two quantitative methods of endobronchial ultrasound real-time elastography for evaluating intrathoracic lymph nodes. *Zhonghua Jie He He Hu Xi Za Zhi* (2017) 40 (6):431–4. doi: 10.3760/cma.j.issn.1001-0939.2017.06.007

23. Zhi X, Li J, Chen J, Wang L, Xie Front, Dai Wang, et al. Automatic Image Selection Model Based on Machine Learning for Endobronchial Ultrasound Strain Elastography Videos. *Front Oncol* (2021) 11:673775. doi: 10.3389/fonc.2021.673775

24. Kundel HL, Polansky M. Measurement of observer agreement. *Radiology* (2003) 228(2):303–8. doi: 10.1148/radiol.2282011860

25. Schmidt-Hansen M, Baldwin DR, Hasler E, Zamora J, Abraira V, Roqué I Figuls M. PET-CT for assessing mediastinal lymph node involvement in patients with suspected resectable non-small cell lung cancer. *Cochrane Database Syst Rev* (2014) 2014(11):CD009519. doi: 10.1002/14651858.CD009519.pub2

26. Herth FJ, Eberhardt R, Krasnik M, Ernst A. Endobronchial ultrasound-guided transbronchial needle aspiration of lymph nodes in the radiologically and positron emission tomography-normal mediastinum in patients with lung cancer. *Chest* (2008) 133(4):887–91. doi: 10.1378/chest.07-2535

27. Lee JR, Madsen MT, Bushnel D, Menda Y. A threshold method to improve standardized uptake value reproducibility. *Nucl Med Commun* (2000) 21(7):685–90. doi: 10.1097/00006231-200007000-00013

28. Chen HH, Chiu NT, Su WC, Guo HR, Lee BF. Prognostic value of whole-body total lesion glycolysis at pretreatment FDG PET/CT in non-small cell lung cancer. *Radiology* (2012) 264(2):559–66. doi: 10.1148/radiol.12111148

29. Abedini A, Razavi F, Farahani M, Hashemi M, Emami H, Mohammadi F, et al. The utility of elastography during EBUS-TBNA in a population with a high prevalence of anthracosis. *Clin Respir J* (2020) 14(5):488–94. doi: 10.1111/crj.13159

30. Shreve PD, Anzai Y, Wahl RL. Pitfalls in oncologic diagnosis with FDG PET imaging: Physiologic and benign variants. *Radiographics* (1999) 19(1):61–77. doi: 10.1148/radiographics.19.1.g99ja0761

31. Culverwell AD, Scarsbrook AF, Chowdhury FU. False-positive uptake on 2-[^{18}F]-Fluoro-2-Deoxy-D-Glucose (FDG) positron-emission Tomography/Computed tomography (PET/CT) in oncological imaging. *Clin Radiol* (2011) 66 (4):366–82. doi: 10.1016/j.crad.2010.12.004

32. Lee SH, Min JW, Lee CH, Park CM, Goo JM, Chung DH, et al. Impact of parenchymal tuberculosis sequelae on mediastinal lymph node staging in patients with lung cancer. *J Korean Med Sci* (2011) 26(1):67–70. doi: 10.3346/jkms.2011.26.1.67

frontiers | Frontiers in Oncology

TYPE Case Report
PUBLISHED 10 August 2022
DOI 10.3389/fonc.2022.924465

OPEN ACCESS

EDITED BY
Samata Kakkad,
Merck, United States

REVIEWED BY
Zhili Yang,
Shanghai Jiao Tong University, China
Qing Song,
PLA General Hospital, China

*CORRESPONDENCE
Chengcheng Niu
niuchengcheng@csu.edu.cn

†These authors have contributed equally to this work

SPECIALTY SECTION
This article was submitted to Cancer Imaging and Image-directed Interventions, a section of the journal Frontiers in Oncology

RECEIVED 20 April 2022
ACCEPTED 21 July 2022
PUBLISHED 10 August 2022

CITATION
Gong Y, Tang S, Tan W, Liao L, Li X and Niu C (2022) Papillary thyroid microcarcinoma with contralateral large humerus metastasis and cervical lymph node metastasis: A case report. *Front. Oncol.* 12:924465. doi: 10.3389/fonc.2022.924465

Papillary thyroid microcarcinoma with contralateral large humerus metastasis and cervical lymph node metastasis: A case report

Yi Gong[1†], Shixiong Tang[2†], Wanlin Tan[3,4], Liyan Liao[5], Xiaodu Li[3,4] and Chengcheng Niu[3,4*]

[1]Department of Thyroid Surgery, The Second Xiangya Hospital, Central South University, Changsha, China, [2]Department of Radiology, The Second Xiangya Hospital, Central South University, Changsha, China, [3]Department of Ultrasound Diagnosis, The Second Xiangya Hospital, Central South University, Changsha, China, [4]Research Center of Ultrasonography, The Second Xiangya Hospital, Central South University, Changsha, China, [5]Department of Pathology, The Second Xiangya Hospital, Central South University, Changsha, China

Introduction: Papillary thyroid microcarcinoma (PTMC) that metastasizes to bone, especially metastasizes to contralateral humerus with so large mass, is rarely reported before.

Case report: We presented a 50-year-old female patient with a large painful mass in the right humerus for 5 years, presenting with swelling of the right shoulder with limited mobility. Positron emission tomography–computed tomography (PET/CT) showed a large mass in the right humerus, bilateral lung lesions, and enlarged lymph nodes in the right supraclavicular fossa. Right humerus lesion biopsy and immunohistochemical evaluations confirmed that the lesion originated from the thyroid tissue. Then, the thyroid ultrasonography showed a hypo-echoic solid nodule with an irregular taller-than-wide shape in the upper of left thyroid lobe and enlarged lymph nodes with the absence of fatty hilum in the contralateral right IV compartment. The total thyroidectomy and cervical lymph node dissection were undertaken; the histopathology confirmed the diagnosis of PTMC with contralateral cervical lymph node metastasis.

Conclusion: We reported a case of PTMC with contralateral large humerus and cervical lymph node metastasis and demonstrated the PET/CT images of the metastatic large humerus and thyroid ultrasonographic appearances of the PTMC and enlarged cervical lymph node.

KEYWORDS

papillary thyroid microcarcinoma (PTMC), cervical lymph node metastases, large humerus metastasis, bone metastases, PET/CT, thyroid ultrasonography

Introduction

Papillary thyroid microcarcinoma (PTMC) is defined as papillary thyroid carcinoma (PTC) measuring equal to or less than 1 cm, which is the common well-differentiated thyroid cancer with an excellent prognosis and extremely low lethality (1). PTMC usually metastasizes to the regional cervical lymph nodes, but metastases to the bones are rarely reported (2, 3). The most common primary sites of metastatic humerus tumors were the breast, myeloma, renal, lung, and prostate carcinomas being the most common sources, and only 2% of these originate from the thyroid (4). To our knowledge, humerus metastasis as an initial presentation of PTMC is almost never reported in the previous literature works, especially as huge as the head of a 3-year-old child. Here, we reported a case of PTMC with contralateral large humerus and cervical lymph node metastasis and demonstrated the positron emission tomography–computed tomography (PET/CT) images of the metastatic large humerus and thyroid ultrasonographic appearances of the PTMC and enlarged cervical lymph node.

Case report

We presented a 50-year-old female patient with a large painful mass in the right humerus for 5 years, presenting with swelling of the right shoulder with limited mobility. PET/CT with 18F-fluorodeoxyglucose (18F-FDG) showed a large mass in the right humerus (130 × 115 × 174 mm), bilateral lung lesions, and enlarged lymph nodes in the right supraclavicular fossa (Figure 1). Right humerus lesion biopsy was carried, and the histopathology of the specimen displayed fistular and sieve distribution with obvious nuclear heterogeneity (Figure 2A). The immunohistochemical stains were positive for thyroid transcription factor (TTF-1), thyroglobulin (TG), cytokeratin (CK) pan, and CK7 and negative for hepatocyte (HPC), alpha fetoprotein (AFP), Syn, CgA, special AT-rich sequence-binding protein 2 (SATB2), calcitonin, P53, Napsin A, estrogen receptor (ER), progesterone receptor (PR), and cadual type homeobox gene 2 (CDX2), which indicates that the lesion originated from the thyroid follicular epithelial cells and not from the liver, breast, colon, lung, or thyroid parafollicular cells; Ki67 proliferation index was about 10% (Figures 2B-F). Then, the thyroid ultrasonography was carried and revealed a hypo-echoic solid nodule with an irregular taller-than-wide shape (4.7 × 3.7 × 5.3 mm) in the upper of left thyroid lobe; this thyroid nodule has nine points and classified as ACR Thyroid Imaging, Reporting and Data System (TI-RADS) (5). The thyroid nodule showed uneven iso-enhancement on the contrast-enhanced ultrasonography (CEUS), which indicates that the enhancement of thyroid nodule was equal to that of the surrounding tissue. The enlarged lymph nodes with the absence of fatty hilum were displayed in the contralateral right IV compartment of cervical lymph nodes (Figure 3). The total thyroidectomy and right lateral cervical lymph node dissection were undertaken; the histopathology confirmed the diagnosis of PTMC with contralateral cervical lymph node metastasis (2/18), indicating two lymph nodes involved in the right IV compartment of cervical lymph nodes, and the total number of the right lateral cervical lymph nodes was 18 (Figure 4). Interestingly, the patients had no central cervical lymph node metastasis (0/7), and the $BRAF^{V600E}$ mutation of the PTMC was wild type. According to the eighth edition of the American Joint Committee on Cancer/Tumor Lymph Node Metastasis (TNM) staging system, the patient was in TNM stage IVb (T, N1, of M1) (6).

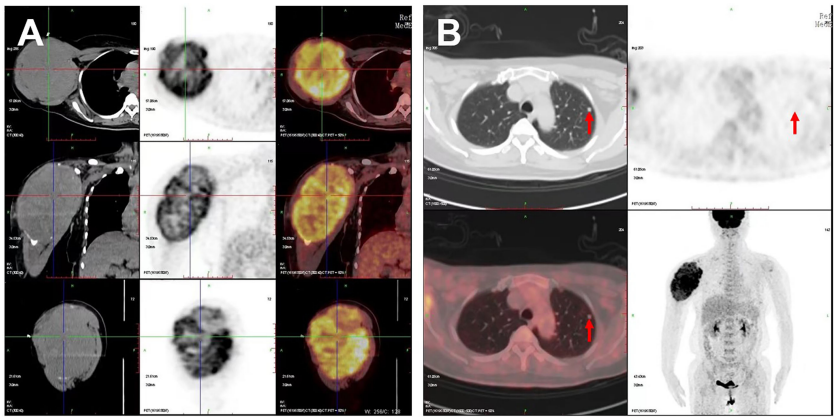

FIGURE 1
PET/CT images of the patient. Increased 18F-FDG metabolism showed in **(A)** the large right humerus (130 × 115 × 174 mm) on the cross, sagittal, and coronal sections and in **(B)** the left lung (6.5 × 6.0 mm); red arrows indicate the lung lesion.

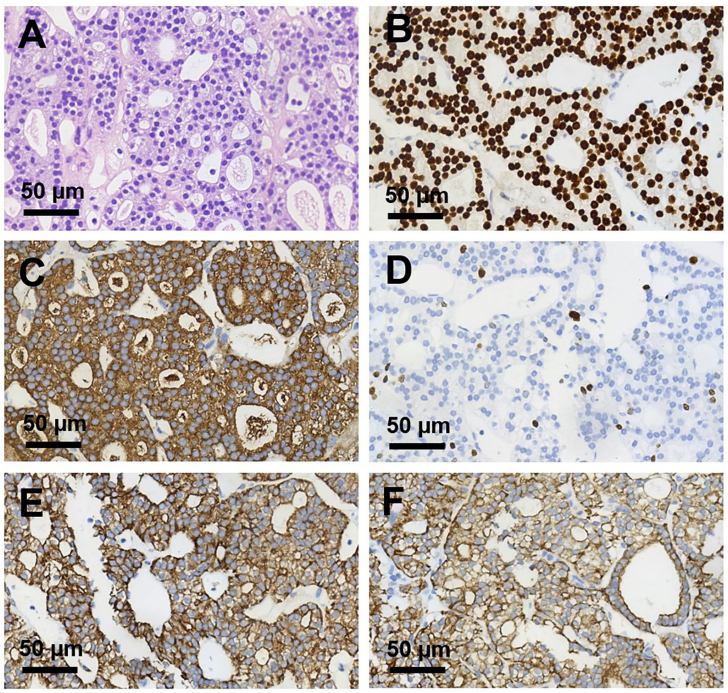

FIGURE 2
Histopathological sections of right humerus lesion (magnification, ×400). **(A)** H&E staining and **(B–F)** Immunohistochemical staining of **(B)** TTF-1, **(C)** TG, **(D)** Ki 67, **(E)** CK pan, **(F)** CK 7. TTF-1, TG, CK pan, and CK7 were deeply stained (positive); Ki 67 proliferation index was about 10%.

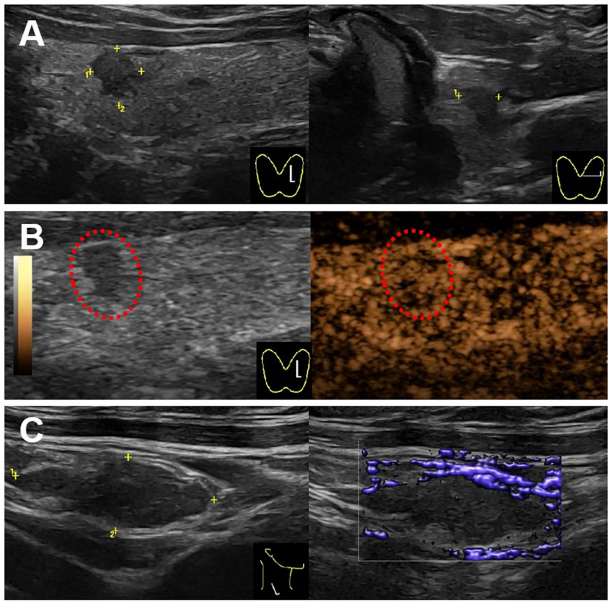

FIGURE 3
Ultrasound images for the thyroid and cervical lymph node. **(A)** A hypo-echoic solid nodule with an irregular margin and a taller-than-wide shape (4.7 × 3.7 × 5.3 mm) showed in the upper of left thyroid lobe on the gray-mode ultrasonography. **(B)** The nodule showed uneven iso-enhancement on the CEUS mode ultrasonography. **(C)** A swollen lymph node with the absence of fatty hilum (17.4 × 6.6 mm) showed in the right IV compartment of cervical lymph nodes, with no obvious blood flow in the lymph node.

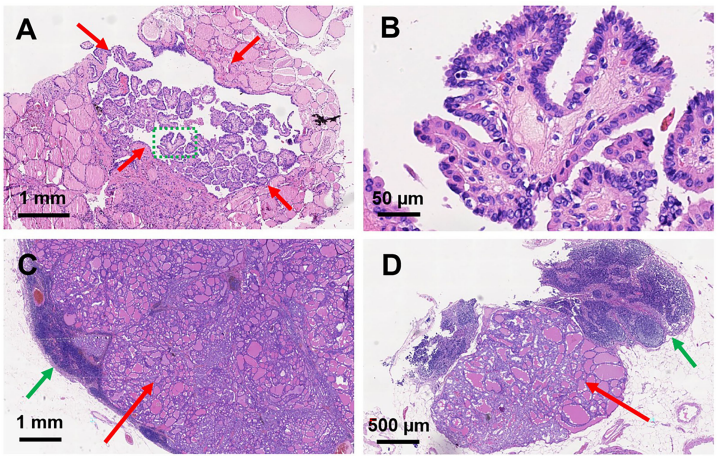

FIGURE 4
Histopathological sections of papillary thyroid microcarcinoma and metastatic lymph nodes. H&E staining of papillary thyroid microcarcinoma in the left thyroid lobe: **(A)** magnification, × 40; **(B)** magnification, × 400. Red arrows indicate the PTMC; green dashed circle indicates the amplification part in **(B)**. H&E staining of metastatic lymph nodes: **(C)** magnification, ×16; **(D)** magnification, ×34. Red arrows indicate the metastatic thyroid tissue in the lymph nodes; green arrows indicate the normal part of the metastatic lymph nodes.

Discussion

PTC is the most common malignant carcinoma, with PTMC being one of PTCs with the maximum tumor size of 10 mm, which is considered as the most indolent variant of thyroid cancer (1). The incidence of PTMC is increasing due to the improved diagnostic ultrasonography and fine-needle aspiration biopsy (1). Cervical lymph node metastases are the most metastatic sites for PTMC, whereas the bones and lungs are seldom reported in the literature (7, 8).

Bone metastasis from differentiated thyroid carcinoma is estimated to be 2%–13%; depending on the histologic origin of cancer, follicular thyroid carcinoma (FTC) is more likely to cause bone metastases than PTC (7, 9, 10). The typical metastatic lesions of bone are the spine, ribs, pelvis, and femur; humerus is the most common location of the bone metastases in the upper extremity (11). More than 80% of bone metastases are located in the axial skeleton red marrow, where blood flow is high and tumor cell adhesive molecules are more inclined to bind the tumor cells to migrate (10).

18F-FDG PET/CT has been a predictor of increased aggressiveness and a poor prognosis in many malignant tumors and is helpful in the management of patients with anaplastic and medullary thyroid carcinoma (12). However, it is difficult to identify and estimate the standard uptake value of PTMC on PET/CT due to the tumor size less than 1 cm (13). In this case, increased 18F-FDG metabolism showed on a large mass in the right humerus, bilateral lung lesions, and enlarged lymph nodes in the right supraclavicular fossa, whereas the primary tumor of thyroid without visually identifiable 18F-FDG uptake is missed on PET/CT imaging. For the high 18F-FDG uptake of a mass in the right humerus, the PET/CT images on the cross, sagittal, and coronal sections visually revealed the three-dimensional huge size and high metabolism of the tumor, providing important information for the patient management.

Thyroid ultrasonography is a recommended diagnostic method for thyroid nodes. The typical malignant sonographic features of PTC were solid composition, hypo-echogenicity, irregular margin, presence of calcification, and taller-than-wide shape (5, 14). In this case, this PTMC had four typical malignant sonographic features: solid composition, hypo-echogenicity, irregular margin, and taller-than-wide shape. Hong et al. found that presence of calcification had the predicative for the presence of central compartment lymph node metastases; coincidentally, this case accurately had no central compartment lymph node metastases, but it had contralateral cervical lymph node metastases (15). The mechanism of this jump lymph node metastases is unclear now.

Although PTMC is generally associated with an excellent prognosis and very low mortality rate of 0.5% (16), a study of Orita et al. found that patients with PMTC showed significantly worse survival than patients with standard variant PTC and FTC (9). Another study of Kim et al. found that some PMTC will show aggressive behavior, causing regional or even distant metastases in their earlier presentation, and should not be considered as indolent thyroid carcinoma (17). Weng et al. found that the prognosis of patients with PTMC becomes worse after the development of distant metastases (18). Thus, not all PTMCs are associated with a good prognosis; the mechanism of thyroid metastases in rare sites is unknown, and further research on PTMCs is required, which has a significant impact on patient management.

Conclusion

In this case, we have reported a case of a large mass in the humerus with swelling of the right shoulder and limited mobility as the first clinical presentation; the humerus lesion biopsy confirmed that it originated from the thyroid tissue. The PET/CT images of the metastatic large humerus and thyroid ultrasonographic appearances of the thyroid nodule and enlarged cervical lymph node were provided. The postoperative histopathology confirmed it as a PTMC with contralateral cervical lymph node metastases. Hence, our case emphasizes that clinically significant metastases can arise from PTMC.

Data availability statement

The original contributions presented in the study are included in the article/Supplementary Material. Further inquiries can be directed to the corresponding author.

Ethics statement

This study was reviewed and approved by the Ethics Committee of Second Xiangya Hospital, Central South University, China. The patients/participants provided their written informed consent to participate in this study.

Author contributions

All authors listed have made a substantial, direct, and intellectual contribution to the work and approved for publication.

Funding

This project was funded by the National Natural Science Foundation of China (81974267), Science and Technology Innovation Program of Hunan Province (2021RC3033), and Hunan Provincial Natural Science Foundation of China (2022JJ30827 and 2022JJ30806).

Conflict of interest

The authors declare that the research was conducted in the absence of any commercial or financial relationships that could be construed as a potential conflict of interest.

Publisher's note

References

1. Haugen BR, Alexander EK, Bible KC, Doherty GM, Mandel SJ, Nikiforov YE, et al. 2015 American thyroid association management guidelines for adult patients with thyroid nodules and differentiated thyroid cancer: The American thyroid association guidelines task force on thyroid nodules and differentiated thyroid cancer. *Thyroid* (2016) 26(1):1–133. doi: 10.1089/thy.2015.0020

2. Pittas AG, Adler M, Fazzari M, Tickoo S, Rosai J, Larson SM, et al. Bone metastases from thyroid carcinoma: clinical characteristics and prognostic variables in one hundred forty-six patients. *Thyroid* (2000) 10(3):261–8. doi: 10.1089/thy.2000.10.261

3. Zheng W, Tan J, Zhang G. Extensive bone metastases as the initial symptom of papillary thyroid microcarcinoma: A case report. *Exp Ther Med* (2015) 9 (6):2104–8. doi: 10.3892/etm.2015.2423

4. Bashore CJ, Temple HT. Management of metastatic lesions of the humerus. *Orthop Clin North Am* (2000) 31(4):597–609. doi: 10.1016/s0030-5898(05)70178-4

5. Tessler FN, Middleton WD, Grant EG, Hoang JK, Berland LL, Teefey SA, et al. ACR thyroid imaging, reporting and data system (TI-RADS): White paper of the ACR TI-RADS committee. *J Am Coll Radiol* (2017) 14(5):587–95. doi: 10.1016/j.jacr.2017.01.046

6. Lamartina L, Grani G, Arvat E, Nervo A, Zatelli MC, Rossi R, et al. 8th edition of the AJCC/TNM staging system of thyroid cancer: what to expect (ITCO#2). *Endocr Relat Cancer* (2018) 25(3):L7–L11. doi: 10.1530/ERC-17-0453

7. Duntas LH. Thyroid cancer-related bone metastases: increasingly good prospects for treatment. *Endocrine* (2018) 61(1):1–3. doi: 10.1007/s12020-018-1616-2

8. Wu K, Hou SM, Huang TS, Yang RS. Thyroid carcinoma with bone metastases: A prognostic factor study. *Clin Med Oncol* (2008) 2:129–34. doi: 10.4137/cmo.s333

9. Orita Y, Sugitani I, Matsuura M, Ushijima M, Tsukahara K, Fujimoto Y, et al. Prognostic factors and the therapeutic strategy for patients with bone metastasis from differentiated thyroid carcinoma. *Surgery* (2010) 147(3):424–31. doi: 10.1016/j.surg.2009.10.009

10. Muresan MM, Olivier P, Leclere J, Sirveaux F, Brunaud L, Klein M, et al. Bone metastases from differentiated thyroid carcinoma. *Endocr Relat Cancer* (2008) 15(1):37–49. doi: 10.1677/ERC-07-0229

11. Frassica FJ, Frassica DA. Metastatic bone disease of the humerus. *J Am Acad Orthop Surg* (2003) 11(4):282–8. doi: 10.5435/00124635-200307000-00008

12. Mosci C, Iagaru A. PET/CT imaging of thyroid cancer. *Clin Nucl Med* (2011) 36(12):e180–5. doi: 10.1097/RLU.0b013e3182291d03

13. Hwang SO, Lee SW, Kang JK, Choi HH, Kim WW, Park HY, et al. Clinical value of visually identifiable 18F-fluorodeoxyglucose uptake in primary papillary thyroid microcarcinoma. *Otolaryngol Head Neck Surg* (2014) 151(3):415–20. doi: 10.1177/0194599814537224

14. Kwak JY, Han KH, Yoon JH, Moon HJ, Son EJ, Park SH, et al. Thyroid imaging reporting and data system for US features of nodules: A step in establishing better stratification of cancer risk. *Radiology* (2011) 260(3):892–9. doi: 10.1148/radiol.11110206

15. Hong YR, Yan CX, Mo GQ, Luo ZY, Zhang Y, Wang Y, et al. Conventional US, elastography, and contrast enhanced US features of papillary thyroid microcarcinoma predict central compartment lymph node metastases. *Sci Rep* (2015) 5:7748. doi: 10.1038/srep07748

16. Yu XM, Wan Y, Sippel RS, Chen H. Should all papillary thyroid microcarcinomas be aggressively treated? An analysis of 18,445 cases. *Ann Surg* (2011) 254(4):653–60. doi: 10.1097/SLA.0b013e318230036d

17. Kim HY, Park WY, Lee KE, Park WS, Chung YS, Cho SJ, et al. Comparative analysis of gene expression profiles of papillary thyroid microcarcinoma and papillary thyroid carcinoma. *J Cancer Res Ther* (2010) 6(4):452–7. doi: 10.4103/0973-1482.77103

18. Weng HY, Yan T, Qiu WW, Xi C, Hou LY, Yang ZL, et al. Long-term outcomes and prognostic factors in papillary thyroid microcarcinoma patients with distant metastases. *Endocrine* (2022) 75(2):495–507. doi: 10.1007/s12020-021-02906-8

frontiers | Frontiers in Oncology

TYPE Case Report
PUBLISHED 12 August 2022
DOI 10.3389/fonc.2022.911442

OPEN ACCESS

EDITED BY
Ellen Ackerstaff,
Memorial Sloan Kettering Cancer Center, United States

REVIEWED BY
Nguyen Minh Duc,
Pham Ngoc Thach University of Medicine, Vietnam
Sung Bin Park,
Chung-Ang University Hospital, South Korea

*CORRESPONDENCE
Fengdan Wang
wangfengdan@pumch.cn

†These authors have contributed equally to this work

SPECIALTY SECTION
This article was submitted to Cancer Imaging and Image-directed Interventions, a section of the journal Frontiers in Oncology

RECEIVED 02 April 2022
ACCEPTED 20 July 2022
PUBLISHED 12 August 2022

CITATION
Wang W, Xiao Y, Fang S, Qiao Y, Rong S, Wang F, Sun H and Jin Z (2022) Case report: Giant unilocular prostate cystadenoma: A rarer condition with a single cystic mass. *Front. Oncol.* 12:911442. doi: 10.3389/fonc.2022.911442

Case report: Giant unilocular prostate cystadenoma: A rarer condition with a single cystic mass

Wenda Wang[1†], Yu Xiao[2†], Shiyuan Fang[3], Yi Qiao[1], Shi Rong[1], Fengdan Wang[4*], Hao Sun[4] and Zhengyu Jin[4]

[1]Department of Urology, Peking Union Medical College Hospital, Chinese Academy of Medical Sciences and Peking Union Medical College, Beijing, China, [2]Department of Pathology, Peking Union Medical College Hospital, Chinese Academy of Medical Sciences and Peking Union Medical College, Beijing, China, [3]School of Clinical Medicine, Chinese Academy of Medical Sciences and Peking Union Medical College, Beijing, China, [4]Department of Radiology, Peking Union Medical College Hospital, Chinese Academy of Medical Sciences and Peking Union Medical College, Beijing, China

Prostate cystadenoma is a rare benign prostatic neoplasm, which grows outside prostate and locates midline between the urinary bladder and rectum. It usually presents as multilocular cysts, thus, named giant multilocular prostate cystadenoma. The definite diagnosis is difficult to be made before surgery, and it depends on histopathology. Here, we report a rarer condition of prostate cystadenoma, which manifests as a giant unilocular cyst with a solid nodule inside. The 55-year-old Chinese male patient presented with dysuria and constipation. MRI revealed a 10.5 × 8.2 cm mono-cystic lesion displacing the rectum to the posterior, prostate, and bladder to the anterior, with a 2.8 × 2.1 cm solid nodule at the anterior wall. ^{18}F-FDG PET/CT demonstrated an elevated SUV_{max} (3.5) of the solid nodule. Laparoscopic pelvic mass resection was performed and prostate cystadenoma was diagnosed. In conclusion, when a mass of single locular cyst sits in the male pelvis, the diagnosis of prostate cystadenoma could not be excluded.

KEYWORDS

prostatic cystadenoma, unilocular, diagnosis, treatment, surgery

Introduction

Prostate cystadenoma is an extremely rare benign tumor deriving from the prostate. It usually locates between the urinary bladder and rectum and presents as a large multilocular cystic mass, thus, named giant multilocular prostate cystadenoma. The patient usually complain of discomfort, such as lower urinary tract symptoms and defecation problems, and histopathological examination is needed for final diagnosis. Since 1991, fewer than 40 cases of giant multilocular prostate cystadenoma are reported

(1, 2). As far as we know, prostate cystadenoma presenting as a unilocular cyst has not been reported in English literature. Here, we report a rarer condition of prostate cystadenoma manifesting as a giant unilocular cyst with a solid nodule, which is challenging for both diagnosis and surgery.

Case presentation

A 55-year-old Chinese male patient presented with dysuria and constipation for 4 months. Four months ago, he experienced severe dysuria and intermitted lower abdominal pain, without fever or hematuria. In the meantime, the patient also developed constipation. Two months later, he experienced constant hematuria and painful urination. Then, he suffered from urinary retention and a urinary catheter was placed to alleviate his lower abdominal pain and hematuria. Physical examination was unremarkable. Urinary occult blood was positive in urinary analysis confirming hematuria. Serum tumor markers including carcinoembryonic antigen (CEA), cancer antigen (CA) 19-9, CA125, CA72-4, and CA242 were all normal. Serum prostate-specific antigen (PSA) was also normal. Pelvic magnetic resonance imaging (MRI) revealed a 10.5 × 8.2 cm mono-cystic lesion displacing the rectum to the posterior, prostate, and bladder to the anterior, with a 2.8 × 2.1 cm solid nodule at the anterior wall (Figure 1, Supplement). The cystic component was hyperintense on T1 weighted image (WI) and T2WI, without diffusion restriction on diffusion weighted image (DWI) nor enhancement on gadolinium-enhanced fat-saturated T1WI, indicating protein rich or hemorrhagic fluid. By contrast, the solid nodule, which was isointense on both T1WI and T2WI, showed diffusion restriction and marked enhancement. In addition, ^{18}F-FDG positron emission tomography/computed tomography (PET/CT) demonstrated an elevated SUV_{max} (3.5) of the solid nodule. Cystoscope could not be entered due to obstruction caused by the mass.

The diagnosis was difficult before surgery as the lesion was too large and the origin was hard to define. Although there was no obvious invasion of adjacent organs, both MRI and PET-CT suggested that the solid nodule is malignant.

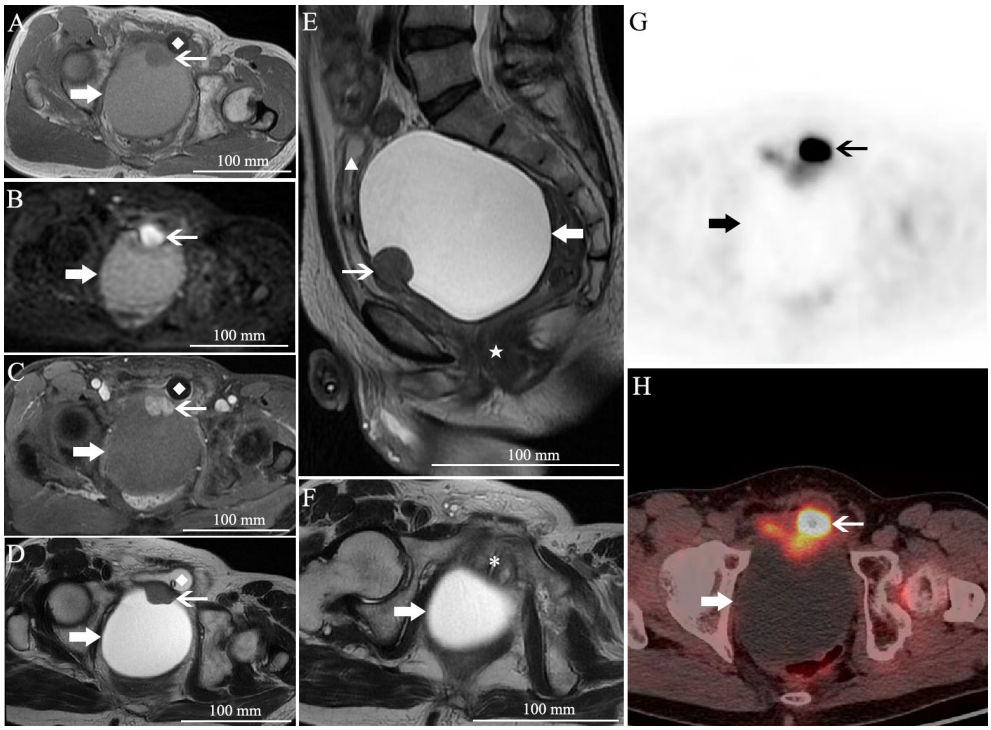

FIGURE 1
Pelvic MRI and PET/CT. **(A)** Axial T1 weighted image (WI), **(B)** axial diffusion weighted image (DWI), **(C)** axial gadolinium-enhanced fat-saturated T1WI, **(D)** axial T2WI, **(E)** sagittal T2WI, and **(F)** axial T2WI. **(G, H)** ^{18}F-FDG PET/CT. There is a giant unilocular cystic lesion measured 10.5 × 8.2 cm in size displacing the rectum (★) to the posterior, prostate (*), and bladder (▲) to the anterior. It was hyperintense on T1WI and T2WI, without diffusion restriction nor enhancement. At the anterior wall, a 2.8 × 2.1 cm solid nodule with isointensity on both T1WI and T2WI, diffusion restriction and marked enhancement, was also noted. PET/CT demonstrated an elevated SUVmax (3.5) of the solid nodule. Please note the catheter in the bladder (◆). The thick arrow, the unilocular cystic lesion; the thin arrow, the solid nodule.

However, biopsy under CT guidance was not possible due to the cystic entity and the unavoidable bladder just in front of it. Therefore, laparoscopic pelvic mass resection was performed. During exploration, the giant mass was found to be located between the bladder and rectum, and with marked adhesion to the adjacent organs. Bilateral vas deferens were not able to be detached from the tumor, thus, they were ligated. The cystic capsule was incised from the top, and the brown fluid was aspirated in order to minimize the tumor size. The inner wall of the tumor was smooth, and a solid nodule was noted on the anterior wall. While protecting the rectum from damage, the tumor was completely removed. Pathologically, the tumor is a solitary cystic mass that contains multilevel branching papillary structure, lining benign double-layer prostatic epithelial cells. Overall, the cells lining the cysts were strongly and uniformly positive for PSA and prostate specific membrane antigen (PSMA) and negative for P504S (Figure 2, Supplement). Basal cells were identified on light microscopy and with immunohistochemical staining for high-molecular weight cytokeratin CK34βE12 and p63 (Figure 2, Supplement). Prostate cystadenoma was diagnosed. The patient was discharged on post-operative day 5, and his symptoms of dysuria, hematuria, and constipation completely resolved 2 weeks after the surgery.

Discussion

Prostate cystadenoma, a benign prostatic origin tumor, usually presents as a giant multilocular cystic pelvic mass. The age varies from 14 to 80 years old among the patients reported (3, 4). Patients usually complain of symptoms related to mass effect, including lower urinary tract symptoms and defecation problems (5). The level of PSA may be not specific for diagnosis, for PSA value may be elevated or normal (4, 6). On the other hand, PSA level is not associated with tumor size or recurrence, either.

Computed tomography (CT) and MRI usually show a large multicystic mass along the midline between the bladder and rectum. The tumor can be attached to the prostate or entirely separate from the prostate in imaging (7). The septations of the multilocular cyst could be enhanced, and enhanced solid portion may be found in some cases (5). However, our case presented as a large unilocular cystic mass with a solid nodule inside, while no septations were found in the huge cyst. This manifestation of unilocular prostate cystadenoma is rarer. Although the mass located between the bladder and rectum, it was hard to confirm the origin of the mass since it was too large, and the prostate was separated from the lesion and compressed. The normal PSA also increase the difficulty of diagnosis. The diffusion restriction on DWI and elevated SUV_{max} on ^{18}F-FDG PET/CT of the solid

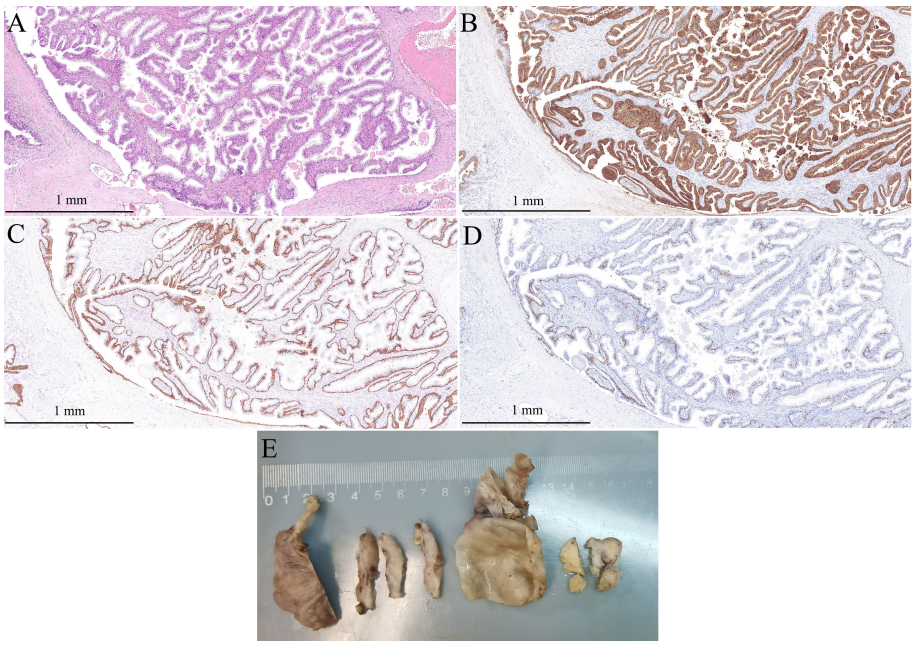

FIGURE 2
Pathological diagnosis of the mono-cystic mass. **(A)** HE staining slide shows branching papillary structure, lining benign double-layer prostatic epithelial cells (original magnification, ×100); **(B)** The cells lining the cysts were strongly and uniformly positive for PSA (original magnification, ×100); **(C)** Basal cells were immunohistochemical staining for high-molecular weight cytokeratin (34βE12) (original magnification, ×100); **(D)** Basal cells were immunohistochemical staining for p63 (original magnification, ×100); **(E)** The gross specimen.

nodule highly suspected the potential of malignancy. The final diagnosis was made according to the histopathology. The benign PSA-positive epithelial cells on immunohistochemistry analysis confirms the prostatic origin.

Before obtaining the tumor tissue for histological examination, the diagnosis of prostate cystadenoma is difficult. Radiological differential diagnoses of retroperitoneal cystic mass include Müllerian cysts, utricle cysts, and seminal vesicle cysts. It may be easier to distinguish these diseases from typical giant multilocular prostate cystadenomas, for their imaging manifestations are usually not multilocular (2, 8). However, the unilocular cyst of our case is more difficult to be distinguished from them aside from the size. The location of cystic mass between bladder and rectum, and the solid nodule in the cyst may provide considerable and critical information for identification. Other prostatic and retroperitoneal cystic lesions, including cystic change of benign prostatic hyperplasia, prostatic retention cysts, prostatic abscess, and lymphangioma and sarcoma should also be considered for differential diagnosis (5, 9).

Although prostate cystadenoma is a benign tumor, the operation choice is necessary for prognosis. The complete resection is necessary for prevention of recurrence (2, 9). However, the procedure for giant multilocular prostate cystadenomas varies from cystic debulking to pelvic exenteration in previous reports, and the choice depends on the diagnosis and suspicion of benignancy or malignancy and adjacent organ invasion (2). It is reported that gonadotropin-releasing hormone antagonist is effective for recurrence (2, 4, 10).

In conclusion, our case report adds to the recognition that prostate cystadenoma could present as both multilocular and unilocular cystic form. When a mass of single locular cyst sits in the male pelvis, the diagnosis of prostate cystadenoma could not be excluded.

Data availability statement

The original contributions presented in the study are included in the article/supplementary material. Further inquiries can be directed to the corresponding author.

Ethics statement

The studies involving human participants were reviewed and approved by the Ethics Committee of Peking Union Medical College Hospital. The patients/participants provided their written informed consent to participate in this study.

Author contributions

Manuscript writing: WW and YX; Clinical case diagnosis and treatment: WW, YX, FW, YQ, and SR; Data collection and literature resarch: WW, YX, FW, and SF; Manuscript review and revision: HS and ZJ. All authors contributed to the article and approved the submitted version.

Funding

This study was supported by the Youth Fund of National Natural Science Foundation of China (Grant No. 82001900), and CAMS Innovation Fund for Medical Sciences (2021-I2M-1-051).

Conflict of interest

The authors declare that the research was conducted in the absence of any commercial or financial relationships that could be construed as a potential conflict of interest.

Publisher's note

All claims expressed in this article are solely those of the authors and do not necessarily represent those of their affiliated organizations, or those of the publisher, the editors and the reviewers. Any product that may be evaluated in this article, or claim that may be made by its manufacturer, is not guaranteed or endorsed by the publisher.

References

1. Maluf HM, King ME, DeLuca FR, Navarro J, Talerman A, Young RH. Giant multilocular prostatic cystadenoma: a distinctive lesion of the retroperitoneum in men. a report of two cases. *Am J Surg Pathol* (1991) 15:131–5. doi: 10.1097/00000478-199102000-00005

2. Nakamura Y, Shida D, Shibayama T, Yoshida A, Matsui Y, Shinoda Y, et al. Giant multilocular prostatic cystadenoma. *World J Surg Oncol* (2019) 17:42. doi: 10.1186/s12957-019-1579-7

3. Quiring M, Berry S, Uffman J, Pinto K, Kaye J. Giant multilocular prostatic cystadenoma in a 14-Year-Old Male: A case report of a pediatric pelvic mass. *Pediatr Dev Pathol* (2022) 25(3):334–338. doi: 10.1177/10935266211073291

4. Kong JJ, Li HZ, Zheng KW. Giant multilocular prostatic cystadenoma in a 16-year-old male with difficulty in defecation: case report and literature review. *Int J Clin Exp Pathol* (2020) 13:1468–73.

5. Saadi MH, Saadi A, Charkoun M, Saadi C, Ghorbel Z, Bouafif M, et al. Prostatic cystadenoma presenting as a large multilocular pelvic male mass. *J Surg Case Rep* (2020) 2020:rjaa244. doi: 10.1093/jscr/rjaa244

6. Portugal Teixeira I, Pereira PR, Silva A, Castro M. Giant multilocular prostatic cystadenoma, a diagnosis to consider in large pelvic male masses. *Radiol Case Rep* (2019) 14:1473–7. doi: 10.1016/j.radcr.2019.09.017

7. Zeng XW, Zhu SX, Xu YP, Zheng LF, Wang ZP, Chen JC, et al. Giant dumbbell-shaped prostatic cystadenoma presenting as pelvic and scrotal mass. *J Pak Med Assoc* (2021) 71:759–62. doi: 10.47391/JPMA.1169

8. Shebel HM, Farg HM, Kolokythas O, El-Diasty T. Cysts of the lower male genitourinary tract: embryologic and anatomic considerations and differential diagnosis. *Radiographics* (2013) 33:1125–43. doi: 10.1148/rg.334125129

9. Choi TS, Lee DG, Yoo KH, Min GE. Rapid recurrence of giant multilocular prostatic cystadenoma after laparoscopic excision for primary case: A case report. *Med (Kaunas)* (2021) 57:870. doi: 10.3390/medicina57090870

10. Datta MW, Hosenpud J, Osipov V, Young RH. Giant multilocular cystadenoma of the prostate responsive to GnRH antagonists. *Urology* (2003) 61:225. doi: 10.1016/s0090-4295(02)02109-x

frontiers | Frontiers in Oncology

TYPE Original Research
PUBLISHED 02 September 2022
DOI 10.3389/fonc.2022.994456

OPEN ACCESS

EDITED BY
Xin-Wu Cui,
Huazhong University of Science and Technology, China

REVIEWED BY
Yi Dong,
Fudan University, China
Man Lu,
Sichuan Cancer Hospital, China

*CORRESPONDENCE
Lianzhong Zhang
zlz8777@zzu.edu.cn
Shaobo Duan
dustin2662@163.com

SPECIALTY SECTION
This article was submitted to Cancer Imaging and Image-directed Interventions, a section of the journal Frontiers in Oncology

RECEIVED 14 July 2022
ACCEPTED 10 August 2022
PUBLISHED 02 September 2022

CITATION
Zhang L, Qi Q, Li Q, Ren S, Liu S, Mao B, Li X, Wu Y, Yang L, Liu L, Li Y, Duan S and Zhang L (2022) Ultrasomics prediction for cytokeratin 19 expression in hepatocellular carcinoma: A multicenter study. *Front. Oncol.* 12:994456. doi: 10.3389/fonc.2022.994456

Ultrasomics prediction for cytokeratin 19 expression in hepatocellular carcinoma: A multicenter study

Linlin Zhang[1,2], Qinghua Qi[3], Qian Li[4], Shanshan Ren[1,2], Shunhua Liu[2], Bing Mao[2], Xin Li[1,2], Yuejin Wu[1,2], Lanling Yang[1,2], Luwen Liu[1,2], Yaqiong Li[2], Shaobo Duan[2,5]* and Lianzhong Zhang[1,2]*

[1]Department of Ultrasound, Henan University People's Hospital, Henan Provincial People's Hospital, Zhengzhou University People's Hospital, Zhengzhou, China, [2]Henan Engineering Technology Research Center of Ultrasonic Molecular Imaging and Nanotechnology, Henan Provincial People's Hospital, Zhengzhou, China, [3]Department of Ultrasound, First Affiliated Hospital of Zhengzhou University, Zhengzhou, China, [4]Department of Ultrasound, Henan Provincial Cancer Hospital, Zhengzhou, China, [5]Department of Health Management, Henan University People's Hospital, Henan Provincial People's Hospital, Zhengzhou University People's Hospital, Zhengzhou, China

Objective: The purpose of this study was to investigate the preoperative prediction of Cytokeratin (CK) 19 expression in patients with hepatocellular carcinoma (HCC) by machine learning-based ultrasomics.

Methods: We retrospectively analyzed 214 patients with pathologically confirmed HCC who received CK19 immunohistochemical staining. Through random stratified sampling (ratio, 8:2), patients from institutions I and II were divided into training dataset (n = 143) and test dataset (n = 36), and patients from institution III served as external validation dataset (n = 35). All gray-scale ultrasound images were preprocessed, and then the regions of interest were then manually segmented by two sonographers. A total of 1409 ultrasomics features were extracted from the original and derived images. Next, the intraclass correlation coefficient, variance threshold, mutual information, and embedded method were applied to feature dimension reduction. Finally, the clinical model, ultrasonics model, and combined model were constructed by eXtreme Gradient Boosting algorithm. Model performance was assessed by area under the receiver operating characteristic curve (AUC), sensitivity, specificity, and accuracy.

Results: A total of 12 ultrasomics signatures were used to construct the ultrasomics models. In addition, 21 clinical features were used to construct the clinical model, including gender, age, Child-Pugh classification, hepatitis B surface antigen/hepatitis C virus antibody (positive/negative), cirrhosis (yes/no), splenomegaly (yes/no), tumor location, tumor maximum diameter, tumor number, alpha-fetoprotein, alanine aminotransferase, aspartate aminotransferase, alkaline phosphatase, glutamyl-transpeptidase, albumin, total bilirubin, conjugated bilirubin, creatinine, prothrombin time, fibrinogen,

and international normalized ratio. The AUC of the ultrasomics model was 0.789 (0.621 – 0.907) and 0.787 (0.616 – 0.907) in the test and validation datasets, respectively. However, the performance of the combined model covering clinical features and ultrasomics signatures improved significantly. Additionally, the AUC (95% CI), sensitivity, specificity, and accuracy were 0.867 (0.712 – 0.957), 0.750, 0.875, 0.861, and 0.862 (0.703 – 0.955), 0.833, 0.862, and 0.857 in the test dataset and external validation dataset, respectively.

Conclusion: Ultrasomics signatures could be used to predict the expression of CK19 in HCC patients. The combination of clinical features and ultrasomics signatures showed excellent effects, which significantly improved prediction accuracy and robustness.

KEYWORDS

hepatocellular carcinoma, machine learning, radiomics, cytokeratin 19 (CK19), ultrasonography

Introduction

Hepatocellular carcinoma (HCC) is the leading primary liver cancer, which is one of the major global health challenges (1). In 2020, liver cancer ranked sixth and third in incidence rate and mortality among all malignant tumors in the world, and there were approximately 905,000 new cases and 830,000 deaths (2). With a 5-year survival rate of 18%, liver cancer has become the second most fatal tumor, just secondary to pancreatic cancer (3). Although many treatment strategies are available in clinical practice, the recurrence rate of HCC remains high, and the prognosis is generally poor (4–6). Accumulating evidence suggests that HCC is a heterogeneous tumor with a multimolecular phenotype (7, 8), and that inter- and intratumoral heterogeneity is often highly resistant to clinical interventions, leading to treatment failure (9, 10). The key factors associated with the prognosis of HCC include microvascular invasion, tumor grade, Ki67 expression, etc. (11–13). Compared with these factors, CK19 is not only a prognostic marker of HCC (14), but also a stemness-related marker (15). Tumor hepatocytes are capable of self-renewal, differentiation and proliferation, with stronger tumorigenicity and chemoresistance (16, 17). Transarterial chemoembolization and systemic chemotherapy play an important role in the treatment of HCC (4, 6). However, CK19-positive HCC patients are more likely to develop resistance to chemotherapeutic drugs, resulting in treatment failure (18). Therefore, one manifestation of HCC heterogeneity is the expression of Cytokeratin (CK) 19.

Cytokeratins are important structural components in the epithelial cell skeleton (19). In adult liver, CK8 and CK18 are expressed in mature hepatocytes, while CK7 and CK19 are expressed in cholangiocytes and hepatic progenitor cells (20). CK19 has been shown to be expressed in 4-28% of HCC patients (21–23). *In vitro* studies have confirmed that CK19-positive HCC cells are closely related to invasiveness, epithelial-mesenchymal transition, and angiogenesis (23, 24). Compared with CK19-negative HCC patients, CK19-positive patients have a poorer prognosis, their clinical manifestations are not only more prone to resistance to chemotherapeutic drugs, but also have a higher incidence of extrahepatic metastasis and vascular invasion (14, 18, 23). Due to its high invasiveness, this molecular subtype has been considered as a new subtype of HCC (16, 25). It has been found that some liver transplant patients without CK19 expression and CK19-related gene expression have a good prognosis, even if they do not meet the Milan criteria (18, 24). It has been suggested that preoperative assessment of CK19 expression may help to determine judge whether patients beyond the Milan criteria meet the condition of liver transplantation, potentially expanding the criteria for liver transplantation (26). Therefore, preoperative assessment of

Abbreviations: HCC, hepatocellular carcinoma; CK19, Cytokeratin 19; MRI, Magnetic resonance imaging; MRI, magnetic resonance imaging; HBsAg, hepatitis B surface antigen; HCV Ab, hepatitis C virus antibody; AFP, alpha-fetoprotein; DICOM, digital imaging and communications in medicine; ROI, region of interest; GLCM, gray-level cooccurrence matrix; GLSZM, gray-level size-zone matrix; GLRLM, gray-level run length matrix; GLDM, gray-level dependence matrix; NGTDM, neighboring gray-tone-difference matrix; ICC intra-class correlation coefficient; ALT, alanine aminotransferase; AST, aspartate aminotransferase; ALP, alkaline phosphatase; GGT, glutamyl-transpeptidase; TB, total bilirubin; CB, conjugated bilirubin; PT, prothrombin time; INR, international normalized ratio, AUC, area under the receiver operating characteristic curve; CI, confidence interval.

CK19 expression in HCC patients is critical for the effective development of individualized treatment strategies.

Immunohistochemical analysis of biopsy tissues is a reliable method for the clinical preoperative assessment of CK19 expression in HCC patients (27). However, tissue biopsy is expensive, and the invasive procedure may bring a series of complications, such as intra-abdominal or subcapsular bleeding, needle-path metastasis and intra-abdominal metastasis (28, 29). In addition, the sample size of biopsy tissues is small which can easily leading to missed diagnosis (30). In addition, the biopsy is not recommended as a routine test for diagnosis of HCC by the current guidelines (6, 31). Therefore, the current preoperative detection of CK19 is somewhat limited. Radiomics is a powerful tool for modern precision medicine (32). It captures high-throughput radiomics features from medical images combined with clinically relevant information to further improve the accuracy of diagnosis and prognosis prediction, since these features can provide additional information, such as tumor phenotypes and immune microenvironment (33). As one field of radiomics, ultrasomics plays an important role in the diagnosis and treatment of liver cancer (34). Mao et al. successfully classified primary and metastatic liver cancer using k-nearest neighbor, logistic regression, multilayer perceptron, random forest, and SVM algorithms based on grayscale ultrasound images (35). Based on ultrasound original radio frequency signals of HCC, Dong et al. effectively predicted MVI using sparse representation algorithm and machine learning algorithm combined with signal analysis and processing techniques (36). Ma et al. developed a radiomics model based on dynamic contrast-enhanced ultrasound (CEUS) (37). They found that the model performed well in predicting early HCC recurrence after ablation, while combining CEUS, US radiomics and clinical Combination models of factors can stratify high risk of late recurrence. The above studies demonstrate that multiple modalities of ultrasomics can successfully predict diagnosis and differential diagnosis of HCC, early recurrence and key prognostic factors. At present, some studies have successfully constructed radiomics models for predicting CK19 status based on Magnetic resonance imaging (MRI) images with good performance (38–40). However, MRI cannot be applied to some special populations, such as those with claustrophobia or metal-containing implants in their bodies. Furthermore, MRI is time-consuming and expensive, which limits its clinical application (41). Ultrasound has become one of the most common examination methods for the liver because of its non-invasive and non-radiative properties, more applicable population, repeated observation and relatively low cost (42). As a branch of radiomics, ultrasomics has been successfully applied to the accurate diagnosis of various malignant tumors, such as liver cancer, thyroid cancer and breast cancer, with good results (43–47). However, there are few reports about the prediction of CK19 expression in HCC patients based on ultrasomics method.

Therefore, this study aims to explore the value of machine learning-based ultrasomics for non-invasive prediction of CK19 expression in HCC patients, and to further evaluate the generalization ability of the prediction model using an independent external validation dataset.

Materials and methods

Study population

This retrospective study was approved by the ethics review boards of three medical institutions, Henan Provincial People's Hospital (Institution I), the First Affiliated Hospital of Zhengzhou University (Institution II), and Henan Cancer Hospital (Institution III), and the patients' informed consent was waived. From May 2019 to December 2021, clinical, pathological and imaging data of 1535 hospitalized patients from the above three medical institutions were collected, and the population was screened according to the following criteria. Inclusion criteria: (1) pathologically confirmed HCC with CK19 results; (2) performed liver ultrasound with two weeks before the surgery; (3) clinical and imaging data integrity. Exclusion criteria: (1) recurrent HCC; (2) history of radiotherapy, chemotherapy, radiofrequency ablation, or other anti-tumor therapies; (3) abdominal ultrasonography performed at other hospitals; (4) preoperative imaging and clinical examinations showing obvious metastases or concurrent malignant tumors of other natures; (5) low quality image. A total of 214 patients were finally included in this study, of which 179 patients from institution I and II were divided into training dataset (n = 143) and test dataset (n = 36) by random stratified sampling (ratio, 8:2), and 35 patients from institution III served as an independent external validation dataset. The screening and grouping flow chart of the study population is shown in Figure 1.

The indicators of the patients mainly included gender, age, hepatitis B surface antigen (HbsAg)/hepatitis C virus antibody (HCV-Ab), serum liver and kidney function indicators, coagulation function indicators, liver cirrhosis, splenomegaly, tumor location, maximum tumor diameter and tumor number. HCC specimens from all patients were pathologically examined and diagnosed according to World Health Organization criteria. In this study, all patients were divided into CK19-positive and CK19-negative groups, where CK19 positive is defined as the presence of membranous or cytoplasmic immunoreactivity in ≥5% of tumor cells (21).

Image acquisition, preprocessing and ROI segmentation

All patients fasted for more than 8 hours before abdominal ultrasonography. Preoperative ultrasonography was performed

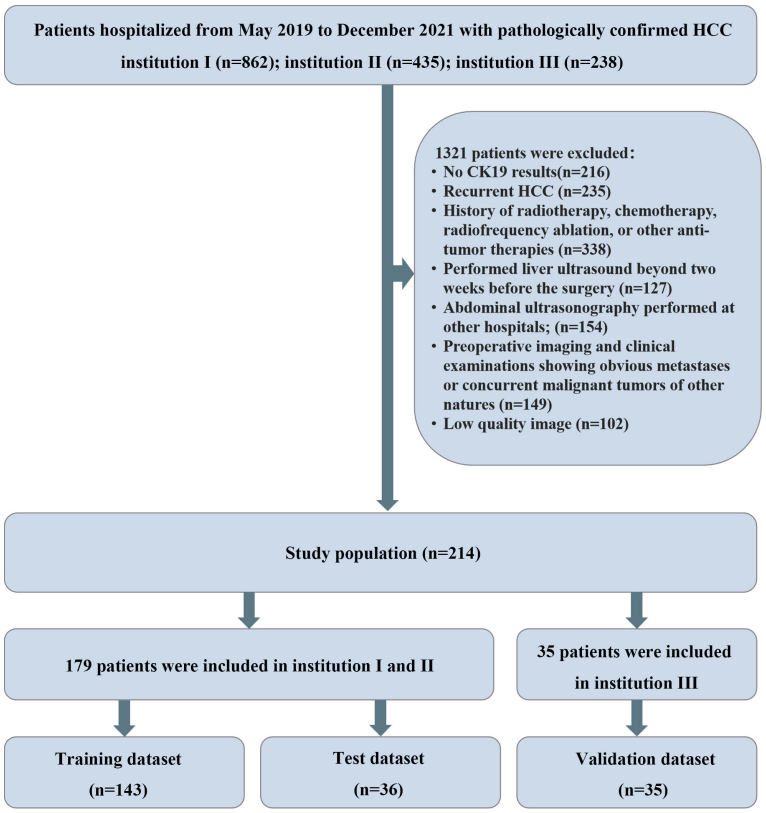

FIGURE 1
Flowchart: Cases were screened and enrolled according to the established exclusion criteria.

by sonographers with more than 10 years of experience in liver ultrasonography, and the echogenicity, lesion size, and blood flow signals of the lesions were also assessed and recorded. At least one original ultrasound image clearly showing the maximum lesion diameter and one original ultrasound image containing the measured parameters in the same section should be stored in Digital Imaging and Medicine Communication (DICOM) format, respectively. The models of ultrasound equipment used were: GE Logiq E20, GE Vivid E9, HIVISION Ascendus, HIALOK ProSound A5, Philips EPIQ 7 or Philips EPIQ 5, etc. All ultrasound probes were C75, with the frequency of 1 – 5 MHZ.

In order to eliminate differences caused by different ultrasound equipment and different operators and to ensure the comparability of the features, researchers with 6 years of experience carried out image preprocessing. To ensure the distribution of baseline features, we first used stratified sampling to divide the training dataset and test dataset for patients in institutions I and II in a ratio of 8:2. Then, we used b-spline for ultrasound images reconstructed with different voxel sizes. The images were resampled to a pixel size of 1 mm x1 mm, and gray-level discretized in the histogram with the bin width set to a fixed 25.

Region of interest (ROI) segmentation for this study was performed by a sonographer with 30 years of experience in abdominal ultrasound diagnosis (sonographer 1), and a sonographer with 10 years of experience in abdominal ultrasound diagnosis (sonographer 2). First, under the guidance of sonographer 1, sonographer 2 used ITK-SNAP software (http://www.itksnap.org) to manually segment each patient's ultrasound image along the lesion margin on the largest transverse section of the tumor. To assess the reproducibility of features, 50 cases of the ultrasound images were randomly selected for segmentation by the sonographer 2. Both sonographers were blinded to the clinical and pathological data of all patients. The flowchart of this research is shown in Figure 2. The representative lesion segmentation images are shown in Figure 3.

Ultrasomics feature extraction and screening

First, 14 filters were used to process the original image of each patient to obtain the corresponding derived images, and

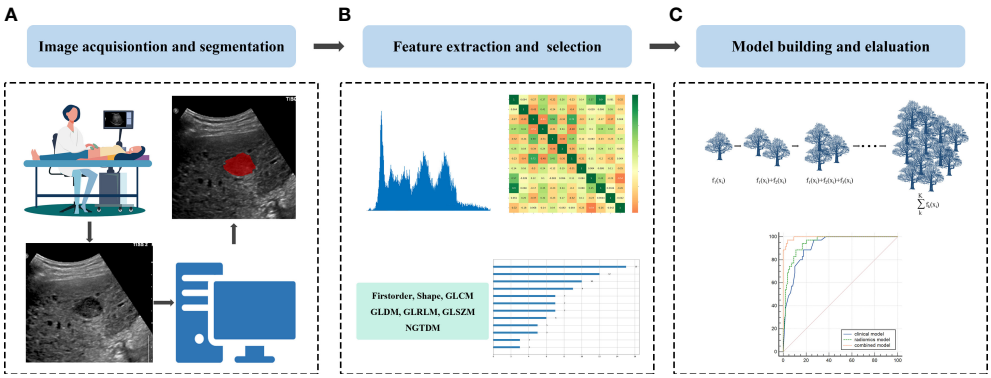

FIGURE 2
Schematic diagram of the overall study: **(A)** Image acquisition and lesion segmentation; **(B)** Feature extraction and feature selection, and **(C)** Model construction and evaluation.

then the open-source software package pyradiomics 2.1.2 was used to extract the information in all original images and derived images in high-throughput and converted them into quantitative features. Seven major radiomics features below were obtained: first order, shape, gray level co-occurrence matrix (GLCM), gray level run length matrix (GLRLM), gray level size zone matrix (GLSZM), neighboring gray tone difference matrix (NGTDM) and gray level dependence matrix (GLDM). After extracting all feature values, the missing value of each feature was filled with the median. Finally, the data were normalized (Z-score normalization) according to the mean and standard deviation to make the data conformed to a normal distribution. Details of the feature extraction methods and the filters used are provided in the Supplementary Material 1.

The optimal feature subset was selected by feature dimensionality reduction as follows: firstly, the reproducibility of the extracted features was evaluated by the intraclass correlation coefficient (ICC), where the features with ICC > 0.8 were considered to be reproducible (48); secondly, the features with variance of 0 (i.e., features that did not contribute anything to the classification) were excluded by the variance threshold; thirdly, the linear or nonlinear information relationships between each feature and the label were captured by mutual information, and the features with maximal information coefficient (MIC) of 0 were filtered. Finally, dimensionality reduction was further performed using the embedding method in combination with eXtreme Gradient Boosting (XG Boost).

Model construction and evaluation

The ultrasomics model, the clinical model and the combined model were constructed using the eXtreme Gradient Boosting (XGBoost) algorithm in combination with the learning curve and the grid search for tuning parameter, respectively. XGBoost, an efficient and widely used machine learning algorithm, incorporated regularization and parallel processing, which could reduce both overfitting and computation (49).

Firstly, the ultrasomics model was constructed using the optimal ultrasomics signatures selected above. Secondly, the clinical model was constructed by 21 clinical features, including gender, age, Child-Pugh classification, HbsAg/HBC Ab (positive/negative), cirrhosis (yes/no), splenomegaly (yes/no), tumor location, tumor maximum diameter, tumor number, and serum biochemical parameters, including alpha-fetoprotein (AFP), alanine aminotransferase (ALT), aspartate aminotransferase (AST),

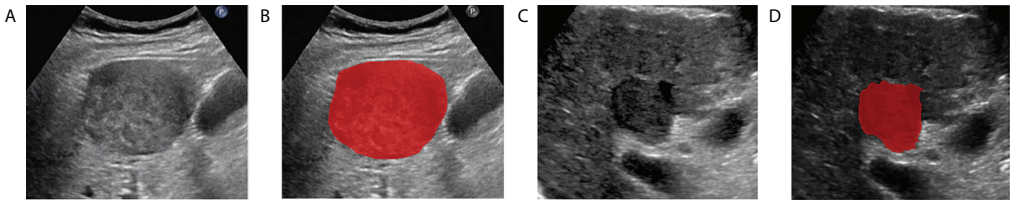

FIGURE 3
Examples of delineating regions of interest (ROI) on a grayscale ultrasound image. **(A, B)** are the CK19-positive HCC patient, **(C, D)** are the CK19-negative HCC patient.

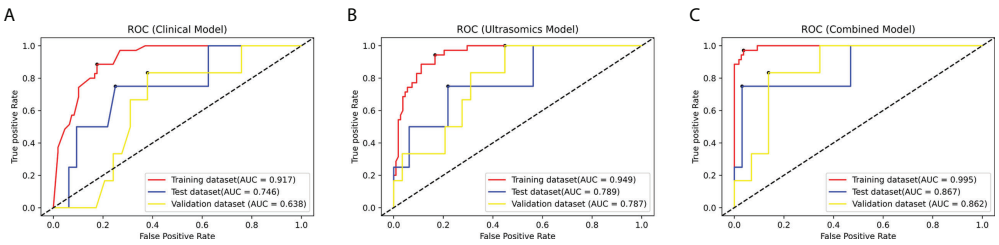

FIGURE 4
The ROC curves of the modes in the training dataset, test dataset and validation dataset: **(A)** The clinical model. **(B)** The ultrasomics model. **(C)** The combined model.

alkaline phosphatase (ALP), glutamyl-transpeptidase (GGT), albumin, total bilirubin (TB), conjugated bilirubin (CB), creatinine, prothrombin time (PT), fibrinogen, international normalized ratio (INR). Finally, the combined model was constructed based on all the above clinical features and ultrasomics signatures to explore whether the combination of the two can show better performance. Supplementary Material 2 includes details of parameter tuning for model building.

The performance of the three prediction models was assessed in the test dataset and the external validation dataset, and expressed as four indicators: area under the receiver operating characteristic curve (AUC) with 95% confidence interval (CI), accuracy, sensitivity and specificity. Model construction and evaluation were performed in the Python environment using the scikit-learn 0.23.2 package.

Statistical analysis

Statistical analysis was performed by IBM SPSS Statistics 23.0 software. The distribution of continuous variables was first determined by the Shapiro – Wilk test, expressed as mean ± standard deviation or median (25th to 75th percentile) for continuous variables. Categorical variables were expressed as frequency and relative frequency. Statistical differences between the two groups of CK19-positive and CK19-negative patients were then analyzed as described above using t-test or Mann-Whitney U test for continuous variables and chi-square test or Fisher's exact probability test for categorical variables. A value of $p < 0.05$ was considered statistically significant.

Results

Baseline characteristics of the study population

A total of 214 HCC patients were finally included in this study. Patients from institution I and II were mixed and divided into training dataset (n = 143) and test dataset (n = 36) by random stratified sampling (ratio, 8:2), and patients from institution III separately served as external validation dataset (n = 35). In the whole study cohort, CK19 negative and positive patients accounted for 78.97% (169/214) and 21.03% (45/214), respectively, and male and female patients accounted for 80.37% (172/214) and 19.63% (42/214), respectively. The baseline clinical and pathological characteristics of all patients are shown in Table 1.

Feature extraction and screening

A total of 1,409 features were extracted from the original and derived images, including first order, shape, GLCM, GLRLM, GLSZM, NGTDM and GLDM of 18, 14, 24, 16, 16, 5 and 14, respectively. All but 14 shape features were obtained from the original and derived images. Details of the features were provided in the Supplementary Material 3.

Firstly, a total of 992 features were retained according to the ICC of features. Secondly, 16 features with zero variance and 487 features with zero MIC were excluded using variance threshold and mutual information. Finally, 12 most valuable signatures were selected using the embedding method combined with XGBoost for further dimension reduction. Supplementary Figures 1, 2 showed the importance of the 12 signatures.

The performance Of ultrasomics, clinical and combined models

Three prediction models, that's ultrasomics model, clinical model and combined model, were constructed using XGBoost algorithm, respectively. The results showed that the ultrasomics signatures showed satisfactory performance in predicting CK19 expression in HCC patients, and the AUCs of the test dataset and the external validation dataset were 0.789 (95% CI, 0.621 – 0.907) and 0.787 (95% CI, 0.616 – 0.907), respectively. The AUC of the clinical model constructed based on the relevant clinical

TABLE 1 Preoperative clinical baseline characteristics of 214 patients.

Clinical characteristics	CK19- (n = 169), n (%)	CK19+ (n = 45), n (%)	*p* value
Sex			0.181
male	139 (82.25%)	33 (73.33%)	
female	30 (17.75%)	12 (26.67%)	
Age (years)	56.30 ± 11.079	55.16 ± 10.388	0.535
Child-Pugh Class			0.041
A	151 (89.35%)	35 (77.78%)	
B	18 (10.65%)	10 (22.22%)	
HbsAg/HCV Ab			0.980
positive	128 (75.74%)	34 (75.56%)	
negative	41 (24.26%)	11 (24.44%)	
Cirrhosis			0.922
Yes	140 (82.84%)	37 (82.22%)	
No	29 (17.16%)	8 (17.78%)	
Splenomegaly			0.391
Yes	78 (46.15%)	24 (53.33%)	
No	91 (53.85%)	21 (46.67%)	
AFP (ng/ml)	14.60 (4.79-280.84)	33.80 (5.64-589.68)	<0.001
ALT (U/L)	29.00 (20.15-46.9)	31.00 (21.00-48.00)	0.274
AST (U/L)	86.00 (69.00-114.00)	36.00 (25.00-49.85)	0.831
ALP (U/L)	86.00 (69.00-114.00)	88.50 (69.00-114.08)	0.283
GGT (U/L)	54.00 (30.15-103.50)	54.00 (30.00-113.50)	0.384
Albumin (g/L)	40.80 (36.90-44.40)	40.80 (36.98-44.40)	0.752
TB (umol/L)	13.2 (9.50-18.70)	13.70 (9.65-19.88)	0.070
CB (umol/L)	5.20 (3.50-7.80)	5.25 (3.70-7.80)	0.216
Creatinine (umol/L)	65.00 (56.00-76.00)	64.00 (56.00-75.25)	0.222
PT (s)	12.30 (11.40-13.20)	12.30 (11.40-13.20)	0.924
Fibrinogen (g/L)	2.44 (1.95-2.88)	2.45 (2.00-2.92)	0.108
INR	1.04 (0.98-1.11)	1.05 (0.98-1.11)	0.952
Tumor location			0.729
right lobe	139 (82.25%)	38 (84.44%)	
left lobe	30 (17.75%)	7 (15.56%)	
Maximum diameter (mm)	42.00 (28.00-67.00)	41.00 (27.00-66.25)	0.203
Tumor Number			0.208
1	136 (80.47%)	33 (73.33%)	
2	12 (7.10%)	7 (15.56%)	
>2	21 (12.43%)	5 (11.11%)	

CK19, Cytokeratin 19; AFP, alpha-fetoprotein; ALT, alanine aminotransferase; AST, aspartate aminotransferase; ALP, alkaline phosphatase; GGT, glutamyl-transpeptidase; TB, total bilirubin; CB, conjugated bilirubin; PT, prothrombin time; INR, international normalized ratio; Unless otherwise specified, data in parentheses are percentages.

characteristics was 0.746 (95% CI, 0.574 – 0.876) and 0.638 (95% CI, 0.459 – 0.793) in the test and validation datasets, respectively. However, when the clinical features and ultrasomics features were combined, the combined model achieved an excellent performance in predicting CK19 expression, and the AUC increased to 0.867 (95% CI, 0.712 – 0.957) and 0.862 (95% CI, 0.703 – 0.955), respectively. The ROC curves of all models in the three datasets are presented in Figure 4, and the detailed indicators of performance evaluation are presented in Table 2.

Discussion

HCC with positive CK19 expression is a new subtype of primary liver cancer (16, 25). In HCC, positive CK19 expression is one of the independent risk factors for prognosis, and is significantly correlated with invasion, chemotherapy drug resistance, and lymph node metastasis (14, 15, 18, 22). It has been reported that recurrence-free survival was significantly reduced in CK19-positive patients after surgical resection

TABLE 2 The performance of training dataset, test dataset and verification datase.

Dataset	Model	Accuracy (%)	Sensitivity (%)	Specificity (%)	AUC (95%CI)	*p* value
Training dataset	Clinical	82.52	88.57	80.56	0.917 (0.859-0.956)	<0.0001
	Ultrasomics	85.31	88.57	84.26	0.949 (0.899-0.979)	<0.0001
	Combined	95.80	94.29	96.30	0.995 (0.965-1.000)	<0.0001
Test dataset	Clinical	63.89	75.00	62.50	0.746 (0.574-0.876)	0.0750
	Ultrasomics	77.78	75.00	78.12	0.789 (0.621-0.907)	0.0289
	Combined	86.11	75.00	87.50	0.867 (0.712-0.957)	0.0016
Validation dataset	Clinical	62.86	83.33	58.62	0.639 (0.459-0.793)	0.2513
	Ultrasomics	71.43	66.67	72.41	0.787 (0.616-0.907)	0.0011
	Combined	85.71	83.33	86.21	0.862 (0.703-0.955)	<0.0001

AUC, area under the receiver operating characteristic curve; CI, confidence interval.

compared with CK19-negative HCC patients, with 26.1% decrease in 1-year survival, 16% decrease in 2-year survival, and 16.4% decrease in 3-year survival, which seriously affected prognosis of the patients (50). Therefore, preoperative assessment of CK19 expression in HCC patients is critical for the development of individualized treatment strategies, and improving the prognosis of patients. Preoperative immunohistochemistry is the main choice for clinical detection of CK19 (27). However, preoperative tissue biopsy may increase the risk of unwanted complications, such as abdominal or subcapsular hemorrhage, as well as needle tract metastasis (28, 29). Meanwhile, in current guidelines, biopsy is not a routine test for HCC diagnosis (6, 31). Therefore, the current preoperative detection of CK19 is somewhat limited.

Radiomics could extract a large number of macro unrecognizable, high- dimensional features through advanced data mining technology to help clinicians to further improve the accuracy of diagnosis and prognosis prediction (32). As a field of radiomics, ultrasomics plays an important role in the diagnosis and treatment of liver cancer (34). In this multicenter study, we fully mined the high-throughput information in gray-scale ultrasound images, and constructed and validated three models to predict CK19 expression in HCC patients. Firstly, we extracted a total of 1,409 ultrasomics features from the original and derived images. In order to avoid curse of dimensionality, we used ICC, variance threshold, and embedding method combined with XGBoost to reduce the dimensionality of the features, resulting in 12 optimal signatures. Then, the XGBoost algorithm combined with the learning curve and the grid search parameter adjustment method was used to train three prediction models: the ultrasound omics model, the clinical model and the combined model. The results showed that ultrasomics signatures based on machine-learning could predict and classify the expression of CK19 in HCC.As can be seen from Table 2, the combined model incorporating ultrasomics signatures and clinical factors performed excellently, with AUC improving to 0.867 (95% CI, 0.712 – 0.957) and 0.862 (95% CI, 0.703 – 0.955), respectively. In addition, in external validation dataset, the combined model not only reached an AUC of more than 0.85, but also reached an accuracy, sensitivity, and specificity of more than 80% (85.71%, 83.33%, and 86.21%, respectively), which indicated that the combined model had a more stable performance. Notably, the reproducibility of the results is one of the main limitations of radiomics in clinical application, but the current radiomics prediction studies of HCC are mostly based on a single center. On one hand, the heterogeneity of the images collected by the single center is relatively low, and the model had not been verified externally, which might be an overfitting phenomenon. On the other hand, the cases selected from multiple centers have a wide range of disease distribution and other aspects compared to a single center study. These were the reasons why we conducted a multicenter study. The results showed that model performance on the test dataset were comparable to the performance on the external validation dataset, especially the AUCs of the combined model were as high as 0.86. Therefore, the models had a reliable generalization ability.

To date, only a few scholars explored the correlation between HCC radiomics signatures and CK19 expression, mostly based on MRI (38–40). Wang et al. identified HCC patients with positive CK19 expression based on texture features of conventional MRI image sequences (38). They manually segmented lesions and extracted texture features in diffusion-weighted imaging (DWI) sequences, and then analyzed 7 conventional sequence MRI appearances, clinicopathological characteristics, and 2,415 texture features using univariate and multivariate analysis methods. Finally, serum AFP level ≥ 400 ng/mg, arterial rim enhancement, and StdSeparation 3D texture features were identified as predictive variables associated with CK19 positivity in HCC patients, and then a logistic regression prediction model was constructed using the above variables. The AUCs predicted by each of the three factors was 0.650 (95% CI, 0.533 – 0.754), 0.635 (95% CI, 0.518 – 0.741), and 0.765 (95% CI, 0.655 – 0.853), respectively. While combining the three characteristics, the prediction model performed optimally, with an AUC of 0.844 (95% CI, 0.744 – 0.916). Wang et al. developed a nomogram for the prediction of CK19 expression, which incorporates both clinico-radiological features and fused

radiomics features (39). They extracted 647 radiomics features from enhanced MRI multi-sequence images based on a machine learning algorithm, and then used the least absolute shrinkage and selection operator regression and decision tree for feature screening and model construction. Finally, in the validation dataset, the AUC of the radiomics model fused with 17 optimal signatures was 0.822 (95% CI, 0.716 – 0.928), and the AUC of the combined model incorporating clinical factors, conventional imaging features, and radiomics signatures reached 0.846 (95% CI, 0.730 – 0.963). Yang et al. developed four CK19 expression classifiers based on HCC-enhanced MRI images from three centers and compared their performance (40). They constructed predictive classifiers using four machine learning algorithms: multiple logistic regression, support vector machine, random forest, and artificial neural network algorithm (ANN), respectively, and evaluated the generality of the optimal classifier in two validation datasets. The results showed that the ANN classifier constructed from the 12 optimal features exhibited the best diagnostic performance. The AUC was 0.857, 0.726, and 0.790 in the training, validation 1, and validation 2 datasets, respectively. In this study, the AUC of the ultrasomics model and the combined model reached 0.789 (95% CI, 0.621 – 0.907) and 0.867 (95% CI, 0.712 – 0.957) in the test dataset, respectively. In addition, the two models also achieved similar performance in the external validation dataset, with AUC of 0.787 (95% CI, 0.616 – 0.907) and 0.862 (95% CI, 0.703 – 0.955), respectively. The results showed that although the gray-scale ultrasound images used in this study were not as rich as the image sequences contained in MRI, our ultrasomics model achieved similar prediction performance with the prediction model constructed by integrating multiple sequence radiomics features of MRI. This fully demonstrated that gray-scale ultrasound images included a variety of information and also had a great potential in predicting the level of tumor heterogeneity. In addition, our prediction model also showed excellent prediction performance in the independent external validation dataset, and the ultrasonography is relatively cheap, which makes the ultrasomics method a better choice for popularization.

However, this study also had some limitations. Firstly, this was a retrospective study and there might be selection bias. And the data came from three medical institutions, especially with relatively few positive samples. In the future, we hope to expand the research scope and increase the sample size. Secondly, the images used in this study were acquired by multiple ultrasound devices. Although feature extraction was preprocessed before, there might still be some device-related differences which were not eliminated. Again, this study extracted features from the largest section of the tumor only, and will include more sections in the future for in-depth study. Finally, only gray-scale ultrasound images were collected, but we hope to collect more ultrasound images with multiple parameters and modalities to further investigate CK19 expression prediction in HCC patients by ultrasomics.

In conclusion, ultrasomics signatures could be used for noninvasive prediction of CK19 expression in HCC, and the combined prediction of clinical features and optimal ultrasomics feature subset showed an excellent performance, which improved the prediction of CK19 expression in HCC significantly. Therefore, machine learning-based ultrasomics methods may be used to predict tumor heterogeneity and facilitate the development of precision medicine.

Data availability statement

The original contributions presented in the study are included in the article/Supplementary Material, further inquiries can be directed to the corresponding author.

Ethics statement

The studies involving human participants were reviewed and approved by 1. Medical Ethics Committee of Henan Provincial People's Hospital (Affiliated to Henan Provincial People's Hospital) 2. Ethics Review Committee of Scientific Research Projects of the First Affiliated Hospital of Zhengzhou University (Affiliated to the First Affiliated Hospital of Zhengzhou University) 3. Medical Ethics Committee of Henan Provincial Cancer Hospital (Affiliated to Henan Provincial Cancer Hospital. The ethics committee waived the requirement of written informed consent for participation. Written informed consent was not obtained from the individual(s) for the publication of any potentially identifiable images or data included in this article.

Author contributions

LLZ: data collection, study design, statistical analysis and interpretation, manuscript writing. QQ, QL, XL, YW, LY: data collection and management. SR: study design and manuscript review. SL, BM: data analysis, software processing. LL, YL: study design support. SD: data collection, study design, manuscript review and funding. LZZ: manuscript review and editing, study design and supervision, project management, and funding. All authors contributed to the article and approved the submitted version.

Funding

This study was sponsored by the National Key Research and Development Program of China (Grant No. 2018YFC0114606) and Henan Nature Science Foundation (Grant No. 212300410389), and Medical Science and Technology Breakthrough Plan Project of Henan Province (Grant No. LHGJ20210020).

Acknowledgments

I am appreciative to LZZ and the Henan Engineering Technology Research Center of Ultrasonic Molecular Imaging and Nanotechnology s for providing the assistance and facilities to accomplish the whole research. I also want to express my thanks to Long Yang, Ye Zhang, Shuaiyang Wang, Guoxin Deng, Simeng Wang, Xiaoxia Xu and Qiwei Cheng for their assistance in data collection.

Conflict of interest

The authors declare that the research was conducted in the absence of any commercial or financial relationships that could be construed as a potential conflict of interest.

Publisher's note

Supplementary material

The Supplementary Material for this article can be found online at: https://www.frontiersin.org/articles/10.3389/fonc.2022.994456/full#supplementary-material

References

1. Villanueva A. Hepatocellular carcinoma. *N Engl J Med* (2019) 380(15):1450–62. doi: 10.1056/NEJMra1713263

2. Sung H, Ferlay J, Siegel RL, Laversanne M, Soerjomataram I, Jemal A, et al. Global cancer statistics 2020: Globocan estimates of incidence and mortality worldwide for 36 cancers in 185 countries. *CA Cancer J Clin* (2021) 71(3):209–49. doi: 10.3322/caac.21660

3. Jemal A, Ward EM, Johnson CJ, Cronin KA, Ma J, Ryerson B, et al. Annual report to the nation on the status of cancer, 1975-2014, featuring survival. *J Natl Cancer Inst* (2017) 109(9):djx030. doi: 10.1093/jnci/djx030

4. Heimbach JK, Kulik LM, Finn RS, Sirlin CB, Abecassis MM, Roberts LR, et al. Aasld guidelines for the treatment of hepatocellular carcinoma. *Hepatology* (2018) 67(1):358–80. doi: 10.1002/hep.29086

5. European Association For The Study Of The Liver, European Organisation For R, and Treatment Of C. Easl-eortc clinical practice guidelines: Management of hepatocellular carcinoma. *J Hepatol* (2012) 56(4):908–43. doi: 10.1016/j.jhep.2011.12.001

6. Easl clinical practice guidelines: Management of hepatocellular carcinoma. *J Hepatol* (2018) 69(1):182–236. doi: 10.1016/j.jhep.2018.03.019

7. Dagogo-Jack I, Shaw AT. Tumour heterogeneity and resistance to cancer therapies. *Nat Rev Clin Oncol* (2018) 15(2):81–94. doi: 10.1038/nrclinonc.2017.166

8. Zhang Q, Lou Y, Yang J, Wang J, Feng J, Zhao Y, et al. Integrated multiomic analysis reveals comprehensive tumour heterogeneity and novel immunophenotypic classification in hepatocellular carcinomas. *Gut* (2019) 68(11):2019–31. doi: 10.1136/gutjnl-2019-318912

9. Nault JC, Galle PR, Marquardt JU. The role of molecular enrichment on future therapies in hepatocellular carcinoma. *J Hepatol* (2018) 69(1):237–47. doi: 10.1016/j.jhep.2018.02.016

10. Wang XW, Thorgeirsson SS. The biological and clinical challenge of liver cancer heterogeneity. *Hepat Oncol* (2014) 1(4):349–53. doi: 10.2217/hep.14.18

11. Erstad DJ, Tanabe KK. Prognostic and therapeutic implications of microvascular invasion in hepatocellular carcinoma. *Ann Surg Oncol* (2019) 26(5):1474–93. doi: 10.1245/s10434-019-07227-9

12. Martins-Filho SN, Paiva C, Azevedo RS, Alves VAF. Histological grading of hepatocellular carcinoma-a systematic review of literature. *Front Med (Lausanne)* (2017) 4:193. doi: 10.3389/fmed.2017.00193

13. Luo Y, Ren F, Liu Y, Shi Z, Tan Z, Xiong H, et al. Clinicopathological and prognostic significance of high ki-67 labeling index in hepatocellular carcinoma patients a meta-analysis. *Int J Clin Exp Med* (2015) 8(7):10235–47.

14. Uenishi T, Kubo S, Yamamoto T, Shuto T, Ogawa M, Tanaka H, et al. Cytokeratin 19 expression in hepatocellular carcinoma predicts early postoperative recurrence. *Cancer Sci* (2003) 94(10):851–7. doi: 10.1111/j.1349-7006.2003.tb01366.x

15. Kim H, Choi GH, Na DC, Ahn EY, Kim GI, Lee JE, et al. Human hepatocellular carcinomas with "Stemness"-related marker expression: Keratin 19 expression and a poor prognosis. *Hepatology* (2011) 54(5):1707–17. doi: 10.1002/hep.24559

16. Mishra L, Banker T, Murray J, Byers S, Thenappan A, He AR, et al. Liver stem cells and hepatocellular carcinoma. *Hepatology* (2009) 49(1):318–29. doi: 10.1002/hep.22704

17. Yin S, Li J, Hu C, Chen X, Yao M, Yan M, et al. Cd133 positive hepatocellular carcinoma cells possess high capacity for tumorigenicity. *Int J Cancer* (2007) 120(7):1444–50. doi: 10.1002/ijc.22476

18. Rhee H, Nahm JH, Kim H, Choi GH, Yoo JE, Lee HS, et al. Poor outcome of hepatocellular carcinoma with stemness marker under hypoxia: Resistance to transarterial chemoembolization. *Mod Pathol* (2016) 29(9):1038–49. doi: 10.1038/modpathol.2016.111

19. Moll R, Divo M, Langbein L. The human keratins: Biology and pathology. *Histochem Cell Biol* (2008) 129(6):705–33. doi: 10.1007/s00418-008-0435-6

20. Roskams T. Liver stem cells and their implication in hepatocellular and cholangiocarcinoma. *Oncogene* (2006) 25(27):3818–22. doi: 10.1038/sj.onc.1209558

21. Durnez A, Verslype C, Nevens F, Fevery J, Aerts R, Pirenne J, et al. The clinicopathological and prognostic relevance of cytokeratin 7 and 19 expression in hepatocellular carcinoma. A possible progenitor cell origin. *Histopathology* (2006) 49(2):138–51. doi: 10.1111/j.1365-2559.2006.02468.x

22. Tsuchiya K, Komuta M, Yasui Y, Tamaki N, Hosokawa T, Ueda K, et al. Expression of keratin 19 is related to high recurrence of hepatocellular carcinoma after radiofrequency ablation. *Oncology* (2011) 80(3-4):278–88. doi: 10.1159/000328448

23. Govaere O, Komuta M, Berkers J, Spee B, Janssen C, de Luca F, et al. Keratin 19: A key role player in the invasion of human hepatocellular carcinomas. *Gut* (2014) 63(4):674–85. doi: 10.1136/gutjnl-2012-304351

24. Kawai T, Yasuchika K, Ishii T, Katayama H, Yoshitoshi EY, Ogiso S, et al. Keratin 19, a cancer stem cell marker in human hepatocellular carcinoma. *Clin Cancer Res* (2015) 21(13):3081–91. doi: 10.1158/1078-0432.Ccr-14-1936

25. Zhuo JY, Lu D, Tan WY, Zheng SS, Shen YQ, Xu X. Ck19-positive hepatocellular carcinoma is a characteristic subtype. *J Cancer* (2020) 11(17):5069–77. doi: 10.7150/jca.44697

26. Miltiadous O, Sia D, Hoshida Y, Fiel MI, Harrington AN, Thung SN, et al. Progenitor cell markers predict outcome of patients with hepatocellular carcinoma beyond Milan criteria undergoing liver transplantation. *J Hepatol* (2015) 63(6):1368–77. doi: 10.1016/j.jhep.2015.07.025

27. Takahashi Y, Dungubat E, Kusano H, Ganbat D, Tomita Y, Odgerel S, et al. Application of immunohistochemistry in the pathological diagnosis of liver tumors. *Int J Mol Sci* (2021) 22(11):5780. doi: 10.3390/ijms22115780

28. Filingeri V, Sforza D, Tisone G. Complications and risk factors of a Large series of percutaneous liver biopsies in patients with liver transplantation or liver disease. *Eur Rev Med Pharmacol Sci* (2015) 19(9):1621–9.

29. Silva MA, Hegab B, Hyde C, Guo B, Buckels JA, Mirza DF. Needle track seeding following biopsy of liver lesions in the diagnosis of hepatocellular cancer: A systematic review and meta-analysis. *Gut* (2008) 57(11):1592–6. doi: 10.1136/gut.2008.149062

30. Robert M, Sofair AN, Thomas A, Bell B, Bialek S, Corless C, et al. A comparison of hepatopathologists' and community pathologists' review of liver biopsy specimens from patients with hepatitis c. *Clin Gastroenterol Hepatol* (2009) 7(3):335–8. doi: 10.1016/j.cgh.2008.11.029

31. Marrero JA, Kulik LM, Sirlin CB, Zhu AX, Finn RS, Abecassis MM, et al. Diagnosis, staging, and management of hepatocellular carcinoma: 2018 practice guidance by the American association for the study of liver diseases. *Hepatology* (2018) 68(2):723–50. doi: 10.1002/hep.29913

32. Lambin P, Rios-Velazquez E, Leijenaar R, Carvalho S, Stiphout RGPMV, Granton P, et al. Radiomics: Extracting more information from medical images using advanced feature analysis. *Eur J Cancer* (2012) 48(4):441–6. doi: 10.1016/j.ejca.2011.11.036

33. Lambin P, Leijenaar RTH, Deist TM, Peerlings J, de Jong EEC, van Timmeren J, et al. Radiomics: The bridge between medical imaging and personalized medicine. *Nat Rev Clin Oncol* (2017) 14(12):749–62. doi: 10.1038/nrclinonc.2017.141

34. Yin R, Jiang M, Lv WZ, Jiang F, Li J, Hu B, et al. Study processes and applications of ultrasomics in precision medicine. *Front Oncol* (2020) 10:1736. doi: 10.3389/fonc.2020.01736

35. Mao B, Ma J, Duan S, Xia Y, Tao Y, Zhang L. Preoperative classification of primary and metastatic liver cancer *Via* machine learning-based ultrasound radiomics. *Eur Radiol* (2021) 31(7):4576–86. doi: 10.1007/s00330-020-07562-6

36. Dong Y, Wang QM, Li Q, Li LY, Zhang Q, Yao Z, et al. Preoperative prediction of microvascular invasion of hepatocellular carcinoma: Radiomics algorithm based on ultrasound original radio frequency signals. *Front Oncol* (2019) 9:1203. doi: 10.3389/fonc.2019.01203

37. Ma QP, He XL, Li K, Wang JF, Zeng QJ, Xu EJ, et al. Dynamic contrast-enhanced ultrasound radiomics for hepatocellular carcinoma recurrence prediction after thermal ablation. *Mol Imaging Biol* (2021) 23(4):572–85. doi: 10.1007/s11307-021-01578-0

38. Wang HQ, Yang C, Zeng MS, Rao SX, Ji Y, Weng X, et al. Magnetic resonance texture analysis for the identification of cytokeratin 19-positive hepatocellular carcinoma. *Eur J Radiol* (2019) 117:164–70. doi: 10.1016/j.ejrad.2019.06.016

39. Wang W, Gu D, Wei J, Ding Y, Yang L, Zhu K, et al. A radiomics-based biomarker for cytokeratin 19 status of hepatocellular carcinoma with gadoxetic acid-enhanced mri. *Eur Radiol* (2020) 30(5):3004–14. doi: 10.1007/s00330-019-06585-y

40. Yang F, Wan Y, Xu L, Wu Y, Shen X, Wang J, et al. Mri-radiomics prediction for cytokeratin 19-positive hepatocellular carcinoma: A multicenter study. *Front Oncol* (2021) 11:672126. doi: 10.3389/fonc.2021.672126

41. Dyer RKJr., Nakmali D, Dormer KJ. Magnetic resonance imaging compatibility and safety of the soundtec direct system. *Laryngoscope* (2006) 116 (8):1321–33. doi: 10.1097/01.mlg.0000230479.39551.4a

42. Kim T-H, Kim SY, Tang A, Lee JM. Comparison of international guidelines for noninvasive diagnosis of hepatocellular carcinoma: 2018 update. *Clin Mol Hepatol* (2019) 25(3):245–63. doi: 10.3350/cmh.2018.0090

43. Mao B, Zhang L, Ning P, Ding F, Wu F, Lu G, et al. Preoperative prediction for pathological grade of hepatocellular carcinoma *Via* machine learning-based radiomics. *Eur Radiol* (2020) 30(12):6924–32. doi: 10.1007/s00330-020-07056-5

44. Ren S, Li Q, Liu S, Qi Q, Duan S, Mao B, et al. Clinical value of machine learning-based ultrasomics in preoperative differentiation between hepatocellular carcinoma and intrahepatic cholangiocarcinoma: A multicenter study. *Front Oncol* (2021) 11:749137. doi: 10.3389/fonc.2021.749137

45. Ren S, Qi Q, Liu S, Duan S, Mao B, Chang Z, et al. Preoperative prediction of pathological grading of hepatocellular carcinoma using machine learning-based ultrasomics: A multicenter study. *Eur J Radiol* (2021) 143:109891. doi: 10.1016/j.ejrad.2021.109891

46. Ma J, Duan S, Zhang Y, Wang J, Wang Z, Li R, et al. Efficient deep learning architecture for detection and recognition of thyroid nodules. *Comput Intell Neurosci* (2020) 2020:1242781. doi: 10.1155/2020/1242781

47. Conti A, Duggento A, Indovina I, Guerrisi M, Toschi N. Radiomics in breast cancer classification and prediction. *Semin Cancer Biol* (2021) 72:238–50. doi: 10.1016/j.semcancer.2020.04.002

48. Bektas CT, Kocak B, Yardimci AH, Turkcanoglu MH, Yucetas U, Koca SB, et al. Clear cell renal cell carcinoma: Machine learning-based quantitative computed tomography texture analysis for prediction of fuhrman nuclear grade. *Eur Radiol* (2019) 29(3):1153–63. doi: 10.1007/s00330-018-5698-2

49. Chen T, Guestrin C. (2016). Xgboost: A scalable tree boosting system, in: *Proceedings of the 22nd ACM SIGKDD International Conference on Knowledge Discovery and Data Mining*, (San Francisco, California, USA: Computing Machinery). doi: 10.1145/2939672.2939785

50. Choi SY, Kim SH, Park CK, Min JH, Lee JE, Choi YH, et al. Imaging features of gadoxetic acid-enhanced and diffusion-weighted Mr imaging for identifying cytokeratin 19-positive hepatocellular carcinoma: A retrospective observational study. *Radiology* (2018) 286(3):897–908. doi: 10.1148/radiol.2017162846

frontiers | Frontiers in Oncology

TYPE Original Research
PUBLISHED 13 September 2022
DOI 10.3389/fonc.2022.895575

OPEN ACCESS

EDITED BY
Po-Hsiang Tsui,
Chang Gung University, Taiwan

REVIEWED BY
Fatemeh Ghahremani,
Arak University of Medical Sciences, Iran
Sumit Kumar Banchhor,
National Institute of Technology Raipur, India

*CORRESPONDENCE
Can-Xu Song
569276969@qq.com

SPECIALTY SECTION
This article was submitted to Cancer Imaging and Image-directed Interventions, a section of the journal Frontiers in Oncology

RECEIVED 14 March 2022
ACCEPTED 26 August 2022
PUBLISHED 13 September 2022

CITATION
Ma J-J, Meng S, Dang S-J, Wang J-Z, Yuan Q, Yang Q and Song C-X (2022) Evaluation of a new method of calculating breast tumor volume based on automated breast ultrasound. *Front. Oncol.* 12:895575. doi: 10.3389/fonc.2022.895575

Evaluation of a new method of calculating breast tumor volume based on automated breast ultrasound

Jing-Jing Ma[1], Shan Meng[2], Sha-Jie Dang[3], Jia-Zhong Wang[4], Quan Yuan[5], Qi Yang[6] and Can-Xu Song[5]*

[1]Department of Internal Medicine, Xi'an Fifth Hospital, Xi'an, China, [2]Department of Hematology, The Second Affiliated Hospital of Xi'an Jiaotong University, Xi'an, China, [3]Department of Anesthesia, Shaanxi Provincial Cancer Hospital, Affiliated to Xi'an Jiaotong University, Xi'an, China, [4]Department of General Surgery, The Second Affiliated Hospital of Xi'an Jiaotong University, Xi'an, China, [5]Department of Ultrasound, Shaanxi Provincial Cancer Hospital, Affiliated to Xi'an Jiaotong University, Xi'an, China, [6]Department of Surgery, Shaanxi Provincial Cancer Hospital, Affiliated to Xi'an Jiaotong University, Xi'an, China

Objective: To evaluate the effectiveness and advantages of a new method for calculating breast tumor volume based on an automated breast ultrasound system (ABUS).

Methods: A total of 42 patients (18–70 years old) with breast lesions were selected for this study. The Ivenia ABUS 2.0 (General Electric Company, USA) was used, with a probe frequency of 6–15 MHz. Adobe Photoshop CS6 software was used to calculate the pixel ratio of each ABUS image, and to draw an outline of the tumor cross-section. The resulting area (in pixels) was multiplied by the pixel ratio to yield the area of the tumor cross-section. The Wilcoxon signed rank test and Bland-Altman plot were used to compare mean differences and mean values, respectively, between the two methods.

Results: There was no significant difference between the tumor volumes calculated by pixel method as compared to the traditional method ($P>0.05$). Repeated measurements of the same tumor volume were more consistent with the pixel method.

Conclusion: The new pixel method is feasible for measuring breast tumor volume and has good validity and measurement stability.

KEYWORDS

breast lesion, volume, automated breast ultrasound system, pixel method, surgery

Introduction

Breast cancer ranks first in cancer deaths among women. The latest data on global cancer burden (2020) show that breast cancer accounts for 11.7% of all new cancer cases, officially displacing lung cancer as the most prevalent cancer type worldwide (1). In China, there were 420,000 new breast cancer cases, ranking it first in the world (2). Chemotherapy is one of the most commonly prescribed treatment methods for breast cancer (3), and its effectiveness relies heavily on imaging methods to evaluate tumor volume (4).

Various methods have been used to assess tumor volume (5). Magnetic resonance imaging (MRI) has excellent soft tissue resolution, uses no radiation, and offers multi-directional and multi-sequence imaging; however, the examination is time-consuming and expensive (6). Computerized tomography (CT) examination has high spatial and density resolution (7), but uses a large radiation dose and contrast agents with negative side effects. In comparison, ultrasound examination offers the advantages of being affordable, easy to administer, and radiation-free, and is thus recognized as the preferred imaging method for breast cancer (8). It is difficult to achieve accurate measurement of dynamic and complex entities with two-dimensional ultrasound, so volumetric parameters are measured with three-dimensional ultrasound (9, 10).

Automated breast ultrasound (ABUS) is a three-dimensional ultrasound technology for breast examination (11). It uses a standardized, automated imaging system that stores image data and has good repeatability (12). Its unique advantages contribute to its important role in the diagnosis and treatment of breast tumors (13). Currently, only tumor length can be measured on the ABUS system, not cross-sectional area or volume (14). Therefore, ABUS can only estimate volume according to the ellipsoid formula using tumor length, width and height (15). It is clinically necessary to overcome this limitation to ensure accurate and stable measurement of breast tumor volumes (16). Therefore, the authors designed a new method to measure tumor volume using ABUS and evaluated its validity and measurement stability.

Materials and methods

General information

This study was approved by the ethics committee of Shaanxi Provincial Cancer Hospital (2021-137) and granted a waiver of informed consent before commencement of the study. The ABUS imaging data of 42 patients with breast tumors who underwent ABUS examination in our hospital from June 2018 to June 2021 were retrospectively analyzed. The validity and measurement stability of the pixel method were compared with those of the traditional method (length × width × height/2). Inclusion criteria: 1) female patients; 2) aged 18–70 years old; 3) with breast tumors - if there were multiple breast tumors, the one with the largest length and diameter was selected; 4) the breast tumor had a well-defined boundary; 5) the long diameter of the tumor was ≥1cm and ≤5 cm. Exclusion criteria: 1) age < 18 years old or > 70 years old; 2) breast tumor with ill-defined boundary; 3) the long diameter of breast tumor was <1cm or >5 cm.

Instrument and ABUS inspection process

The Invenia ABUS 2.0 (General Electric Company, USA) was used, with a probe frequency of 6–15 MHz, field of view of 15.3 cm, scanning length of 16.9 cm, and maximum scanning depth of 5.0 cm. The patient was instructed to lie in a supine position and breathe calmly. Preset scanning conditions were selected on the instrument according to the size of the patient's breast. Lateral, medial, and anteroposterior scans were performed bilaterally for all patients, and upper and lower scans were added for larger breasts. After the scan the images were imported into the image viewing system that comes with ABUS for 3D reconstruction, and transverse, sagittal, and coronal cross-sections were obtained.

Tumor volume measurement

ABUS imaging data of breast tumor volume was evaluated by two physicians, each using both the pixel method and the traditional method. The traditional method is to measure the length, width, and height of the tumor using the image viewing system that comes with ABUS. Using an ABUS coronal image, the length was defined as the largest diameter of the tumor and the width was defined as the largest diameter perpendicular to the length. Using an ABUS cross-section, the height was defined as the largest diameter of the tumor perpendicular to the plane of the ABUS probe on the cross-section was selected as the height (equivalent to the anteroposterior diameter of the tumor *in vivo*). The volume of the tumor was calculated by length*width*height/2. For the pixel method, first the pixel ratio was calculated according to the scale of the original image, and then the tumor was outlined in order to obtain the number of pixels in each cross-section. This process is done in Adobe Photoshop CS6 software. Tumor cross-section area was then calculated by multiplying pixel ratio by the number of pixels in each cross-section. On ABUS images, each breast tumor was divided on the coronal plane at 0.1-cm intervals. For each layer, the area was measured by pixel method, and volume was calculated by

multiplying area by height (the height of each layer was 0.1 cm). The total tumor volume was calculated as the sum of the volumes of each layer. Consistency and stability of the two methods were then compared.

Statistical methods

SPSS 26.0 software was used to perform all statistical analyses. All measurement data were expressed as mean ± SD, and Bland-Altman plots or Wilcoxon signed rank test were used to compare the mean values and differences of the two methods. $P < 0.05$ was considered statistically significant.

Results

The 42 patients studied ranged from 19 to 65 years old, with an average age of 37.3 ± 12.6 years old. Tumor lengths ranged from 1.0 to 4.9 cm with an average length of 2.17 cm.

The analysis of tumor pixels is shown in Figures 1, 2. Coronal images were imported into Adobe Photoshop CS6 software, and the area-to-pixel ratio was calculated according to the scale on the image. Figure 3 shows the mean volume of each tumor as measured by both pixel and traditional methods.

Patients' ages and tumor lengths are shown in Table 1, along with the differences in tumor volumes as measured by two physicians using both pixel and traditional methods. The mean volume of 42 lesions measured by the pixel method was 1.073 times that measured by the traditional method (standard deviation: 0.266, 95% confidence interval: 0.541–1.605). There was no significant difference in the volume measured by the pixel method as compared to that measured by the traditional method, indicating that the pixel method is feasible and effective for tumor volume measurement (signed rank test, P=0.542). The stability of the two methods was assessed by comparing the mean difference between physicians. The mean difference for the pixel method was significantly less than that of the traditional method (P<0.01).

In addition, the consistency of the two physicians' measurements was assessed using Bland-Altman analysis. As shown in Figure 4, the majority of tumor volumes measured by the pixel method were within the 95% confidence range. In contrast, more tumor volumes measured by the traditional method fell outside the 95% confidence range (shown in Figure 5), further illustrating the higher consistency of the

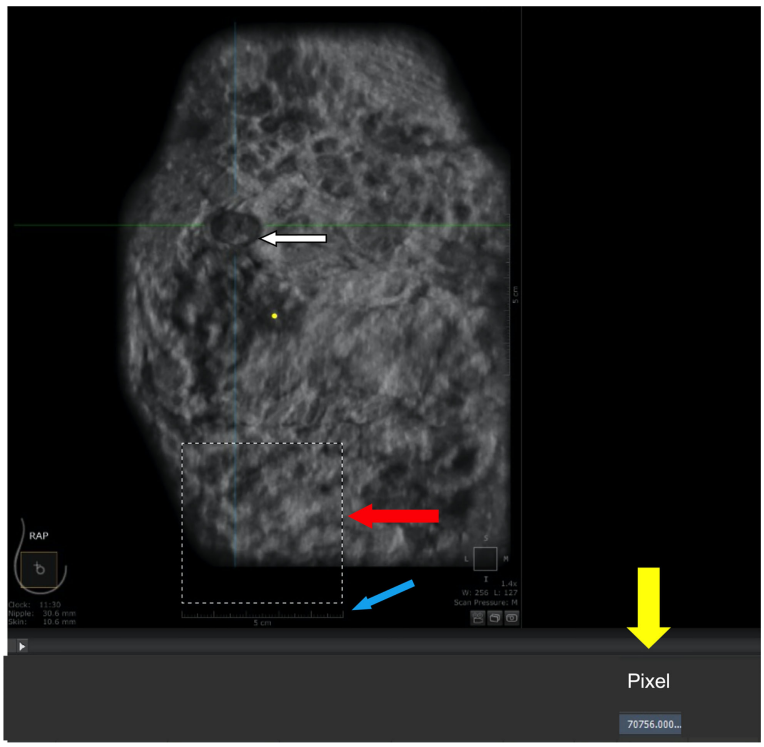

FIGURE 1
Calculation of area-to-pixel ratio using Adobe Photoshop CS6 software. **(A)** scale bar (5 cm). **(B)** square with a length of 5 cm and actual area of 25 cm^2. **(C)** number of pixels (70756) automatically counted by the software within the outlined region. **(D)** tumor.

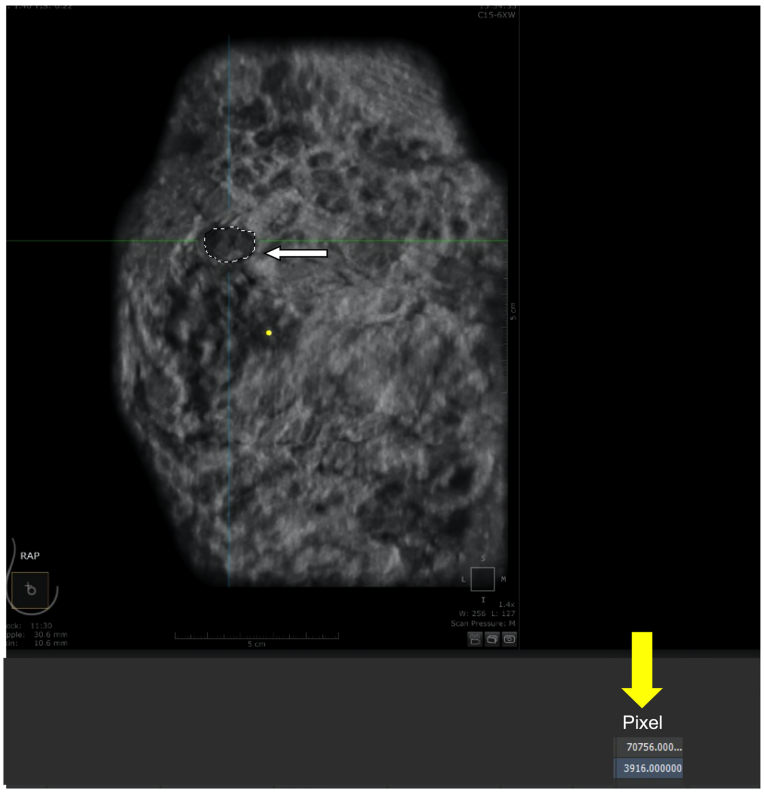

FIGURE 2
Calculation of pixels within the tumor. **(A)** tumor (outlined by white dashed line). **(B)** number of pixels (3916) automatically counted by the software within the outlined region.

pixel method. The mean and standard deviation of the difference between the measured values of the two physician based on the pixel method was smaller, and there was no statistical difference between the measured values of the two doctors (signed rank test, P=0.300). In contrast, there was a statistically significant difference between the two doctors' measurement values using the traditional method (signed rank test, P=0.001) (Table 2). These results show that the pixel method has smaller measurement errors, more stable results, and less subjective influence by physician.

Discussion

In this study, a new pixel method was developed to measure the volume of breast tumors based on ABUS imaging. The

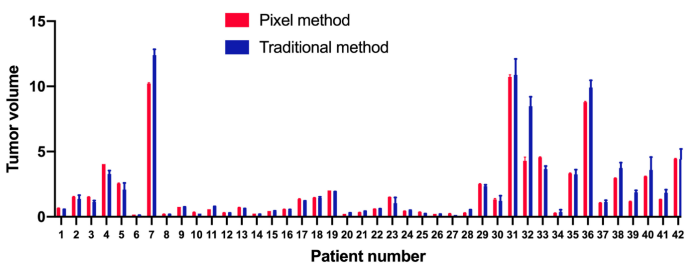

FIGURE 3
Means and standard deviations of each tumor volume as measured by pixel (red) and traditional (blue) methods.

TABLE 1 Patient age and tumor length, and difference in tumor volumes measured by two physicians using either the pixel or traditional method.

Patient number	Age	Tumor length (cm)	Tumor volume (cm^3, Pixel method)		Difference (Pixel method)	Tumor volume (cm^3, Traditional method)		Difference (Traditional method)
			Doctor1	Doctor2		Doctor1	Doctor2	
1	46	1.8	0.676	0.665	0.011	0.531	0.560	0.029
2	31	2.5	1.503	1.558	0.055	1.152	1.574	0.422
3	30	2.5	1.526	1.541	0.015	1.210	1.059	0.151
4	20	2.4	4.040	4.040	0.000	3.466	3.091	0.375
5	19	2.1	2.535	2.580	0.045	1.716	2.443	0.727
6	19	1.4	0.171	0.172	0.001	0.117	0.102	0.015
7	46	3.3	10.174	10.261	0.087	12.078	12.708	0.630
8	36	1.0	0.218	0.208	0.010	0.177	0.165	0.012
9	29	2.2	0.758	0.760	0.002	0.692	0.750	0.058
10	40	1.0	0.330	0.358	0.028	0.246	0.243	0.003
11	32	1.6	0.582	0.578	0.004	0.788	0.733	0.055
12	51	1.2	0.320	0.325	0.005	0.263	0.290	0.027
13	37	1.8	0.730	0.719	0.011	0.552	0.619	0.067
14	28	1.4	0.246	0.245	0.001	0.165	0.184	0.019
15	41	1.6	0.444	0.441	0.003	0.367	0.436	0.069
16	65	1.3	0.571	0.586	0.015	0.444	0.542	0.098
17	35	1.8	1.384	1.328	0.056	1.154	1.211	0.057
18	25	2.2	1.487	1.451	0.036	1.403	1.505	0.102
19	51	2.6	2.017	2.022	0.005	1.926	1.905	0.021
20	37	1.3	0.228	0.227	0.001	0.275	0.302	0.027
21	21	1.2	0.347	0.329	0.018	0.421	0.388	0.033
22	28	1.3	0.619	0.610	0.009	0.611	0.569	0.042
23	18	2.3	1.508	1.518	0.010	0.724	1.355	0.631
24	36	1.9	0.447	0.449	0.002	0.431	0.490	0.059
25	45	1.4	0.362	0.376	0.014	0.227	0.243	0.016
26	55	1.2	0.232	0.232	0.000	0.174	0.204	0.030
27	27	1.1	0.225	0.260	0.035	0.148	0.147	0.001
28	25	1.4	0.301	0.311	0.010	0.479	0.534	0.055
29	37	2.9	2.538	2.483	0.055	2.257	2.418	0.161
30	47	1.8	1.286	1.384	0.098	0.931	1.496	0.565
31	25	4.9	10.606	10.848	0.242	10.023	11.749	1.726
32	57	4.1	4.501	4.099	0.402	8.992	7.965	1.027
33	28	2.8	4.550	4.598	0.048	3.480	3.825	0.345
34	26	1.9	0.290	0.302	0.012	0.252	0.496	0.244
35	59	3.1	3.299	3.358	0.059	3.512	3.009	0.503
36	52	4.4	8.838	8.748	0.090	9.523	10.309	0.786
37	32	2.0	1.077	1.090	0.013	1.228	1.043	0.185
38	25	3.8	2.954	2.984	0.030	3.456	4.033	0.577
39	59	2.9	1.164	1.198	0.034	1.774	1.983	0.209
40	55	2.6	3.114	3.076	0.038	2.891	4.288	1.397
41	27	2.2	1.351	1.344	0.007	1.665	2.013	0.348
42	51	3.0	4.466	4.421	0.045	3.889	4.980	1.091

difference values were compared using the Wilcoxon signed rank test (W_-=879, W_+=24, $T_{0.01(42)}$ =247-656, P<0.01).

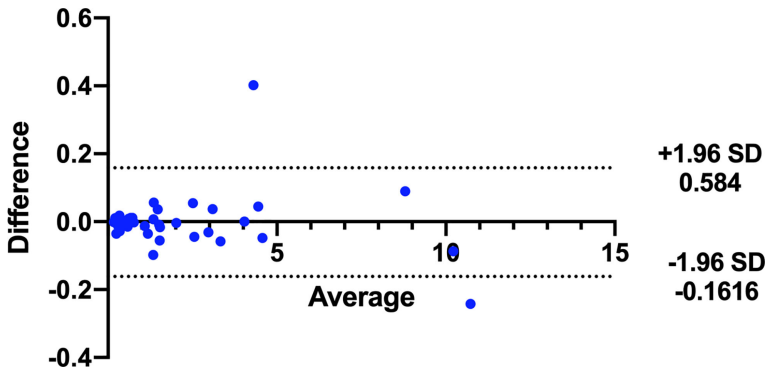

FIGURE 4
Bland-Altman analysis of tumor volumes measured by two doctors using the pixel method.

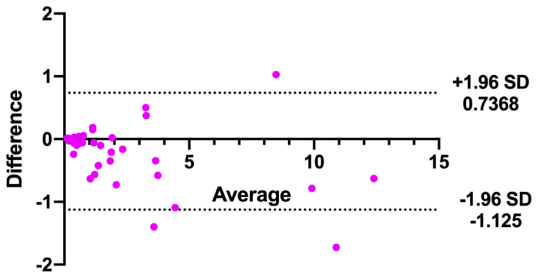

FIGURE 5
Bland-Altman analysis of tumor volumes measured by two doctors using the traditional method.

TABLE 2 Comparison between the difference of tumor volumes measured by two physicians using either the pixel or traditional method.

	Pixel method		Traditional method	
	Difference	P	Difference	P
Mean (SD)	-0.0016 (0.0816)	0.300	-0.194 (0.475)	0.001
median (Q1, Q3)	-0.002 (-0.028,0.010)		-0.058 (-0.348,0.012)	

difference values were compared using the signed rank test.

results demonstrate that compared with the traditional method, the pixel method offers less error and more stability in measuring the volume of breast tumors.

ABUS uses a standardized, automated system for the acquisition and storage of image data (13, 17). Tomographic images similar to MRI and CT can be obtained in transverse, sagittal, and coronal planes, providing sufficient information from which to calculate target volume (18, 19). However, the current ABUS system can only measure tumor length, and has not yet been used to measure cross-sectional area or volume. The present study used pixel ratios to calculate cross-sectional areas and whole-tumor volumes from ABUS images. Results indicated that tumor volumes calculated by the pixel method were slightly higher than, but not significantly different from, those calculated by the traditional method. This indicates that the performance of the pixel method is comparable to that of the traditional method. Bland-Altman analysis showed that more tumor volumes measured by the pixel method fell within the 95% confidence range as compared to those measured by the traditional method, further illustrating the higher consistency of the two physicians' measurements by the pixel method. The ultimate goal of the pixel method is to enable automated measurement of tumor volumes by a computer.

Not only does the pixel method offer smaller error and greater measurement stability, but it can also measure tumors with irregular shapes. However, one disadvantage is that the measurement time is long. In this study, the time required to

calculate the breast tumor volume of each patient was about 2-10 minutes. If the method were to be merged into existing clinical software, rather than having to import to Photoshop, then the calculation time would be significantly reduced (20). In addition, the present study only considered tumors with well-defined boundaries. Many malignant breast lesions are ill-defined, and whether the pixel method would be suitable for them requires further investigation.

In conclusion, the pixel method is feasible and effective to measure the volume of breast tumors, with small error and good stability of the measured value.

Data availability statement

The raw data supporting the conclusions of this article will be made available by the authors, without undue reservation.

Ethics statement

This study was approved by the ethics committee of Shaanxi Provincial Cancer Hospital (2021-137). The ethics committee waived the requirement of written informed consent for participation.

Author contributions

J-JM and SM contributed to the manuscript writing. S-JD and J-ZW conducted literature research and enrolled the participants. QYa and QYu contributed to the data acquisition and analysis. C-XS contributed to the study design and revised the manuscript. All authors contributed to the article and approved the submitted version. All authors agree to be accountable for all aspects of the work in ensuring that questions related to the accuracy or integrity of the work are appropriately investigated and resolved.

Funding

This work was supported by scientific research project of Shaanxi Provincial Cancer Hospital (No. SXZL-2021-001A).

Acknowledgments

We thank Medjaden Inc. for scientific editing of this manuscript.

Conflict of interest

The authors declare that the research was conducted in the absence of any commercial or financial relationships that could be construed as a potential conflict of interest.

Publisher's note

References

1. Sung H, Ferlay J, Siegel RL, Laversanne M, Soerjomataram I, Jemal A, et al. Global cancer statistics 2020: GLOBOCAN estimates of incidence and mortality worldwide for 36 cancers in 185 countries. *CA Cancer J Clin* (2021) 71:209–49. doi: 10.3322/caac.21660

2. Xia C, Dong X, Li H, Cao M, Sun D, He S, et al. Cancer statistics in China and united states, 2022: profiles, trends, and determinants. *Chin Med J (Engl)* (2022) 135:584–90. doi: 10.1097/cm9.0000000000002108

3. Alkabban FM, Ferguson T. Breast cancer. In: *StatPearls*. Treasure Island (FL: StatPearls Publishing (2021).

4. Tripathy D, Im SA, Colleoni M, Franke F, Bardia A, Harbeck N, et al. Ribociclib plus endocrine therapy for premenopausal women with hormone-receptor-positive, advanced breast cancer (MONALEESA-7): a randomised phase 3 trial. *Lancet Oncol* (2018) 19:904–15. doi: 10.1016/s1470-2045(18)30292-4

5. Youn I, Choi S, Choi YJ, Moon JH, Park HJ, Ham SY, et al. Contrast enhanced digital mammography versus magnetic resonance imaging for accurate measurement of the size of breast cancer. *Br J Radiol* (2019) 92:20180929. doi: 10.1259/bjr.20180929

6. Li H, Yao L, Jin P, Hu L, Li X, Guo T, et al. MRI And PET/CT for evaluation of the pathological response to neoadjuvant chemotherapy in breast cancer: A systematic review and meta-analysis. *Breast* (2018) 40:106–15. doi: 10.1016/j.breast.2018.04.018

7. Li J, Gao W, Yu B, Wang F, Wang L. Multi-slice spiral CT evaluation of breast cancer chemotherapy and correlation between CT results and breast cancerspecific gene 1. *J Buon* (2018) 23:378–83.

8. Dobruch-Sobczak K, Piotrzkowska-Wróblewska H, Klimonda Z, Roszkowska-Purska K, Litniewski J. Ultrasound echogenicity reveals the response of breast cancer to chemotherapy. *Clin Imaging* (2019) 55:41–6. doi: 10.1016/j.clinimag.2019.01.021

9. Vourtsis A. Three-dimensional automated breast ultrasound: Technical aspects and first results. *Diagn Interv Imaging* (2019) 100:579–92. doi: 10.1016/j.diii.2019.03.012

10. Schmachtenberg C, Fischer T, Hamm B, Bick U. Diagnostic performance of automated breast volume scanning (ABVS) compared to handheld ultrasonography with breast MRI as the gold standard. *Acad Radiol* (2017) 24:954–61. doi: 10.1016/j.acra.2017.01.021

11. Depretto C, Liguori A, Primolevo A, Di Cosimo S, Cartia F, Ferranti C, et al. Automated breast ultrasound compared to hand-held ultrasound in surveillance after breast-conserving surgery. *Tumori* (2021) 107:132–8. doi: 10.1177/0300891620930278

12. Vourtsis A, Kachulis A. The performance of 3D ABUS versus HHUS in the visualisation and BI-RADS characterisation of breast lesions in a large cohort of 1,886 women. *Eur Radiol* (2018) 28:592–601. doi: 10.1007/s00330-017-5011-9

13. Chiang TC, Huang YS, Chen RT, Huang CS, Chang RF. Tumor detection in automated breast ultrasound using 3-d CNN and prioritized candidate aggregation. *IEEE Trans Med Imaging* (2019) 38:240–9. doi: 10.1109/tmi.2018.2860257

14. Zhang P, Ma Z, Zhang Y, Chen X, Wang G. Improved inception V3 method and its effect on radiologists' performance of tumor classification with automated breast ultrasound system. *Gland Surg* (2021) 10:2232–45. doi: 10.21037/gs-21-328

15. Li Y, Wu W, Chen H, Cheng L, Wang S. 3D tumor detection in automated breast ultrasound using deep convolutional neural network. *Med Phys* (2020) 47:5669–80. doi: 10.1002/mp.14477

16. Lacson R, Goodrich ME, Harris K, Brawarsky P, Haas JS. Assessing inaccuracies in automated information extraction of breast imaging findings. *J Digit Imaging* (2017) 30:228–33. doi: 10.1007/s10278-016-9927-4

17. Lee CY, Chang TF, Chou YH, Yang KC. Fully automated lesion segmentation and visualization in automated whole breast ultrasound (ABUS) images. *Quant Imaging Med Surg* (2020) 10:568–84. doi: 10.21037/qims.2020.01.12

18. Lagendijk M, Vos EL, Ramlakhan KP, Verhoef C, Koning AHJ, van Lankeren W, et al. Breast and tumour volume measurements in breast cancer patients using 3-d automated breast volume scanner images. *World J Surg* (2018) 42:2087–93. doi: 10.1007/s00268-017-4432-6

19. Huang A, Zhu L, Tan Y, Liu J, Xiang J, Zhu Q, et al. Evaluation of automated breast volume scanner for breast conservation surgery in ductal carcinoma in situ. *Oncol Lett* (2016) 12:2481–4. doi: 10.3892/ol.2016.4924

20. Moon WK, Huang YS, Hsu CH, Chang Chien TY, Chang JM, Lee SH, et al. Computer-aided tumor detection in automated breast ultrasound using a 3-d convolutional neural network. *Comput Methods Programs BioMed* (2020) 190:105360. doi: 10.1016/j.cmpb.2020.105360

frontiers | Frontiers in Oncology

TYPE Original Research
PUBLISHED 24 October 2022
DOI 10.3389/fonc.2022.952763

OPEN ACCESS

EDITED BY
Rathan Subramaniam,
University of Otago, New Zealand

REVIEWED BY
Lei Zeng,
Second Affiliated Hospital of Nanchang University, China
Lijun Lu,
Southern Medical University, China

*CORRESPONDENCE
Roshini Kulanthaivelu
roshini.kulanthaivelu@uhn.ca

SPECIALTY SECTION
This article was submitted to Cancer Imaging and Image-directed Interventions, a section of the journal Frontiers in Oncology

RECEIVED 25 May 2022
ACCEPTED 03 October 2022
PUBLISHED 24 October 2022

CITATION
Kulanthaivelu R, Kohan A, Hinzpeter R, Liu ZA, Hope A, Huang SH, Waldron J, O'Sullivan B, Ortega C, Metser U and Veit-Haibach P (2022) Prognostic value of PET/CT and MR-based baseline radiomics among patients with non-metastatic nasopharyngeal carcinoma. *Front. Oncol.* 12:952763. doi: 10.3389/fonc.2022.952763

Prognostic value of PET/CT and MR-based baseline radiomics among patients with non-metastatic nasopharyngeal carcinoma

Roshini Kulanthaivelu[1]*, Andres Kohan[1], Ricarda Hinzpeter[1], Zhihui Amy Liu[2], Andrew Hope[3], Shao Hui Huang[3], John Waldron[3], Brian O'Sullivan[3], Claudia Ortega[1], Ur Metser[1] and Patrick Veit-Haibach[1]

[1]Joint Department of Medical Imaging, University Health Network, Mount Sinai Hospital and Women's College Hospital, University of Toronto, Toronto, ON, Canada, [2]Department of Biostatistics, Princess Margaret Cancer Centre, University Health Network, Dalla Lana School of Public Health, University of Toronto, Toronto, ON, Canada, [3]Department of Radiation Oncology, University Health Network, Mount Sinai Hospital and Women's College Hospital, University of Toronto, Toronto, ON, Canada

Purpose: Radiomics is an emerging imaging assessment technique that has shown promise in predicting survival among nasopharyngeal carcinoma (NPC) patients. Studies so far have focused on PET or MR-based radiomics independently. The aim of our study was to evaluate the prognostic value of clinical and radiomic parameters derived from both PET/CT and MR.

Methods: Retrospective evaluation of 124 NPC patients with PET/CT and radiotherapy planning MR (RP-MR). Primary tumors were segmented using dedicated software (LIFEx version 6.1) from PET, CT, contrast-enhanced T1-weighted (T1-w), and T2-weighted (T2-w) MR sequences with 376 radiomic features extracted. Summary statistics describe patient, disease, and treatment characteristics. The Kaplan–Meier (KM) method estimates overall survival (OS) and progression-free survival (PFS). Clinical factors selected based on univariable analysis and the multivariable Cox model were subsequently constructed with radiomic features added.

Results: The final models comparing clinical, clinical + RP-MR, clinical + PET/CT and clinical + RP-MR + PET/CT for OS and PFS demonstrated that combined radiomic signatures were significantly associated with improved survival prognostication (AUC 0.62 *vs* 0.81 *vs* 0.75 *vs* 0.86 at 21 months for PFS and 0.56 *vs* 0.85 *vs* 0.79 *vs* 0.96 at 24 months for OS). Clinical + RP-MR features initially outperform clinical + PET/CT for both OS and PFS (<18 months), and later in the clinical course for PFS (>42 months).

Conclusion: Our study demonstrated that PET/CT-based radiomic features may improve survival prognostication among NPC patients when combined with baseline clinical and MR-based radiomic features.

KEYWORDS

NPC, Radiomics, PET/CT, MRI, prognosis

Introduction/Background

Nasopharyngeal carcinoma (NPC) is an epithelial malignancy arising from the mucosa of the nasopharynx, and it accounts for 0.7% of all malignancies (1). NPC affects less than one person per 100,000 in North America (2), but is endemic in Southern China, the Middle East, and North Africa (2). Although the prognosis of NPC is largely good, with 5-year survival rates reaching up to 80% (3), 20%–30% of patients experience treatment failure from locoregional recurrence or distant metastasis (4).

Radiotherapy with or without concurrent chemotherapy is regarded as the standard of care for NPC, and accurate staging, including optimized imaging, is crucial for appropriate treatment stratification (5). MR assessment is performed due to superior soft tissue contrast resolution compared with CT, and ^{18}Fluoride-Fluorodeoxyglucose-Position Emission Tomography/Computed Tomography (PET/CT) is utilized to evaluate for both the presence of a primary lesion in cases of diagnostic uncertainty, and for the presence of local lymph node and distant metastatic disease. Increasing stages have been demonstrated to be associated with poorer prognosis (3, 6). However, if these patients are identified early, escalated therapy strategies can be employed.

Outside of conventional TNM staging, there is no consensus on specific prognostic biomarkers that can potentially improve survival among NPC patients (4). Various clinical factors such as EBV titer, hemoglobin, LDH, CRP, neutrophil to lymphocyte ratio, and platelet counts have been identified as factors potentially associated with poor survival (6, 7). However, the clinical utility of these parameters, outside of EBV titer (4), is limited and new tools are required to identify patients at risk of poor prognosis. In recent years, radiomics has emerged as a promising field that can potentially provide a means of improved prognostication.

Radiomics is an extension of computer-aided diagnosis and detection and relies upon the concept that "medical images contain information about disease-specific processes that are imperceptible to the human eye" (8). Images are converted to mineable data that are analyzed using computer algorithms both quantitatively in terms of the spatial distribution of signal intensities and pixel interrelationships and qualitatively in terms of differences in intensity, shape, or texture (8–10).

Multiple studies, dating as far back as 2017, have demonstrated that multiparametric MR-based radiomic parameters can be utilized to predict prognosis, progression-free survival (PFS), and recurrence in patients with advanced NPC (6, 11–19) and non-metastatic NPC (20, 21) with superior prognostic performance over TNM staging (17, 22).

Metabolic parameters derived from PET/CT have revolutionized oncological imaging (7). In terms of radiomic analysis, more recent studies have utilized radiomic features from baseline PET/CT to quantitatively characterize intra-tumoral heterogeneity and provide prognostic information among patients with NPC, with the prediction of locoregional recurrence and distant metastasis in advanced NPC (7, 23–26).

There have not, however, been any studies in the literature so far that have evaluated the combined prognostication value between radiomic signatures on both PET/CT and MR and clinical parameters among patients with NPC. The aim of this study was to therefore evaluate and compare the prognostic value of clinical data, radiomic features extracted from PET/CT and MR both separately and combined.

Materials and methods

This retrospective study was approved by the institutional review board and the need to obtain informed consent from patients was waived.

Patient selection

A total of 146 patients with pathologically confirmed NPC (Stages I–IVC) underwent staging with PET/CT between December 2012 and July 2018 at the University Hospital Network, Toronto. Of these, 130 patients had undergone MR for the purpose of radiotherapy planning (RP-MR). Six patients with stage M1 (treated with palliative intent) were excluded. Subsequently, 124 patients with curative therapeutic intent with both PET/CT and RP-MR scans were included for analysis.

Demographic details (age, sex), as well as clinical variables including ECOG, smoking history, pathology, EBER, EBV titer,

HPV, TNM staging, date of diagnosis and last follow up, treatment intent and regimen, RT dates, dose, and follow up data including local, regional, or distant failure, date, and status at last follow up were collated and are summarized in Table 1. Staging was performed according to the American Joint Committee on Cancer TNM Staging System Manual, 7th edition. Patient follow-up was measured from the date of diagnosis to the last day of follow up. Overall Survival (OS) time was defined as at the time from the date of diagnosis to the date of death or last follow-up, with PFS time defined from the date of diagnosis to the date of local, regional, or distant failure, or death/last follow-up.

TABLE 1 Population characteristics.

	n = 124
Sex (n)	
Male	84% (104)
Female	16% (20)
mean Age in years (SD)	54.8 (11.6)
Smoking History (n)	
Current	21% (26)
Ex-Smoker	26% (32)
Never	50% (62)
Unknown	3% (4)
Primary (n)*	
NPC Type 1/2	25% (31)
NPC Type 3	75% (93)
Viral State (n)	
EBER +	89% (110)
HPV +	6% (8)
Non-Viral	3% (4)
Unknown	2% (2)
mean EBV Titer (IU/ml, SD)	30,433.3 (175,831.1)
T Stage (n)‡	
1/2	43% (54)
3	31% (38)
4	26% (32)
N Stage (n)‡	
0	15% (18)
1	32% (40)
2	43% (53)
3	10% (13)
Overall Stage (n)‡	
I	7% (9)
II	13% (16)
III	46% (57)
IV	1% (1)
IVA	23% (28)
IVB	10% (13)
RT/CRT Regimen (n)	
CCRT – RT	36% (45)
CCRT + AC – IC + CCRT	64% (79)

*WHO classification ‡7th edition UICC/AJCC staging system, CCRT, concurrent chemoradiation therapy; RT, Radiation Therapy, AC, adjuvant chemotherapy; IC, induction chemotherapy.

Image acquisition

PET

Pretreatment whole-body PET/CT was acquired on a Siemens mCT40 PET/CT scanner (Siemens Healthineers, Erlangen, Germany). Patients were positioned supine with images obtained from the top of the skull to the upper thighs. Iodinated oral contrast material was administered for bowel opacification; no intravenous iodinated contrast material was used. Patients were injected with 300–400 MBq (4–5 MBq/kg) of ^{18}Fluoride-Fluorodeoxyglucose (^{18}F-FDG) after having fasted for 6 h, and PET/CT scanning was performed after approximately 60 min. Overall, five to nine bed positions were obtained, depending on patient height, with an acquisition time of 2–3 min per bed position. The CT settings were as follows: 120 kV; 3.0 mm slice width; 2.0 mm collimation; 0.8 s rotation time; and 8.4 mm feed/rotation. A PET emission scan using time of flight with scatter correction was obtained, covering the identical transverse field of view. The PET parameters were as follows: image size: 2.6 pixels; slice: 3.27; and a 5-mm full width at half-maximum (FWHM) gaussian filter type. Overall, patient data has been acquired as published by our group previously (27).

RP-MRI

All patients were examined on a 3.0T MRI scanner for radiotherapy planning (Siemens Magnetom Verio syngo MR B17, Siemens Healthineers, Erlangen, Germany). Post contrast T1-weighted (T1-w) and T2-weighted (T2-w) MR images were acquired with the following parameters: axial T1-w turbo spin-echo fat saturated images post contrast (TR 1,240 ms/TE 11 ms, ET 256 × 205, FOV 24 × 24 cm, slice thickness 3 mm) and axial T2-w turbo spin-echo fat saturated images (TR 8,290 ms, TE 117 ms, ET 22, FOV 24 × 24 cm, slice thickness 3 mm).

Radiomic feature extraction

Radiomic features were extracted using the LIFEx platform version 6.1 (IMIV/CEA, Orsay, France) (28) from axial PET, low-dose unenhanced CT (acquired as part of the PET/CT), axial fat saturated and contrast-enhanced T1-w and T2-w RP-MR Digital Imaging and Communications in Medicine (DICOM) images that had been archived in PACS (Table 1 Supplemental Material). Semi-automatic segmentation of the PET component was performed using a thresholding method, with minor manual correction as required. PET volumes of interest (VOI) were defined based on (a) background threshold; (b) threshold at 40%; and (c) threshold at 70% of the SUVmax.

Volumetric segmentation of the tumor on CT and MRI was carried out manually. Because there is no thresholding method available for the CT or MR component, the contours for the CT-derived VOI were drawn manually in a slice-by-slice fashion to cover the entire tumor. The minimal VOI included at least 64 voxels and was confirmed (by the "CheckTex" feature in the software) to make sure it created a single contiguous piece that enabled consistent textural feature calculation.

To account for the impact of different resampling schemes in MR, a fixed bin width of 128 bins, which corresponded to absolute resampling, was chosen after the initial sampling of healthy normal tissue (masseter muscle) for reference (29). Segmentation was performed by one radiologist with 7 years of experience (RK). Only primary lesions were considered in the study; lymph nodes or secondary lesions were not included. A total of 94 radiomic features were obtained from each imaging sequence.

Statistical analysis and modeling

Summary statistics were used to describe patient, disease, and treatment characteristics. The Kaplan–Meier (KM) method was used to estimate overall survival (OS) and progression-free survival (PFS).

Preprocessing of the radiomic data included removing features with more than 50% missing observations, i.e., due to too few voxels to analyze, and removing features with little variation (those with <4 unique values). The value of the 99.9 percentile was used to cap the upper extreme values for each feature. All features were standardized with a mean of zero and a standard deviation of one.

Clinical factors were selected based on statistical significance with a p-value <0.05 in the univariable analyses (UVA) to build multivariable Cox proportional hazards models for OS and PFS, respectively. Subsequently, each radiomic feature was added to the clinical model, and features with a p-value <0.01 were selected for correlation assessment to filter out highly correlated features using the *caret* (30) package in R. If the absolute pairwise correlation was higher than 0.5, then the feature with the larger mean absolute correlation was removed. The final model included both clinical variables and radiomic features. Model performance was quantified and visualized using the area under the time-dependent ROC curve (AUC) (31) calculated using leave-one-out cross-validation. All statistical analyses were conducted in R version 4.0.2 (32).

Results

Population characteristics

Out of the 124 patients analyzed, 84% (n = 104) were males, 50% (n = 62) had never smoked, and 95% (n = 118) had had previous infection by either HPV or EBV, with a mean EBV titer of 30,433.5 IU/ml. The mean age was 54.8 y (± 11.6) and the majority had stage III disease or lower (66%, n = 82) (Table 1).

The OS and PFS of our population can be seen in Figures 1, 2. The median follow up period was 50.3 months (a range of 4.5 to 88.3 months). Overall, 13 cancer-related deaths and 28 patients with relapse of their index disease were noted during the follow-up period. In both cases, most of these events (100% for OS and 96% for PFS) happened before 48 months.

Statistical analysis of prognostic factors

Univariable statistical analysis was performed for the clinical variables, as shown in Table 2. Age was found to be significant for OS, and both age and treatment regimen were found to be significant for PFS, and thus these variables were included in the final multivariable models. On top of the selected clinical variables, statistically significant radiomic features with a p-value <0.01 are shown in Table 3 for OS and Table 4 for PFS.

After filtering out highly correlated features, the final models are presented in Table 5. For OS, age (p = 0.026), PET_CONVENTIONAL_SUVbwQ1 (p = 0.009), and RP_T1_GLZLM_GLNU (p = 0.006) were significant prognostic factors, while for PFS PET DISCRETIZED SUVbwmin (0.006) and RP T1 NGLDM Busyness (p = 0.043) were significant prognostic factors.

Model performance

The performance of the following models was compared; clinical alone, clinical + PET/CT features, clinical + RP-MR, and clinical + PET/CT + RP-MR, for both OS and PFS, as shown in Figures 3, 4. In both situations, models considering clinical + PET/CT + RP-MR features outperformed those considering only clinical, clinical + PET/CT or clinical + RP-MR features (AUC 0.96 *vs* 0.56 *vs* 0.85 *vs* 0.79 at 24 months in OS and 0.86 *vs* 0.62 *vs* 0.81 *vs* 0.75 at 21 months in PFS), which suggests a synergy between PET/CT and RP-MR features. It is to be noted that in both the OS and PFS models, clinical + RP-MR features appear to initially outperform clinical + PET/CT features (AUC 0.87 *vs* 0.78 at 18 months in OS and AUC 0.82 *vs* 0.76 at 14 months in PFS). In the OS model, clinical + PET/CT outperformed clinical + RP-MR thereafter (AUC 0.89 *vs* 0.78 at 39 months), while in the PFS model, clinical + PET/CT features outperformed clinical + RP-MR features from 18 to 39 months (AUC 0.81 *vs* 0.75 at 21 months), with clinical + RP-MR outperforming those of clinical + PET/CT features from 42 months thereafter (AUC 0.76 *vs* 0.74 at 45 months).

Discussion

To the best of our knowledge, no study so far has evaluated PET/CT combined with MR-based radiomics and baseline

10.3389/fonc.2022.952763

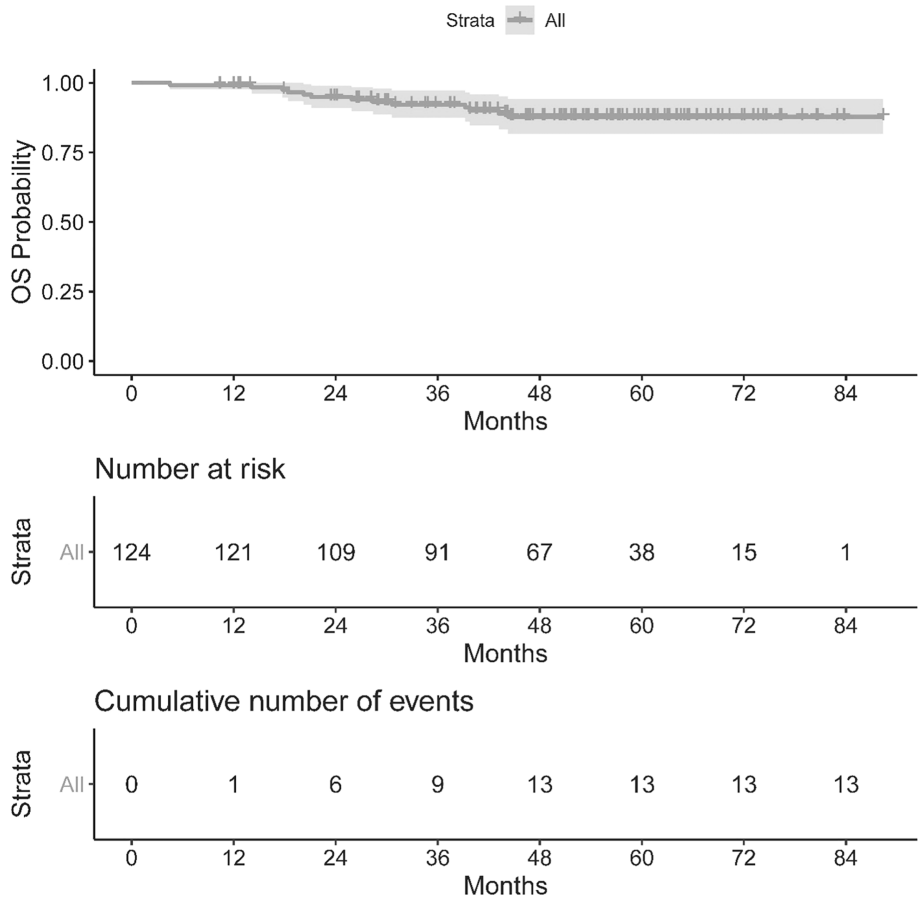

FIGURE 1
Kaplan–Meier curve for Overall Survival.

clinical parameters among patients with NPC. We identified that radiomic features from MR and PET/CT were associated with improved prediction of OS and PFS, particularly when combined (AUC of 0.96 and 0.86, respectively). Clinical + MR features initially outperformed those of Clinical + PET/CT (<18 months), with Clinical + PET/CT features then outperforming those of Clinical + RP-MR consistently in the OS model, while Clinical + RP-MR features subsequently outperformed those of Clinical + PET/CT (>42 months) in the PFS model.

Our study confirms the findings of multiple studies in the literature that have demonstrated the pre-treatment prognostic value of MR-based radiomics among patients with NPC, consistently showing that MR-based radiomics outperform clinical features alone when predicting either PFS or OS (4, 6, 11–20, 22). The AUC for clinical + RP-MR in our study was as high as 0.84 for PFS and 0.87 for OS, which is comparable with the literature where AUC varies from 0.8 (18) to 0.886 (12), and the C-index from 0.72 (19) to 0.874 (20).

A significant proportion of these studies were only performed among patients with advanced (stages III–IV), non-metastatic NPC (4, 6, 11–14), with the remainder performed among non-metastatic NPC patients of all stages, similar to our study (15, 17–20, 22).

Similar to the majority of MR-based radiomic studies, we included both contrast-enhanced T1-w and T2-w MR sequences in our study (4, 6, 11–14, 16–18, 20, 22). However, although both contrast-enhanced T1-w and T2-w MR sequences were evaluated, ultimately only radiomic features from the contrast enhanced T1-w sequences were found to be significant and included in our final OS and PFS models (RP_T1_GLZLM_GLNU, RP T1 CONVENTIONAL Skewness, and RP T1 NGLDM Busyness). This is partly different when compared to other studies which have shown that joint contrast-enhanced T1 and T2 radiomic features have a better prognostic performance than T1 or T2 features alone and may be as a result of better performing PET-based radiomic features being incorporated into our model (11, 12).

Another differentiation compared to the literature are the methods used for radiomic feature extraction (e.g., MATLAB), with only one other NPC radiomic study also using LIFEx

10.3389/fonc.2022.952763

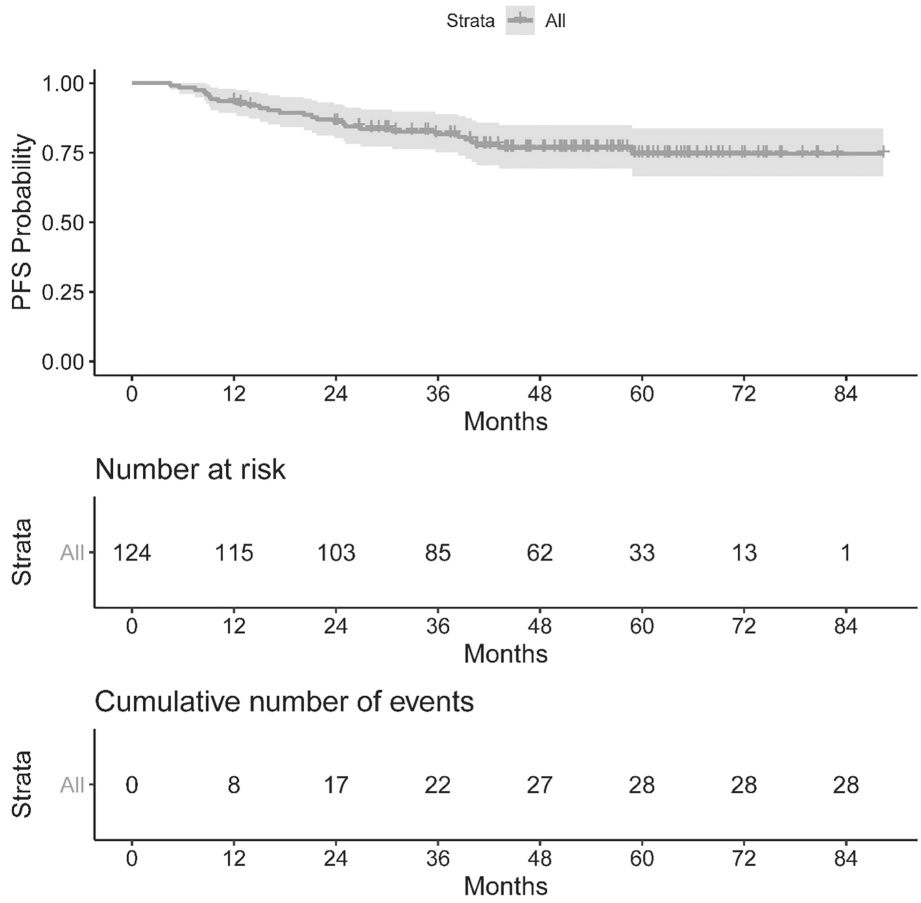

FIGURE 2
Kaplan Meier curve for Progression Free Survival.

software for radiomic feature extraction (14). Despite utilization of the same MR sequences (contrast enhanced T1-w and T2-w sequences) and radiomic extraction software, different radiomic features were found to be significant [RP_T1_GLZLM_GLNU, RP T1 CONVENTIONAL Skewness, and RP T1 NGLDM Busyness in our study, and GLCM_Energy, GLCM_Corre, and CONV_st in (14)]. This may reflect our utilization of 3.0 T fat-saturated MR sequences with different technical parameters. Similar to the majority of studies into NPC radiomics, our study evaluated radiomic parameters within the primary tumor. However, there are a number of studies that assess both the primary NPC tumor and adjacent locoregional lymph nodes, with similar findings, confirming the prognostic value of combined baseline clinical and MR-based radiomics (14, 19).

There are three studies in the literature exploring the performance of PET/CT based radiomic features among NPC patients. Similar to our study, they demonstrated that combined clinical with PET/CT features improved the prediction of PFS with a c-index of 0.77 (23), 0.69 (24), and an AUC of 0.829 (7) compared with 0.81 in our study. The study from Peng et al. only examined patients with advanced NPC (stages II–IV) (7), compared with ours and the remaining PET/CT radiomic studies. In the study by Lv et al. age was identified as a significant clinical parameter, as in our study, in addition to IgA, N, and M stage (23). Our study identified PET_CONVENTIONAL_SUVbwQ1 and PET DISCRETIZED SUVbwmin as significant PET radiomic parameters, but no PET features were retained following multivariable analysis in the study of Lv et al. (23). By comparison, other parameters like PET-NGTDM-Complexity, CT-GLGLM-LGGE, and PET-GLGLM-SGLGE were found to be significant in the study by Xu et al. (24).

Our study evaluated both the PET and the CT components of the PET/CT study, but no CT parameters were found to have significant prognostic value in our study, unlike the remaining PET/CT-based radiomic studies (7, 23, 24). We routinely evaluate the CT component in our radiomics studies since PET/CT is used clinically as a combined imaging modality. The complementary value of the CT component has previously been demonstrated in the literature (27), and if radiomics should

10.3389/fonc.2022.952763

TABLE 2 Univariable analysis of clinical variables.

Covariate	OS			PFS		
	HR (95% CI)	p-value	Global p-value	HR (95%CI)	p-value	Global p-value
Age (years)	1.05 (1.00, 1.10)		0.043	1.05 (1.01, 1.08)		0.0046
Sex			1			0.19
Female	Reference			Reference		
Male	Not estimable			2.64 (0.63, 11.11)		
ECOG PS			0.074			0.33
ECOG 0	Reference			Reference		
ECOG 1-2	2.70 (0.91, 8.04)			1.46 (0.68, 3.12)		
Smoking pack year	1.01 (0.98, 1.05)		0.38	1.01 (0.99, 1.03)		0.51
History of Smoking			0.92			0.67
Current	Reference			Reference		
Ex-smoker	1.83 (0.34, 10.01)	0.48		2.05 (0.63, 6.65)	0.23	
Non-smoker	1.40 (0.29, 6.74)	0.67		1.46 (0.48, 4.45)	0.5	
Unknown	Not estimable	1		1.91 (0.21, 17.14)	0.56	
Primary Pathology			0.55			0.97
NPC, Type 1/2 (WHO I/IIA)	Reference			Reference		
NPC: Type 3 (WHO IIB)	0.70 (0.22, 2.27)			0.98 (0.42, 2.31)		
EBER			0.37			0.095
Negative	Reference			Reference		
Positive	0.50 (0.11, 2.29)			0.44 (0.17, 1.16)		
EBV Titer pre RT	1.00 (1.00, 1.00)		0.59	1.00 (1.00, 1.00)		0.59
T stage 7th			0.46			0.43
T1–2	Reference			Reference		
T3	1.39 (0.35, 5.56)	0.64		0.63 (0.24, 1.66)	0.35	
T4	2.28 (0.61, 8.48)	0.22		1.24 (0.53, 2.91)	0.62	
N stage 7th			0.75			0.93
N0	Reference			Reference		
N1	0.43 (0.09, 2.11)	0.3		1.52 (0.42, 5.54)	0.52	
N2	0.69 (0.17, 2.78)	0.61		1.44 (0.41, 5.12)	0.57	
N3	0.46 (0.05, 4.45)	0.5		1.59 (0.32, 7.87)	0.57	
Overall Stage 7th			0.27			0.18
I-III	Reference			Reference		
IV	1.85 (0.62, 5.50)			1.67 (0.79, 3.54)		
RT/CRT Regimen			0.32			0.035
CCRT - RT	Reference			Reference		
CCRT+AC - IC+CCRT	0.58 (0.19, 1.72)			0.45 (0.21, 0.95)		

ever make it into clinical routine decision-making in the future, then the combined value of PET and CT radiomics would be beneficial per disease site.

There is currently only a single study examining the prognostic value between PET and MR in the existing literature (5), however, this only utilizes T2-w MR and PET images. Our study is the first demonstrating the improved prognostic value of combined clinical + PET/CT + MR features compared with clinical, PET/CT, or MR features individually for both OS and PFS (AUC 0.96 at 24 months in OS and 0.86 at 21 months in PFS). Since our results indicated that mainly PET and MR radiomic features seem to have a prognostic value, combined PET/MR imaging could be considered as a clinical tool for staging, prognostication, and potentially surveillance of NPC. This may offer the patient (and the hospital) improved staging logistics (one combined exam compared to PET/CT and MR separately) as well as possibly a better prognostication tool in the future.

Interestingly, clinical + RP-MR features initially outperformed clinical + PET/CT for both OS and PFS in the follow up period (<18 months), and for PFS (>42 months). Since MRI is used mostly for local staging (because of its well-documented superiority), one consideration is that the local tumor may potentially be the dominant driver and dictate short-term tumoral behavior. PET, however, may provide improved overall prognostication, representing the overall pathophysiological behavior in a better

10.3389/fonc.2022.952763

TABLE 3 Feature selection for OS.

Covariate	HR	95% CI lower BOUND	95% CI upper BOUND	p-value
PET_CONVENTIONAL_SUVbwQ1*	1.81	1.15	2.84	0.00981
PET_CONVENTIONAL_SUVbwQ2	1.83	1.17	2.86	0.00808
PET_CONVENTIONAL_TLG.mL.onlyForPETorNM.	1.72	1.15	2.59	0.00862
PET_DISCRETIZED_SUVbwQ1	1.88	1.20	2.96	0.00627
PET_DISCRETIZED_SUVbwQ2	1.82	1.17	2.85	0.00825
PET_DISCRETIZED_TLG.mL.onlyForPETorNM.	1.75	1.16	2.63	0.00781
PET40_CONVENTIONAL_TLG.mL.onlyForPETorNM.	1.77	1.18	2.64	0.00573
PET40_DISCRETIZED_TLG.mL.onlyForPETorNM.	1.80	1.20	2.71	0.00449
PET40_GLZLM_GLNU	1.76	1.18	2.62	0.00572
CT_GLZLM_ZLNU	1.69	1.13	2.53	0.00991
RP_T1_SHAPE_Volume.vx.	1.67	1.28	2.19	0.00019
RP_T1_GLRLM_LRE	1.57	1.14	2.18	0.00634
RP_T1_GLRLM_GLNU	1.83	1.38	2.43	0.00002
RP_T1_NGLDM_Busyness	1.60	1.18	2.17	0.00234
RP_T1_GLZLM_GLNU*	1.68	1.15	2.46	0.00688

*Chosen variables for the model after correlation analysis.

TABLE 4 Feature selection for PFS.

Covariate	HR	95% CI lower BOUND	95% CI upper BOUND	p-value
PET_CONVENTIONAL_SUVbwmin	1.78	1.34	2.37	0.00008
PET_CONVENTIONAL_SUVbwQ1	1.90	1.38	2.61	0.00007
PET_CONVENTIONAL_SUVbwQ2	1.71	1.23	2.38	0.00157
PET_DISCRETIZED_SUVbwmin*	1.80	1.35	2.40	0.00006
PET_DISCRETIZED_SUVbwQ1	1.94	1.40	2.67	0.00006
PET_DISCRETIZED_SUVbwQ2	1.72	1.23	2.39	0.00133
PET_GLZLM_SZLGE	0.49	0.29	0.84	0.00884
RP_T1_CONVENTIONAL_Skewness*	1.64	1.16	2.31	0.00538
RP_T1_GLRLM_GLNU	1.49	1.14	1.94	0.00393
RP_T1_NGLDM_Busyness*	1.41	1.10	1.82	0.00766

*Chosen variables for the model after correlation analysis.

TABLE 5 Final prognostic models for PFS and OS.

Final Model for OS			RT MRI Model for PFS		
Covariate	**HR (95% CI)**	**p-value**	**Covariate**	**HR (95%CI)**	**p-value**
Age	1.06 (1.01, 1.11)	0.026	Age	1.04 (1.00, 1.08)	0.06
PET CONVENTIONAL SUVbwQ1	1.92 (1.18, 3.13)	0.0092	Regimen = CCRT + AC – IC+CCRT (vs CCRT – RT)	0.63 (0.27, 1.47)	0.28
RMP T1 GLZLM GLNU	1.70 (1.16, 2.49)	0.0062	PET DISCRETIZED SUVbwmin	1.58 (1.14, 2.19)	0.0056
			RP T1 CONVENTIONAL Skewness	1.38 (0.94, 2.02)	0.097
			RP T1 NGLDM Busyness	1.31 (1.01,1.70)	0.043

way than morphological imaging procedures. Ultimately, these findings remain indeterminate and would need to be confirmed in similar studies.

Our study had some limitations, predominantly in terms of methodology. This was a retrospective study with a moderate number of patients (124) [sample sizes ranged from 85 to 737 subjects in the literature (3)], with mixed clinical stages of NPC (I–IV). Other prognostic molecular biomarkers, such as hemoglobin, LDH, neutrophil–lymphocyte ration, c-Met, ERBB3, and MTDH, were not available for inclusion in the

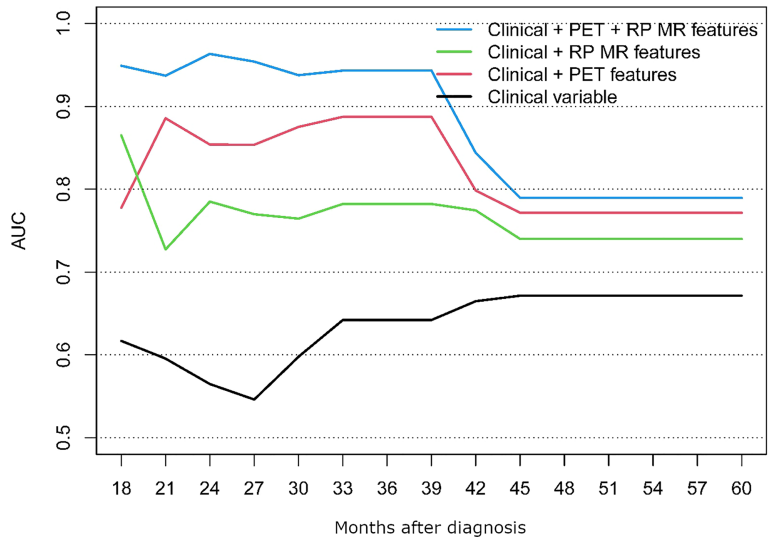

FIGURE 3
OS AUC comparison between the different prognostic models.

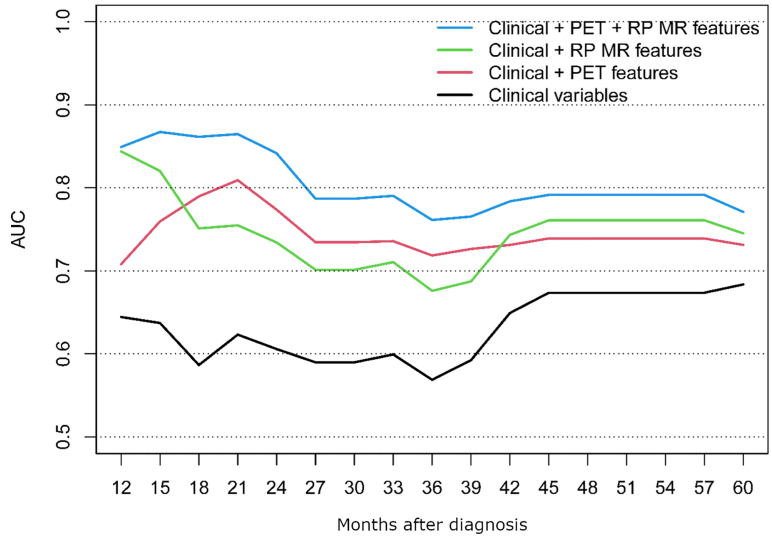

FIGURE 4
PFS AUC comparison between the different prognostic models.

study (21). These were not routinely obtained among our patient cohort, at our institution, at the time of treatment.

Although the PET/CT and RP-MR images were obtained from the same institution and scanners, maintaining uniformity in image acquisition, no image preprocessing was performed prior to segmentation. However, there is currently no general consensus available regarding whether and which image preprocessing should be performed. Some researchers are even opposed to image preprocessing since it would be prohibitive to implement clinically on a large scale. Also related to study acquisition, CT was performed without intravenous contrast, which could have contributed to its failure to produce significant radiomic features, although other studies in different cancer entities actually did find prognostic value in the CT component of PET/CT. Finally, segmentation was also only performed manually for CT and MR, without reproducibility evaluation.

Statistical methodology, in terms of feature selection and modeling, is highly variable between radiomic studies (LASSO,

RFE, univariable analysis; RS, CR, and nomogram; Chi-squared test, SFFS, and SVM). We performed a univariable analysis followed by the construction of multivariable Cox regression models into which radiomic features were then added. This approach allowed us to identify prognostic factors by using interpretable models. A major difference between our studies and those in the literature is that the majority of studies use both training and validation cohorts to assess model performance, with only one other study utilizing internal cross-validation (19). Thus, the lack of an external validation cohort is a potential limitation of our study, and therefore, future/other studies would be needed to further validate our results. Because of the absence of an independent validation cohort, this study can only be classified as explorative (19).

Conclusions

In conclusion, our study demonstrated that PET/CT-based radiomic features may improve survival prognostication when combined with baseline clinical and MR-based radiomic features among NPC patients.

Data availability statement

The raw data supporting the conclusions of this article will be made available by the authors, without undue reservation.

Ethics statement

This study was reviewed and approved by the UHN Ethics Committee. Written informed consent for participation was not required for this study in accordance with the national legislation and the institutional requirements.

Author contributions

All authors contributed to the article and approved the submitted version.

Conflict of interest

The authors declare that the research was conducted in the absence of any commercial or financial relationships that could be construed as a potential conflict of interest.

Publisher's note

All claims expressed in this article are solely those of the authors and do not necessarily represent those of their affiliated organizations, or those of the publisher, the editors and the reviewers. Any product that may be evaluated in this article, or claim that may be made by its manufacturer, is not guaranteed or endorsed by the publisher.

Supplementary material

The Supplementary Material for this article can be found online at: https://www.frontiersin.org/articles/10.3389/fonc.2022.952763/full#supplementary-material

References

1. Bray F, Ferlay J, Soerjomataram I, Siegel RL, Torre LA, Jemal A. Global cancer statistics 2018: GLOBOCAN estimates of incidence and mortality worldwide for 36 cancers in 185 countries. *CA: A Cancer J Clin* (2018) 68:394–424. doi: 10.3322/caac.21492

2. Chang ET, Ye W, Zeng YX, Adami HO. The evolving epidemiology of nasopharyngeal carcinoma. *Cancer Epidemiol Prev Biomarkers* (2021) 30:1035–47. doi: 10.1158/1055-9965.EPI-20-1702

3. Li S, Deng YQ, Zhu ZL, Hua HL, Tao ZZ. A comprehensive review on radiomics and deep learning for nasopharyngeal carcinoma imaging. *Diagn (Basel Switzerland)* (2021) 11:1523. doi: 10.3390/diagnostics11091523

4. Ouyang FS, Guo BL, Zhang B, Dong YH, Zhang L, Mo XK, et al. Exploration and validation of radiomics signature as an independent prognostic biomarker in stage III-IVb nasopharyngeal carcinoma. *Oncotarget* (2017) 8:74869–79. doi: 10.18632/oncotarget.20423

5. Feng Q, Liang J, Wang L, Niu J, Ge X, Pang P, et al. Radiomics analysis and correlation with metabolic parameters in nasopharyngeal carcinoma based on PET/MR imaging. *Front Oncol* (2020) 10:1619. doi: 10.3389/fonc.2020.01619

6. Zhang B, Tian J, Dong D, Gu D, Dong Y, Zhang L, et al. Radiomics features of multiparametric MRI as novel prognostic factors in advanced nasopharyngeal carcinoma. *Clin Cancer Res An Off J Am Assoc Cancer Res* (2017) 23:4259–69. doi: 10.1158/1078-0432.CCR-16-2910

7. Peng L, Hong X, Yuan Q, Lu L, Wang Q, Chen W. Prediction of local recurrence and distant metastasis using radiomics analysis of pretreatment nasopharyngeal [18F]FDG PET/CT images. *Ann Nucl Med* (2021) 35(4):458–68. doi: 10.1007/S12149-021-01585-9

8. van Timmeren JE, Cester D, Tanadini-Lang S, Alkadhi H, Baessler B. Radiomics in medical imaging–"how-to" guide and critical reflection. *Insights Into Imaging* (2020) 11:1–16. doi: 10.1186/s13244-020-00887-2

9. Gillies RJ, Kinahan PE, Hricak H. Radiomics: Images are more than pictures, they are data. *Radiology* (2016) 278:563–77. doi: 10.1148/radiol.2015151169

10. Rizzo S, Botta F, Raimondi S, Origgi D, Fanciullo C, Morganti AG, et al. Radiomics: The facts and the challenges of image analysis. *Eur Radiol Experimental* (2018) 2:36. doi: 10.1186/s41747-018-0068-z

11. Zhang B, He X, Ouyang F, Gu D, Dong Y, Zhang L, et al. Radiomic machine-learning classifiers for prognostic biomarkers of advanced nasopharyngeal carcinoma. *Cancer Lett* (2017) 403:21–7. doi: 10.1016/j.canlet.2017.06.004

12. Zhang B, Ouyang F, Gu D, Dong Y, Zhang L, Mo X, et al. Advanced nasopharyngeal carcinoma: pre-treatment prediction of progression based on multi-parametric MRI radiomics. *Oncotarget* (2017) 8:72457–65. doi: 10.18632/ONCOTARGET.19799

13. Zhang LL, Huang MY, Li Y, Liang JH, Gao TS, Deng B, et al. Pretreatment MRI radiomics analysis allows for reliable prediction of local recurrence in non-

metastatic T4 nasopharyngeal carcinoma. *EBioMedicine* (2019) 42:270–80. doi: 10.1016/J.EBIOM.2019.03.050

14. Yang K, Tian J, Zhang B, Li M, Xie W, Zou Y, et al. A multidimensional nomogram combining overall stage, dose volume histogram parameters and radiomics to predict progression-free survival in patients with locoregionally advanced nasopharyngeal carcinoma. *Oral Oncol* (2019) 98:85–91. doi: 10.1016/J.ORALONCOLOGY.2019.09.022

15. Ming X, Oei RW, Zhai R, Kong F, Du C, Hu C, et al. MRI-Based radiomics signature is a quantitative prognostic biomarker for nasopharyngeal carcinoma. *Sci Rep* (2019) 9:10412. doi: 10.1038/S41598-019-46985-0

16. Zhang L, Zhou H, Gu D, Tian J, Zhang B, Dong D, et al. Radiomic nomogram: Pretreatment evaluation of local recurrence in nasopharyngeal carcinoma based on MR imaging. *J Cancer* (2019) 10:4217–25. doi: 10.7150/jca.33345

17. Mao J, Fang J, Duan X, Yang Z, Cao M, Zhang F, et al. Predictive value of pretreatment MRI texture analysis in patients with primary nasopharyngeal carcinoma. *Eur Radiol* (2019) 29:4105–13. doi: 10.1007/s00330-018-5961-6

18. Du R, Lee VH, Yuan H, Lam K-O, Pang HH, Chen Y, et al. Radiomics model to predict early progression of nonmetastatic nasopharyngeal carcinoma after intensity modulation radiation therapy: A multicenter study. *Radiol: Artif Intel* (2019) 1:e180075. doi: 10.1148/ryai.2019180075

19. Bologna M, Corino V, Calareso G, Tenconi C, Alfieri S, Iacovelli NA, et al. Baseline MRI-radiomics can predict overall survival in non-endemic EBV-related nasopharyngeal carcinoma patients. *Cancers* (2020) 12:1–20. doi: 10.3390/cancers12102958

20. Shen H, Wang Y, Liu D, Lv R, Huang Y, Peng C, et al. Predicting progression-free survival using MRI-based radiomics for patients with nonmetastatic nasopharyngeal carcinoma. *Front Oncol* (2020) 10:618. doi: 10.3389/fonc.2020.00618

21. Kim MJ, Choi Y, Sung YE, Lee YS, Kim YS, Ahn KJ, et al. Early risk-assessment of patients with nasopharyngeal carcinoma: The added prognostic value of MR-based radiomics. *Trans Oncol* (2021) 14:101180. doi: 10.1016/j.tranon.2021.101180

22. Zhuo EH, Zhang WJ, Li HJ, Zhang GY, Jing BZ, Zhou J, et al. Radiomics on multi-modalities MR sequences can subtype patients with non-metastatic nasopharyngeal carcinoma (NPC) into distinct survival subgroups. *Eur Radiol* (2019) 29:5590–9. doi: 10.1007/s00330-019-06075-1

23. Lv W, Yuan Q, Wang Q, Ma J, Feng Q, Chen W, et al. Radiomics analysis of PET and CT components of PET/CT imaging integrated with clinical parameters: Application to prognosis for nasopharyngeal carcinoma. *Mol Imaging Biol* (2019) 21:954–64. doi: 10.1007/s11307-018-01304-3

24. Xu H, Lv W, Feng H, Du D, Yuan Q, Wang Q, et al. Subregional radiomics analysis of PET/CT imaging with intratumor partitioning: Application to prognosis for nasopharyngeal carcinoma. *Mol Imaging Biol* (2020) 22(5):1414–26. doi: 10.1007/s11307-019-01439-x

25. Peng H, Dong D, Fang MJ, Li L, Tang LL, Chen L, et al. Prognostic value of deep learning PET/CT-based radiomics: Potential role for future individual induction chemotherapy in advanced nasopharyngeal carcinoma. *Clin Cancer Res* (2019) 25:4271–9. doi: 10.1158/1078-0432.CCR-18-3065

26. Xie C, Du R, Ho JW, Pang HH, Chiu KW, Lee EY, et al. Effect of machine learning re-sampling techniques for imbalanced datasets in (18)F-FDG PET-based radiomics model on prognostication performance in cohorts of head and neck cancer patients. *Eur J Nucl Med Mol Imaging* (2020) 47:2826–35. doi: 10.1007/s00259-020-04756-4

27. Anconina R, Ortega C, Metser U, Liu ZA, Suzuki C, McInnis M, et al. Influence of sarcopenia, clinical data, and 2-[18F] FDG PET/CT in outcome prediction of patients with early-stage adenocarcinoma esophageal cancer. *Eur J Nucl Med Mol Imaging* (2021) 49(3):1012–20. doi: 10.1007/S00259-021-05514-W

28. Nioche C, Orlhac F, Boughdad S, Reuze S, Goya-Outi J, Robert C, et al. Lifex: A freeware for radiomic feature calculation in multimodality imaging to accelerate advances in the characterization of tumor heterogeneity. *Cancer Res* (2018) 78:4786–9. doi: 10.1158/0008-5472.CAN-18-0125

29. Goya-Outi J, Orlhac F, Calmon R, Alentorn A, Nioche C, Philippe C, et al. Computation of reliable textural indices from multimodal brain MRI: suggestions based on a study of patients with diffuse intrinsic pontine glioma. *Phys Med Biol* (2018) 63:105003. doi: 10.1088/1361-6560/aabd21

30. Kuhn M, Wing J, Weston S, Williams A, Keefer C, Engelhardt A, et al. *Caret: Classification and regression training. r package version 6.0-86.* Cambridge, MA, USA: Astrophysics Source Code Library (2020).

31. Heagerty PJ, Zheng Y. Survival model predictive accuracy and ROC curves. *Biometrics* (2005) 61:92–105. doi: 10.1111/j.0006-341X.2005.030814.x

32. Team RC. *R: A language and environment for statistical computing.* (2013). Available at:http://www.R-project.org/.

frontiers | Frontiers in Oncology

TYPE Original Research
PUBLISHED 09 November 2022
DOI 10.3389/fonc.2022.1007990

OPEN ACCESS

EDITED BY
Pilar López-Larrubia,
Spanish National Research Council (CSIC), Spain

REVIEWED BY
Shuji Isaji,
Mie University Hospital, Japan
Lukas Vrba,
University of Arizona, United States

*CORRESPONDENCE
Debiao Li
Debiao.Li@cshs.org
Sehrish Javed
Sehrish.Javed@cshs.org

†These authors have contributed equally to this work

SPECIALTY SECTION
This article was submitted to Cancer Imaging and Image-directed Interventions, a section of the journal Frontiers in Oncology

RECEIVED 31 July 2022
ACCEPTED 24 October 2022
PUBLISHED 09 November 2022

CITATION
Javed S, Qureshi TA, Gaddam S, Wang L, Azab L, Wachsman AM, Chen W, Asadpour V, Jeon CY, Wu B, Xie Y, Pandol SJ and Li D (2022) Risk prediction of pancreatic cancer using AI analysis of pancreatic subregions in computed tomography images. *Front. Oncol.* 12:1007990. doi: 10.3389/fonc.2022.1007990

Risk prediction of pancreatic cancer using AI analysis of pancreatic subregions in computed tomography images

Sehrish Javed[1*†], Touseef Ahmad Qureshi[1†], Srinivas Gaddam[2], Lixia Wang[1], Linda Azab[1], Ashley Max Wachsman[3], Wansu Chen[4], Vahid Asadpour[4], Christie Younghae Jeon[5,6], Beichien Wu[4], Yibin Xie[1], Stephen Jacob Pandol[2] and Debiao Li[1*]

[1]Biomedical Imaging Research Institute, Cedars-Sinai Medical Center, Los Angeles, CA, United States, [2]Gastroenterology, Cedars-Sinai Medical Center, Los Angeles, CA, United States, [3]Department of Radiology, Cedars-Sinai Medical Center, Los Angeles, CA, United States, [4]Department of Research and Evaluation, Southern California Kaiser Permanente Medical Center, Los Angeles, CA, United States, [5]Division of Hematology, Cedars-Sinai Medical Center, Los Angeles, CA, United States, [6]Division of Oncology, Cedars-Sinai Medical Center, Los Angeles, CA, United States

Early detection of Pancreatic Ductal Adenocarcinoma (PDAC) is complicated as PDAC remains asymptomatic until cancer advances to late stages when treatment is mostly ineffective. Stratifying the risk of developing PDAC can improve early detection as subsequent screening of high-risk individuals through specialized surveillance systems reduces the chance of misdiagnosis at the initial stage of cancer. Risk stratification is however challenging as PDAC lacks specific predictive biomarkers. Studies reported that the pancreas undergoes local morphological changes in response to underlying biological evolution associated with PDAC development. Accurate identification of these changes can help stratify the risk of PDAC. In this retrospective study, an extensive radiomic analysis of the precancerous pancreatic subregions was performed using abdominal Computed Tomography (CT) scans. The analysis was performed using 324 pancreatic subregions identified in 108 contrast-enhanced abdominal CT scans with equal proportion from healthy control, pre-diagnostic, and diagnostic groups. In a pairwise feature analysis, several textural features were found potentially predictive of PDAC. A machine learning classifier was then trained to perform risk prediction of PDAC by automatically classifying the CT scans into healthy control (low-risk) and pre-diagnostic (high-risk) classes and specifying the subregion(s) likely to develop a tumor. The proposed model was trained on CT scans from multiple phases. Whereas using 42 CT scans from the venous phase, model validation was performed which resulted in ~89.3% classification accuracy on average, with sensitivity and specificity reaching 86% and 93%, respectively, for predicting the development of PDAC (i.e., high-risk). To our knowledge, this is the first model that unveiled microlevel precancerous changes across pancreatic

subregions and quantified the risk of developing PDAC. The model demonstrated improved prediction by 3.3% in comparison to the state-of-the-art method that considers the global (whole pancreas) features for PDAC prediction.

KEYWORDS

pancreatic ductal adenocarcinoma (PDAC), pancreatic cancer, PDAC prediction, radiomics, pancreatic subregions, abdominal CT scans

Introduction

Pancreatic Ductal Adenocarcinoma (PDAC) is a lethal cancer that accounts for more than 90% of pancreatic cancer incidences (1–3). At present, PDAC is the 4th key cause of cancer-related deaths (1, 4, 5), with a high expectancy to become the 2nd most by 2030, in both males and females (4, 6, 7). The American Cancer Society anticipates 62, 210 new incidences, and 49, 830 deaths, related to PDAC for the year 2022 in the US (8). The PDAC mostly remains subclinical in the initial stages but progresses rapidly once established. Resultantly, in more than 80% of the cases, cancer has already progressed to later stages by the time of diagnosis (9–12). The negative margin (R0) resection of the PDAC promises long-term survival which is only possible when the cancer is identified at its earliest stages. Treatment, whether surgical or non-surgical, initiated at later stages of the PDAC is associated with poor survival benefits. Although the current overall five-year survival rate of PDAC is barely 11.5%, recent research suggests that detecting PDAC in the earliest stage can increase the survival rate up to 50% (1, 13, 14).

Risk prediction of the PDAC assists in improving the chances of diagnosis at an early stage as follow-up surveillance of high-risk individuals on a regular basis would allow early intervention reducing the chance of missing the initial stages of the disease (15–17). However, since the conventional predictive biomarkers of PDAC lack specificity, risk prediction is challenging. Further, signs and symptoms of pancreatic cancer are either absent or are nonspecific as these are associated with several different diseases (2, 15–18). Factors including the complex location and variability of the pancreas may underlie, in part, the difficulty with an early diagnosis with imaging.

The pancreas undergoes several morphological changes, both locally (e.g., subregional variations) and globally (alterations to the whole pancreas), during the development of PDAC (1, 2). Empirical observations associate PDAC with several preconditioning disorders that usually lead to such morphological and textural changes in the pancreas. For example, complications including IPMN pancreatic tumors (19), distal parenchymal atrophy (20), and pancreatolithiasis (intraductal calculi) (21) gradually increase the heterogeneity of the pancreatic tissue and can potentially be used as a noninvasive risk predictor. Other deformations may include shape and size variations in the pancreas that are consistently associated with ductal dilation (22) and inflammation (23) in the pancreas. However, studies reported that these alterations can be highly subtle and unique to each pancreatic subregion (the term *pancreatic subregion* and *subregion* are used interchangeably). For instance, tumor histology differs across pancreatic subregions (i.e., head, body, and tail) (24, 25) which causes spatial heterogeneity within the pancreas. Also, most of these micro-level variations are difficult to comprehend by visual assessment of abdominal imaging and require computer-based quantification.

AI is the primary choice to perform image-based extensive analysis of such minute alterations and identify potential risk predictors for disease (4, 26, 27). AI systems, as opposed to manual approaches, execute complex tasks without interruption and ensure highly accurate and precise outcomes. In the domain of automated processing and analysis of medical images, AI offers numerous techniques and tools to extract accurate measurements from different structures, identify nonlinear features, and evaluate tissue properties. For prediction modeling, radiomic analysis (28, 29), and machine and deep learning (26, 27, 30) are regarded as the most reliable and common AI approaches.

In our recently published work (31), risk prediction of PDAC was performed using AI analysis of the global features of the pancreas. However, since the morphology of the pancreas was assessed "as a whole", it remained unknown whether the identified precancerous changes (predictors) were merely the manifestation of local changes that occurred in a specific subregion (presumably where the tumor developed) or all subregions simultaneously adopted such changes.

In this extended study, we thoroughly examined the precursory changes taking place across pancreatic subregions during cancer development and characterized the pancreas that is likely to develop PDAC. A rigorous radiomic analysis of morphological and textural features of three pancreatic subregions (head, body, tail) in the pre-diagnostic abdominal CT scans was performed to identify the features potentially

predictive of cancer. Subsequently, a machine learning model was developed that performs risk prediction by automatically classifying the abdominal CT scans into the pre-diagnostic (pancreas at high-risk for cancer) and healthy control (pancreas at low risk for cancer) groups and specifying the subregion of the pancreas that is expected to develop most part of the tumor than its neighboring subregions. To our knowledge, it is the first proposed model to perform the prediction of PDAC based on the subregional analysis of the pancreas. The model remained stable throughout the analysis and outperformed our previous model. The results are promising and encouraging and further validation with a much larger dataset is warranted.

Materials

CT imaging for PDAC Diagnosis

Of many imaging modalities, CT plays an important role in the screening for early detection of PDAC. During the initial evaluation of subjects with suspected PDAC, the abdominal CT examination is the common choice to seek primary and secondary signs of cancer. Two institutes, the Cedars-Sinai Medical Center (CSMC) and the Kaiser Permanente Southern California (KPSC) in Los Angeles, collaborated in the proposed study and provided eligible CT scans for analysis. All CT scans were anonymized before transferring to the host institute CSMS. No informed consent was required as the study design is retrospective.

Datasets for the analysis

The data obtained for the study consisted of contrast-enhanced abdominal CT scans from Diagnostic, Pre diagnostic, and Healthy controls groups. The diagnostic scan belongs to the subject with biopsy confirmed PDAC and observable tumor on the CT scan. These patients do not have any history of pancreatic tumor resection. The pre-diagnostic scan was acquired for the same subject, as in the diagnostic class, 6 months to 3 years before their PDAC was diagnosed. No primary or secondary signs of PDAC were present at the time the pre-diagnostic scan was acquired. The healthy control scan was obtained for a different subject having healthy ('normal') pancreas with no history of any pancreatic disorders. The gender and age of each subject in the healthy control class and the year their scan was acquired match those of exactly one unique subject in the pre-diagnostic class to reduce instrumental and morphologic differences, respectively. No subject in the healthy control class developed PDAC within the next 36 months of their scan. The data design of the study is shown in Figure 1.

The two institutes obtained 108 CT scans from 72 subjects and were divided into Internal and External datasets. The former consists of 66 scans (22 from each of the three groups) and the latter consists of 42 scans (14 from each of the three groups) from 44 and 28 subjects at CSMC and KPSC respectively. Also, 58 scans (19 diagnostic, 17 pre-diagnostic, 22 healthy control) in the internal dataset and all 42 scans in the external dataset were venous phase images, whereas the rest of 8 scans in the internal dataset belong to multiple phases such as arterial, venous, and connecting phases. The external dataset was used for external validation of the proposed prediction model. Table 1 provides the split of both internal and external dataset.

Data reference labeling and preprocessing

For precise measurements of pancreatic features, accurate delineation of the pancreas and the subregions is a prerequisite. The anatomy of the pancreas is complex and requires considerable attention and skills during outlining the pancreas and its subregions. The general shape of the pancreas resembles a hockey stick (J-shaped) structure. On the axial view of an

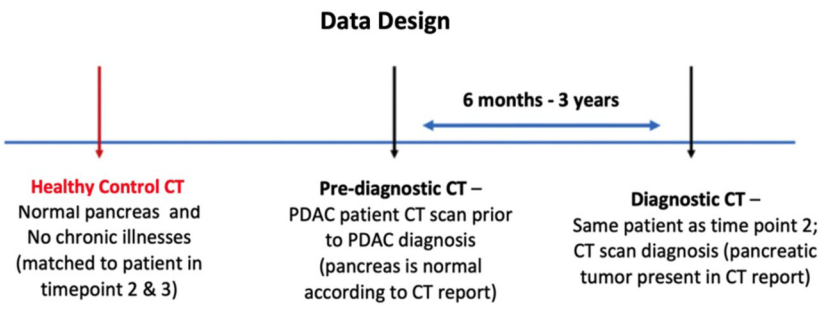

FIGURE 1
Proposed design of the data for the study. Each case in the dataset consists of three types of abdominal CT scans: Healthy control, Pre-diagnostic, and Diagnostic. The Pre-diagnostic and Diagnostic scans were obtained from the same patient.

TABLE 1 The table provides the split of the total 108 CT scans used in the study.

	Healthy Control scans	Pre-diagnostic scans	Diagnostic scans	Total scans	Number of subjects
Internal dataset	22 scans (20 Venous, 2 Arterial)	22 scans (20 Venous, 2 Arterial)	22 scans (18 Venous, 4 Arterial)	66	44
External dataset	14 Venous scans	14 Venous scans	14 Venous scans	42	28

abdominal CT, the pancreas lies across the posterior abdomen. Anatomical subregions of the pancreas consist of the head, body, and tail that appear in the left-to-right order on the axial view of the CT. The head is the expanded medial part lying at the duodenum curve and is attached to the body subregion that connects to a tapered tail subregion. The anteroposterior diameter and the length of the pancreas usually lie between 1 to 3 and 12 to 15 centimeters (32) with the head, body, and tail covering 40%, 33%, and 26% portion of the whole pancreas respectively.

Two experienced radiologists at CSMC manually outlined the boundary of the pancreas and three subregions in all 108 scans using the commercial software ITK-Snap (33). To avoid any prejudgment, findings or information attached to the scans from previous assessments were removed before labeling. A three-step labeling process was performed to ensure labeling consensus. In the first labeling phase, the two readers independently specified the boundary of the whole pancreas and subregions in all scans to limit the inter-reader variability, resulting in 85.4% labeling consistency. In the second phase, both readers were allowed to evaluate each other's labels and update their original labels which resulted in 97% labeling overlap. Lastly, the 3% labeling conflict in the updated label sets was discussed and resolved with mutual agreement of both graders.

In each diagnostic scan, the readers also specified the subregion that contained the greatest amount of pancreatic tumor. This helped grade the subregions in the corresponding pre-diagnostic scans into high-risk and low-risk classes. For instance, if most parts of the tumor were observed in the 'head' subregion of the pancreas in a diagnostic scan, then the 'head' subregion in the corresponding pre-diagnostic scan was graded as a high-risk subregion, whereas the rest of the neighboring subregions in the same pre-diagnostic scan were graded as low-risk subregions, as given in Figure 2. Multiple subregions were graded as high-risk in the same pre-diagnostic scan if the tumor was observed in more than one subregion in the corresponding diagnostic scan. Note that all subregions in the healthy control scans were graded as low-risk subregions. Moreover, from 132 subregions in 44 CT scans (22 healthy control, 22 pre-diagnostic) of the internal dataset, the grading identified a total of 66 and 44 low-risk subregions in healthy control and pre-diagnostic scans respectively, and 22 high-risk subregions in pre-diagnostic scans. For 84 subregions from 28 CT scans (14 healthy control, 14 pre-diagnostic) of the external dataset, the grading identified 42 and 28 low-risk subregions in healthy control and pre-diagnostic scans respectively, and 14 high-risk subregions in pre-diagnostic scans. Furthermore, the pancreas 'as a whole' was graded as low-risk and high-risk in healthy control and pre-diagnostic groups respectively.

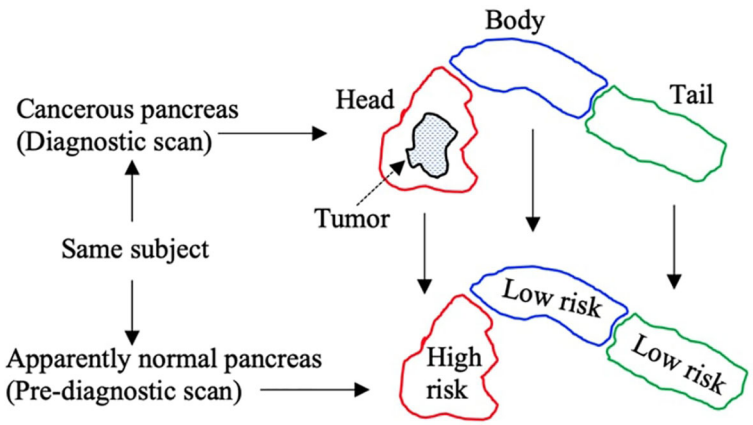

FIGURE 2
Pictorial description of specifying grades to subregions in pre-diagnostic scans. Tumor is observed in head subregion of diagnostic scans, and so the corresponding head subregion in pre-diagnostic scan is marked 'high risk', whereas the rest of subregions are marked 'low risk'.

Each of the 108 scans has 16-bit depth and a slice resolution of 512 by 512 (along the x- and y-axis) and variable z-axis. No preprocessing was performed on any of the scans except the signal intensities in each scan were scaled between 0 and 1.

Methods

Risk prediction modeling was carried out by thoroughly examining the morphology and the texture of the precancerous subregions to seek predictive features, followed by utilizing these features in a machine learning classifier to automatically characterize the pancreas and subregions into high-risk and low-risk classes for PDAC. The methodology is explained below.

Radiomic analysis of pancreatic subregions

A large amount of radiomic features were obtained from each of 194 subregions in 66 CT scans (22 healthy control, 22 pre-diagnostic, 22 diagnostic) of the internal dataset, i.e., three sets of features – one for each of the three groups, whereas each set consists of three subsets: one for each of three subregions. Each feature in the set expressed a unique quantifiable property of a subregion that provided information about the spatial relationship of neighboring voxels in predefined proximity (29). To calculate a numerical value for each feature, signal intensities of all 3D pixels specified within a volumetric subregion (all slices) of a scan were considered.

An important aspect of radiomic analysis is to consider the variations in a radiomic feature determined by the three parameters that include the *Kernel* size, the *Angle*, and the *Bin* size (29). Different combinations of these parameters influence the entire analyzation to a high extent. The kernel is the square convolution matrix that specifies the area (proximity) *A* surrounding a voxel *x*, for which the spatial relationships are calculated with its neighbors lying within area *A*. The *Angle* specifies the directions when calculating associations of *x* with its neighbors within the area *A*. The *Bin* size was the number used to discretize the continuous values of voxels in the CT image into their counter parts equal bins to avoid considering two pixels (having too-close signal intensities) any different. Each radiomic feature represented one of the major characteristics of a subregion that includes shape, size, texture, and signal intensity using a unique mathematical expression. Common types of radiomic features considered include first-order statistics (e.g., kurtosis, coefficient of variation, entropy) and higher-order statistics (e.g., contrast, homogeneity, coarseness). With different combinations of three parameters, around 4000 radiomic features from each of 194 subregions were extracted by considering the whole subregion as a single 'region of interest'.

Using the 132 subregions in 44 CT scans (22 healthy control, 22 pre-diagnostic) in the internal dataset, a pairwise feature comparison between the corresponding subregions (i.e., head-to-head, body-to-body, tail-to-tail) was performed to identify the features that were significantly different between high-risk and low-risk subregions. For example, the extracted features from all low-risk head subregions in the internal dataset were compared with the same set of features extracted from all high-risk head subregions in the internal dataset. About 3.5% of the extracted features showed significance (found potentially predictive) at a p-value of 0.05 in the statistical t-tests—supporting the core hypothesis about the presence of precancerous changes occurring locally within the subregions undergoing tumor development. Note that the only purpose of considering the features extracted from the 66 subregions in 22 CT diagnostic scans in the internal dataset during the analysis was to help sub-selecting the predictive features that are highly stable and do not become insignificant when pre-diagnostic and diagnostic scans are mixed.

Risk prediction of PDAC

The significant features (predictors) identified through the subregional analysis were used to perform automated risk prediction of PDAC by classifying the pancreas into either low-risk or high-risk categories. The criteria set to perform binary classification was to mark the pancreas as low-risk if none of its subregions was classified as high-risk, whereas the pancreas was marked as high-risk, if at least one of its subregions was classified as high-risk. A misclassification is counted if a) the classifier marks one or more subregions as high-risk in a healthy control scan, or b) the classifier identifies a high-risk subregion as low-risk in the pre-diagnostic scan or vice versa.

The Naïve Bayes (NB) model was trained for binary classification in conjunction with the Recursive Feature Elimination (RFE) (34, 35) method in which the RFE method eliminated the weak features using different combinations of identified predictors while maximizing the overall training accuracy based on the given classification criteria. Of note, the RFE was prespecified to select up to the seven best features to avoid overfitting the NB classifier. The NB-RFE identified seven features (Long-run low grey-level emphasis, Gaussian left polar, Inverse gaussian left polar, Inverse cluster shade, Inverse cluster prominence, Inverse cluster tendency, Short-run low grey-level emphasis) as the best predictors for the classifier to get the maximum classification accuracy during training the model on all the 44 CT scans (132 subregions) of the internal dataset. The external validation of the trained model was then performed using 24 CT scans (84 subregions) of the external dataset. An overview of the prediction process is provided in Figure 3.

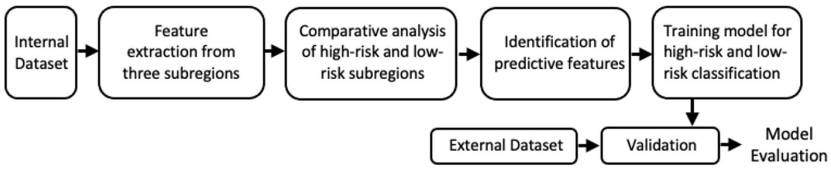

FIGURE 3
The major steps performed in the analysis and prediction process.

Results

Model performance was evaluated in terms of classification accuracy, sensitivity, and specificity. The classification accuracy was calculated as the total number of correctly classified scans (both healthy control and pre-diagnostic) to the total number of scans input to the NB classifier. The sensitivity is the true positive rate which refers to the total number of correctly classified pre-diagnostic scans (high-risk pancreas) to the total number of pre-diagnostic scans input to the NB classifier. Whereas the specificity is the true negative rate which refers to the total number of correctly classified healthy control scans (low-risk pancreas) to the total number of healthy control scans input to the NB classifier.

The mean classification accuracy achieved on the training data (internal dataset) was 93% (41/44), i.e., the number of correctly classified scans to the total number of scans observed. The external validation of the classifier was performed using the 56 subregions in 28 scans (14 healthy control and 14 pre-diagnostic) in the external dataset. The validation achieved the mean classification accuracy of 89.3% (25/28), with the sensitivity and specificity reaching 86% and 93% respectively, as given in the confusion matrix Table 2.

Compared to the performance of our previous prediction system (31) which produced 86% classification accuracy, the proposed model demonstrated improved accuracy by 3.3%. Also, it was empirically observed that the inter-variability between the features extracted from corresponding 'low-risk' subregions identified in healthy control and pre-diagnostic scans was significantly low at a p-value of 0.05. This supports our primary hypothesis that the precancerous changes predominately occur locally and are specific to the subregion within which the tumor is likely developing. Also, the 95% confidence interval (CI) achieved in the current study is 78-100, showing modest improvement on the lower bound of the CI obtained in the previous study (i.e., 73-99). Further improvement in the current CI was possible if the model training was not enforced to use a fixed limited number of predictors to avoid model overfitting.

Moreover, the radiomic analysis infers that it is essentially the texture of the pancreas that changes locally and appears abnormal on a CT scan during cancer development. These textural changes are the possible indication of the stage the underlying healthy cells are transitioning into tumor cells (e.g., the tumorous region turns more hypointense than the non-tumorous peripheral region on a CT image). Furthermore, the shape of the whole pancreas (in healthy and pre-diagnostic scans) and subregions (belong to high-risk and low-risk classes) was observed indifferent, partly because the shape of the pancreas is highly irregular in general. However, the size of the high-risk subregions was observed slightly higher than their corresponding low-risk subregions, though not significantly different to be considered a stable predictor.

TABLE 2 Confusion matrix for classification of 28 CT scans of the external set consisting of 14 from each of Healthy control and Pre-diagnostic group.

	True Healthy	True Pre-diagnostic
Predicted Healthy	13	2
Predicted Pre-diagnostic	1	12

Numbers in the orange blocks show true positives.

Discussion

Clinical significance of PDAC prediction using CT imaging

The Centers for Disease Control and Prevention reports that 7 million patients with abdominal pain visit to ER in the US each year. These patients undergo CT examinations as per the standard care protocol. The initial evaluation of these scans assists clinicians to identify the underlying cause of abdominal pain. Though the scans of majority of these patients do not present any signs of cancer at this stage, some ultimately develop PDAC in coming years. These pre-diagnostic scans, even with no prominent signs of cancer, are clinically useful as these might contain significant morphological signatures of early biological adaptations associated with cancer. AI techniques can efficiently

assist in identifying these signs and forecasting cancer incidence for the future. However, AI-based exploration of precancerous signs is challenged by data scarcity as the PDAC has a low prevalence. In this retrospective study, we examined the quantitative difference of the CT-based features between pre-diagnostic and healthy control scans. The study allowed quantitative analysis of the subregional changes that occurred in the precancerous or pre-symptomatic pancreas and helped reduce limitations of low prevalence and low cancer yield in prospective studies as half of the subjects have cancer.

The unique data structure designed for this study is the foundation of the proposed prediction model as it allowed examining precancerous changes retrospectively. Although the overall prevalence of PDAC is significantly low, the percentage of enrolled subjects who were at the preclinical stage was set to 50% to reduce the risk of class imbalance during model development. Also, most of the literature considers that the duration of 6-36 months between the pre-diagnostic and diagnostic scan is a reasonable window to seek early signs.

Also, most of the scans used for mode training and testing are portal venous phase. It is because tumors slowly uptake contrast whereas the venous phase provides the optimal view of the tumor edges and is thus considered the most valuable phase for PDAC diagnosis. Also, viewing of the vasculature passing across or alongside the pancreas is optimized in this phase. Changes occurring to the vasculature during PDAC development can be quantified and used as potential predictors. Nevertheless, other phases also provide valuable information during PDAC screening and treatment. For example, the arterial phase provides a unique value when seeking lesions or during surgical treatment of PDAC when the arteries are encased or distorted by the pancreatic tumor. Thus, including multiphase scans in the model training helped identify highly stable predictors to ensure the model is sufficiently robust.

In accordance with the evidence provided, the proposed research work assures the appropriate blend of imaging type, feature analysis, and modeling techniques to address the challenges of prediction and elevate the chances of cancer diagnosis in the earliest stage. To our knowledge, it is the first automated system developed that predicts the PDAC by identifying early signs through analyzing the precancerous irregularities occurring within pancreatic subregions using CT scans. The proposed model not only demonstrated improved prediction accuracy to existing models but also enabled the system to identify subregions that are at higher risk of developing tumors.

Significance of the subregional analysis

Several studies suggest that tumor development differs across pancreatic subregions (Head:*H* , Body: B, Tail:*T*) in terms of histology, presentation, and symptoms (24, 25, 36–39). For instance, tumors in the head are mostly non-squamous, whereas the body and tail tumors are usually squamous. This results in spatial heterogeneity and various discrepancies across the pancreatic sub-regions; such as tumor presentation (e.g., head tumors are usually well-differentiated and less aggressive than those in body/tail), related symptoms (head tumors: unexplained weight loss, body tumors: pain in the upper abdomen, tail tumors: pain in the lower abdomen), sensitivity to drugs (head tumors are highly responsive to Gemcitabine regimen and less responsive to Fluorouracil regimen, whereas the body and tail tumors are vice-versa), and the different rates of incidence (*H*: 71%, *B*: 13%, *T*: 16%), metastasis (*H*: 42%,*B*: 68%, *T*: 84%), %), 2-year survival (*H*: 44%, *B*: 27%, *T*: 27%), and resection (*H*: 17%,*B*: 4%, *T*: 7%) (24, 25, 36–39).

This study examined the subregional changes in the precancerous pancreas and enabled automated identification of subregions undergoing tumor development. Knowledge of the location of likely tumor will not only alert clinicians/radiologists to pay attention to certain regions of the pancreas to avoid misdetection of PDAC at an early stage but also enhance the overall management of PDAC by helping determine more appropriate and effective treatment, improving forecasting of the treatment outcome, planning better resection, and ultimately increasing the overall survival rate.

Improvement to previous model

In our previous study (31), we proposed the first model for risk prediction of PDAC using AI analysis of the morphology of the 'whole pancreas'. The current study has three major new contributions which were not included in the previous study (31): a) investigation performed to identify whether all three subregions concurrently adopt precancerous changes, or the changes are predominant (or only occur) in the subregion where the tumor is likely developing, b) analysis performed to identify new CT-based predictors and improved the prediction (in terms of model accuracy), and c) trained the model to specify the subregion that is at highest risk of developing most part of the tumor or where the tumor will likely originate.

Study limitations and future work

Due to the low prevalence of PDAC, the eligible pre-diagnostic CT scans were found rare in the data archives of the CSMC and KPSC. Limited training data may have increased the chance of overfitting during model development. Another limitation is the insufficiency of pre-diagnostic CT scans of non-venous CT phases. Also, since the

incidence of PDAC in the general population is fairly low, the model specificity of 93% still requires further enhancement to avoid too many false-positive cases. The aim of the study was to present the proof of the concept which encourages the collection of larger datasets including the information on non-imaging factors associated with risk of PDAC from the repositories of different institutes for substantial training and validation of the proposed prediction model. With sufficient data, the biological interpretation of predictive image features and their correlation with genetics would be achievable. A model trained on large data will improve model specificity and will efficiently assist in future prospective research on detecting PDAC at the initial stages.

Conclusion

The current study presented the findings of the AI analysis of precancerous changes that occurred across three subregions of the pancreas using pre-diagnostic abdominal CT scans. The study concluded that the pancreas adopts textural changes during PDAC development, predominantly within the subregion undergoing tumor development, potentially regarded as a 'high-risk' subregion. A first model was built that performed risk quantification of PDAC using the identified textural changes as potential predictors and characterized the pancreas into 'high risk' and 'low risk' for PDAC classes. The model also specified the subregion that is likely to develop the tumor, which can potentially assist in improving early diagnosis, treatment planning, forecasting treatment outcome, and overall disease management. The proposed model demonstrates a 3.3% improved prediction when compared with the existing prediction model that considers the global changes occurring in the whole pancreas during PDAC development. The results of this preliminary study are promising and encouraging to further validate the model on a large dataset.

Data availability statement

The original contributions presented in the study are included in the article/supplementary material. Further inquiries can be directed to the corresponding authors.

Author contributions

DL, SP, SG, BW, CJ, and TQ were responsible for the conception and design. LW, LA, AW, WC, and VA performed data extraction and data labeling. SJ and TQ conducted basic investigation, performed statistical analysis, developed prediction model, and wrote original manuscript. DL performed quality control of this study. All authors contributed to the article and approved the submitted version.

Funding

NIH R01 CA260955.

Conflict of interest

The authors declare that the research was conducted in the absence of any commercial or financial relationships that could be construed as a potential conflict of interest.

Publisher's note

All claims expressed in this article are solely those of the authors and do not necessarily represent those of their affiliated organizations, or those of the publisher, the editors and the reviewers. Any product that may be evaluated in this article, or claim that may be made by its manufacturer, is not guaranteed or endorsed by the publisher.

References

1. Adamska A, Domenichini A, Falasca M. Pancreatic ductal adenocarcinoma: Current and evolving therapies. *Int J Mol Sci* (2017) 18(7):1338. doi: 10.3390/ijms18071338

2. Nolen BM, Brand RE, Prosser D, Velikokhatnaya L, Allen PJ, Zeh HJ, et al. Prediagnostic serum biomarkers as early detection tools for pancreatic cancer in a large prospective cohort study. *PloS One* (2014) 9(4):e94928. doi: 10.1371/journal.pone.0094928

3. Almeida PP, Cardoso CP, de Freitas LM. PDAC-ANN: an artificial neural network to predict pancreatic ductal adenocarcinoma based on gene expression. *BMC Cancer* (2020) 20(1):1–11. doi: 10.1186/s12885-020-6533-0

4. Muhammad W, Hart GR, Nartowt B, Farrell JJ, Johung K, Liang Y, et al. Pancreatic cancer prediction through an artificial neural network. *Front Artif Intelligence* (2019) 2:2. doi: 10.3389/frai.2019.00002

5. Pannala R, Basu A, Petersen GM, Chari ST. New-onset diabetes: A potential clue to the early diagnosis of pancreatic cancer. *Lancet Oncol* (2009) 10(1):88–95. doi: 10.1016/S1470-2045(08)70337-1

6. Klein AP, Lindström S, Mendelsohn JB, Steplowski E, Arslan AA, Bueno-de-Mesquita HB, et al. An absolute risk model to identify individuals at elevated risk for pancreatic cancer in the general population. *PloS One* (2013) 8(9):e72311. doi: 10.1371/journal.pone.0072311

7. Boursi B, Finkelman B, Giantonio BJ, Haynes K, Rustgi AK, Rhim AD, et al. A clinical prediction model to assess risk for pancreatic cancer among patients with new-onset diabetes. *Gastroenterology* (2017) 152(4):840–850.e3. doi: 10.1053/j.gastro.2016.11.046

8. *Key statistics for pancreatic cancer* (Accessed July 30, 2022).

9. Kleeff J, Korc M, Apte M, La Vecchia C, Johnson CD, Biankin AV, et al. Pancreatic cancer. *Nat Rev Dis primers* (2016) 2(1):1–22. doi: 10.1038/nrdp.2016.22

10. Orth M, Metzger P, Gerum S, Mayerle J, Schneider G, Belka C, et al. Pancreatic ductal adenocarcinoma: biological hallmarks, current status, and future perspectives of combined modality treatment approaches. *Radiat Oncol* (2019) 14 (1):141. doi: 10.1186/s13014-019-1345-6

11. Stark A, Eibl G. Pancreatic ductal adenocarcinoma, in: *Pancreapedia: The exocrine pancreas knowledge base* (Accessed July 30, 2022).

12. Kaur S, Baine MJ, Jain M, Sasson AR, Batra SK. Early diagnosis of pancreatic cancer: challenges and new developments. *biomark Med* (2012) 6(5):597–612. doi: 10.2217/bmm.12.69

13. Ansari D, Aronsson L, Sasor A, Welinder C, Rezeli M, Marko-Varga G, et al. The role of quantitative mass spectrometry in the discovery of pancreatic cancer biomarkers for translational science. *J Transl Med* (2014) 12(1):87. doi: 10.1186/1479-5876-12-87

14. Egawa S, Takeda K, Fukuyama S, Motoi F, Sunamura M, Matsuno S. Clinicopathological aspects of small pancreatic cancer. *Pancreas* (2004) 28(3):235–40. doi: 10.1097/00006676-200404000-00004

15. Singha AD, Koay EJ, Chari ST, Maitra A. Early detection of pancreatic cancer: Opportunities and challenges. *Gastroenterology* (2019) 156(7):2024–40. doi: 10.1053/j.gastro.2019.01.259

16. Sharma A, Kandlakunta H, Nagpal SJ, Feng Z, Hoos W, Petersen GM, et al. Model to determine risk of pancreatic cancer in patients with new-onset diabetes. *Gastroenterology* (2018) 155(3):730–739.e3. doi: 10.1053/j.gastro.2018.05.023

17. Hart PA. Early detection of pancreatic cancer in high-risk individuals: Where do we go from here? *Am J Gastroenterol* (2019) 114(4):560–1. doi: 10.14309/ajg.192

18. Qureshi TA, Javed S, Sarmadi T, Pandol SJ, Li D. Artificial intelligence and imaging for risk prediction of pancreatic cancer: A narrative review. *Chin Clin Oncol* (2022) 11(1):1. doi: 10.21037/cco-21-117

19. Machado NO, al Qadhi H, al Wahibi K. Intraductal papillary mucinous neoplasm of pancreas. *N Am J Med Sci* (2015) 7(5):160–75. doi: 10.4103/1947-2714.157477

20. Ahn SS, Kim M-J, Choi J-Y, Hong H-S, Chung YE, Lim JS. Indicative findings of pancreatic cancer in prediagnostic CT. *Eur Radiol* (2009) 19(10):2448–55. doi: 10.1007/s00330-009-1422-6

21. Konishi K, Izumi R, Kato O, Yamaguchi A, Miyazaki I. Experimental pancreatolithiasis in the dog. *Surgery* (1981) 89(6):687–91.

22. Tanaka S, Nakaizumi A, Ioka T, Oshikawa O, Uehara H, Nakao M, et al. Main pancreatic duct dilatation: A sign of high risk for pancreatic cancer. *Jpn J Clin Oncol* (2002) 32(10):407–11. doi: 10.1093/jjco/hyf093

23. Farrow B, Evers BM. Inflammation and the development of pancreatic cancer. *Surg Oncol* (2002) 10(4):153–69. doi: 10.1016/S0960-7404(02)00015-4

24. Ling Q, Xu X, Zheng SS, Kalthoff H. The diversity between pancreatic head and body/tail cancers: clinical parameters and *in vitro* models. *HBPD Int* (2013) 12(5):480–7. doi: 10.1016/s1499-3872(13)60076-4

25. Birnbaum DJ, Bertucci F, Finetti P, Birnbaum D, Mamessier E. Head and body/tail pancreatic carcinomas are not the same tumors. *Cancers* (2019) 11(4):.497. doi: 10.3390/cancers1104049

26. Kumar Y, Gupta S, Singla R, Hu YC. A systematic review of artificial intelligence techniques in cancer prediction and diagnosis. *Archives of Computational Methods in Engineering*. (2021) 27:1–28. doi: 10.1007/s11831-021-09648-w

27. Roffman D, Hart G, Girardi M, Ko CJ, Deng J. Predicting non-melanoma skin cancer *via* a multi-parameterized artificial neural network. *Sci Rep* (2018) 8(1):1701. doi: 10.1038/s41598-018-19907-9

28. Gillies RJ, Kinahan PE, Hricak H. Radiomics: images are more than pictures, they are data. *Radiology* (2016) 278(2):563–77. doi: 10.1148/radiol.2015151169

29. Parekh V, Jacobs MA. Radiomics: A new application from established techniques. *Expert Rev Precis Med Drug Dev* (2016) 1(2):207–26. doi: 10.1080/23808993.2016.1164013

30. Commandeur F, Slomka PJ, Goeller M, Chen X, Cadet S, Razipour A, et al. Machine learning to predict the long-term risk of myocardial infarction and cardiac death based on clinical risk, coronary calcium, and epicardial adipose tissue: A prospective study. *Cardiovasc Res* (2019) 116(14):2216–25. doi: 10.1093/cvr/cvz321

31. Qureshi TA, Gaddam S, Wachsman AM, Wang L, Azab L, Asadpour V, et al. Predicting pancreatic ductal adenocarcinoma using artificial intelligence analysis of pre-diagnostic computed tomography images. *Cancer Biomarkers* (2022) 33(2):211–7. doi: 10.3233/CBM-210273

32. Kreel L, Haertel M, Katz D. Computed tomography of the normal pancreas. *J Comput Assist Tomogr* (1977) 1(3):290–9. doi: 10.1097/00004728-197707000-00002

33. Yushkevich PA, Piven J, Hazlett HC, Smith RG, Ho S, Gee JC. User-guided 3D active contour segmentation of anatomical structures: significantly improved efficiency and reliability. *Neuroimage* (2006) 31(3):1116–28. doi: 10.1016/j.neuroimage.2006.01.015

34. Granitto PM, Furlanaello C, Biasioli F, Gasperi F. Recursive feature elimination with random forest for PTR-MS analysis of agroindustrial products. *Chemom Intell Lab Syst* (2006) 83(2):83–90. doi: 10.1016/j.chemolab.2006.01.007

35. Yan K, Zhang D. Feature selection and analysis on correlated gas sensor data with recursive feature elimination. *Sens Actuators B Chem* (2015) 212:353–63. doi: 10.1016/j.snb.2015.02.025

36. Zhang X, Feng S, Wang Q, Huang H, Chen R, Xie Q, et al. Comparative genomic analysis of head and body/tail of pancreatic ductal adenocarcinoma at early and late stages. *J Cell Mol Med* (2021) 25(3):1750–8. doi: 10.1111/jcmm.16281

37. Mackay TM, van Erning FN, van der Geest LGM, de Groot JW, Haj MN, Lemmens VE, et al. Association between primary origin (head, body and tail) of metastasised pancreatic ductal adenocarcinoma and oncologic outcome: A population-based analysis. *Eur J Cancer* (2019) 106:99–105. doi: 10.1016/j.ejca.2018.10.008

38. Luo G, Jin K, Cheng H, Guo M, Gong Y, Fa Z, et al. Prognosis of distal pancreatic cancers controlled by stage. *Exp Ther Med* (2020) 20(2):1091–7. doi: 10.3892/etm.2020.8795

39. Tomasello G, Ghidini M, Costanzo A, Ghidini A, Russo A, Barni S, et al. Outcome of head compared to body and tail pancreatic cancer: A systematic review and meta-analysis of 93 studies. *J Gastrointest Oncol* (2019) 10(2):259. doi: 10.21037/jgo.2018.12.08

frontiers | Frontiers in Oncology

TYPE Original Research
PUBLISHED 23 November 2022
DOI 10.3389/fonc.2022.948557

OPEN ACCESS

EDITED BY
Pilar López-Larrubia,
Spanish National Research Council (CSIC), Spain

REVIEWED BY
Roberto Cannella,
University of Palermo, Italy
Vishwa S. Parekh,
University of Maryland, Baltimore, United States

*CORRESPONDENCE
Defeng Liu
defeng1979@163.com
Yuan Fang
nmjfy@sohu.com

SPECIALTY SECTION
This article was submitted to Cancer Imaging and Image-directed Interventions, a section of the journal Frontiers in Oncology

RECEIVED 20 May 2022
ACCEPTED 02 November 2022
PUBLISHED 23 November 2022

CITATION
Yang L, Du D, Zheng T, Liu L, Wang Z, Du J, Yi H, Cui Y, Liu D and Fang Y (2022) Deep learning and radiomics to predict the mitotic index of gastrointestinal stromal tumors based on multiparametric MRI.
Front. Oncol. 12:948557.
doi: 10.3389/fonc.2022.948557

Deep learning and radiomics to predict the mitotic index of gastrointestinal stromal tumors based on multiparametric MRI

Linsha Yang[1], Dan Du[1], Tao Zheng[1], Lanxiang Liu[1], Zhanqiu Wang[1], Juan Du[1], Huiling Yi[1], Yujie Cui[1], Defeng Liu[1]* and Yuan Fang[2]*

[1]Medical Imaging Center, The First Hospital of Qinhuangdao, Qinhuangdao, China, [2]Medical Imaging Center, Chongqing Yubei District People's Hospital, Chongqing, China

Introduction: Preoperative evaluation of the mitotic index (MI) of gastrointestinal stromal tumors (GISTs) represents the basis of individualized treatment of patients. However, the accuracy of conventional preoperative imaging methods is limited. The aim of this study was to develop a predictive model based on multiparametric MRI for preoperative MI prediction.

Methods: A total of 112 patients who were pathologically diagnosed with GIST were enrolled in this study. The dataset was subdivided into the development (n = 81) and test (n = 31) sets based on the time of diagnosis. With the use of T2-weighted imaging (T2WI) and apparent diffusion coefficient (ADC) map, a convolutional neural network (CNN)-based classifier was developed for MI prediction, which used a hybrid approach based on 2D tumor images and radiomics features from 3D tumor shape. The trained model was tested on an internal test set. Then, the hybrid model was comprehensively tested and compared with the conventional ResNet, shape radiomics classifier, and age plus diameter classifier.

Results: The hybrid model showed good MI prediction ability at the image level; the area under the receiver operating characteristic curve (AUROC), area under the precision–recall curve (AUPRC), and accuracy in the test set were 0.947 (95% confidence interval [CI]: 0.927–0.968), 0.964 (95% CI: 0.930–0.978), and 90.8 (95% CI: 88.0–93.0), respectively. With the average probabilities from multiple samples per patient, good performance was also achieved at the patient level, with AUROC, AUPRC, and accuracy of 0.930 (95% CI: 0.828–1.000), 0.941 (95% CI: 0.792–1.000), and 93.6% (95% CI: 79.3–98.2) in the test set, respectively.

Discussion: The deep learning-based hybrid model demonstrated the potential to be a good tool for the operative and non-invasive prediction of MI in GIST patients.

KEYWORDS

deep learning, radiomics, magnetic resonance imaging, convolutional neural network, gastrointestinal stromal tumor

Introduction

Gastrointestinal stromal tumors (GISTs) are the most common mesenchymal tumors of the digestive tract wall in that they are more common in the stomach and small intestine (1). It is widely believed that GIST originates in Cajal cells, which are involved in gastrointestinal motility (2). GIST occurs at a median age of 60 years (10–100 years), with no sex difference in the distribution (3). Before the advent of tyrosine kinase inhibitors, the most common treatment for most GIST cases was radical surgical resection without any residual tumor. However, even after complete tumor resection, the patients still have a high rate of recurrence and metastasis (4). Another approach for the treatment of GIST was presented through the invention and rational application of targeted drugs, such as imatinib, which significantly improved the recurrence-free survival and overall survival of GIST. The prognosis of GIST is closely related to its risk grade (5). Joensuu and colleagues proposed an improved National Institutes of Health (NIH) grading system to grade the risk of a tumor based on its size, location, mitotic index and whether it is ruptured (6). Different risk grades correspond to different prognoses and treatment methods. For very-low-risk patients, regular follow-up may be used without immediate surgery. For low-risk patients, routine resection similar to benign tumors can be performed without targeted therapy and follow-up. Intermediate- or high-risk patients should receive targeted therapy to shrink the tumor before resection; after surgery, targeted therapy and long-term follow-up should be continued for a period of time (7). Therefore, accurate preoperative assessment of the tumor risk grade has important guiding significance for the treatment plan.

The mitotic index (MI) is an important indicator of GIST risk grading. However, it may be more difficult to perform a preoperative assessment of MI than to obtain morphological information, such as tumor location and size. Pathological examination is still the gold standard to accurately quantify the GIST mitotic index (8). However, as an invasive examination, it may lead to tumor hemorrhage and intraperitoneal spread; hence, a preoperative pathological biopsy is not a routine examination for GIST (9). The application of endoscopic ultrasonography has greatly improved the success rate of preoperative pathological biopsy for mesenchymal tumors. However, a biopsy cannot be performed in some tumors at specific sites (10). For intermediate- or high-risk tumors with active mitosis, preoperative application of the GIST therapy can significantly reduce the tumor size, thus effectively improving the resection rate of surgery and reducing the risk of recurrence (11). In addition, small GIST is usually treated by clinicians as a general benign tumor. However, once its MI > 5 or even 10/HF, it may also be highly invasive and dangerous; thus, it is obviously not suitable to apply the watch-and-wait treatment strategy. Nevertheless, the accurate prediction of tumor MI is of great significance to evaluate the risk of tumor recurrence and guide the treatment strategy before and after surgery.

Morphological information about tumors can be obtained through endoscopic ultrasonography, computerized tomography (CT), and magnetic resonance imaging (MR); hence, they can be used as a basis to determine the location and size of GIST and indicate the occurrence of rupture or hemorrhage before surgery (12–14). Some prior recent CT-based studies have correlated the morphological features of GIST with the NIH risk classification, prediction of mutation status, and prognosis (15, 16). In clinical practice, CT may be the favored imaging method for GIST preoperative assessment, but MR may provide more tumor information because of its multi-sequence advantage. However, whether CT or MR, the advancements in these conventional imaging methods are limited by subjective human eye observation, which does not provide enough information on the internal heterogeneity of tumors. Moreover, it is difficult to characterize the MI of tumors, which represents important pathological information.

Radiomics was first proposed by Lambin in 2012. It emphasizes the high-throughput extraction of image information (including shape, gray scale, and texture) from medical images and adopts traditional statistical models such as support vector machine, random forest, and XGBoost to achieve tumor segmentation, feature extraction, and model establishment (17). Using radiomics, researchers can transform image information into a large number of features for a quantitative study, which has been widely used in tumor grading, staging, and prognosis research (18–20). The concept of deep learning (DL) was proposed by Hinton et al. in 2006, which is a new field in machine learning research. Its motivation lies in the establishment of neural networks that simulate the

analysis and learning process of the human brain, so as to interpret image data by imitating the mechanism of the human brain (21). Unlike radiomics, which relies on predefined artificial features, deep learning algorithms can extract more abstract high-dimensional features in a more automatic way that is not susceptible to subjective influence (22). Therefore, such algorithms have been widely used in the automatic recognition, segmentation, and classification of lung cancer, breast cancer, rectal cancer, and other tumors (23–25). In this study, we trained a convolutional neural network (CNN) classifier based on an integration of two-dimensional (2D) multimodal MR images and three-dimensional (3D) shape-based radiomics features to perform preoperative prediction of mitotic index in GIST.

Materials and methods

This is a retrospective study, and the patients' information was anonymized. The ethics committee of our hospital approved the study and waived the need for informed consent from the patients.

Data

A total of 141 patients who were newly diagnosed with GIST and underwent MR examination in our hospital from January 2013 to May 2022 were initially enrolled. The inclusion criteria were as follows: 1) GIST was confirmed by postoperative pathology after radical resection in our hospital; 2) mitotic index was obtained through postoperative pathological examination; 3) preoperative MR examination is available, including T2-weighted imaging (T2WI) and diffusion-weighted imaging (DWI) sequences. The exclusion criteria were as follows: 1) preoperative MR examination occurred more than 14 days before surgery; 2) two radiologists with 5 years of experience in the diagnosis of abdominal and pelvic MR evaluated the image quality and excluded those whose image quality was too poor to delineate the region of interest due to motion or other artifacts; 3) the patients were treated with imatinib or other tyrosine kinase inhibitors before surgery; 4) the patients were younger than 18 years. The patient inclusion process is shown in Figure 1. Then, based on postoperative pathology results and modified NIH risk classification criteria (6), the patients were classified into the group with the low mitotic index (MI ≤ 5/50 HPFs, 55 patients) and the

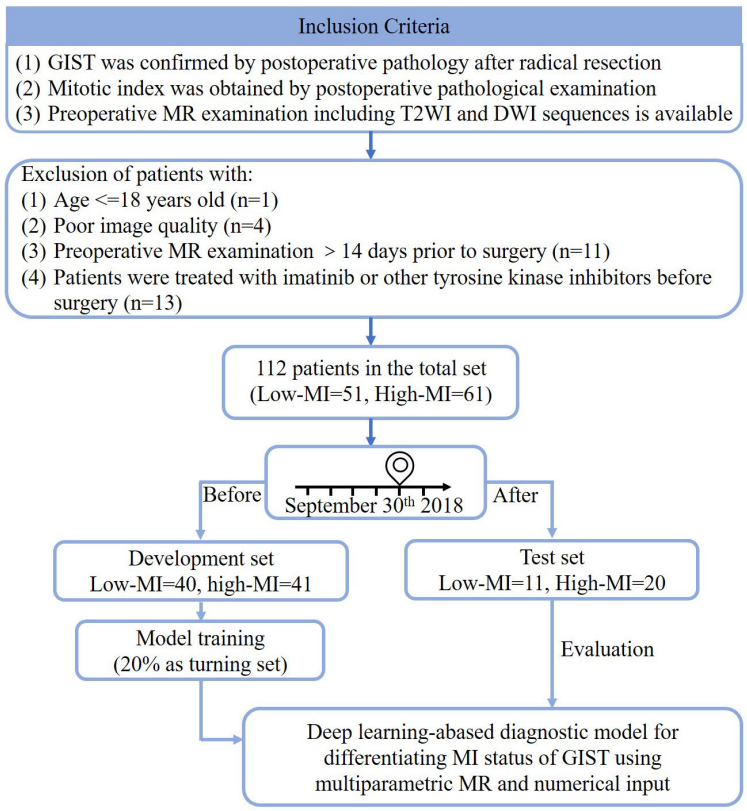

FIGURE 1
The flowchart of dataset setup. Low-MI, low mitotic index; High-MI, high mitotic index.

group with high mitotic index (MI > 5/50 HPFs, 68 patients). The 2008 modified NIH risk classification criteria are discussed in detail in Supplementary Table 1. The data were divided into the development set, consisting of 81 patients who were diagnosed between January 2013 and September 2018, and the test set, consisting of 31 patients who were diagnosed between October 2019 and May 2022.

Image acquisition and processing

All images were scanned using a 1.5T Siemens Avanto MR system (Siemens, Munich, Germany) equipped with an eight-channel phased-front coil dedicated to the abdomen. In order to reduce gastrointestinal motion artifacts, the patients were instructed to abstain from water and food for 4 h before the scan. The imaging sequences included coronal fast imaging, employing the steady-state acquisition (FIESTA) sequence, axial fat-suppression T2WI, axial DWI, and axial in-phase and out-of-phase T1-weighted imaging (T1WI). DWI was collected by echo-planar imaging (EPI), with b values of 0 and 800. The respiratory trigger technique was used for T2WI and DWI, and the end-expiratory breath-holding method was used for FIESTA and T1WI scans to reduce respiratory motion artifacts. Table 1 lists the detailed image acquisition parameters.

Region of interest segmentation and three-dimensional shape feature extraction

The images of all patients were downloaded in the digital imaging and communications in medicine (DICOM) format from the picture archiving and communication system (PACS) of our hospital. Apparent diffusion coefficient (ADC) maps were registered to T2WI images using the Statistical Parametric Mapping software v.12 (SPM12, University College London). A radiologist with more than 5 years of experience in abdominal and pelvic MR diagnoses segmented the entire tumor in three dimensions on T2WI images, such that the segmentation was strictly along the edges of the tumor and included areas of necrosis and cystic degeneration. In addition, the maximum diameter of the tumor was measured, and the tumor location was recorded during segmentation. The abovementioned information was confirmed and corrected by another radiologist with 10 years of experience in abdominal and pelvic MR imaging. In case of any disagreement, consultation continued until an agreement was reached.

Shape radiomics features were extracted using the PyRadiomics package (https://www.radiomics.io/pyradiomics.html), which contained 14 features, as follows: mesh volume, voxel volume, surface area, surface area to volume ratio, sphericity, maximum 3D diameter, maximum 2D diameter (slice), maximum 2D diameter (column), maximum 2D diameter (row) major axis length, minor axis length, least axis length, elongation, and flatness. The definitions and calculation methods of each of these features can be found on the package documentation page https://pyradiomics.readthedocs.io/en/latest/features.html#module-radiomics.shape.

Convolutional neural network classifier for mitotic index status prediction

The CNN structure is shown in Figure 2. The CNN classifier used in this study is derived from the famous 50-layer ResNet structure (hereinafter referred to as conventional ResNet). As shown in Supplementary Figure 1, the network structure

TABLE 1 MRI protocols.

Image acquisition parameter	Parameter values			
Acquisition plane	**FIESTA Coronal**	**T2WI Axial**	**DWI Axial**	**T1WI Axial**
Fat saturation	No	Yes	Yes	No
TR/TE (ms)	3.63/1.82	2,000/96	4,600/63	75/2.38,4.79
Angle (°)	60	70	150	70
Slice thickness (mm)	5	6	6	6
FOV (mm^2)	350 × 350	379 × 284	379 × 308	380 × 320
Matrix	512 × 460	384 × 202	192 × 128	320 × 189
Voxel size (mm^3)	1.0 × 1.0 × 5.0	1.0 × 1.0 × 6.0	2.0 × 2.0 × 6.0	1.2 × 1.2 × 6.0
Interslice gap	10%	10%	10%	10%
Delay (s)				
Scan time (s)	12	165	97	69
b-Value (s/mm^2)			0, 800	

FIESTA, fast imaging employing steady-state acquisition; T2WI, T2-weighted imaging; DWI, diffusion-weighted imaging; T1WI, T1-weighted imaging; TR, repetition time; TE, echo time.

contained the initial 7 × 7 convolution and layers 1 to 4 comprising three, four, six, and three residual blocks, such that each residual block had one 3 × 3 convolution and two 1 × 1 convolutions. For the hybrid model, we included an additional fully connected layer to the conventional ResNet, which used additional image input and numerical input. The image input to the hybrid model comprised axial T2WI and ADC and tumor masks with the size of 128 × 128. To train a model with a high performance given the insufficient sample size, we selected all the images containing GIST for each patient, instead of a certain layer of images. Therefore, based on tumor segmentation, there may be multiple axial sections per patient, which would be used for the development and testing of classification models. As for the numerical input to the hybrid model, it included 14 morphologic features based on general imaging as well as the patient's age and tumor diameter. Before adding the above features to the neural network, we standardized them according to the following formula:

$$\overrightarrow{x_n} = \frac{\overrightarrow{x_n} - \overline{x_n}}{\sqrt{x_{1n}^2 + x_{2n}^2 + \ldots + x_{mn}^2}}$$

where $\overrightarrow{x_n}$ is the nth feature and m is the number of samples.

The training process of the CNN classifier is discussed in detail below. First, the DICOM image was converted to PNG format, which was used for the training and validation of the CNN model. Since our input data size is 384 × 202, which is bigger than the original residual neural network (224 × 224), the image and mask were resampled. Based on tumor segmentation, all layers of each patient's tumor were selected as independent samples; this approach might have a better effect on data enhancement than image flipping or rotation. In this way, our convolutional residual neural network and our CNN classifier obtained 891 development samples and 531 test samples. To train our model, the transfer learning method was used, which is widely used in computer vision, for efficient training and accurate classification performance. A weight file obtained by training an ResNet50 network was used on the large ImageNet dataset to extract the features of target datasets, and the model parameters were fine-tuned *via* the target datasets (891 development samples and 531 test samples) to obtain an optimal conventional ResNet model. Then, the weight value of the optimal pretrained conventional ResNet from the initial 7 × 7 convolutional layers to the third layer, and the mixed model was imported and set as untrainable. During the training of the hybrid model, only the weights from the fully connected layers that received shape, age, and maximum diameter as numerical inputs from layer 4 and below were trained to maximize the synergy between the image features from the pretrained weights

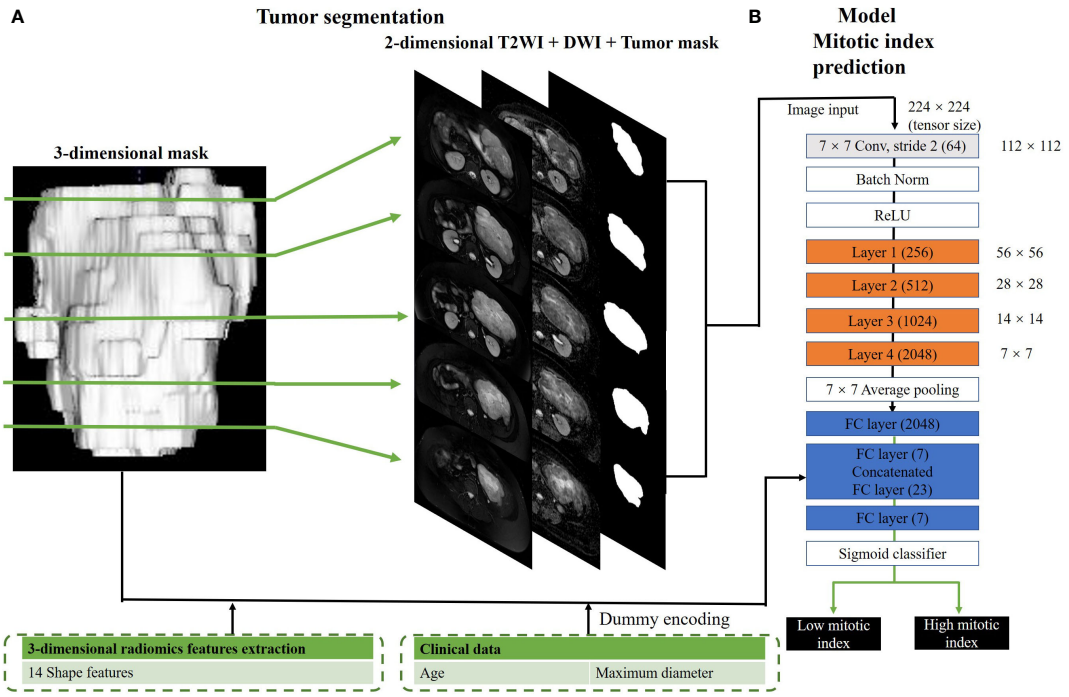

FIGURE 2
Hybrid model for mitotic index prediction. **(A)** shows the process of 3-dimensional and 2-dimensional image segmentation. We convert a three-dimensional mask to several two-dimensional masks. **(B)** shows the structure of hybrid mitotic index prediction model. In this model, layers 1–4 consisted of three, four, six, and three residual blocks, with each block containing 3 × 3 convolution once and 1 × 1 convolution twice.

and numeric inputs. The input images were dynamically enhanced by translation, scaling, rotation, shearing, Gaussian noise, and blur. The Adam optimizer was used to optimize the network (beta1 = 0.9, beta2 = 0.999, initial learning rate = 1e −04), batch size was set to 30, and the maximum training epoch was set to 100, and training was stopped when the lost value of the validation set dropped to a stable level. The resulting model had the lowest validation set loss value. Our CNN model was implemented in PyTorch 1.1.0 (https://pytorch.org) and trained on an NVIDIA Tesla 3080 12 G with a memory of 64 G.

Cross-validation

To generalize the reliability of the networks, threefold cross-validation was performed on the 111 subjects by randomly shuffling the dataset and distributing it into three groups by stratified randomization (27 subjects for each group: 17 low MI and 20 high MI in Group 1, 17 low MI and 20 high MI in Group 2, and 17 low MI and 21 high MI in Group 3). During each fold of the cross-validation procedure, two of the three groups of subjects were combined as the internal training set, and the remaining group was used as the internal validation set. The internal validation set helped improve network performance during training. Note that each fold of the cross-validation procedure represents a new training phase on a unique combination of the three groups. Network performance was reported on the internal validation set for each fold.

Statistical analysis

In this study, the predictive performance of the model was studied at the image level and patient level separately such that the results of the image level prediction can finally be used for patient-level prediction. For a certain patient, the average prediction probability of all images was calculated as the prediction probability of the patient. The probability threshold of the calculation accuracy was set as 0.5, so a prediction probability ≥0.5 was classified as high MI, while a prediction probability <0.5 was classified as low MI. The model discrimination ability was evaluated by drawing the area under the receiver operating characteristic curve (AUROC) and the area under the precision–recall curve (AUPRC). In addition to the hybrid and conventional ResNet models, a traditional shape radiomics feature-based classifier was established in this study; the random forest (RF) algorithm was used in the development set, and the 10-fold cross-validation was performed to evaluate the model, with each fold repeated three times using X&Y software (X&Y Solutions, Inc., Boston, MA, USA) based on the R language. The RF algorithm selected and ranked the parameters according to their importance. The constructed "forest" represents the integration of decision trees (DTs) and was trained with the "bagging" method. Bagging methods involve randomly selecting samples of the derivation dataset with replacement, building classifiers, and finally combining the learned models to increase overall performance. In this study, the number of trees in the RF model was 400, with the variables leading to the minimum "out-bagging" error in the model selected as the optimal model. The feature importance was derived from the mean decrease in impurity (MDI). When the RF model has the best effect, the hyperparameters are set as follows: max_depth = 400, max_features = 4, min_sample_leaf = 1, min_sample_split = 2, and *n*_estimators = 400. In order to evaluate whether the hybrid model achieved better diagnostic efficiency, the DeLong test was used to compare AUROC values (26). A p-value <0.05 was considered statistically significant. Statistical analysis was performed using the R software (V3.6.1).

Results

Characteristics of the study population

The clinical characteristics of 112 patients are summarized in Table 2. The number of patients with low and high MI was 40 and 41 in the development set and 11 and 20 in the test set, respectively. There was no significant difference in the proportion of patients with high MI between the development and test sets (p = 0.186). In the development set, there was a significant difference in age between patients with high and low MI, such that patients with high MI were older (p = 0.032). In the test set, no significant age difference was observed (p = 0.438). In both the development set and test set, there was no significant difference between the high MI group and low MI group in terms of sex (p = 0.224 and p = 0.709, respectively), but the tumor diameter was significantly larger in the high MI group (p < 0.001 and p = 0.003, respectively).

Model evaluation

After the image was provided as an input, the conventional ResNet was pretrained for 30 epochs. Among the 14 shape features, the following four features were screened out by the RF algorithm: Elongation, Maximum 2D Diameter row, Sphericity, and Surface Volume Ratio. The variable importance of the shape features and their different distributions according to MI are shown in Supplementary Figures 2 and 3, respectively. The abovementioned four features along with age and maximum tumor diameter were used as the numerical input to the hybrid model. Then, part of the weights was imported from the pretrained conventional ResNet and fine-tuned by 30 epochs to produce the hybrid model. Table 3 and Figure 3 show the performance of the hybrid model in the development set and test

TABLE 2 Patient characteristics.

	Development set (n = 81)			Test set (n = 31)		
	Low MI (n = 40)	High MI (n = 41)	p	Low MI (n = 11)	High MI (n = 20)	p
Age (years)			**0.032**			0.438
Mean ± SD	52.9 ± 12.8	60.7 ± 18.8		53.7 ± 16.0	59.5 ± 21.0	
Sex			0.224			>0.999
Male	19 (47.5%)	25 (61.0%)		5 (45.5%)	10 (50.0%)	
Female	21 (52.5%)	16 (39.0%)		6 (54.5%)	10 (50.0%)	
Tumor site			0.320			>0.999
Gastric	21 (52.5%)	17 (41.5%)		4 (36.4%)	8 (40.0%)	
Non-gastric	19 (47.5%)	24 (58.5%)		7 (63.6%)	12 (60.0%)	
Diameter (cm)			**<0.001**			**0.003**
Mean ± SD	6.1 ± 1.9	10.8 ± 3.6		4.3 ± 2.5	9.6 ± 6.3	

Data are presented as mean ± SD or number (percentage). Independent samples t-test was applied in continuous variables. Chi-squared test or Fisher's exact test was applied to categorical variables. Bold type indicates statistically significant difference.
Low MI, low mitotic index; High MR, high mitotic index.

set. At the image level, the AUROC, AUPRC, and accuracy were 0.960, 0.968, and 91.4%, respectively, in the development set and 0.947, 0.964, and 90.8, respectively, in the test set. In addition, with the average probabilities from multiple samples per patient, the hybrid model also showed good discrimination ability at the patient level. It achieved AUROC, AUPRC, and accuracy of 0.913, 0.887, and 91.4%, respectively, in the development set and 0.930, 0.941, and 93.6%, respectively, in the test set.

The performance evaluation results of conventional ResNet, shape radiomics classifier, and prediction using age plus diameter are shown in Table 4. In the development set, the conventional ResNet (per slice), conventional ResNet (per patient), shape radiomics classifier, and age plus diameter achieved AUROCs of 0.951, 0.889, 0.677, and 0.698, respectively; AUPRCs of 0.960, 0.871, 0.665, and 0.761, respectively; and accuracies of 0.899, 0.889, 0.680, and 0.716, respectively. In the test set, they achieved AUROCs of 0.927, 0.880, 0.754, and 0.659, respectively; AUPRCs of 0.929, 0.918, 0.851, and 0.824, respectively; and accuracies of 0.887, 0.871, and 0.772, respectively.

Model explanation

Comparison of the hybrid model with other models

The comparison results of AUROCs and accuracies between the hybrid model and age plus diameter, shape radiomics classifier, and conventional ResNet are shown in Supplementary Table 2 and Supplementary Figure 4. In both the development set and the test set, the hybrid model outperformed the prediction of age plus diameter, and there were significant differences in AUROC and accuracy between the two models (all $p < 0.05$ for accuracy and AUROC). In addition, the hybrid model was also superior to the shape radiomics classifier ($p < 0.05$ for both

TABLE 3 Diagnostic performance of the hybrid model for the prediction of mitotic index.

	Development set		Test set	
	Per slice	Per patient[a]	Per slice	Per patient[a]
AUROC (95% CI)	0.960 (0.947–0.973)	0.913 (0.851–0.975)	0.947 (0.927–0.968)	0.930 (0.828–1.000)
AUPRC (95% CI)	0.968 (0.956–0.977)	0.887 (0.787–0.954)	0.964 (0.930–0.978)	0.941 (0.792–1.000)
Acc (95% CI)	91.4 (89.3–93.0)	91.4 (83.2–95.8)	90.8 (88.0–93.0)	93.6 (79.3–98.2)
Sen (95% CI)	91.6 (88.5–93.9)	92.7 (79.0–98.1)	92.1 (88.5–94.6)	95.0 (73.1–99.7)
Spe (95% CI)	91.1 (88.0–93.5)	90.0 (75.4–96.7)	88.5 (82.9–92.5)	90.9 (57.1–99.5)
PPV (95% CI)	91.4 (88.3–93.7)	90.5 (76.5–96.9)	93.4 (90.1–95.7)	95.0 (73.1–99.7)
NPV (95% CI)	91.3 (88.2–93.7)	92.3 (78.0–98.0)	86.2 (80.4–90.6)	90.9 (57.1–99.5)

AUROC, area under the receiver operating characteristics curve; AUPRC, area under the precision–recall curve; Acc, accuracy; Sen, sensitivity; Spe, specificity; PPV, positive predictive value; NPV, negative predictive value.
[a]Since each patient yielded multiple tumor slices, the diagnostic accuracy per patient was calculated from the mean value of the all-predicted probabilities per patient.

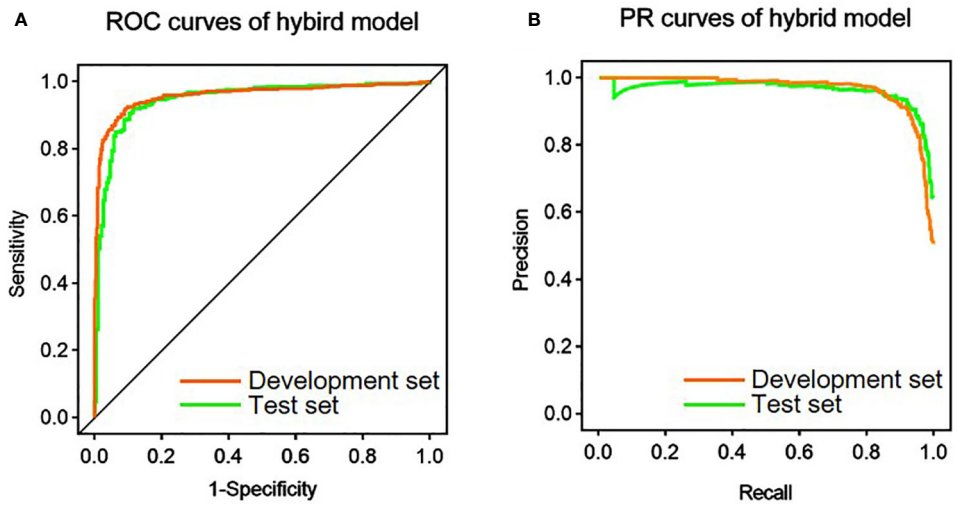

FIGURE 3
Performance of the hybrid model in the prediction of mitotic index. **(A)** Receiver operating characteristic (ROC) curves of the hybrid model in the development and test set. **(B)** Precision-recall (PR) curves of the hybrid model in the development and test set.

accuracy and AUROC). However, compared with conventional ResNet, the hybrid model has slightly higher AUROC and accuracy, but the difference between them is not significant.

Ablation analysis

The results of the ablation analysis are discussed in detail in Supplementary Table 3. Compared with the conventional ResNet, as we reduced the number of input images per patient and reduced the sequences or masked tumor area, we observed a decrease in the diagnostic performance, with accuracies, AUROCs, and AUPRCs at 70.4%–84%, 0.840–0.704, and 0.676–0.814, respectively, in the development set and 61.3%–83.9%, 0.639–0.834, and 0.746–0.873, respectively, in the test set. When we masked the tumor area from image inputs, the lowest diagnostic performance was achieved, with accuracy, AUROC, and AUPRC of 61.7%, 0.618, and 0.602, respectively, in the development set and 54.8%, 0.548, and 0.676, respectively, in the test set.

Cross-validation

To ensure that the performance of the hybrid model was not due to the random selection of the internal test set, we performed a patient-level threefold cross-validation on the entire cohort (n = 112). In the internal validation set, the mean AUROC was 0.910 (range, 0.896–0.927) and 0.903 (range, 0.849–0.980) in the hybrid model (per slice) and hybrid model (per patient), respectively (Supplementary Table 4), similar to those in the test set. The cross-validation results show that the hybrid model has good robustness.

TABLE 4 Diagnostic performance of the conventional ResNet, shape radiomics classifier, and age plus diameter in the prediction of mitotic index.

	Dataset	AUROC (95% CI)	AUPRC (95% CI)	Acc (95% CI)
Conventional ResNet (per slice)	Development set	0.951 (0.937–0.966)	0.960 (0.947–0.970)	89.9 (87.8–91.7)
	Test set	0.927 (0.901–0.953)	0.929 (0.880–0.959)	88.7 (85.7–91.1)
Conventional ResNet (per patient)[a]	Development set	0.889 (0.820–0.958)	0.871 (0.769–0.946)	88.9 (80.2–94.0)
	Test set	0.880 (0.760–1.000)	0.918 (0.746–0.979)	87.1 (71.2–94.9)
Shape radiomics classifier	Development set	0.677 (0.641–0.712)	0.665 (0.629–0.709)	68.0 (64.9–71.0)
	Test set	0.754 (0.712–0.797)	0.851 (0.823–0.876)	77.2 (73.5–80.6)
Age plus diameter	Development set	0.698 (0.574–0.803)	0.761 (0.657–0.852)	71.6 (61.0–80.3)
	Test set	0.659 (0.465–0.853)	0.824 (0.690–0.915)	61.3 (43.8–76.3)

AUROC, area under the receiver operating characteristics curve; AUPRC, area under the precision–recall curve.
[a]Since each patient yielded multiple tumor slices, the diagnostic accuracy per patient was calculated from the mean value of the all-predicted probabilities per patient.

Discussion

In this study, based on a ResNet50 CNN, we developed a hybrid model to predict the MI status of GIST patients. The CNN integrating 2D tumor signal intensity, 3D tumor shape, patient age, and tumor size showed good predictive power in both the development and test sets.

GIST mitotic index is an important indicator of metastasis and prognosis, which is independent of the tumor size and location; this led to the integration of this indicator in the NIH system. Although radical resection is still the most commonly used standard treatment for GIST, due to the high risk of postoperative recurrence for patients with high MI, surgical resection following neoadjuvant therapy may improve the prognosis (27). Preoperative prediction of MI potentially helps in setting the treatment plan, which leads to the investigation of radiological findings to predict the MI status. A previous CT study showed that GIST with high MI and high-risk grade is more prone to internal necrosis, neovascularization, and peripheral invasion, while low MI tumors have more regular morphology and clearer boundaries with the surrounding tissues (28). In addition, an MR study with higher soft tissue resolution showed that tumor enhancement was significantly stronger in patients with high MI compared with patients with low MI, which may be related to the formation of new tumor vessels inside (29). Some studies tried to evaluate the grading of GIST using a DWI-based ADC map and PET-CT parameter map, and they found the ADC value to be negatively correlated with the grading of the GIST tumor, while the metabolic rate was negatively correlated with it (30, 31). Changes in ADC caused by targeted therapy may be related to a variety of cell death mechanisms, including mitotic catastrophe, which indicates that ADC can provide more information to evaluate mitosis from a therapeutic perspective (32). Therefore, the ADC map was taken as one of the sequences of the multimodal study in this study.

Radiomics can be used to obtain high-level features of tumor images, which can reflect the heterogeneity of tumors and provide a basis to evaluate biological behavior (33). A recent enhanced CT-based study found a close relationship between the mitotic number and 14 radiomics features of GIST, which suggests that it may be another possible method to predict the number of GIST (34). However, this study was based only on 2D images of the maximum cross-section of the tumor, which did not fully obtain the overall information about the tumor. Moreover, the study only included enhanced CT images, with a single type of image. As a result, the accuracy of its prediction model in the test set was only 85.4%. In this study, the accuracy of the hybrid model reached 93.6% after including the information at all layers of the tumor.

Deep learning refers to a technology that combines low-level features to form more abstract high-level features or categories and then learns effective features from a large number of input elements and uses these features to perform classification, regression, and information retrieval. There are many kinds of DL models, among which CNN is most widely used in the field of medical imaging. Unlike traditional radiomics based on manual feature extraction, high-throughput image features can be directly extracted from deep neural networks (DNNs) without additional feature extraction operations; thus, no additional error occurs in the analysis due to feature calculation, and the effectiveness of the feature is only related to the segmentation quality (35, 36). At present, CNN has been successfully applied in many aspects, such as genotype prediction, preoperative staging, lymph node metastasis prediction, and prognosis evaluation of malignant tumors (37–39). The application of the DL algorithm to extract image information can overcome the influence of observer subjectivity.

Researchers have begun to explore the application of DL in the diagnosis and evaluation of GIST. Previously, a DL model for predicting the mitotic index of GIST was preliminarily established by providing venous images as input into CNN. The results showed that the image-based DL model could evaluate the MI of GIST before surgery (40). However, the generalization ability of the model proposed in their study was not high, and the area under the curve (AUC) in the internal test set was only 0.771–0.800. In our study, the AUC of the conventional ResNet model reached 0.880–0.927 in the test set, while the hybrid model achieved an even better predictive ability, with an AUC of 0.930–0.947. The reason may be that MR has a higher soft tissue resolution as compared with CT, so images may contain more information, and the extracted DL features may have better discrimination ability. The input images in this study were multimodal MR images (including T2WI and DWI images). Previous studies have confirmed that multimodal images can improve the final effect of the DL model. In a previous study, researchers also fed endoscopic ultrasound images into neural networks for auxiliary diagnosis of GIST and gastrointestinal leiomyoma. Their study showed that the two tumor types could not be distinguished based on naked-eye observation, and the accuracy was only 63%, while the accuracy of the CNN system reached 86.98% (41). Another study confirmed that an EUS–CNN system can be helpful not only for less-experienced endoscopists but also for experienced ones (42).

ResNet50 CNN was selected as the basic model in this study. ResNet50 is a network framework of residual learning that solves the degradation problem of decreasing accuracy caused by increasing the network depth. Compared with previous models, the residual network is easier to optimize and can derive accuracy from a significantly increased depth (43). Many previous studies have used this network to classify tumors and achieved good results (44–46). The transfer learning method was adopted, and a fully connected layer was added to the hybrid model. The results of multi-slice CT images can better reflect the overall biological behavior and mitotic rate of the tumor than that of single-slice CT images (47).

In addition to the multi-modal image input, the construction process of the proposed hybrid model proposed was different from that of the image-based CNN model reported in previous studies (40). While the hybrid model combined shape features and clinical indicators, in order to ensure the robustness of the model, only shape features in traditional radiomics were selected to establish the model. The main factor limiting the repeatability of radiomics features is that the extraction results of first-order and texture features depend on the range and number of bins of signal intensity, and there is currently no accepted standard to set the signal strength-related parameters (48, 49). Unlike the intensity feature, the morphological feature is independent of the abovementioned settings and can thus remain stable across studies. This improves the stability of the research model.

The hybrid model fuses the 3D tumor morphology and mitotic-related clinical indicators (age and tumor size) with the CNN model, thus producing an enhanced model performance compared with image-based CNN alone. Previous studies showed that age and tumor size are independent risk factors for prognosis in GIST patients (50). In this study, there were significant differences in the age and maximum diameter between the high MI group and low MI group. It was previously shown that older patients with meningiomas are more likely to have more active mitosis and larger tumors, which indicates that they have faster tumor division and may have a higher MI (51). However, the relationship between MI and the factors of age and tumor size needs to be further confirmed in GIST. Despite the differences between groups, the prediction efficiency of these two indicators alone for MI is very low, which also indicates that it is difficult to use only clinical indicators for the MI status of tumors in clinical practice, and we need to combine more indicators reflecting the internal heterogeneity of the tumor.

This study used radiomics and deep learning analysis based on MR plain scan images to predict mitosis in GIST. However, due to the limited time resolution, MR is highly susceptible to respiratory movement and intestinal peristalsis during abdominal imaging, which limits its application in GIST assessment. Compared with MR, CT is more widely used in the preoperative evaluation of GIST in clinical at present, which has the advantages of low cost, short examination time, and low susceptibility to motion artifacts (52). However, plain CT has the inherent defect of insufficient soft tissue resolution, so contrast-enhanced CT is often adopted for preoperative evaluation of GIST, which may increase the renal burden and allergy risk of patients. In addition, CT imaging is single-parameter imaging based on tissue density, which provides limited information. However, MRI has the advantage of multi-sequence and arbitrary angle imaging, which is more conducive to displaying the relationship between tumors and surrounding organs from different angles. Given the above advantages of MR, GIST can be accurately assessed clinically using only MR plain scan sequences (53). In addition to higher tissue contrast, the application of functional imaging sequences such as DWI can provide microscopic information about the tumor from the tissue level and even the cell level (30). Radiomics or deep learning features based on such specially weighted images may better reflect the heterogeneity of the tumor.

This study has some limitations that merit discussion. First, the sample size of this study is small, so future studies should continue the data collection and use a larger sample size. Second, this study is a single-center study. Although internal verification has been performed, the repeatability and generalization ability of the model should be further verified by external datasets. Finally, because GIST is irregular in shape and may occur in any part of the digestive tract and its adjacent tissues and organs are complex, it is difficult to achieve automatic segmentation of the tumors. In this study, manual segmentation was adopted, which is more difficult but more accurate.

In conclusion, we developed a deep learning-based model that used radiomics and clinical features to reliably predict the MI status in GIST based on conventional, unenhanced MR images. Our model is expected to serve as a practical tool for the non-invasive characterization of GIST to support personalized treatment plans.

Data availability statement

The raw data supporting the conclusions of this article will be made available by the authors, without undue reservation.

Ethics statement

The studies involving human participants were reviewed and approved by The Ethics Committee of the First Hospital of Qinhuangdao. Written informed consent for participation was not required for this study in accordance with the national legislation and the institutional requirements. Written informed consent was not obtained from the individual(s) for the publication of any potentially identifiable images or data included in this article.

Author contributions

DL, ZW, LL, and YC designed and coordinated the study. LY, DD, TZ, HY, JD, and YF carried out the experiment and data processing and drafted the manuscript. All authors gave the final approval for the publication.

Funding

The research leading to these results has received funding from the National Science Foundation of China (81871029).

Conflict of interest

The authors declare that the research was conducted in the absence of any commercial or financial relationships that could be construed as a potential conflict of interest.

Publisher's note

All claims expressed in this article are solely those of the authors and do not necessarily represent those of their affiliated organizations, or those of the publisher, the editors and the reviewers. Any product that may be evaluated in this article, or claim that may be made by its manufacturer, is not guaranteed or endorsed by the publisher.

Supplementary material

The Supplementary Material for this article can be found online at: https://www.frontiersin.org/articles/10.3389/fonc.2022.948557/full#supplementary-material

References

1. Sharma AK, de la Torre J, IJ NS, Sutton TL, Zhao B, Khan TM, et al. Location of gastrointestinal stromal tumor (GIST) in the stomach predicts tumor mutation profile and drug sensitivity. *Clin Cancer* (2021) 27:5334–42. doi: 10.1158/1078-0432.CCR-21-1221

2. Wu CE, Tzen CY, Wang SY, Yeh CN. Clinical diagnosis of gastrointestinal stromal tumor (GIST): From the molecular genetic point of view. *Cancers* (2019) 11:679. doi: 10.3390/cancers11050679

3. Søreide K, Sandvik OM, Søreide JA, Giljaca V, Jureckova A, Bulusu VR. Global epidemiology of gastrointestinal stromal tumours (GIST): A systematic review of population-based cohort studies. *Cancer Epidemiol* (2016) 40:39–46. doi: 10.1016/j.canep.2015.10.031

4. Rubin JL, Sanon M, Taylor DC, Coombs J, Bollu V, Sirulnik L. Epidemiology, survival, and costs of localized gastrointestinal stromal tumors. *Int J Gen Med* (2011) 4:121–30. doi: 10.2147/IJGM.S16090

5. Farid M, Ong J, Chia C, Tan G, Teo M, Quek R, et al. Treatment of gastrointestinal tumor (GIST) of the rectum requiring abdominoperineal resection following neoadjuvant imatinib: a cost-effectiveness analysis. *Clin sarcoma Res* (2020) 10:13. doi: 10.1186/s13569-020-00135-7

6. Joensuu H. Risk stratification of patients diagnosed with gastrointestinal stromal tumor. *Hum Pathol* (2008) 39:1411–9. doi: 10.1016/j.humpath.2008.06.025

7. Sicklick JK, Lopez NE. Optimizing surgical and imatinib therapy for the treatment of gastrointestinal stromal tumors. *J gastrointestinal Surg Off J Soc Surg Alimentary Tract* (2013) 17:1997–2006. doi: 10.1007/s11605-013-2243-0

8. Poveda A, García Del Muro X, López-Guerrero JA, Cubedo R, Martínez V, Romero I, et al. GEIS guidelines for gastrointestinal sarcomas (GIST). *Cancer Treat Rev* (2017) 55:107–19. doi: 10.1016/j.ctrv.2016.11.011

9. Demetri GD, von Mehren M, Antonescu CR, DeMatteo RP, Ganjoo KN, Maki RG, et al. NCCN task force report: update on the management of patients with gastrointestinal stromal tumors. *J Natl Compr Cancer Network JNCCN* (2010) 8 Suppl 2:S1–41; quiz S2-4. doi: 10.6004/jnccn.2010.0116

10. Mullady DK, Tan BR. A multidisciplinary approach to the diagnosis and treatment of gastrointestinal stromal tumor. *J Clin Gastroenterol* (2013) 47:578–85. doi: 10.1097/MCG.0b013e3182936c87

11. Lim KT, Tan KY. Current research and treatment for gastrointestinal stromal tumors. *World J Gastroenterol* (2017) 23:4856–66. doi: 10.3748/wjg.v23.i27.4856

12. Szukics B, Wagner A. [Diagnostic endoscopy and endoscopic ultrasonography of gastrointestinal stroma tumors]. *Der Radiologe* (2009) 49:1117–21. doi: 10.1007/s00117-009-1851-x

13. Grazzini G, Guerri S, Cozzi D, Danti G, Gasperoni S, Pradella S, et al. Gastrointestinal stromal tumors: relationship between preoperative CT features and pathologic risk stratification. *Tumori* (2021) 107:556–63. doi: 10.1177/0300891621996447

14. Sandrasegaran K, Rajesh A, Rushing DA, Rydberg J, Akisik FM, Henley JD. Gastrointestinal stromal tumors: CT and MRI findings. *Eur Radiol* (2005) 15:1407–14. doi: 10.1007/s00330-005-2647-7

15. Cannella R, Tabone E, Porrello G, Cappello G, Gozzo C, Incorvaia L, et al. Assessment of morphological CT imaging features for the prediction of risk stratification, mutations, and prognosis of gastrointestinal stromal tumors. *Eur Radiol* (2021) 31:8554–64. doi: 10.1007/s00330-021-07961-3

16. Zhou C, Duan X, Zhang X, Hu H, Wang D, Shen J. Predictive features of CT for risk stratifications in patients with primary gastrointestinal stromal tumour. *Eur Radiol* (2016) 26:3086–93. doi: 10.1007/s00330-015-4172-7

17. Lambin P, Rios-Velazquez E, Leijenaar R, Carvalho S, van Stiphout RG, Granton P, et al. Radiomics: extracting more information from medical images using advanced feature analysis. *Eur J Cancer (Oxford Engl 1990)* (2012) 48:441–6. doi: 10.1016/j.ejca.2011.11.036

18. Lin X, Zhao S, Jiang H, Jia F, Wang G, He B, et al. A radiomics-based nomogram for preoperative T staging prediction of rectal cancer. *Abdominal Radiol (New York)* (2021) 46:4525–35. doi: 10.1007/s00261-021-03137-1

19. Liu Y, Zhang Y, Cheng R, Liu S, Qu F, Yin X, et al. Radiomics analysis of apparent diffusion coefficient in cervical cancer: A preliminary study on histological grade evaluation. *J magnetic resonance Imaging JMRI* (2019) 49:280–90. doi: 10.1002/jmri.26192

20. Guerrisi A, Russillo M, Loi E, Ganeshan B, Ungania S, Desiderio F, et al. Exploring CT texture parameters as predictive and response imaging biomarkers of survival in patients with metastatic melanoma treated with PD-1 inhibitor nivolumab: A pilot study using a delta-radiomics approach. *Front Oncol* (2021) 11:704607. doi: 10.3389/fonc.2021.704607

21. Hinton GE, Salakhutdinov RR. Reducing the dimensionality of data with neural networks. *Sci (New York NY)* (2006) 313:504–7. doi: 10.1126/science.1127647

22. Avanzo M, Wei L, Stancanello J, Vallières M, Rao A, Morin O, et al. Machine and deep learning methods for radiomics. *Med Phys* (2020) 47:e185–202. doi: 10.1002/mp.13678

23. Chen Y, Tian X, Fan K, Zheng Y, Tian N, Fan K. The value of artificial intelligence film reading system based on deep learning in the diagnosis of non-Small-Cell lung cancer and the significance of efficacy monitoring: A retrospective, clinical, nonrandomized, controlled study. *Comput Math Methods Med* (2022) 2022:2864170. doi: 10.1155/2022/2864170

24. Liu H, Chen Y, Zhang Y, Wang L, Luo R, Wu H, et al. And clinical factors facilitates the malignancy prediction of BI-RADS 4 microcalcifications in breast cancer screening. *Eur Radiol* (2021) 31:5902–12. doi: 10.1007/s00330-020-07659-y

25. Zhang W, Yin H, Huang Z, Zhao J, Zheng H, He D, et al. Development and validation of MRI-based deep learning models for prediction of microsatellite instability in rectal cancer. *Cancer Med* (2021) 10:4164–73. doi: 10.1002/cam4.3957

26. DeLong ER, DeLong DM, Clarke-Pearson DL. Comparing the areas under two or more correlated receiver operating characteristic curves: a nonparametric approach. *Biometrics* (1988) 44:837–45. doi: 10.2307/2531595

27. Ishikawa T, Kanda T, Kameyama H, Wakai T. Neoadjuvant therapy for gastrointestinal stromal tumor. *Trans Gastroenterol Hepatol* (2018) 3:3. doi: 10.21037/tgh.2018.01.01

28. Iannicelli E, Carbonetti F, Federici GF, Martini I, Caterino S, Pilozzi E, et al. Evaluation of the relationships between computed tomography features, pathological findings, and prognostic risk assessment in gastrointestinal stromal tumors. *J Comput assisted tomography* (2017) 41:271–8. doi: 10.1097/RCT.0000000000000499

29. Amano M, Okuda T, Amano Y, Tajiri T, Kumazaki T. Magnetic resonance imaging of gastrointestinal stromal tumor in the abdomen and pelvis. *Clin Imaging* (2006) 30:127–31. doi: 10.1016/j.clinimag.2005.09.025

30. Wong CS, Gong N, Chu YC, Anthony MP, Chan Q, Lee HF, et al. Correlation of measurements from diffusion weighted MR imaging and FDG PET/CT in GIST patients: ADC versus SUV. *Eur J Radiol* (2012) 81:2122–6. doi: 10.1016/j.ejrad.2011.09.003

31. Gong NJ, Wong CS, Chu YC, Guo H, Huang B, Chan Q. Increasing the accuracy of volume and ADC delineation for heterogeneous tumor on diffusion-weighted MRI: correlation with PET/CT. *Int J Radiat oncology biology Phys* (2013) 87:407–13. doi: 10.1016/j.ijrobp.2013.05.026

32. Morse DL, Galons JP, Payne CM, Jennings DL, Day S, Xia G, et al. MRI-Measured water mobility increases in response to chemotherapy *via* multiple cell-death mechanisms. *NMR biomedicine* (2007) 20:602–14. doi: 10.1002/nbm.1127

33. Mayerhoefer ME, Materka A, Langs G, Häggström I, Szczypiński P, Gibbs P, et al. Introduction to radiomics. *J Nucl Med Off publication Soc Nucl Med* (2020) 61:488–95. doi: 10.2967/jnumed.118.222893

34. Wang C, Li H, Jiaerken Y, Huang P, Sun L, Dong F, et al. Building CT radiomics-based models for preoperatively predicting malignant potential and mitotic count of gastrointestinal stromal tumors. *Trans Oncol* (2019) 12:1229–36. doi: 10.1016/j.tranon.2019.06.005

35. Driver CN, Bowles BS, Bartholmai BJ, Greenberg-Worisek AJ. Artificial intelligence in radiology: A call for thoughtful application. *Clin Trans Sci* (2020) 13:216–8. doi: 10.1111/cts.12704

36. Chen L, Zhou Z, Sher D, Zhang Q, Shah J, Pham NL, et al. Combining many-objective radiomics and 3D convolutional neural network through evidential reasoning to predict lymph node metastasis in head and neck cancer. *Phys Med Biol* (2019) 64:075011. doi: 10.1088/1361-6560/ab083a

37. Tang Z, Xu Y, Jin L, Aibaidula A, Lu J, Jiao Z, et al. Deep learning of imaging phenotype and genotype for predicting overall survival time of glioblastoma patients. *IEEE Trans Med Imaging* (2020) 39:2100–9. doi: 10.1109/TMI.2020.2964310

38. Nasrullah N, Sang J, Alam MS, Mateen M, Cai B, Hu H. Automated lung nodule detection and classification using deep learning combined with multiple strategies. *Sensors (Basel Switzerland)* (2019) 19:3722. doi: 10.3390/s19173722

39. Kather JN, Krisam J, Charoentong P, Luedde T, Herpel E, Weis CA, et al. Predicting survival from colorectal cancer histology slides using deep learning: A retrospective multicenter study. *PloS Med* (2019) 16:e1002730. doi: 10.1371/journal.pmed.1002730

40. Yang J, Chen Z, Liu W, Wang X, Ma S, Jin F, et al. Development of a malignancy potential binary prediction model based on deep learning for the mitotic count of local primary gastrointestinal stromal tumors. *Korean J Radiol* (2021) 22:344–53. doi: 10.3348/kjr.2019.0851

41. Seven G, Silahtaroglu G, Seven OO, Senturk H. Differentiating gastrointestinal stromal tumors from leiomyomas using a neural network trained on endoscopic ultrasonography images. *Digestive Dis (Basel Switzerland)* (2022) 40:427–435. doi: 10.1159/000520032

42. Oh CK, Kim T, Cho YK, Cheung DY, Lee BI, Cho YS, et al. Convolutional neural network-based object detection model to identify gastrointestinal stromal tumors in endoscopic ultrasound images. *J Gastroenterol Hepatol* (2021) 36:3387–94. doi: 10.1111/jgh.15653

43. He K, Zhang X, Ren S, Sun J. Deep residual learning for image recognition. In: *Proceedings of the IEEE conference on computer vision and pattern recognition*. Las Vegas, NV, USA (2016).

44. Sadad T, Rehman A, Munir A, Saba T, Tariq U, Ayesha N, et al. Brain tumor detection and multi-classification using advanced deep learning techniques. *Microscopy Res technique* (2021) 84:1296–308. doi: 10.1002/jemt.23688

45. Zhou J, Zhang Y, Chang KT, Lee KE, Wang O, Li J, et al. Diagnosis of benign and malignant breast lesions on DCE-MRI by using radiomics and deep learning with consideration of peritumor tissue. *J magnetic resonance Imaging JMRI* (2020) 51:798–809. doi: 10.1002/jmri.26981

46. Houssein EH, Emam MM, Ali AA. An optimized deep learning architecture for breast cancer diagnosis based on improved marine predators algorithm. *Neural computing Appl* (2022) 34:18015–33. doi: 10.1007/s00521-022-07445-5

47. Watabe T, Tatsumi M, Watabe H, Isohashi K, Kato H, Yanagawa M, et al. Intratumoral heterogeneity of f-18 FDG uptake differentiates between gastrointestinal stromal tumors and abdominal malignant lymphomas on PET/CT. *Ann Nucl Med* (2012) 26:222–7. doi: 10.1007/s12149-011-0562-3

48. Traverso A, Wee L, Dekker A, Gillies R. Repeatability and reproducibility of radiomic features: A systematic review. *Int J Radiat oncology biology Phys* (2018) 102:1143–58. doi: 10.1016/j.ijrobp.2018.05.053

49. Li Q, Bai H, Chen Y, Sun Q, Liu L, Zhou S, et al. A fully-automatic multiparametric radiomics model: Towards reproducible and prognostic imaging signature for prediction of overall survival in glioblastoma multiforme. *Sci Rep* (2017) 7:14331. doi: 10.1038/s41598-017-14753-7

50. Harlan LC, Eisenstein J, Russell MC, Stevens JL, Cardona K. Gastrointestinal stromal tumors: treatment patterns of a population-based sample. *J Surg Oncol* (2015) 111:702–7. doi: 10.1002/jso.23879

51. Mermanishvili TL, Dzhorbenadze TA, Chachia GG. [Association of the degree of differentiation and the mitotic activity of intracranial meningiomas with age and gender]. *Arkhiv patologii* (2010) 72:16–8.

52. Liu X, Yin Y, Wang X, Yang C, Wan S, Yin X, et al. Gastrointestinal stromal tumors: associations between contrast-enhanced CT images and KIT exon 11 gene mutation. *Ann Trans Med* (2021) 9:1496. doi: 10.21037/atm-21-3811

53. Yu MH, Lee JM, Baek JH, Han JK, Choi BI. MRI Features of gastrointestinal stromal tumors. *AJR Am J Roentgenol* (2014) 203:980–91. doi: 10.2214/AJR.13.11667

frontiers | Frontiers in Oncology

TYPE Original Research
PUBLISHED 12 December 2022
DOI 10.3389/fonc.2022.925186

OPEN ACCESS

EDITED BY
Pilar López-Larrubia,
Spanish National Research Council (CSIC), Spain

REVIEWED BY
Nataliya Lutay,
Skåne University Hospital, Sweden
Xiaoming Qiu,
Huangshi Central Hospital, China

*CORRESPONDENCE
Hongmei Sun
sunhongmei2020@yeah.net

SPECIALTY SECTION
This article was submitted to Cancer Imaging and Image-directed Interventions, a section of the journal Frontiers in Oncology

RECEIVED 21 April 2022
ACCEPTED 21 November 2022
PUBLISHED 12 December 2022

CITATION
Sun H, Du F, Liu Y, Li Q, Liu X and Wang T (2022) DCE-MRI and DWI can differentiate benign from malignant prostate tumors when serum PSA is ≥10 ng/ml.
Front. Oncol. 12:925186.
doi: 10.3389/fonc.2022.925186

DCE-MRI and DWI can differentiate benign from malignant prostate tumors when serum PSA is ≥10 ng/ml

Hongmei Sun[1]*, Fengli Du[2], Yan Liu[3], Qian Li[1], Xinai Liu[1] and Tongming Wang[1]

[1]Department of Magenetic Resonance Imaging (MRI), Henan Province Hospital of Traditional Chinese Medicine (The Second Affiliated Hospital of Henan University of Chinese Medicine), Zhengzhou, China, [2]Henan University of Chinese Medicine, Zhengzhou, China, [3]School of Medical Engineering, Xinxiang Medical University, Xinxiang, China

Background: This study investigated the diagnostic utility of dynamic contrast-enhanced magnetic resonance imaging (DCE-MRI) and diffusion-weighted imaging (DWI) parameters for distinguishing between benign and malignant prostate tumors when serum prostate-specific antigen (PSA) level is ≥10 ng/ml.

Methods: Patients with prostate cancer (PCa) and benign prostatic hyperplasia (BPH) with serum PSA ≥10 ng/ml before treatment were recruited. Transrectal ultrasound-guided biopsy or surgery was performed for tumor classification and patients were stratified accordingly into PCa and BPH groups. Patients underwent DCE-MRI and DWI scanning and the transfer constant (K_{trans}), rate constant (K_{ep}), fractional volume of the extravascular extracellular space, plasma volume (V_p), and Prostate Imaging Reporting and Data System Version 2 (PI-RADS v2) score were determined. The apparent diffusion coefficient (ADC) was calculated from DWI. The diagnostic performance of these parameters was assessed by receiver operating characteristic (ROC) curve analysis, and those showing a significant difference between the PCa and BPH groups were combined into a multivariate logistic regression model for PCa diagnosis. Spearman's correlation was used to analyze the relationship between Gleason score and imaging parameters.

Results: The study enrolled 65 patients including 32 with PCa and 33 with BPH. Ktrans (P=0.006), Kep (P=0.001), and Vp (P=0.009) from DCE-MRI and ADC (P<0.001) from DWI could distinguish between the 2 groups when PSA was ≥10 ng/ml. PI-RADS score (area under the ROC curve [AUC]=0.705), Ktrans (AUC=0.700), Kep (AUC=0.737), Vp (AUC=0.688), and ADC (AUC=0.999) showed high diagnostic performance for discriminating PCa from BPH. A combined model based on PI-RADS score, Ktrans, Kep, Vp, and ADC had a

higher AUC (1.000), with a sensitivity of 0.998 and specificity of 0.999. Imaging markers showed no significant correlation with Gleason score in PCa.

Conclusion: DCE-MRI and DWI parameters can distinguish between benign and malignant prostate tumors in patients with serum PSA ≥10 ng/ml.

KEYWORDS

prostate cancer, prostate-specific antigen, PI-RADS, dynamic contrast-enhanced magnetic resonance imaging, diffusion-weighted imaging

Introduction

Prostate cancer (PCa) has a high morbidity and mortality (1). Prostate tumors are small, slow-growing lesions that are potentially curable at an early stage. Prostate tumor cells can undergo malignant transformation and overproliferate within a short period of time, which is associated with a poor outcome (2). Current diagnostic methods for PCa include measurement of prostate-specific antigen (PSA), fine needle aspiration biopsy, and postoperative pathologic examination. PSA is a highly expressed marker in the prostate; however, abnormally high PSA concentrations are not necessarily indicative of PCa, as serum PSA is also elevated in benign prostatic hyperplasia (BPH) (3). Thus, measurement of serum PSA lacks specificity and sensitivity for diagnosing PCa. The gold standard is biopsy but pathologic information can only be obtained after surgery or through invasive method by needle biopsy, which is unacceptable for high-risk patients. Transrectal ultrasound (TRUS) scanning is efficient for screening but is associated with complications.

Solid tumors exist in a complex microenvironment that contributes to tumor heterogeneity (4). Increased angiogenesis is correlated with tumor cell proliferation and metastasis. Dynamic contrast enhancement magnetic resonance imaging (DCE-MRI) is widely used to monitor changes in vascular permeability (5–7). Five quantitative parameters that can be extracted from DCE-MRI are the transfer constant (K_{trans}), rate constant (K_{ep}), fractional volume of the extravascular extracellular space (V_e), and plasma volume (V_p) (8–10). K_{trans} represents the diffusion rate of the gadolinium (Gd) contrast agent; Ve is the volume of Gd contrast relative to the total extravascular extracellular space volume; K_{ep} is K_{trans}/V_e; and V_p is calculated from the volume of Gd contrast agent in plasma. These parameters can be used to measure vessel density and the permeability of the vessel endothelium. Diffusion-weighted imaging (DWI) reflects the Brownian motion of H_2O; the diffusion rate is used to calculate the apparent diffusion coefficient (ADC), which is directly proportional to the metabolic rate—and accordingly, the aggressivity—of the tumor. ADC has been applied to the classification of a variety of tumors including breast tumors, glioma, etc. (11) Prostate Imaging Reporting and Data System Version 2 (PI-PRADS v2) is recommended as a noninvasive method for diagnosing PCa, although it has low specificity (12).

Given the limitations of PSA, TRUS, and PI-PRADS v2, the present study investigated the clinical utility of DCE-MRI and DWI parameters for differentiating between PCa and BPH. We also established a multivariate logistic regression model that can be used to predict the malignancy of PCa.

Abbreviations: ADC, apparent diffusion coefficient; AIF, arterial input function; AUC, area under the receiver operating characteristic curve; BPH, benign prostatic hyperplasia; BW, bandwidth; CI, confidence interval; DCE, dynamic contrast-enhanced; DWI, diffusion-weighted imaging; FA, fractional anisotropy; FOV, field of view; Gd, gadolinium; K_{ep}, rate constant; K_{trans}, transfer constant; LAVA, liver acquisition with volume acceleration; mpMRI, multiparameter magnetic resonance imaging; MRI, magnetic resonance imaging; NEX, number of excitations; PCa, prostate cancer; PI-RADS, Prostate Imaging Reporting And Data System; PSA, prostate-specific antigen; ROC, receiver operating characteristic; ROI, region of interest; T1WI, T1-weighted imaging; T2WI, T2-weighted imaging; TCM, traditional Chinese medicine; TE, echo time; TR, repetition time; TRUS, transrectal ultrasound scanning; V_e, fractional volume of the extravascular extracellular space; Vp, plasma volume.

Materials and methods

Patients

For this retrospective study, patients with elevated PSA and clinically suspected PCa or BPH were recruited at Henan Province Hospital of Traditional Chinese Medicine (TCM) (Zhengzhou, China) between December 2016 and October 2020. The inclusion criteria were as follows: 1) PCa or BPH confirmed by pathologic examination following ultrasound-guided puncture or surgical tumor biopsy; 2) no treatment prior to MRI scanning; 3) no MRI within 3 weeks of

pathologic examination; 4) no MRI contraindications such as claustrophobia; 5) PSA ≥10 ng/ml before MRI; and 6) good image quality sufficient for diagnosis. The study was approved by the institutional review board of Henan Province Hospital of TCM. A flow diagram of the study protocol is shown in Figure 1.
MRI scanning

All patients underwent DCE-MRI examination with a 3.0T MRI scanner (Signa HDxt; GE Healthcare, South Burlington, VT, USA). MRI scanning data no more than 1 month before surgery. The MRI protocol was set according to PI-RADS v2 (12). Patients lay in the supine position and were scanned feet-first. The 8-channel body phased surface coil (GE Healthcare) was located above the pelvis. The general MRI scan included T1-weighted imaging (T1WI), T2WI, liver acquisition with volume acceleration (LAVA), and DWI. The LAVA sequence parameters were as follows: repetition time (TR)=3.368 ms, echo time (TE)=1.672 ms, flip angle=15°, number of excitations (NEX)=1, acquisition matrix=256×192, bandwidth (BW) =244.141 Hz, field of view (FOV)=512×512, slice thickness=5, time resolution=10 s, period images=21, and scanning time=3.5 min. Before LAVA, patients were scanned with multiple fractional anisotropy (FA) sequences (FA=3°, 9°, and 12°) with only 1 phase of LAVA. Gadopentetate dimeglumine (Omniscan®; GE Healthcare) was injected with a high-pressure injector at a rate of 2 ml/s at 0.1 ml/kg body weight, followed by flushing with 20 ml saline solution. DWI was performed with the following parameters: b value=100 and 800, TR=5200 ms, TE=75.9 ms, FA=90, slice thickness=4, FOV=256×256, NEX=6, acquisition matrix=96×130, and BW=1953.12 Hz.

Imaging data analysis

An ADC map was obtained from the DWI scan. Two radiologists with 5–10 years of experience delineated the suspected lesions in all slices on ADC maps by comparing T1WI and T2WI data. At same time, seminal vesicles, vessels, calcification, hemorrhage, and artifacts were excluded from the region of interest (ROI). Each ROI was segmented twice to calculate the mean ADC value. DCE-MRI images were input into Omni-Kinetics v2.1.0.R software (GE Healthcare, Shanghai, China) (9). The T1 map was generated, and T10 was calculated from the multi-FA sequence (10). We selected the femoral artery to calculate arterial input function (AIF) of normal vessels and obtained a concentration–time curve (10). We used the Tofts model (13) to calculate the vascular permeability parameters K_{trans}, K_{ep}, V_e, and V_p and generated a map. In order to obtain the vascular permeability parameter values in lesions, the ROI was marked as the lesion in all DCE-MRI images to ensure that the ROI could be identified in the biopsy specimens (Figure 1).

Two relatively experienced radiologists (HS and FD) who were blinded to the clinical information of patients retrospectively and independently evaluated the images and assigned a PI-RADS score to suspicious lesions according to PI-RADS v2 guidelines (12); any disagreements were resolved by a third senior radiologist. (Figure 2).

Pathologic examination

All patients with abnormal PSA underwent a pathologic examination. Tissue samples were obtained from 24 patients who underwent surgery and 41 who underwent conventional 6 + 4- or 6 + 3-needle TRUS-guided prostate biopsy (6 standard needle points, 2 points to side of the peripheral area, and 1 or 2 points to the suspicious area).[14] The tissue specimens were fixed in 4% paraformaldehyde for 1 week at 24°C and then embedded in paraffin. The tissue blocks were cut into sections that were stained with hematoxylin and eosin and examined under a light microscope by a pathologist with 5 years of experience. A Gleason score—which was calculated as the sum of primary and secondary patterns and ranged from 2 to 10, with a higher score indicating poorer differentiation (14)—was assigned to each sample.

Statistical analysis

The Mann–Whitney U test or t test was performed with Prism 8 software (GraphPad, La Jolla, CA, USA). Vascular permeability parameters and ADC are presented as mean ± standard deviation. Receiver operating characteristic (ROC) curve analysis was performed with MedCalc software (MedCalc, Ostend, Belgium). After calculating the maximum Youden index, the area under the ROC curve (AUC) was determined and a cutoff value was obtained. Spearman correlation analysis was used to assess the relationship between variables. Significant parameters were used to construct the multivariate logistic regression model. The diagnostic performance of the model was evaluated by AUC analysis. Differences with P values <0.05 were considered statistically significant.

Results

Clinical characteristics of patients

Five patients were excluded from the analysis because of poor DCE-MRI image quality; 7 were excluded because serum PSA was unavailable; and 25 were excluded because they had not undergone a pathologic examination. Ultimately, 65 patients met the inclusion criteria, including 32 with PCa and 33 with BPH. PI-RADS scores differed significantly between the 2 groups (P=0.003; Table 1). The Gleason score distribution was as follows: 5 points, n=1; 6 points, n=2; 3 + 4 points, n=8; 4 + 3 points, n=9; 8 points, n=7; 9 points, n=3; and 10 points, n=2 (Table 1 and Figure 2).

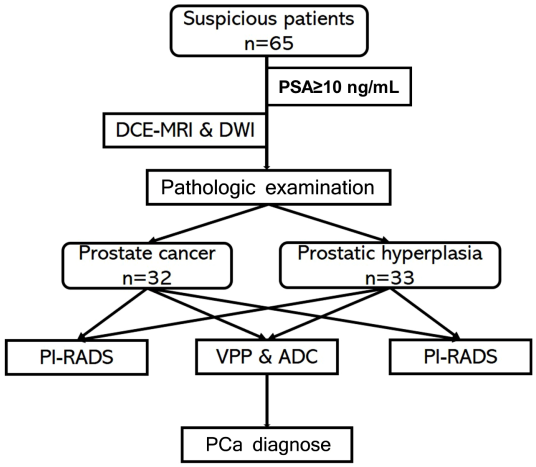

FIGURE 1
Flow diagram of the study protocol.

DCE-MRI parameters and ADC in PCa and BPH patients

DCE-MRI parameters in PCa patients were as follows: K_{trans}, 1.811 ± 0.128 min^{-1}; K_{ep}, 1.504 ± 0.170 min^{-1}; V_e, 0.704 ± 0.052; V_p, 0.261 ± 0.031; and ADC, (1.069 ± 0.177)×10^{-3} mm (2)/s (Table 2). The following 4 parameters in the BPH group showed a significant difference compared to the PCa group: K_{trans} (1.698 ± 0.169 min^{-1}, P=0.006; Figure 3A); K_{ep} (1.367 ± 0.095 min^{-1}, P=0.001; Figure 3B); V_p (0.286 ± 0.036, P=0.009; Figure 3D), and ADC ([1.794 ± 0.180]×10^{-3} mm(2)/s, P<0.001; Figure 3E and Table 2). V_e in the BPH group (0.702 ± 0.056) did not differ significantly from the value in the PCa group (P=0.911; Table 2 and Figure 3C).

Performance of imaging parameters and PI-RADS in the differential diagnosis of PCa vs BPH

Imaging parameters and PI-RADS score showed high diagnostic performance in discriminating between PCa and BPH patients, with AUCs of 0.705 for K_{trans}, 0.700 for K_{ep}, 0.737 for V_p,

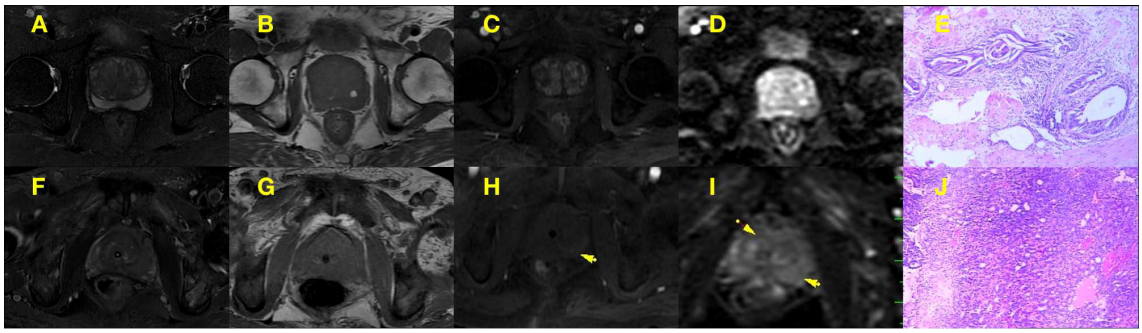

FIGURE 2
(A–E) PI-RADS 2 scored alterations. An example of PI-RADS 2 lesion confirmed at biopsy as pathologic examination of BPH patient **(E)**, multi-parameter MRI showed hypoint T2 signal intensity in the peripheral zone, iso and hyper T2 signal intensity in the central gland**(A)**, iso and hyper T1 signal intensity in the central gland **(B)**, normal diffusivity at b800 DWI **(C)** with contrast enhancement **(D)**, that the peripheral zone in the multi parameter MRI showed 2 points and the central gland in the multi parameter MRI showed 2 points, DWI showed 1 points. **(F–J)** PI-RADS 5 scored alterations. An example of PI-RADS 5 lesion confirmed at biopsy as pathologic examination of PCa patient **(J)**, multi-parameter MRI showed so and hyper T2 signal intensity in the central gland and peripheral zone **(F)**, iso and hyper T1 signal intensity in the central gland **(G)**, hyperintensity signal at b800 DWI **(H)** with contrast enhancement **(I)**, that the T2WI showed 5 points and DWI showed 5 points.

TABLE 1 Patients' demographic information.

Variable	PCA n = 32 n = 32	BPH n = 33 n = 33	P value[a]
Age, years (mean ± SD)	64.5 ± 6.2	59.0 ± 8.4	0.013[b]
PI-RADS			0.003[b]
1	3	14	
2	0	2	
3	14	7	
4	14	10	
5	2	0	
Gleason score			
5	1		
6	2		
3+4	8		
4+3	9		
8	7		
9	3		
10	2		

[a]P value with the Mann–Whitney U test; [b]significant difference.
BPH, benign prostatic hyperplasia; PCa, prostate cancer; PI-RADS, Prostate Imaging Reporting And Data System.

0.688 for ADC, and 0.999 for PI-RADS score (Table 3 and Figure 4A). The sensitivity values of PI-RADS, K_{trans}, and ADC were higher than those of K_{ep} and V_p, whereas the specificity values of K_{ep}, V_p, and ADC were higher than those of PI-RADS and K_{trans} (Table 3). Given the significant differences in PI-RADS score and imaging parameters between the PCa and BPH groups (PI-RADS, P=0.0009; K_{trans}, P=0.0022; K_{ep}, P=0.0003; V_p, P=0.0049; ADC, P<0.0001; Table 3), we compared their diagnostic performance with the Delong test but found no significant difference between PI-RADS and K^{trans} (P=0.958; Figure 4B), K_{ep} (P=0.722; Figure 4B), V_p (P=0.845; Figure 4B), and ADC (P=0.088; Figure 4B). ADC showed the highest diagnostic performance among imaging parameters (ADC vs K^{trans}, K_{ep}, and V_p; P<0.001), whereas there was no significant difference in performance among DCE-MRI parameters (P≥0.05).Diagnostic performance of the combined model

PI-RADS score and imaging parameters (K_{trans}, K_{ep}, V_p, and ADC) were used to construct a multivariate logistic regression model, which distinguished between PCa and BPH with an AUC of 1.000 (95% confidence interval [CI]: 0.945–1.000; Table 4). The logistic regression analysis identified PI-RADS score and imaging parameters (K_{trans}, K_{ep}, V_p, and ADC) as independent predictors of PCa malignancy with high sensitivity (0.983) and specificity (0.999) (Table 4). The model incorporating the above independent predictors is presented as a nomogram (Figure 5).

Correlation between Gleason stage and DCE-MRI parameters and ADC

A Spearman correlation analysis was performed to examine the relationship between imaging parameters and Gleason stage. The values of DCE-MRI parameters of the tumor region were negatively correlated with Gleason stage, but not significantly (K_{trans}, r=−0.220, P=0.226; $K_{ep,}$ −0.177, P=0.332; V_e, −0.080, P=0.663; and $V_{p,}$ −0.058, P=0.754; Table 5). The ADC of the tumor region was positively correlated with Gleason stage (r=0.145), but this association was also nonsignificant (P=0.430; Table 5).

TABLE 2 DCE-MRI parameters and ADC for PCa and BPH groups.

Parameter	PCa	BPH	P value[a]
DCE-MRI			
K_{trans}, min^{-1}	1.811 ± 0.128	1.698 ± 0.169	0.006[b]
K_{ep}, min^{-1}	1.504 ± 0.170	1.367 ± 0.095	0.001[b]
V_e	0.704 ± 0.052	0.702 ± 0.056	0.911
V_p	0.261 ± 0.031	0.286 ± 0.036	0.009[b]
ADC, 10^{-3} mm^2/s	1.069 ± 0.177	1.794 ± 0.180	<0.001[b]

Data represent mean ± SD. [a]P value with the Mann–Whitney U test; [b]significant difference.
ADC, apparent diffusion coefficient; BPH, benign prostatic hyperplasia; DCE-MRI, dynamic contrast-enhanced magnetic resonance imaging; K_{ep}, rate constant; K_{trans}, transfer constant; PCa, prostate cancer; V_e, fractional volume of the extravascular extracellular space; V_p, plasma volume.

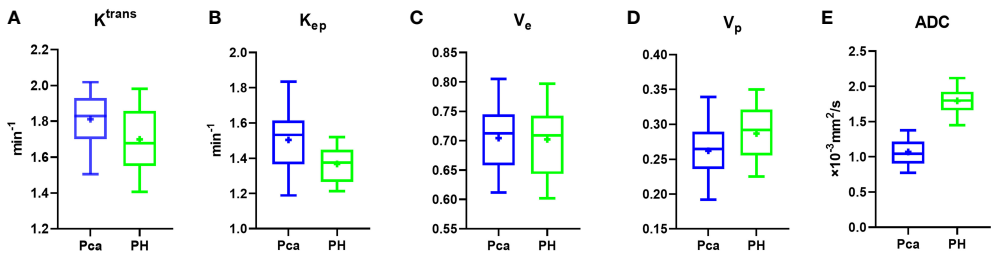

FIGURE 3
Box plot of vascular permeability parameters and ADC. **(A–E)** K_{trans} **(A)**, K_{ep} **(B)**, and ADC **(E)** differed significantly between PCa and BPH patients, whereas V_e **(C)** and V_p **(D)** were similar between the 2 groups.

TABLE 3 Diagnostic performance of imaging parameters and PI-RADS score in discriminating between PCa vs BPH.

	AUC	Sensitivity	Specificity	Youden indexJ statistic	95% CI	P value[a]
PI-RADS	0.705	0.937	0.485	0.422	0.579–0.812	0.0009[b]
DCE-MRI						
K_{trans}	0.700	0.906	0.485	0.391	0.574–0.808	0.0022[b]
K_{ep}	0.737	0.531	1.000	0.531	0.613–0.839	0.0003[b]
V_p	0.688	0.469	0.879	0.347	0.560–0.797	0.0049[b]
ADC	0.999	0.998	0.999	1.000	0.945–1.000	<0.0001[b]

[a]P value with the Mann–Whitney U test; [b]significant difference.
ADC, apparent diffusion coefficient; AUC, area under the curve; BPH, benign prostatic hyperplasia; CI, confidence interval; DCE-MRI, dynamic contrast-enhanced magnetic resonance imaging; K_{ep}, rate constant; K_{trans}, transfer constant; PCa, prostate cancer; PI-RADS, Prostate Imaging Reporting And Data System; V_p, plasma volume.

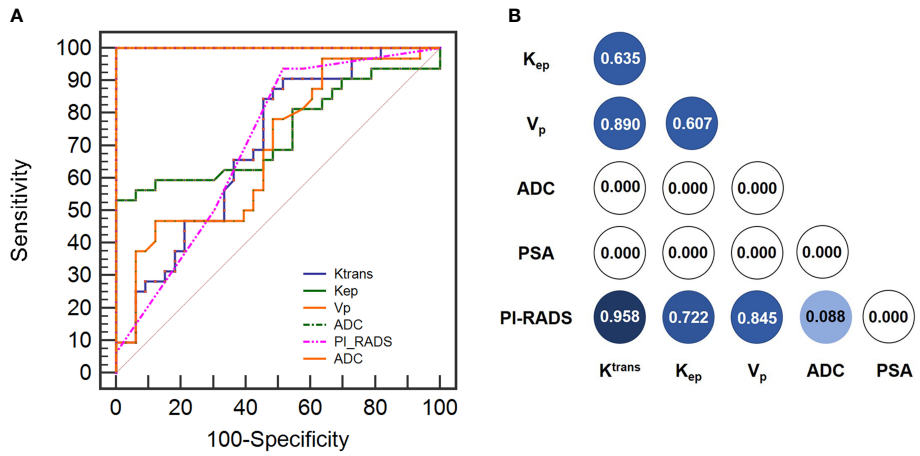

FIGURE 4
(A) Diagnostic performance of imaging parameters (K_{trans}, K_{ep}, Vp and ADC) and PI-RADS score in discriminating between PCa and BPH based on ROC curve analysis. **(B)** Delong analysis among imaging paramters (Ktrans, Kep, Vp and ADC) and PI-RADS score in discrimination between PCa and BPH.

Discussion

The results of this study demonstrate that DCE-MRI and DWI parameters can differentiate between benign and malignant prostate tumors when serum PSA is ≥10 ng/ml. Thus, K_{trans} (AUC=0.700), K_{ep} (AUC=0.737), V_p (AUC=0.688), and ADC (AUC=0.999) can be used as imaging biomarkers to evaluate PCa along with PI-RADS score. In order to improve diagnostic specificity and sensitivity, we established a multivariate logistic regression model to predict tumor

TABLE 4 Diagnostic performance of DCE-MRI parameters, ADC, and the combined model.

	Coefficient	OR	AUC	95% CI lower	95% CI upper
Intercept	−23.465				
PI-RADS	9.929	1491.79			
ADC	−134.766	9.52×10^{-34}			
K_{trans}	23.988	42909.20			
K_{ep}	114.729	1.27×10^{27}			
V_p	−87.606	3.21×10^{-13}			
Nomogram			1.000	0.945	1.000

ADC, apparent diffusion coefficient; AUC, area under the curve; CI, confidence interval; DCE-MRI, dynamic contrast-enhanced magnetic resonance imaging; K_{ep}, rate constant; K_{trans}, transfer constant; OR, odds ratio; PI-RADS, Prostate Imaging Reporting And Data System; V_p, plasma volume.

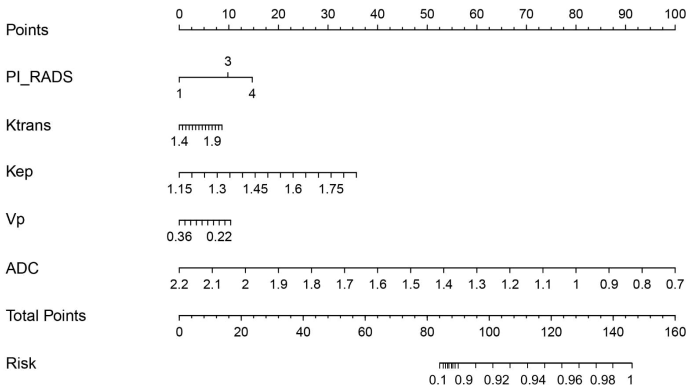

FIGURE 5
Nomogram for differentiating PCa from BPH. The nomogram was developed with PI-RADS, K_{trans}, K_{ep}, V_p, and ADC. This nomogram can be used to classification of Pca from BPH. Before biopsy or surgery performed, patients underwent DCE-MRI and DWI scanning that, K_{trans}, K_{ep}, V_p, ADC and PI-RADS were determined. All of these results will put into the Nomogram as follow: Points_PI_RADS will calculate by the score of Points which is vertically projected on the line of Points by PI-RADS. K_{trans}, K_{ep}, V_p and ADC should be vertically projected on the line of Points to get Points_K_{trans}, Points_K_{ep}, Points_V_p and Points_ADC. After this, the Total points is the sum of Points_PI_RADS, Points_K_{trans}, Points_K_{ep}, Points_V_p and Points_ADC. After this, total points is vertically projected on the line of Risk for patients' probability of PCa.

TABLE 5 Spearman correlations between imaging parameters and Gleason stage.

	K_{trans}	K_{ep}	V_e	V_p	ADC
r	−0.220	−0.177	−0.080	−0.058	0.145
P value	0.226	0.332	0.663	0.754	0.430

ADC, apparent diffusion coefficient; K_{ep}, back flow rate constant; K_{trans}, volume transfer rate constant; V_e, extravascular extracellular space volume fraction; V_p, plasma volume fraction.

malignancy based on 3 vascular permeability parameters; ADC and PI-RADS differed significantly between PCa and BPH patients. We also established a nomogram to visualize the multivariate logistic regression model, which showed higher AUC (1.000) and higher sensitivity (0.983) and specificity (0.999). However, vascular permeability parameters and ADC did not show significant correlations with Gleason stage in PCa patients.

PCa is diagnosed as high risk when PSA is ≥10 ng/ml (15). The goal of PSA screening is to classify PCa at an earlier stage. However, a diagnosis cannot be made based solely on PSA level. The typical PSA level in PCa is 4 ng/ml; this is too low for biopsy, which is usually recommended for PSA levels of 4–10 ng/ml (16). The AUC of PSA (4–10 ng/ml) for differentiating between PCa and BPH was 0.708, with a sensitivity of 0.837 and specificity of 0.583 (17); thus, screening based on PSA can lead to overdiagnosis and

overtreatment (18). Some DCE-MRI studies have shown that the vascular permeability parameters K_{trans} and K_{ep} were higher in PCa than in BPH (19, 20), which is supported by our results. However, the latter study also showed that V_e and V_p differed between these 2 groups, which was confirmed by another report (20) and is contrary to our findings. Ours is the first investigation of the diagnostic performance of DCE-MRI and DWI parameters in PCa when serum PSA is ≥10 ng/ml, which is more closely associated with PCa risk than any specific marker (16). Vascular permeability values reported in PCa vary across the literature, even considering a 95% CI; this may be attributable to the reference vessel for AIF (21), parameters of the DCE-MRI sequence (eg, temporal resolution) of different instrument manufacturers, and interindividual differences among patients (22). There is accumulating clinical evidence that DWI is a useful tool for the quantitative assessment of tumor characteristics and prognosis (23, 24). ADC reflects the Brownian motion of H_2O, which is constantly interacting with other molecules in the tissue microenvironment. Proliferating tumor cells can inhibit H_2O movement, resulting in a change in the ADC value; therefore, ADC is used as a marker for tumor malignancy and prognosis (25, 26) and to discriminate between cancer and noncancer tissue (27). In the current study, ADC values differed significantly between PCa and BPH, suggesting that aggressive tumors block the diffusion of H_2O to a greater extent than those that are benign. DWI of 60 patients revealed that ADC was an independent factor that could distinguish between BPH and transition zone cancer (1.32 ± 0.19 vs 0.89 ± 0.17 mm(2)/s; P<0.001) (19). Compared to vascular permeability parameters, ADC showed better diagnostic performance in detecting PCa, with an AUC of 0.999, sensitivity of 0.998, and specificity of 0.999.

PI-RADS v2 is a noninvasive method to predict PCa with low specificity (28), which was confirmed in our study. To improve sensitivity and specificity, we constructed an imaging-based model combining PI-RADS score, ADC, K_{trans}, K_{ep}, and V_p that was visualized as a nomogram and had a sensitivity of 0.983 and specificity of 0.999; these were higher than the corresponding values for PI-RADS score and vascular permeability parameters. In fact, ADC also showed high sensitivity (0.998) and specificity (0.999) in our study. Multiparameter (mp)MRI is increasingly recommended for noninvasive PCa screening (17). A combined model based on mpMRI showed higher diagnostic performance compared to a single imaging parameter (17). Additional studies with a larger sample size are needed to determine whether ADC can serve as an imaging biomarker for the differentiation of PCa from BPH.

In this study, we have built a multiple logistic model to classification of Pca and BPH with an amazing diagnostic discrimination (AUC=1.000) by combining PI-RADS score, ADC, K_{trans}, K_{ep}, and V_p. To provide the clinician with a simplified quantitative tool to predict individual probability of PCa, Nomogram was drawn on the basis of imaging-based model combining PI-RADS score, ADC, K_{trans}, K_{ep}, and V_p. For example, there were a representative case to illustrate the discriminative ability of nomograms for the classification of Pca. A 62-year-old man with PSA=12 ng/ml. After MRI scanning, his PI-RADS score was 3, K_{trans} was 1.723 min^{-1}, K_{ep} was 1.43 min-1, V_p was 0.367, ADC was $1.025x10^{-3}$ mm(2)/s. After put these value into the nomogram, we have got the score of PI_RADS (Points=9.5), K_{trans} (Points=7.3), K_{ep}(Points=30.1), V_p (Points=0.1)and ADC (Points=79.1) that the total points is 126. After vertically projected on the line of Risk the probability of PCa is 96%.

We also analyzed the correlation between imaging parameters and Gleason score, which is used for histologic staging of PCa and is an important prognostic factor. A significant negative correlation between ADC and Gleason score was reported; this may be explained by the fact that the high proliferation rate of tumor cells leads to a higher cell density, which reduces extracellular space and restricts H_2O movement (19). However, we did not observe a significant correlation between ADC and Gleason score, which may be due to the small number of patients in the PCa group.

The present study had some limitations. Firstly, as the patients were from a single hospital it is unclear whether our findings are generalizable to all PCa patients. Secondly, ROI segmentation was performed by 2 experienced radiologists, but we did not evaluate intraobserver differences. Multicenter studies addressing these shortcomings are needed to achieve a higher level of evidence.

Conclusion

K_{trans} and K_{ep} in DCE-MRI and ADC in DWI can be used as imaging biomarkers to distinguish PCa from BPH. A multivariate logistic regression model combining these 3 parameters showed good diagnostic performance for PCa. Thus, DCE-MRI and DWI are useful noninvasive diagnostic tools that can guide management strategies for PCa patients.

Data availability statement

The raw data supporting the conclusions of this article will be made available by the authors, without undue reservation.

Ethics statement

The studies involving human participants were reviewed and approved by Henan Province Hospital of TCM. The patients/participants provided their written informed consent to participate in this study.

Author contributions

HS, FD, and TW designed the study. HS, FD, and YL performed the experiments. QL, XL, and HS analyzed the data. HS, FD, and TW wrote the manuscript. TW revised the manuscript and supervised the study. All authors contributed to the article and approved the submitted version.

Conflict of interest

The authors declare that the research was conducted in the absence of any commercial or financial relationships that could be construed as a potential conflict of interest.

Publisher's note

Supplementary material

The Supplementary Material for this article can be found online at: https://www.frontiersin.org/articles/10.3389/fonc.2022.925186/full#supplementary-material

References

1. *Analysis data. surveillance, epidemiology, and end results program, national cancer institute*. Available at: https://seer.cancer.gov/statistics/.html.

2. David EN, Jenny LD. Prostate cancer: to screen or not to screen? *Lancet Oncol* (2000) 1(1):17–24. doi: 10.1016/S1470-2045(00)00005-X

3. Coplen DE, Andriole GL, Fueger JJ, Babaian RJ, Newell GR. Familial patterns of prostate cancer: a case-control analysis. *J Urol.* (1991) 146:1305–7. doi: 10.1016/S0022-5347(17)38074-6

4. Mingting W, Qin Z, Yuan L, Saber L, Danna X, Yinghua L, et al. Bevacizumab combined with aptainib enhances antitumor and anti-angiogenesis affects in a lung cancer model in vitro and vivo. *J Drug Target* (2020) 28(9):961–9. doi: 10.1080/1061186X.2020.1764963

5. Barrett T, Brechbiel M, Bernardo M, Choyke PL. MRI Of tumor angiogenesis. *J Magn Reson Imaging.* (2007) 26:235–49. doi: 10.1002/jmri.20991

6. Hylton N. Dynamic contrast-enhanced magnetic resonance imaging as an imaging biomarker. *J Clin Oncol* (2006) 24:3293–8. doi: 10.1200/JCO.2006.06.8080

7. O'Connor j P, Jackson A, Gj P, Roberts C, Jayson GC, et al. Dynamic contrast-enhanced MRI in clinical trials of antivascular therapies. *Nat Rev Clin Oncol* (2012) 9:167–77. doi: 10.1038/nrclinonc.2012.2

8. Leach MO, Brindle KM, Evelhoch JL, Griffiths JR, Horsman M, Jackson A, et al. The assessment of antiangiogenic and antivascular therapies in early-stage clinical trials using magnetic resonance imaging: Issues and recommendations. *Br J Cancer.* (2005) 92:1599–610. doi: 10.1038/sj.bjc.6602550

9. Lei H, YunFei Z, Li W, Xing D, Gong W, Wang J, et al. Quantitative evaluation of vertebral microvascular permeability and fat fraction in alloxan-induced diabetic rabbits. *Radiology.* (2018) 287(1):128–36 doi: 10.1148/radiol.2017170760

10. Tofts PS, Brix G, Buckley DL, et al. Estimating kinetic parameters from dynamic contrast enhanced T1-weighted MRI of a diffusable tracer: standardized quantities and symbols. *J Magn Reson Imaging.* (1999) 10:223–32. doi: 10.1002/(SICI)1522-2586(199909)10:3<223::AID-JMRI2>3.0.CO;2-S

11. Palmisano A, Di Chiara A, Esposito A, Rancoita PMV, Florino C, Passoni P, et al. MRI Prediction of pathological response in locally advanced rectal cancer: when apparent diffusion coefficient radiomics meets conventional volumetry. *Clin Radiol* (2020) 75(10):e1-798. doi: 10.1016/j.crad.2020.06.023

12. Wernerb JC, Barentsz JO, Choyke PL, Cornud F, Haider MA, Macura KJ, et al. PI-RADS prostate imaging-reporting and data system: 2015, version 2. *Eur Urol.* (2016) 69(1):16–40. doi: 10.1016/j.eururo.2015.08.052

13. Sourbron SP, Buckley DL. On the scope and interpretation of the tofts models for DCE-MRI. *Magn Reson Med* (2011) 66(3):735–45. doi: 10.1002/mrm.22861

14. Gleason DF, Mellinger GT. Prediction of prognosis for prostatic adenocarcinoma by combined histological grading and clinical staging. *J Urol.* (1974) 167:58–64. doi: 10.1016/S0022-5347(17)59889-4

15. Tilki D, Mandel P, Karakiewicz Pl, Heinze A, Huland H, Graefen M, et al. The impacht of very high initial PSA on oncological outcomes after radical prostatectomy for clinically localized prostate cancer. *Urol Oncol Semin Orig Investig* (2020) 38:379–85. doi: 10.1016/j.urolonc.2019.12.027

16. Aminsharifi A, Howard L, Wu Y, et al. Prostate specific antigen density as a predictor of clinically significant prostate cancer when the prostate specific antigen is in the diagnostic Gray zone: Defining the optimum cutoff point stratified by race and body mass index. *J Urol.* (2018) 200(4):758–66. doi: 10.1016/j.juro.2018.05.016

17. Qi Y, Zhang S, Wei J, Gumuyang Z, Jing L, Weigang Y, et al. Multiparametric MRI-based radiomics for prostate cancer screening with PSA in 4-10 ng/mL to reduce unnecessary biopsies. *J Magn Reson Imaging.* (2020) 51(6):1890–9. doi: 10.1002/jmri.27008

18. Welch HG, Albertsen PC. Reconsidering prostate cancer mortality - the future of PSA screening. *N Engl J Med* (2020) 382(16):1557–63. doi: 10.1056/NEJMms1914228

19. Xiang ZM, Kun L, Jian LS, Yingxing Y, Peipei P, Maosheng X, et al. Application evaluation of DCE-MRI combined with quantitative analysis of DWI for the diagnosis of prostate cancer. *Oncol Lett* (2019) 17:3077–84. doi: 10.3892/ol.2019.9988

20. Wu X, Reinikainen P, Kapanen M, Vierikko T, Ryymin P, Kellokumpu L, et al. Dynamic contrast-enhanced imaging as a prognostic toll in early diagnosis of prostate cancer: Correlation with PSA and clinical stage. *Contrast Media Mol Imaging* (2018) 09(09):3181258. doi: 10.1155/2018/3181258

21. Huang W, Yiyi C, Fedorov A, Xia L, Jajamovich GH, Malyarenko DI, et al. The impact of arterial input function determination variations on prostate dynamic contrast-enhanced magnetic resonance imaging pharmacokinetic modeling: a multicenter data analysis challenge, part II. *Oncol Lett* (2018) 17(3):3077–84. doi: 10.18383/j.tom.2018.00027

22. Othman AE, Falkner F, Weiss J, Kruck S, Grimm R, Martirosian P, et al. Effect of temporal resolution on diagnostic performance of dynamic contrast-enhanced magnetic resonance imaging of the prostate. *Invest Radiol* (2016) 51(5):290–6. doi: 10.1097/RLI.0000000000000234

23. Park HJ, HY J, SY K, Sojung L, HyungJin W, Sanghyun C, et al. Non-enhanced magnetic resonance imaging as a surveillance tool for hepatocellular carcinoma: Comparison with ultrasound. *J Hepatol* (2020) 72(4):718–24. doi: 10.1016/j.jhep.2019.12.001

24. Fuitterer JJ, Briganti A, De Visschere P, Emberton M, Glannarni G, Krikham A, et al. Can clinically significant prostate cancer be detected with multiparametric magnetic resonance imaging? A systematic review of the literature. *Eur Urol.* (2015) 68(6):1045–53. doi: 10.1016/j.eururo.2015.01.013

25. Oh J, Henry RG, Pirzkall A, Ying L, Xiaojuan L, Catalaa L, et al. Survival analysis in patients with glioblastoma multiforme: predictive value of choline-to-N-acetylaspartate index, apparent diffusion coefficient, and relative cerebral blood volume. *J Magn Reson Imaging.* (2004) 19:546–54. doi: 10.1002/jmri.20039

26. Selnæ KM, Heerschap A, Jensen LR, Tessem ME, Schweder GJ, Goa PE, et al. Peripheral zone prostate cancer localization by multiparametric magnetic resonance at 3T: unbiased cancer identification by matching by matching to histopathology. *Invest Radiol* (2012) 47(11):624–33. doi: 10.1097/RLI.0b013e318263f0fd

27. Lyama Y, Nakaura T, Katahira K, Lyama A, Nagayama Y, Oda S, et al. Development and validation of a logistic regression model to distinguish transition zone cancers from benign prostatic hyperplasia on multi-parametric prostate MRI. *Eur Radiol* (2017) 27(9):3600–8. doi: 10.1007/s00330-017-4775-2

28. Xu N, Wu YP, Chen DN, ZhiBin K, Hai C, Yong W, et al. Can prostate imaging reporting and data system version 2 reduce unnecessary prostate biopsies in men with PSA levels of 4-10 ng/ml? *J Cancer Res Clin Oncol* (2018) 144(5):987–95. doi: 10.1007/s00432-018-2616-6

frontiers | Frontiers in Oncology

TYPE Original Research
PUBLISHED 05 January 2023
DOI 10.3389/fonc.2022.941673

OPEN ACCESS

EDITED BY
Ellen Ackerstaff,
Memorial Sloan Kettering Cancer Center, United States

REVIEWED BY
Salvatore Cannavo,
University of Messina, Italy
Giorgio Grani,
Sapienza University of Rome, Italy

*CORRESPONDENCE
Ping Zhou
zhouping1000@hotmail.com

SPECIALTY SECTION
This article was submitted to Cancer Imaging and Image-directed Interventions, a section of the journal Frontiers in Oncology

RECEIVED 11 May 2022
ACCEPTED 09 December 2022
PUBLISHED 05 January 2023

CITATION
Gong L, Zhou P, Li J-L and Liu W-G (2023) Investigating the diagnostic efficiency of a computer-aided diagnosis system for thyroid nodules in the context of Hashimoto's thyroiditis.
Front. Oncol. 12:941673.
doi: 10.3389/fonc.2022.941673

Investigating the diagnostic efficiency of a computer-aided diagnosis system for thyroid nodules in the context of Hashimoto's thyroiditis

Liu Gong, Ping Zhou*, Jia-Le Li and Wen-Gang Liu

The Department of Ultrasound, Third Xiangya Hospital, Central South University, Changsha, China

Objectives: This study aims to investigate the efficacy of a computer-aided diagnosis (CAD) system in distinguishing between benign and malignant thyroid nodules in the context of Hashimoto's thyroiditis (HT) and to evaluate the role of the CAD system in reducing unnecessary biopsies of benign lesions.

Methods: We included a total of 137 nodules from 137 consecutive patients (mean age, 43.5 ± 11.8 years) who were histopathologically diagnosed with HT. The two-dimensional ultrasound images and videos of all thyroid nodules were analyzed by the CAD system and two radiologists with different experiences according to ACR TI-RADS. The diagnostic cutoff values of ACR TI-RADS were divided into two categories (TR4 and TR5), and then the sensitivity, specificity, and area under the receiver operating characteristic curve (AUC) of the CAD system and the junior and senior radiologists were compared in both cases. Moreover, ACR TI-RADS classification was revised according to the results of the CAD system, and the efficacy of recommended fine-needle aspiration (FNA) was evaluated by comparing the unnecessary biopsy rate and the malignant rate of punctured nodules.

Results: The accuracy, sensitivity, specificity, PPV, and NPV of the CAD system were 0.876, 0.905, 0.830, 0.894, and 0.846, respectively. With TR4 as the cutoff value, the AUCs of the CAD system and the junior and senior radiologists were 0.867, 0.628, and 0.722, respectively, and the CAD system had the highest AUC ($P < 0.0001$). With TR5 as the cutoff value, the AUCs of the CAD system and the junior and senior radiologists were 0.867, 0.654, and 0.812, respectively, and the CAD system had a higher AUC than the junior radiologist ($P < 0.0001$) but comparable to the senior radiologist ($P = 0.0709$). With the assistance of the CAD system, the number of TR4 nodules was decreased by both junior and senior radiologists, the malignant rate of punctured nodules increased by 30% and 22%, and the unnecessary biopsies of benign lesions were both reduced by nearly half.

Conclusions: The CAD system based on deep learning can improve the diagnostic performance of radiologists in identifying benign and malignant

thyroid nodules in the context of Hashimoto's thyroiditis and can play a role in FNA recommendations to reduce unnecessary biopsy rates.

KEYWORDS

thyroid nodule, Hashimoto's thyroiditis, ultrasound, computer-aided diagnosis, unnecessary biopsy

1 Introduction

Hashimoto's thyroiditis (HT) is the most common autoimmune thyroid disease (AITD) (1), with a higher prevalence in women than in men (2). Lymphocytic infiltration and follicular destruction are histological features of autoimmune thyroiditis (AIT), resulting in progressive atrophy and fibrosis of the thyroid tissue (1). HT constitutes a risk factor for primary thyroid lymphoma (PTL), as clonal B cells normally present in lymphomas can be found in patients with HT, and cellular changes caused by long-term chronic antigenic stimulation may evolve into malignancy (3). Although PTL is a rare disease, it usually presents with a more aggressive course and a worse prognosis. The association between HT and thyroid cancer (TC) remains controversial, and while many studies have produced conflicting results (4–6), some scholars have highlighted an immunological link between HT and PTC (7). For these reasons, it is necessary to proactively screen patients for HT and determine whether they are accompanied by suspicious thyroid nodules. HT was clinically diagnosed based on hypothyroidism, elevated thyroglobulin antibodies (TG-Ab) and thyroid peroxidase antibodies (TPO-Ab), inhomogeneous parenchyma on ultrasonography, and lymphocytic infiltration on cytology (8). However, HT remains difficult to diagnose, with only 25%–30% of patients presenting with elevated levels of thyroid-stimulating hormone (TSH) and decreased serum thyroid hormones, and not all patients with HT have elevated TG-Ab and TPO-Ab (9). Thus, in addition to blood markers, ultrasonography and fine-needle aspiration (FNA) also become essential tools to screen for nodules in the context of HT.

HT exhibits varying ultrasound characteristics at different stages of pathology, with inhomogeneous parenchyma being the most common. The characteristics of malignant nodules underlying diffused background of HT in different studies are inconsistent, with some studies suggesting that malignant nodules in HT tend to have smooth margins and varying calcifications (10) while others suggesting irregular margins and microcalcifications (11). The diversity of malignant features leads to more ambiguous diagnostic criteria and makes it more difficult for radiologists to identify the nature of nodules in a heterogeneous background. To manage thyroid nodules effectively, many national and international associations have proposed ultrasound-based diagnostic classifications. Wang et al. compared the efficacy of three thyroid risk stratification systems and found that the TI-RADS proposed by the American College of Radiology (ACR) in 2017 was most effective for thyroid nodules in HT (12). ACR TI-RADS is able to guide whether a nodule requires FNA or follow-up based on the nodule's category and maximum diameter (13). Nodules were scored according to five categories of features, namely, composition, echogenicity, shape, margin, and focal echogenicity, and then the scores of each feature were summed to derive the corresponding category, which is TR1 to TR5. The maximum diameter thresholds for nodules requiring FNA were as follows: TR3 nodules ≥2.5 cm, TR4 nodules ≥1.5 cm, and TR5 nodules ≥1 cm. Nevertheless, the identification of malignant features in ultrasound images is closely related to the experience of the radiologist, which leads to interobserver variability and unnecessary biopsy.

In recent years, computer-aided diagnosis (CAD) has initially been used in the screening of thyroid nodules. There are two types of CAD methods. One is classical machine learning, which builds models based on the features recognized by human experts. Many studies using support vector machines support vector machine (SVM) or random forest algorithms as classifiers found that these can improve the diagnostic accuracy of inexperienced or non-professional radiologists (14, 15), but machine learning requires human experts to extract features in the region of interest (ROI) (16), making the differences in various research results. The other is the deep learning method, which does not require prior definition by human experts (16) and can automatically extract multilevel features that cannot be recognized by radiologists (17). By contrast, deep learning approaches have significant advantages in overcoming heterogeneity using automated learning procedures (18). ITS100 (Med Imaging AI, Wuxi, China), a commercial thyroid CAD software, is an auxiliary diagnosis system based on a deep convolutional neural network (DCNN). Compared with other CAD systems, this software identifies high-dimensional features through DCNN, which enables real-time localization, characterization, and boundary segmentation of lesions in complex backgrounds, thereby eliminating the interobserver's differences. To the best of

our knowledge, most CAD systems have high diagnostic performance in diagnosing thyroid nodules without HT (17), but there are few studies using CAD systems to diagnose diffuse thyroid diseases such as HT.

Therefore, the objectives of this study were to compare the performance of the CAD system and radiologists of different seniority using ACR TI-RADS in diagnosing thyroid nodules coexistent with HT and to investigate whether unnecessary biopsy could be reduced with the assistance of the CAD system.

2 Materials and methods

2.1 Patients

This retrospective study has been approved by the Ethics Committee of the Third Xiangya Hospital of Central South University. This study involved all patients with thyroid nodules who underwent ultrasound examination in our hospital from November 2020 to November 2021. All patients signed an informed consent form.

The inclusion criteria were as follows: 1) ultrasound examination showing heterogeneous echogenicity and 2) histopathological diagnosis suggestive of Hashimoto's thyroiditis. The exclusion criteria were as follows: 1) the patient had a history of partial thyroidectomy or coarse needle aspiration biopsy prior to the examination and 2) the images obtained were not clear.

2.2 Image acquisition and CAD system analysis

The two-dimensional ultrasound images and videos were acquired with the Siemens ACUSON Sequoia color Doppler ultrasound diagnostic instrument with an 18L6 transducer. The patient was placed supine on an examination bed, and the radiologist performed a dynamic scan of the transverse and longitudinal sections of the thyroid and obtained the scanning video of the thyroid nodules and the images of the largest long-axis section.

The CAD system used in this study was Ian Thyroid Solution 100 (ITS100). The CAD system was directly connected to the ultrasonic instrument. After the collected thyroid nodule images and videos were input into the system, the location of the nodule was dynamically identified, and the malignant features in different sections were analyzed, the final results would be obtained by clicking on the screen (Figure 1). All of the above procedures were done by the same radiologist with over 10 years of experience.

2.3 Image review

The acquired 2D ultrasound images and videos were interpreted by another senior radiologist (experience over 10 years) and a junior radiologist (experience within 5 years), who analyzed the thyroid nodules according to the ACR TI-RADS (13). They were blinded to the pathological findings of the thyroid nodules and the results of the CAD system before interpretation.

2.4 CAD system revised recommendation of FNA

The ACR TI-RADS provides clear guidance on whether to perform FNA or follow-up of the thyroid nodules. The criteria for using the CAD system to revise the ACR TI-RADS recommendations for FNA are as follows: when the CAD system indicated that the thyroid nodule was benign, one level was subtracted to the ACR TI-RADS except TR1. Conversely, when the CAD system indicated that the thyroid nodule was malignant, the ACR TI-RADS classification was increased by one level except TR5. According to the modified ACR TI-RADS, the distribution of benign and malignant nodules in each classification was recorded, and suggestions on whether the nodules should be FNA were provided (Figure 2).

2.5 Statistical analysis

The cutoff value of ACR TI-RADS for benign and malignant thyroid nodules was divided into two categories. The first category took TR4 as the cutoff value; TR1, TR2, and TR3 as possibly benign; and TR4 and TR5 as possibly malignant. The second category took TR5 as the cutoff value; TR1, TR2, TR3, and TR4 as possibly benign; and TR5 as possibly malignant. Using surgical pathology results as the gold standard, the receiver operating characteristic (ROC) curve of CAD and radiologists with different cutoff values was established. The sensitivity, specificity, positive predictive value (PPV), negative predictive value (NPV), accuracy, and area under the ROC curve (AUC) were calculated, respectively.

Statistical analyses were performed with SPSS 26.0 and MedCalc 19.0.4. Continuous variables were expressed as mean ± standard deviation. The age of the patients, blood markers, and the maximum diameter of the nodules were compared using *t*-test (or Mann–Whitney *U* test), and the gender of patients and the sonographic features of the nodules were compared using the chi-square test (or Fisher's exact test). The Delong's test was used to determine whether there was any statistical difference in diagnostic efficacy between the CAD system and the radiologists,

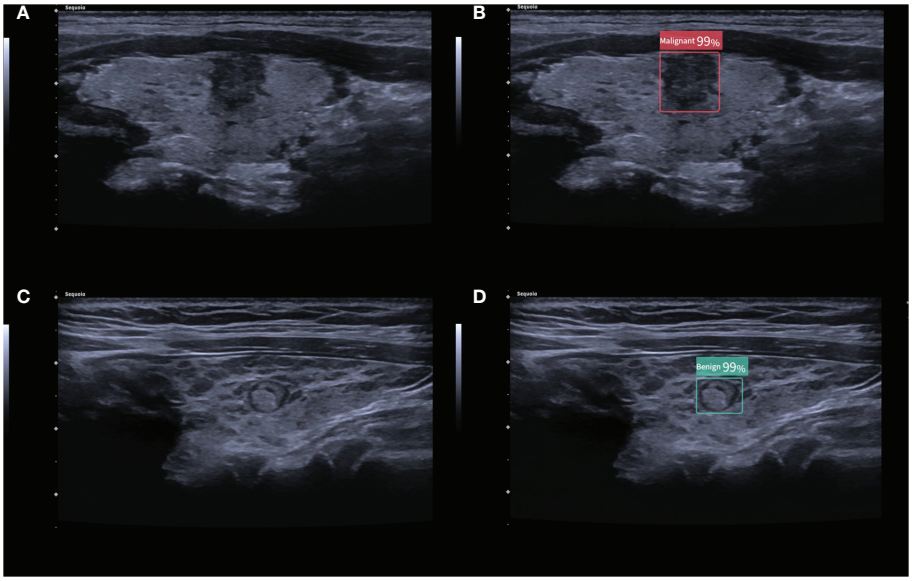

FIGURE 1
(A) 2D ultrasound image of a malignant thyroid nodule with HT; **(B)** the corresponding diagnostic results of the CAD system. **(C)** 2D ultrasound image of a benign thyroid nodule with HT; **(D)** the corresponding diagnostic results of the CAD system. The numbers in the figure are the benign and malignant rates produced by the CAD system. As the numbers from this CAD system are all greater than 95%, these numbers are not significant in our study.

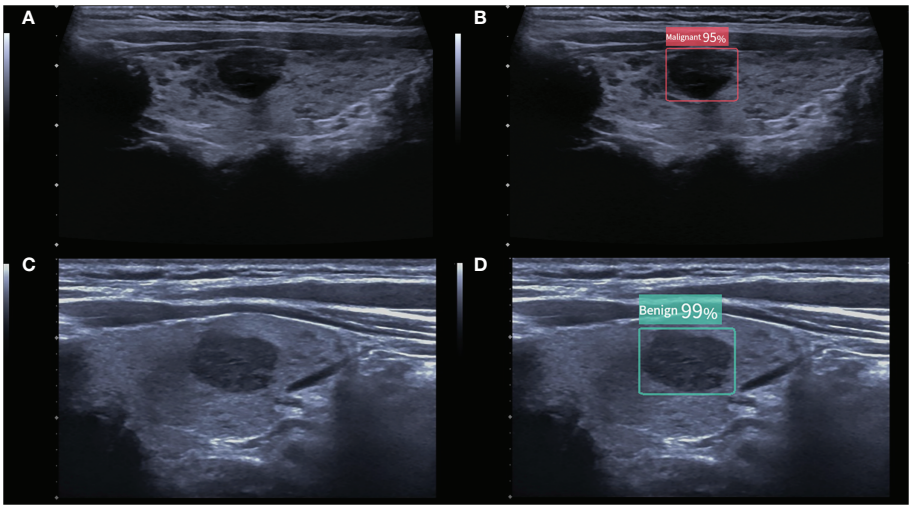

FIGURE 2
(A) A malignant thyroid nodule measuring 11 × 9 mm. The ACR TI-RADS of the nodule given by two radiologists were all TR4, and follow-up was recommended. **(B)** The CAD system indicated that the nodule was malignant, and the modified ACR TI-RADS was TR5, with a recommendation for FNA. **(C)** A benign thyroid nodule measuring 15 × 9 mm. The ACR TI-RADS of the nodule given by the junior radiologist was TR4, and FNA was recommended. **(D)** The CAD system indicated that the nodule was benign, and the modified ACR TI-RADS was TR3, with a recommendation for follow-up. The numbers in the figure are the benign and malignant rates produced by the CAD system. As the numbers from this CAD system are all greater than 95%, these numbers are not significant in our study.

and the McNemar test was used to compare sensitivity and specificity. P <0.05 indicated statistically significant differences.

3 Results

3.1 Demographics and thyroid nodule characteristics

In total, 242 consecutive patients were eligible for ultrasound suggestive of heterogeneous echogenicity and histopathological diagnosis suggestive of HT; however, 41 cases were excluded because of a history of partial thyroidectomy, 12 cases because of a coarse needle aspiration biopsy prior to examination, and 52 cases because of unclear images that prevented recognition by the CAD system. Ultimately, a total of 137 HT patients (mean age, 43.5 ± 11.8 years) were enrolled in this study, consisting of 53 benign patients and 84 malignant patients. In the benign group, some of the patients underwent surgery for suspicious pseudo-nodules. Some of these patients had indeterminate FNA results coupled with ultrasound suggesting possible malignancy, they were treated surgically for safety, and a few other patients underwent surgery for large cystic–solid mixed nodules, with final histopathological findings of pseudo-nodules in 36 cases, nodular goiters in 13 cases, and thyroid adenomas in 4 cases, respectively. In the malignant group, all cases were PTC. The basic characteristics of the patients and nodules are summarized in Table 1. There were no significant differences in gender (P = 0.457) and maximum tumor diameter (P = 0.118) between the benign and malignant groups. However, patients with benign

TABLE 1 The characteristics of patients and nodules.

Characteristics	Total	Benign nodules	Malignant nodules	*P*-value
Sex	–	–	–	0.457
Male	43	19	24	–
Female	94	34	60	–
Age	43.5 ± 11.8	48.2 ± 11.2	40.5 ± 11.2	<0.001
Tumor diameter (mm)	11.2 ± 8.3	12.8 ± 11.1	10.2 ± 5.7	0.118
Blood markers				
TSH	1.6 ± 1.2	1.4 ± 1.3	1.7 ± 1.1	0.316
TG	17 ± 17.4	19.4 ± 18.4	14.6 ± 16.4	0.349
TG-Ab	132.4 ± 263.1	123.7 ± 180.8	141.1 ± 329.6	0.822
TPO-Ab	196.7 ± 281.4	184.6 ± 272.4	208.8 ± 295.4	0.769
Composition				0.028
Solid	83	26	57	
Mixed cystic and solid	54	27	27	
Echogenicity				0
Hypoechoic	113	33	80	
Hyperechoic or isoechoic	24	20	4	
Shape				0.003
Taller than wide	52	12	40	
Wider than tall	85	41	44	
Margin				0.065
Lobulated or irregular	88	29	59	
Smooth or ill-defined	49	24	25	
Calcifications				0
Microcalcifications	78	17	61	
No microcalcifications	59	36	23	

nodules were younger than those with malignant nodules ($P < 0.001$), and the differences in blood markers associated with HT between the groups were not statistically significant (all $P > 0.05$). By comparing the sonographic features of benign and malignant nodules, we observed that there was no remarkable difference in margin ($P = 0.065$), but statistically significant differences in composition, echogenicity, aspect ratio, and presence of microcalcifications (all $P < 0.05$).

3.2 Diagnostic performance of CAD and radiologists

The diagnostic performance of the CAD software and the junior and senior radiologists for thyroid nodules with HT is shown in Table 2 and compared in Table 3. When TR4 was used as the cutoff value, the AUCs of the CAD system and the junior and senior radiologists were 0.867, 0.628, and 0.722, respectively. The CAD system had the highest AUC ($P < 0.0001$), and the specificity of the CAD system was significantly higher than that of both the junior and senior radiologists ($P < 0.0001$), but there was no statistical difference in sensitivity between the CAD system and all radiologists ($P > 0.05$). When TR5 was used as the cutoff value, the AUCs of the CAD system and the junior and senior radiologists were 0.867, 0.654, and 0.812, respectively, and the AUC of the CAD system was superior to that of the junior radiologist ($P < 0.0001$) but not different from that of the senior radiologist ($P = 0.0709$). The sensitivity of CAD was higher than that of both the junior and senior radiologists (all $P < 0.05$), but the specificity was lower than that of the senior radiologist ($P = 0.0375$) and not significantly different from that of the junior radiologist ($P = 0.1797$). The ROC curves for the CAD system, senior radiologist, and junior radiologist under different cutoff values are shown in Figures 3, 4.

3.3 Effectiveness of the CAD system in reducing unnecessary biopsy

The modified ACR TI-RADS classification is presented in Table 4. Compared with the senior radiologist alone, the modified ACR TI-RADS TR3 malignancy rate was lower (20.0% vs 11.1%), and the malignancy rate for both TR4 and TR5 was higher (44.1% vs 83.3%, 91.3% vs 92.8%). Meanwhile, 13 malignant nodules raised from TR4 to TR5, four malignant nodules changed from TR3 to TR4, 15 benign nodules lowered from TR4 to TR3, and 27 benign nodules downgraded from TR3 to TR2. The diagnostic efficacy of the junior radiologist also improved with the assistance of the CAD system, the modified ACR TI-RADS TR3 malignancy rate decreased (39.5% vs. 16.7%), and TR4 and TR5 malignancy rates increased (56.8% vs. 63.2% and 77.4% vs. 88.0%). Furthermore, 18 malignant nodules upgraded from TR4 to TR5, 12 malignant nodules increased from TR3 to TR4, 14 benign nodules lowered from TR4 to TR3, and 22 benign nodules decreased from TR3 to TR2.

The diagnostic efficacy of the radiologists assisted by the CAD system and the comparison with the radiologist alone are shown in Tables 5, 6. Using the modified ACR TI-RADS TR4 as the cutoff value, the AUCs of the senior radiologist + CAD system and the junior radiologist + CAD system were 0.876 and 0.813, respectively, both of which were higher than the performance of the radiologist alone (all $P < 0.0001$). The specificity of the combined diagnosis was also higher than that of the radiologist alone for both junior and senior radiologists (all $P = 0.0001$). When the modified ACR TI-RADS TR5 was used as the cutoff value, the AUCs of the senior radiologist + CAD system and the junior radiologist + CAD system were 0.856 and 0.808, respectively, and the diagnostic efficacy of the junior radiologist + CAD system was higher than when diagnosed alone ($P < 0.0001$), and there was no significant

TABLE 2 Quantitative indicators of the CAD system and the two radiologists with different seniority.

Method	AUC	Accuracy	Sensitivity	Specificity	PPV	NPV
Cutoff value TR4						
CAD	**0.867**	**0.876**	**0.905**	**0.830**	**0.894**	**0.846**
Senior radiologist	0.722	0.766	0.918	0.428	0.755	0.800
Junior radiologist	0.628	0.672	0.821	0.434	0.697	0.605
Cutoff value TR5						
CAD	**0.867**	**0.876**	**0.905**	0.830	0.894	**0.846**
Senior radiologist	0.812	0.796	0.738	**0.887**	**0.912**	0.681
Junior radiologist	0.654	0.635	0.571	0.736	0.774	0.520

The bold values represent the best value of an index in the comparative experiments.
AUC, area under the receiver operating characteristic curve; PPV, positive predictive value; NPV, negative predictive value.

TABLE 3 Quantitative indicators for the two radiologists compared with the CAD system.

	P-value		
	Sensitivity	Specificity	AUC
Cutoff value TR4			
Senior radiologist	1.000	<0.0001*	<0.0001*
Junior radiologist	0.0923	<0.0001*	<0.0001*
Cutoff value TR5			
Senior radiologist	0.0005*	0.0375*	0.0709
Junior radiologist	0.0012*	0.1797	<0.0001*

*Represents statistical significance.

difference between the senior radiologist with or without the assistance of the CAD system ($P = 0.1457$). The sensitivity of all radiologists with the CAD system was higher than the diagnosis alone (all $P < 0.05$).

The effect of the CAD system to reduce unnecessary biopsy is demonstrated in Table 7. With the assistance of the CAD system, the malignancy rate of biopsy increased from 60.8% to 82.8% for senior radiologists and from 48.2% to 78.3% for junior radiologists. Compared with radiologists alone, the unnecessary biopsy rate of the senior radiologist + CAD was reduced (14.6% vs 7.3%, $P = 0.026$), and the unnecessary biopsy rate of the junior radiologist + CAD was more significantly reduced (20.4% vs 9.5%, $P = 0.003$).

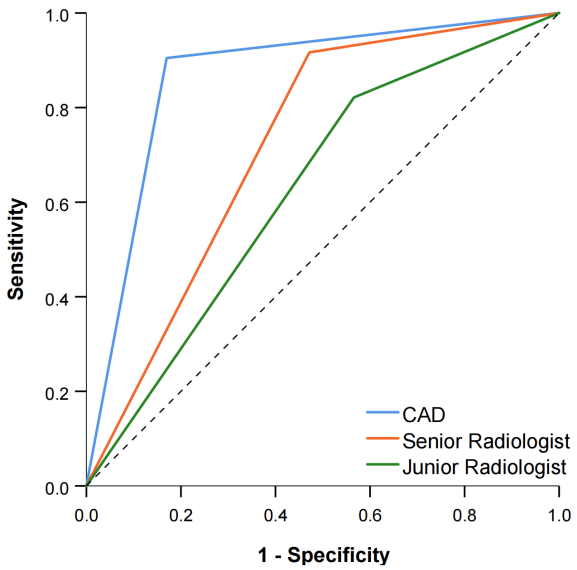

FIGURE 3
Comparison of the ROC curves between CAD and the two radiologists when TR4 was used as the cutoff value.

4 Discussion

As far as we know, several studies have shown that chronic lymphocytic thyroiditis is somehow associated with the development of both PTC and PTL (4, 7, 19), and one case of a patient with both PTC and PTL arising in the setting of HT has been reported (20), such that the treatment and prognosis of the patient would be altered. Ultrasonography and FNA assist in the early identification of patients with malignant changes and should be used promptly in uncertain situations (21). Since FNA is an invasive examination and the ultrasound characteristics of HT make it difficult to identify and aspirate the nodules (22), ultrasound is widely applied in the diagnostic of HT as a non-invasive tool. Conventional sonographic features of HT often present as diffuse parenchyma with numerous inflammatory pseudo-nodules that interfere with the radiologist's judgment, and ultrasound relies on the experience of the radiologist. It can be challenging for young radiologists in remote areas to diagnose thyroid nodules with HT.

Recently, CAD has begun to be used in the diagnosis of thyroid nodules. The results of many studies have shown that the diagnostic efficacy of CAD systems was comparable to that of experienced radiologists and higher than that of inexperienced radiologists (23–27). Gao et al. found that CAD systems possessed a higher sensitivity than experienced radiologists when the ACR TI-RADS TR5 was used as the cutoff value (0.967 *vs.* 0.900, $P < 0.01$) (28). It should be noted that patients with HT were excluded from the above study in order to avoid interference of the CAD system by the complicated context. Hence, different CAD systems had shown high diagnostic performance for thyroid nodules in a homogeneous background. However, such CAD systems were not applicable to all people, and it is our expectation that the CAD system can effectively identify thyroid nodules in a complex background.

Feature selection and extraction are essential steps for traditional CAD systems. It mainly includes four kinds of features, namely, texture features, morphological features,

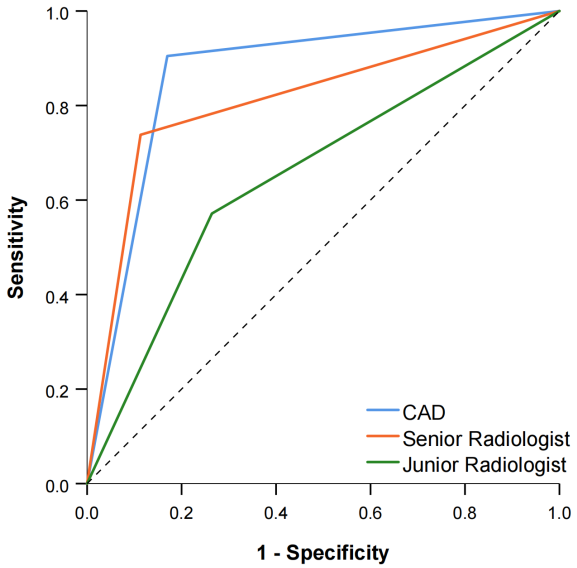

FIGURE 4
Comparison of the ROC curves between CAD and the two radiologists when TR5 was used as the cutoff value.

model-based features, and descriptor features (29), but most of the features are artificially designed, and deep learning CAD systems can automatically extract high-dimensional features that humans cannot recognize. Therefore, some scholars have attempted to use a deep learning CAD system to diagnose thyroid nodules within a complex context. Zhao et al. developed an HT-CAD model based on the convolutional neural network (CNN) with higher diagnostic performance than senior radiologists ($P < 0.001$), and the accuracy was improved by nearly 9% (30). Hou et al. used a deep learning-based CAD system to distinguish nodules in the context of HT, and the AUC was significantly higher than that of three groups of radiologists with different years of experience (all $P < 0.05$) (31). The above studies demonstrated the diagnostic feasibility of CAD systems based on deep learning for nodules in HT, but only static images of the largest section of the nodule were input into the CAD system. As we all know, the malignant features of thyroid nodules vary in different angles and sections, and many nodules with HT have irregular margins and indistinct borders. In this scenario, the CAD system based on deep learning exploited in this study takes advantage of its ability to automatically identify and track the malignant features of each section during dynamic scanning, which can more accurately distinguish the nature of nodules and reduce the interference caused by individual sections compared with static image recognition alone.

Many studies have shown that the CAD system is more beneficial for junior radiologists to improve their diagnostic performance (32–34), which was also confirmed in our study. In this study, we used ACR TI-RADS TR4 and TR5 as the cutoff values separately and found that the AUC of the CAD system was higher than that of both junior and senior radiologists when TR4 was used as the cutoff value, and the specificity of the radiologists was lower than that of the CAD system. The AUC of the CAD system was higher than that of junior radiologists and comparable to that of senior radiologists when TR5 was used as the cutoff value, and the sensitivity of radiologists at this time is lower than that of the CAD system. The reason for this discrepancy may be due to the less distinctive malignant features of nodules in TR4 compared with TR5, resulting in less specificity for radiologists and more reliance on CAD systems. Consequently, we can conclude that no matter whether the ACR TI-RADS cutoff value of TR4 or TR5 was used, the CAD system showed higher diagnostic performance than junior radiologists and was greater than or comparable to senior radiologists. Other than that, regardless of whether the

TABLE 4 Modified ACR TI-RADS according to the CAD system.

ACR TI-RADS	Total	Benign nodules	Malignant nodules	Malignant rate (%)
Senior radiologist/+CAD				
2	0/30	0/30	0/0	0/0
3	35/18	28/16	7/2	20.0/11.1
4	34/6	19/1	15/5	44.1/83.3
5	68/83	6/6	62/77	91.3/92.3
Junior radiologist/+CAD				
2	0/25	0/25	0/0	0/0
3	38/18	23/15	15/3	39.5/16.7
4	37/19	16/7	21/12	56.8/63.2
5	62/75	14/9	48/66	77.4/88.0

TABLE 5 Quantitative indicators of the two radiologists with different seniority assisted by the CAD system.

Method	AUC	Accuracy	Sensitivity	Specificity	PPV	NPV
Cutoff value modified TR4						
Senior radiologist + CAD	0.876	0.891	0.940	0.811	0.888	0.896
Junior radiologist + CAD	0.813	0.839	0.928	0.698	0.830	0.860
Cutoff value modified TR5						
Senior radiologist + CAD	0.856	0.861	0.881	0.830	0.892	0.815
Junior radiologist + CAD	0.808	0.803	0.786	0.830	0.880	0.710

TABLE 6 Quantitative indicators of the two radiologists combined with the CAD system compared with the radiologists alone.

	P-value		
	Sensitivity	Specificity	AUC
Cutoff value modified TR4			
Senior radiologist + CAD	0.6875	0.0001*	<0.0001*
Junior radiologist + CAD	0.0352*	0.0001*	<0.0001*
Cutoff value modified TR5			
Senior radiologist + CAD	0.0018*	0.3750	0.1457
Junior radiologist + CAD	<0.0001*	0.1797	<0.0001*

*Represents statistical significance.

modified ACR TR4 or TR5 was used as the cutoff value, the efficacy of the junior radiologist + CAD was higher than that of the radiologist alone, while the efficacy of the senior radiologist was not significantly different from that of the radiologist alone, which could indicate that the support of the CAD system is more contributing to the diagnostic effectiveness of junior radiologists.

FNA is often performed because of suspicious nodules in patients with HT (35). It was found in our study that radiologists combined with the CAD system, compared with radiologists alone, resulted in a decreased number of TR4 nodules and an increased number of TR2 and TR5 nodules. The junior radiologist, assisted by the CAD system, moved 30 malignant nodules up one level and 43 benign nodules down one level. According to the modified ACR TI-RADS recommendations for FNA, the rate of unnecessary biopsy rate by junior and senior radiologists decreased by 10.9% and 7.3%, and the rate of malignancy in punctured nodules increased by 30.1% and 22.0%, respectively, which were consistent with the results of several studies (23, 36, 37). Therefore, with the assistance of the CAD system, radiologists were capable of reducing unnecessary biopsy of thyroid nodules in the context of HT and improving the malignancy rate of the nodules.

The present study has also some limitations. First, this study is a single-center study with a small sample size, and all patients included in this study were surgical patients, so these limitations increased the possibility of bias. The second is that all of the

TABLE 7 The effectiveness of the CAD system in assisting junior and senior radiologists in FNA.

	FNA		Malignant rate of biopsy (%)	Unnecessary biopsy rate (%)	*P*-value
	Benign	Malignant			
Senior radiologist	20	31	60.8 (31/51)	14.6 (20/137)	–
Junior radiologist	28	26	48.2 (26/54)	20.4 (28/137)	–
Senior radiologist + CAD	10	48	82.8 (48/58)	7.3 (10/137)	0.026*
Junior radiologist + CAD	13	47	78.3 (47/60)	9.5 (13/137)	0.003*

P-value is the comparison of unnecessary biopsy rates before and after the application of the CAD system.
*Represents statistical significance.

malignant thyroid nodules in this study were papillary carcinoma, while other pathological types, such as medullary cancer or lymphoma, need to be investigated. In addition, the background of nodules with HT is complex, which makes the automatic identification of nodules difficult, and further development of a higher-performance CAD system is required. A multicenter, prospective study exploring the value of deep learning CAD software in HT with a large sample of different types of TC is worthy of further development.

5 Conclusion

In conclusion, this study shows that the CAD system based on deep learning is a non-invasive and effective method to identify benign and malignant thyroid nodules in the context of HT. Moreover, radiologists, with the assistance of the CAD system, can play a role in FNA recommendations and reduce the rate of unnecessary biopsies, especially for junior radiologists.

Data availability statement

The original contributions presented in the study are included in the article/supplementary material. Further inquiries can be directed to the corresponding author.

Ethics statement

Written informed consent was obtained from the individual(s) for the publication of any potentially identifiable images or data included in this article.

Author contributions

LG was responsible for the writing of the manuscript and the design of the study. PZ provided major suggestions for the manuscript. JL and WL advised on the data analysis and image collection. All authors contributed to the article and approved the submitted version.

Funding

This research was supported by grants from the National Natural Science Foundation of China (No. 81871367), Project of Hunan Provincial Health Commission (No. 202209025123), and the Natural Science Foundation of Hunan Province, China (No. 2021JJ31037).

Acknowledgments

Thanks to all colleagues in the Department of Ultrasound, Third Xiangya Hospital, Central South University for their help to the authors.

Conflict of interest

The authors declare that the research was conducted in the absence of any commercial or financial relationships that could be construed as a potential conflict of interest.

Publisher's note

References

1. Ragusa F, Fallahi P, Elia G, Gonnella D, Paparo SR, Giusti C, et al. Hashimotos' thyroiditis: Epidemiology, pathogenesis, clinic and therapy. *Best Pract Res Clin Endocrinol Metab* (2019) 33(6):101367. doi: 10.1016/j.beem.2019.101367

2. McLeod DS, Cooper DS. The incidence and prevalence of thyroid autoimmunity. *Endocrine* (2012) 42(2):252–65. doi: 10.1007/s12020-012-9703-2

3. Moshynska OV, Saxena A. Clonal relationship between hashimoto thyroiditis and thyroid lymphoma. *J Clin Pathol* (2008) 61(4):438–44. doi: 10.1136/jcp.2007.051243

4. Lee JH, Kim Y, Choi JW, Kim YS. The association between papillary thyroid carcinoma and histologically proven hashimoto's thyroiditis: A meta-analysis. *Eur J Endocrinol* (2013) 168(3):343–9. doi: 10.1530/eje-12-0903

5. Feldt-Rasmussen U. Hashimoto's thyroiditis as a risk factor for thyroid cancer. *Curr Opin Endocrinol Diabetes Obes* (2020) 27(5):364–71. doi: 10.1097/med.0000000000000570

6. Castagna MG, Belardini V, Memmo S, Maino F, Di Santo A, Toti P, et al. Nodules in autoimmune thyroiditis are associated with increased risk of thyroid cancer in surgical series but not in cytological series: Evidence for selection bias. *J Clin Endocrinol Metab* (2014) 99(9):3193–8. doi: 10.1210/jc.2014-1302

7. Ehlers M, Schott M. Hashimoto's thyroiditis and papillary thyroid cancer: Are they immunologically linked? *Trends Endocrinol Metab* (2014) 25(12):656–64. doi: 10.1016/j.tem.2014.09.001

8. Ralli M, Angeletti D, Fiore M, D'Aguanno V, Lambiase A, Artico M, et al. Hashimoto's thyroiditis: An update on pathogenic mechanisms, diagnostic

protocols, therapeutic strategies, and potential malignant transformation. *Autoimmun Rev* (2020) 19(10):102649. doi: 10.1016/j.autrev.2020.102649

9. Orgiazzi J. Thyroid autoimmunity. *La Presse Médicale* (2012) 41(12, Part 2): e611–e25. doi: 10.1016/j.lpm.2012.10.002

10. Durfee SM, Benson CB, Arthaud DM, Alexander EK, Frates MC. Sonographic appearance of thyroid cancer in patients with hashimoto thyroiditis. *J Ultrasound Med* (2015) 34(4):697–704. doi: 10.7863/ultra.34.4.697

11. Peng Q, Niu C, Zhang M, Peng Q, Chen S. Sonographic characteristics of papillary thyroid carcinoma with coexistent hashimoto's thyroiditis: Conventional ultrasound, acoustic radiation force impulse imaging and contrast-enhanced ultrasound. *Ultrasound Med Biol* (2019) 45(2):471–80. doi: 10.1016/j.ultrasmedbio.2018.10.020

12. Wang D, Du L-Y, Sun J-W, Hou X-J, Wang H, Wu J-Q, et al. Evaluation of thyroid nodules with coexistent hashimoto's thyroiditis according to various ultrasound-based risk stratification Systems: A retrospective research. *Eur J Radiol* (2020) 131:109059. doi: 10.1016/j.ejrad.2020.109059

13. Tessler FN, Middleton WD, Grant EG, Hoang JK, Berland LL, Teefey SA, et al. Acr thyroid imaging, reporting and data system (Ti-rads): White paper of the acr Ti-rads committee. *J Am Coll Radiol* (2017) 14(5):587–95. doi: 10.1016/j.jacr.2017.01.046

14. Zhang B, Tian J, Pei S, Chen Y, He X, Dong Y, et al. Machine learning-assisted system for thyroid nodule diagnosis. *Thyroid* (2019) 29(6):858–67. doi: 10.1089/thy.2018.0380

15. Zhao H-N, Liu J-Y, Lin Q-Z, He Y-S, Luo H-H, Peng Y-L, et al. Partially cystic thyroid cancer on conventional and elastographic ultrasound: A retrospective study and a machine learning–assisted system. *Ann Trans Med* (2020) 8(7):495. doi: 10.21037/atm.2020.03.211

16. Hosny A, Parmar C, Quackenbush J, Schwartz LH, Aerts H. Artificial intelligence in radiology. *Nat Rev Cancer* (2018) 18(8):500–10. doi: 10.1038/s41568-018-0016-5

17. Li X, Zhang S, Zhang Q, Wei X, Pan Y, Zhao J, et al. Diagnosis of thyroid cancer using deep convolutional neural network models applied to sonographic images: A retrospective, multicohort, diagnostic study. *Lancet Oncol* (2019) 20(2):193–201. doi: 10.1016/s1470-2045(18)30762-9

18. Xu L, Gao J, Wang Q, Yin J, Yu P, Bai B, et al. Computer-aided diagnosis systems in diagnosing malignant thyroid nodules on ultrasonography: A systematic review and meta-analysis. *Eur Thyroid J* (2020) 9(4):186–93. doi: 10.1159/000504390

19. Yang L, Zhao H, He Y, Zhu X, Yue C, Luo Y, et al. Contrast-enhanced ultrasound in the differential diagnosis of primary thyroid lymphoma and nodular hashimoto's thyroiditis in a background of heterogeneous parenchyma. *Front Oncol* (2021) 10:597975. doi: 10.3389/fonc.2020.597975

20. Trovato M, Giuffrida G, Seminara A, Fogliani S, Cavallari V, Ruggeri RM, et al. Coexistence of diffuse Large b-cell lymphoma and papillary thyroid carcinoma in a patient affected by hashimoto's thyroiditis. *Arch Endocrinol Metab* (2017) 61(6):643–6. doi: 10.1590/2359-3997000000313

21. Penta L, Cofini M, Lanciotti L, Leonardi A, Principi N, Esposito S. Hashimoto's disease and thyroid cancer in children: Are they associated? *Front Endocrinol* (2018) 9:565. doi: 10.3389/fendo.2018.00565

22. Hu F, Yan Z, Ma B, Jiang Y, Huang H. The impact of concurrent hashimoto thyroiditis on thyroid nodule cytopathology assessed by ultrasound-guided fine-needle aspiration cytology. *Postgrad Med* (2020) 132(6):506–11. doi: 10.1080/00325481.2020.1739462

23. Liang X, Huang Y, Cai Y, Liao J, Chen Z. A computer-aided diagnosis system and thyroid imaging reporting and data system for dual validation of ultrasound-guided fine-needle aspiration of indeterminate thyroid nodules. *Front Oncol* (2021) 11:611436(4037). doi: 10.3389/fonc.2021.611436

24. Chung SR, Baek JH, Lee MK, Ahn Y, Choi YJ, Sung TY, et al. Computer-aided diagnosis system for the evaluation of thyroid nodules on ultrasonography: Prospective non-inferiority study according to the experience level of radiologists. *Korean J Radiol* (2020) 21(3):369–76. doi: 10.3348/kjr.2019.0581

25. Jeong EY, Kim HL, Ha EJ, Park SY, Cho YJ, Han M. Computer-aided diagnosis system for thyroid nodules on ultrasonography: Diagnostic performance and reproducibility based on the experience level of operators. *Eur Radiol* (2019) 29(4):1978–85. doi: 10.1007/s00330-018-5772-9

26. Jin Z, Zhu Y, Zhang S, Xie F, Zhang M, Zhang Y, et al. Ultrasound computer-aided diagnosis (Cad) based on the thyroid imaging reporting and data system (Ti-rads) to distinguish benign from malignant thyroid nodules and the diagnostic performance of radiologists with different diagnostic experience. *Med Sci Monit* (2020) 26:e918452. doi: 10.12659/msm.918452

27. Reverter JL, Ferrer-Estopiñan L, Vázquez F, Ballesta S, Batule S, Perez-Montes de Oca A, et al. Reliability of a computer-aided system in the evaluation of indeterminate ultrasound images of thyroid nodules. *Eur Thyroid J* (2022) 11(1): e210023. doi: 10.1530/etj-21-0023

28. Gao L, Liu R, Jiang Y, Song W, Wang Y, Liu J, et al. Computer-aided system for diagnosing thyroid nodules on ultrasound: A comparison with radiologist-based clinical assessments. *Head Neck* (2018) 40(4):778–83. doi: 10.1002/hed.25049

29. Huang Q, Zhang F, Li X. Machine learning in ultrasound computer-aided diagnostic systems: A survey. *BioMed Res Int* (2018) 2018:5137904. doi: 10.1155/2018/5137904

30. Zhao W, Kang Q, Qian F, Li K, Zhu J, Ma B. Convolutional neural network-based computer-assisted diagnosis of hashimoto's thyroiditis on ultrasound. *J Clin Endocrinol Metab* (2021) 107(4):953–63. doi: 10.1210/clinem/dgab870

31. Hou Y, Chen C, Zhang L, Zhou W, Lu Q, Jia X, et al. Using deep neural network to diagnose thyroid nodules on ultrasound in patients with hashimoto's thyroiditis. *Front Oncol* (2021) 11:614172. doi: 10.3389/fonc.2021.614172

32. Zhang Y, Wu Q, Chen Y, Wang Y. A clinical assessment of an ultrasound computer-aided diagnosis system in differentiating thyroid nodules with radiologists of different diagnostic experience. *Front Oncol* (2020) 10:557169. doi: 10.3389/fonc.2020.557169

33. Fresilli D, Grani G, De Pascali ML, Alagna G, Tassone E, Ramundo V, et al. Computer-aided diagnostic system for thyroid nodule sonographic evaluation outperforms the specificity of less experienced examiners. *J Ultrasound* (2020) 23(2):169–74. doi: 10.1007/s40477-020-00453-y

34. Kang S, Lee E, Chung CW, Jang HN, Moon JH, Shin Y, et al. A beneficial role of computer-aided diagnosis system for less experienced physicians in the diagnosis of thyroid nodule on ultrasound. *Sci Rep* (2021) 11(1):20448. doi: 10.1038/s41598-021-99983-6

35. Capitoli G, Piga I, Clerici F, Brambilla V, Mahajneh A, Leni D, et al. Analysis of hashimoto's thyroiditis on fine needle aspiration samples by maldi-imaging. *Biochim Biophys Acta (BBA) - Proteins Proteomics* (2020) 1868(11):140481. doi: 10.1016/j.bbapap.2020.140481

36. Thomas J, Haertling T. Aibx, artificial intelligence model to risk stratify thyroid nodules. *Thyroid* (2020) 30(6):878–84. doi: 10.1089/thy.2019.0752

37. Ha EJ, Baek JH. Applications of machine learning and deep learning to thyroid imaging: Where do we stand? *Ultrasonography* (2021) 40(1):23–9. doi: 10.14366/usg.20068

frontiers | Frontiers in Oncology

TYPE Original Research
PUBLISHED 06 January 2023
DOI 10.3389/fonc.2022.1007134

OPEN ACCESS

EDITED BY
Pilar López-Larrubia,
Spanish National Research Council (CSIC), Spain

REVIEWED BY
Tao Yu,
China Medical University, China
Zhendong Jin,
Second Military Medical University, China

*CORRESPONDENCE
Debiao Li
Debiao.Li@cshs.org

SPECIALTY SECTION
This article was submitted to Cancer Imaging and Image-directed Interventions, a section of the journal Frontiers in Oncology

RECEIVED 30 July 2022
ACCEPTED 16 November 2022
PUBLISHED 06 January 2023

CITATION
Wang N, Gaddam S, Xie Y, Christodoulou AG, Wu C, Ma S, Fan Z, Wang L, Lo S, Hendifar AE, Pandol SJ and Li D (2023) Multitasking dynamic contrast enhanced magnetic resonance imaging can accurately differentiate chronic pancreatitis from pancreatic ductal adenocarcinoma. *Front. Oncol.* 12:1007134. doi: 10.3389/fonc.2022.1007134

Multitasking dynamic contrast enhanced magnetic resonance imaging can accurately differentiate chronic pancreatitis from pancreatic ductal adenocarcinoma

Nan Wang[1], Srinivas Gaddam[2], Yibin Xie[1], Anthony G. Christodoulou[1,3], Chaowei Wu[1,3], Sen Ma[1], Zhaoyang Fan[1,4], Lixia Wang[1], Simon Lo[2], Andrew E. Hendifar[5], Stephen J. Pandol[2] and Debiao Li[1,3]*

[1]Biomedical Imaging Research Institute, Cedars-Sinai Medical Center, Los Angeles, CA, United States, [2]The Karsh Division of Gastroenterology and Hepatology, Cedars Sinai Medical Center, Los Angeles, CA, United States, [3]Bioengineering Department, University of California, Los Angeles, Los Angeles, CA, United States, [4]Department of Radiology, Keck School of Medicine, University of Southern California, Los Angeles, Los Angeles, CA, United States, [5]Samuel Oschin Comprehensive Cancer Center, Cedars-Sinai Medical Center, Los Angeles, CA, United States

Background and aims: Accurate differentiation of chronic pancreatitis (CP) and pancreatic ductal adenocarcinoma (PDAC) is an area of unmet clinical need. In this study, a novel Multitasking dynamic contrast enhanced (DCE) magnetic resonance imaging (MRI) technique was used to quantitatively evaluate the microcirculation properties of pancreas in CP and PDAC and differentiate between them.

Methods: The Multitasking DCE technique was able to acquire one 3D image per second during the passage of MRI contrast agent, allowing the quantitative estimation of microcirculation properties of tissue, including blood flow F_p, plasma volume fraction v_p, transfer constant K^{trans}, and extravascular extracellular volume fraction v_e. Receiver operating characteristic (ROC) analysis was performed to differentiate the CP pancreas, PDAC pancreas, normal control pancreas, PDAC tumor, PDAC upstream, and PDAC downstream. ROCs from quantitative analysis and conventional analysis were compared.

Results: Fourteen PDAC patients, 8 CP patients and 20 healthy subjects were prospectively recruited. The combination of F_p, v_p, K^{trans}, and v_e can differentiate CP versus PDAC pancreas with good AUC (AUC [95% CI] = 0.821 [0.654 – 0.988]), CP versus normal pancreas with excellent AUC (1.000 [1.000 – 1.000]), PDAC pancreas versus normal pancreas with excellent AUC (1.000 [1.000 – 1.000]), CP versus PDAC tumor with excellent AUC (1.000 [1.000 – 1.000]), CP versus PDAC downstream with excellent AUC (0.917 [0.795 – 1.000]), and CP versus PDAC upstream with fair AUC (0.722 [0.465 – 0.980]).

This quantitative analysis outperformed conventional analysis in differentiation of each pair.

Conclusion: Multitasking DCE MRI is a promising clinical tool that is capable of unbiased quantitative differentiation between CP from PDAC.

KEYWORDS

quantitative imaging, dynamic contrast enhanced magnetic resonance imaging, microcirculation properties, Multitasking DCE, differential diagnosis of chronic pancreatitis and pancreatic ductal adenocarcinoma

Introduction

Pancreatic ductal adenocarcinoma (PDAC) is the third most common cause of cancer-related death in the United States with a poor 5-year survival rate of 9% (1). Currently the only curative treatment for PDAC is complete tumor resection, often in conjugation with adjuvant chemotherapy (2), where an accurate diagnosis at early stage is a prerequisite. Chronic pancreatitis is a fibrotic reaction of the pancreatic connective tissue due to an ongoing inflammation that can damage both endocrine and exocrine pancreas (3). The most worrisome complication of CP is the increased risk for developing PDAC, which can be 2.3 -18.5 folds higher (4–7). On the other hand, 10-20% of CP cases can be mass forming and mimic PDAC, which may cause misdiagnosis and overtreatment (8). PDAC is also likely to be associated with chronic obstructive pancreatitis in the upstream portion of the pancreas as a result of main pancreatic ductal obstruction by tumor (9).

Accurate differentiation of PDAC from CP is of great clinical importance for timely and precise treatment. However, this continues to be a challenging area due to the shared clinical signs, radiologic features, and morphologic appearance of the two diseases (10–13). Conventional imaging techniques including endoscopic ultrasound (EUS), PET/CT, and MRI cannot differentiate well between early PDAC and CP as the typical imaging features of CP (generalized parenchymal glandular atrophy, diffuse pancreatic calcifications, and dilation of the main pancreatic duct) can often be seen in PDAC (14, 15), resulting in reduced diagnostic accuracy. Even a fine needle biopsy (FNB) can be unreliable in this situation (16–18). This may result in further delay of diagnosis and treatment of PDAC or unnecessary surgery and exposure to complications of CP (11, 19).

In recent years, dynamic contrast enhanced (DCE) magnetic resonance imaging (MRI) has been an emerging tool for the clinical diagnosis of PDAC. Investigational studies also showed that DCE MRI may have a promising role in the diagnosis of CP and the differentiation of CP versus PDAC (20–23). It acquires a series of T1-weighted images during the injection and passage of gadolinium (Gd)-based contrast agent (CA). The changes of the signal intensity reflect the CA distribution within the tissue and the underlying microcirculation properties such as tissue blood flow, microvascular density, permeability, and extravascular extracellular space distribution. These microcirculation properties contain crucial information about disease characteristics, progression, and regression, and can be used for diagnosis and therapy monitoring (23–25).

However, DCE MRI has yet to fully realize its potential in the imaging of pancreas due to demanding technical challenges. Existing techniques cannot achieve adequate coverage and high spatiotemporal resolution at the same time. In clinical practice, T1-weighted images are usually acquired for four to six phases during the CA passage (referred as multi-phase MRI) (22, 26, 27), and each phase takes 15-20 seconds. In addition, the presence of respiratory motion and the need to hold breath makes the time intervals even larger, which is insufficient to quantify the microcirculation properties. Consequently, current diagnosis relies only on the morphological information of the pre- and post-contrast images, which are subject to coil positioning, and inter-scanner and inter-reader variability given its qualitative nature.

To overcome these limitations, our research group has developed a quantitative Multitasking DCE MRI technique (28) that has shown promise in the characterization of carotid atherosclerosis (29), PDAC (30), and breast cancer (31). Specifically for pancreas, this technique allows free-breathing acquisition, coverage of the entire abdomen, clinically sufficient spatial resolution, 1-second temporal resolution (one 3D image per second). With the high temporal resolution, Multitasking DCE is able to capture the contrast agent kinetics within the tissues, and thus to quantitatively evaluate the microcirculation properties. Our prior work has preliminarily demonstrated that Multitasking DCE MRI can produce high-quality image with free-breathing acquisition and characterize PDAC tissues (30). In this study, we aim to quantitatively evaluate the microcirculation properties of pancreas in CP and PDAC using Multitasking DCE, and to distinguish them with the quantitative parameters on an objective basis.

Materials and methods

Study population

The prospective study was approved by the local institutional review board and written informed consent was obtained from all participating subjects before the research imaging studies. The study was performed from February 2018 to June 2019 with PDAC patients, CP patients, and healthy volunteers. Among them, nineteen patients with PDAC, which was confirmed by histopathology obtained by EUS-guided FNB, were recruited to the study. All the PDAC patients received clinical CT within 1 week before the research MRI and were undergoing neoadjuvant chemotherapy at the time of the study. Patients were excluded for the following reasons: 1) prior surgical resections of PDAC; 2) intolerance to Gd-based contrast agent. Eight patients with definitive CP were recruited from an NIH-sponsored prospective cohort of patients with pancreatic disease (32). The inclusionary criteria were the clinical diagnosis of unequivocal CP (Cambridge grade >3). All these images were reviewed and confirmed to be CP by a radiologist as part of the PROCEED study (NCT03099850) (32). Healthy volunteers without a history of pancreas diseases or family history of pancreatic cancer were recruited as the normal control group. Subjects with noticeable pancreatic abnormality were excluded from the final analysis.

MRI experiments

All subjects received the research MRI imaging on a 3-Tesla clinical MRI scanner (Biograph mMR, Siemens Medical Solutions, Erlangen, Germany) in head-first supine position with an 18-channel phase array surface coil. In the imaging session, a standard-of-care non-contrast protocol was first performed. It consisted of:

1) 3D T1-weighted gradient echo with Dixon fat suppression in axial orientation with parameters: 18-second breath-holding, flip angle = 9°, field of view (FOV) = 247 × 380 mm, acquisition matrix = 180 × 320, slice thickness = 3 mm, number of slices = 72.
2) Multi-slice T2-weighted single-shot turbo spin-echo in axial and coronal orientations with parameters: 42-second free-breathing, flip angle = 105°, FOV=226 × 330 mm, matrix =176 × 256, slice thickness = 5 mm, slice gap = 1 mm, number of slices = 46.
3) Multi-slice single-shot echo-planar diffusion-weighted imaging with parameters: 5-min free-breathing, *b*-values = 50, 400, and 800 s/mm^2, FOV = 306 × 399 mm; matrix, 132 × 172, slice thickness = 6 mm, slice gap = 1 mm, number of slices = 50.
4) Multi-slice magnetic resonance cholangiopancreatography (MRCP): 10-min respiratory-triggering, flip angle = 100°, FOV = 300 × 300 mm, acquisition matrix = 384 × 384, slice thickness = 1 mm, number of slices = 80.
5) Multitasking DCE. It is a 10-min free-breathing acquisition of saturation-prepared gradient echo sequence with following parameters: saturation recovery time = 500 ms, flip angle = 10°, field of view (FOV) = 268 × 380 mm, acquisition matrix = 200 × 320, slice thickness = 3 mm, number of slices = 120. The Gd-based contrast agent (Gadavist, 0.1 mmol/kg, Bayer Schering Pharma) was administrated intravenously 3 minutes into the scan at a rate of 2 mL/s, followed by a 20 mL saline flush at the same rate. The reconstructed images have a temporal resolution of 1 second.

Detailed imaging parameters for the protocols are summarized in Table 1.

Multitasking DCE reconstruction and quantitative DCE modeling

The reconstruction and quantitative analysis of Multitasking DCE images were processed off-line in MATLAB (R2018a, Mathworks, MA, USA). The details on the reconstruction have been described in Wang et al (30). In this work, the 3D Multitasking DCE images covering the entire abdomen were reconstructed at 6 respiratory states and the images of end-expiration were used for subsequent analysis. The reconstructed spatial resolution is 1.2 × 1.2 × 3.0 mm (3). The reconstructed temporal resolution is 1 second, leading to 600 dynamic T1 maps within the 10-minute acquisition.

With the dynamic T1 maps, the CA concentration can be directly calculated without approximation using the equation:

$$C_t(t_d) = \frac{R_{1,t}(t_d) - R_1(0)}{\gamma}, \quad (1)$$

where C_t is the CA concentration in a certain tissue (any type of tissue within the FOV), t_d is the DCE time points from 0 to 10 minutes at an interval of 1 second, $R_{1,t}$ is the relaxation rate (1/$T_{1,t}$) of the tissue, and γ= 4.0 L·mmol^{-1}·s^{-1} is the relaxivity rate of Gadavist. The CA concentration in the arterial plasma C_p, termed as arterial input function (AIF), can also be derived using Equation 1.

With the CA concentration of plasma C_p and of the target tissue C_t, the two-compartment exchange model (33) was used to describe the contrast agent activities and estimate the microcirculation parameters including tissue plasma flow F_p, fractional plasma volume v_p, transfer constant K^{trans}, and extravascular extracellular faction v_e. The microcirculation parameters were derived using following equations (31):

TABLE 1 List of imaging parameters.

parameters	T1W GRE	T2W HASTE	SS-EPI DWI	MRCP	Multitasking DCE
Slice thickness (mm)	3	5	6	1	3
Slice resolution	50%	N/A	N/A	N/A	50%
Gap (mm)	N/A	1	1	0	N/A
Number of slices acquired	72	86	50	80	120
TR (ms)	4.15	1000	4500	8903	5.60
TE (ms)	1.39/2.65(OP/IP)	99	47	701	2.45
Number of averages	1	1	6	1	1
FOV (mm^2)	247×380	226×330	306×339	300×300	268×380
Acquisition matrix	180×320	176×256	132×172	384×384	200×320
Flip angle (°)	9	105	90	100	10
iPAT factor	3	2	2	2	N/A
Scan time	18-second breath hold	42-second free-breathing	5-min free-breathing	10-min resp-triggered	10-min free-breathing

T1W GRE, T1-weighted gradient echo; T2W HASTE, T2-weighted single-shot turbo spin-echo; SS-EPI-DWI, single-shot echo-planar diffusion weighted imaging; MRCP, magnetic resonance cholangiopancreatography; N/A, Not applicable.

$$C_t(t_d) = F_p \cdot C_p(t_d) \star \left(M e^{-\alpha t_d} + (1 - M) e^{-\beta t_d} \right), \quad (2)$$

$$v_p = \frac{F_p}{M\alpha + (1-M)\beta}, \quad K^{trans} = F_p \frac{M(1-M)(\alpha-\beta)^2}{M\alpha^2 + (1-M)\beta^2}, \quad v_e = v_p \frac{M(1-M)(\alpha-\beta)^2}{\alpha\beta}, \quad (3)$$

where * denotes convolution, and M, α, and β are intermediate variables. The plasma flow F_p and three intermediate parameters M, α, and β are first fitted from C_p and C_t using Equation 2. The v_p, K^{trans}, and v_e are subsequently calculated using Equation 3.

Pancreas segmentation and image analysis

A radiologist (LW), who has 11-year clinical experience in the reading of abdominal MRIs and was blinded to the histopathological diagnosis, evaluated all the MRI images. The margin of the pancreas for all subjects were drawn manually on the Multitasking DCE images. For PDAC images, the tumor boundary was identified by cross-referencing the non-contrast MRI protocols of the same imaging session and the clinical contrast-enhanced CT images acquired within 1 week before the study. The region of interest (ROI) of PDAC tumor was then defined on multiple slices within the boundary of tumor avoiding edges and vessels. The ROI of pancreas upstream and downstream were defined subsequently, if applicable. The ROI of the PDAC pancreas was a combination of the ROIs of PDAC tumor, upstream (if any), and downstream (if any). For CP and normal control pancreas, the ROI was maximized within the pancreas margin. As a summary, six types of tissues were defined: 1) PDAC tumor, 2) PDAC upstream, 3) PDAC downstream, 4) PDAC pancreas, 5) CP pancreas, and 6) normal control pancreas. The microcirculation parameters reported for each type of tissue for each case were the average of all voxels within the ROI.

Statistical analysis

Statistical analysis was conducted in SPSS (Version 24, IBM, NY, USA). The descriptive statistics including mean and standard deviation (SD) were obtained for six type of tissues: PDAC pancreas, PDAC tumor, PDAC upstream, PDAC downstream, CP pancreas, and normal control pancreas. Analysis of variance (ANOVA) with Bonferroni correction was used to assess the multi-group comparison. The value of $P< 0.05$ was considered statistically significant. The performance of the microcirculation parameters in the differentiation of the tissues were assessed with receiver operating characteristic (ROC) analysis. The sensitivity, specificity, and area under the ROC curve (AUC) of each single microcirculation parameter and combination of all parameters were evaluated. An AUC of 0.5 to 0.6 suggests no discrimination, 0.6 to 0.7 is considered poor, 0.7 to 0.8 is fair, 0.8 to 0.9 is good, and > 0.9 is excellent (34).

Comparison of quantitative DCE analysis versus conventional time-signal intensity curve analysis

For clinical multi-phase MRI, quantitative microcirculation parameters are unavailable due to the small number of DCE phases acquired and the low temporal resolution. Under this circumstance, time-signal intensity curve (TIC) approach serves as an alternative way to analyze the CA dynamics (22). It classifies the shape of the time-signal intensity curves into

several categories based on the time to the peak and the wash-out patterns, as shown in Supplementary Figure S1 in the supplementary materials. The enhancement patterns are useful to differentiate pathological tissues from normal. Zhang et al (22) reported that conventional multi-phase MRI with TIC analysis was able to differentiate mass-forming pancreatitis from PDAC. To compare the differentiation ability of the quantitative DCE analysis versus the TIC analysis, the high-temporal-resolution Multitasking DCE images were averaged to a temporal resolution of 18-second per phase and 6 key phases were chosen for analysis: pre-contrast, 18-second, 45-second, 75-second, 2.5-minute, 4-min post-contrast. The pattern of the signal intensity curves were classified into 5 types (18), as illustrated in Supplementary Figure S1A in the supplementary material: type I, a rapid rise to the peak at 18 s after injection; type II to V, a slower rise to a peak at 45s, 75s, 2.5 or 4 min after the injection, respectively. For each type of curve, two subtypes were defined based on the wash-out pattern (Supplementary Figure S1B): subtype-a, more than 10% signal decrease after reaching the peak; subtype-b, less than 10% signal decrease after the peak. Each tissue of each case was assigned to a category and the ROC analysis was performed to differentiate the tissues based on their categories. Subsequently, a significance test was performed to compare the AUC values produced by the ROC analysis using TIC versus using quantitative DCE approach according to DeLong test using MedCalc (MedCalc Software Ltd, Belgium).

Results

Demographics

The demographics of this study are summarized in Figure 1. Among the 19 PDAC patients, two of them had undergone surgery on the pancreas in the past. Additionally, two others were not able to receive MRI contrast agent. Finally, another one patient had excess bulk motion during the study, yielding unreadable MR images. These patients were excluded, and the final group included 14 PDAC patients (51 to 77 years old, 7 females). The mean size of the tumors, defined as the largest diameter in axial CT images according to RECIST 1.1 criteria31, was 3.9 cm, ranging from 1.6 cm to 6.7 cm. Six tumors were in the pancreatic head, three in the pancreatic neck, three in the pancreatic body, and two in the pancreatic tail. The PDAC downstream was measurable in 10 cases, while the PDAC upstream was measurable in 9 cases. A total of 8 CP patients (30 to 72 years old, 4 females) underwent MRI imaging. Upon review of the images, all of them met the Cambridge criteria for CP. In addition, a total of 20 healthy subjects (23 to 60 years old, 9 females) were included as normal control group in the study.

Quantifications of microcirculation parameters for different tissues

The microcirculation parameters were estimated successfully for all the involved subjects. Figure 2 (A) shows the example microcirculation parametric maps from a 72-year-old PDAC patient with the tumor located at the neck of the pancreas, as labeled by red solid boundary on the gray-scale image. The CA concentration curve of PDAC tumor shows slower and progressive enhancement, while the concentration curve of downstream pancreas showed faster wash-in and moderate wash-out. Reduced F_p, v_p, K^{trans}, and increased v_e was observed in PDAC tumor. Figure 2B is an example from a 65-year-old patient with CP, labeled by yellow dashed boundary. An example of normal control pancreas from a 32-year-old healthy subject is shown in Figure 2C.

The mean and standard deviation measurement of F_p, v_p, K^{trans}, and v_e for the six types of tissues are displayed in the bar

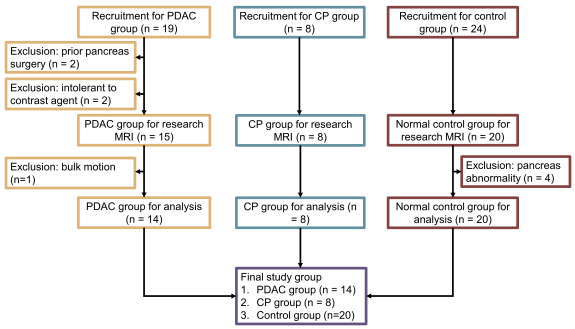

FIGURE 1
Flow chart for subject recruitment and grouping.

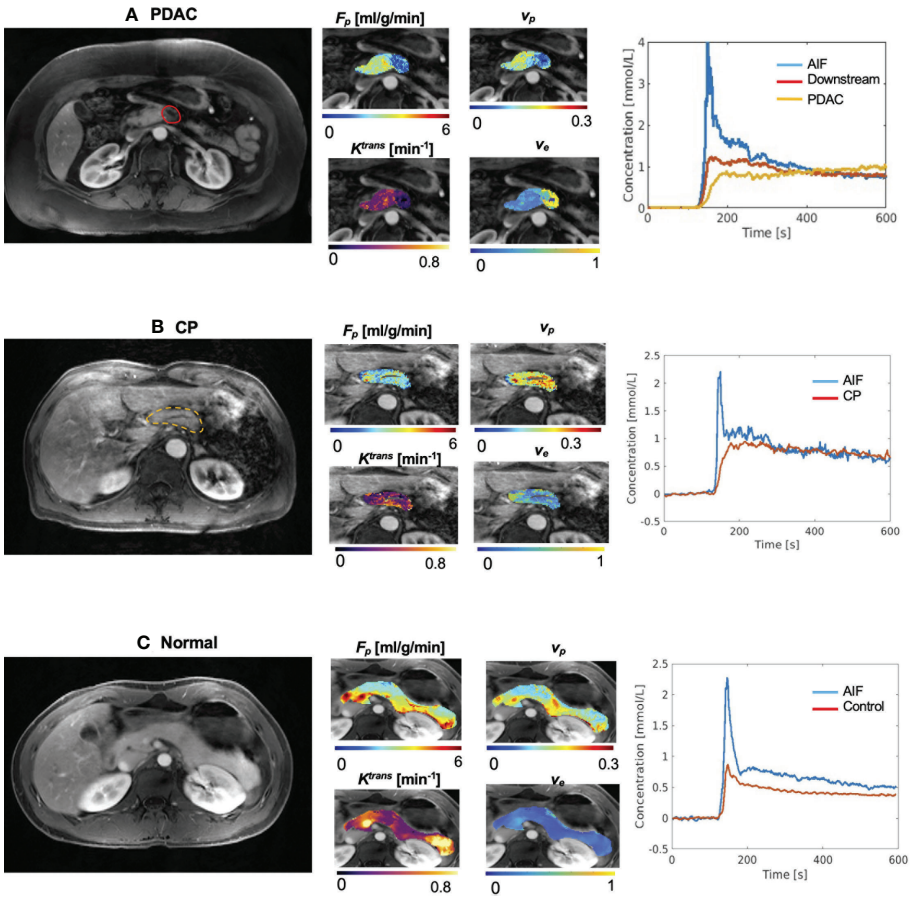

FIGURE 2
Example microcirculation parametric maps. **(A)** Example maps from 72-year-old patient with PDAC, whose tumor is located at the neck of pancreas. First panel shows a gray-scale Multitasking image at the arterial phase at the center slice of the tumor. The tumor was labeled by the red solid boundary. Downstream was visible in this slice. The second panel shows estimated microcirculation parametric maps. PDAC tumor showed lower F_p, lower v_p, and elevated v_e compared to downstream. The third panel shows the averaged contrast agent concentration curves for blood, PDAC tumor, and PDAC downstream. **(B)** Example maps from a 65-year-old patient with CP. The pancreas was labeled by the yellow dashed boundary. **(C)** Representative maps of a 32-year-old subject in the normal control group.

graphs in Figure 3. The detailed mean values and standard deviations of each microcirculation parameter for each tissue are displayed in Table 2. The ANOVA test with Bonferroni correction of each microcirculation parameters between some pairs of tissues are listed in Table 3. The former half of Table 3 shows the comparison of each pair of CP, PDAC pancreas, and normal control pancreas. With Bonferroni correction, significant differences were observed in F_p for CP versus PDAC pancreas (P = 0.015), and in F_p and v_e for CP versus normal control (P = 0.012,<0.001, respectively) and PDAC pancreas versus normal control (P<0.001,<0.001, respectively). The latter half of Table 3 compares the measurements between CP versus PDAC tumor, downstream, and upstream. F_p, K^{trans}, and v_e showed significant differences between CP and PDAC tumor (P<0.001, = 0.012,<0.001, respectively); v_e was significantly different between CP and PDAC downstream (P =0.024); None of the microcirculation parameters showed significant differences between CP and PDAC upstream.

Prediction of type of tissue using microcirculation parameters

The ROC analysis was successfully carried out to evaluate the performance of microcirculation parameters in differentiating CP versus other tissues using either each single parameter or a combination of the four parameters. In the differentiation of CP and PDAC pancreas (Figure 4A, F_p showed the highest accuracy (AUC [95% CI] = 0.795 [0.604 - 0.985]) as a single parameter; the combination of the four parameters produced improved differentiation ability with good AUC (0.821 [0.654 – 0.988]). In the differentiation of CP and normal control pancreas (Figure 4B), v_e showed the highest AUC (0.981 [0.938 – 1.000]) when using

10.3389/fonc.2022.1007134

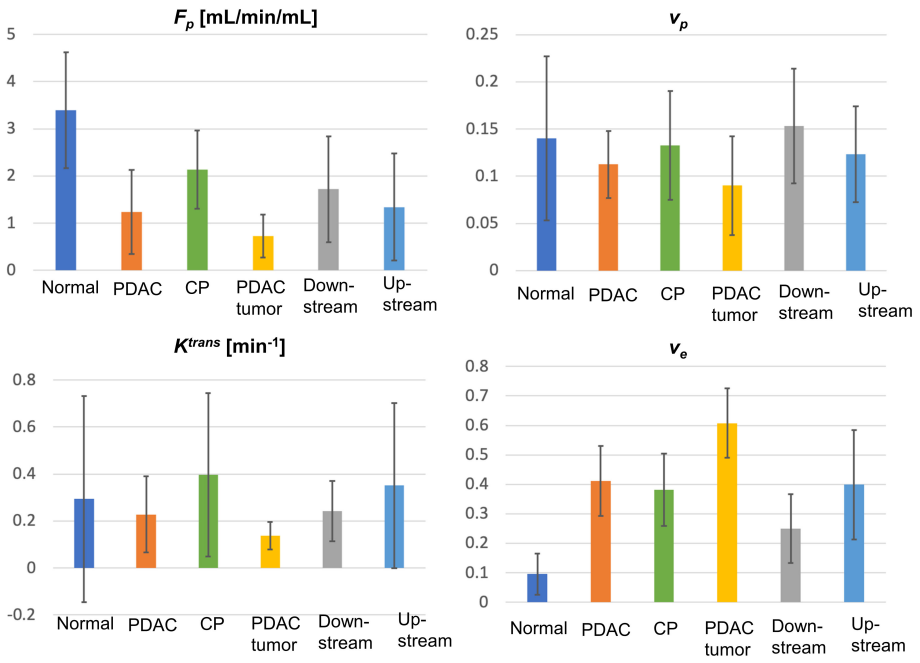

FIGURE 3
Bar graphs for the mean and standard deviation (error bar on top of each bar) for F_p, v_p, K^{trans}, and v_e for all types of tissues (normal, normal control pancreas; PDAC, PDAC pancreas; CP, CP pancreas).

TABLE 2 The mean and standard deviation of F_p, v_p, K^{trans}, and v_e for the six types of tissues.

	F_p (mL/min/mL)	v_p	K^{trans} (min^{-1})	v_e
Control	3.39±1.23	0.14±0.09	0.29 ± 0.43	0.10±0.07
PDAC whole	1.24±0.89	0.11±0.04	0.23 ± 0.16	0.41±0.11
CP	2.13±0.83	0.13±0.06	0.40 ± 0.35	0.38±0.12
PDAC mass	0.72±0.04	0.09±0.05	0.14 ± 0.06	0.61±0.11
Downstream	1.71±1.21	0.15±0.06	0.24 ± 0.13	0.25±0.12
Upstream	1.34±1.13	0.12±0.05	0.35 ± 0.35	0.40±0.18

TABLE 3 The *P* value between some pairs of the tissues using one-way ANOVA analysis.

Comparison pairs		F_p (mL/min/mL)	v_p	K^{trans} (min^{-1})	v_e
CP	PDAC pancreas	0.015*	0.327	0.136	0.583
CP	Normal control pancreas	0.012*	0.827	0.561	<0.001*
PDAC pancreas	Normal control pancreas	<0.001*	0.276	0.601	<0.001*
CP	PDAC tumor	<0.001*	0.093	0.012*	<0.001*
CP	PDAC downstream	0.383	0.454	0.175	0.024*
CP	PDAC upstream	0.125	0.732	0.795	0.830

* indicate statistical significance after Bonferroni correction.

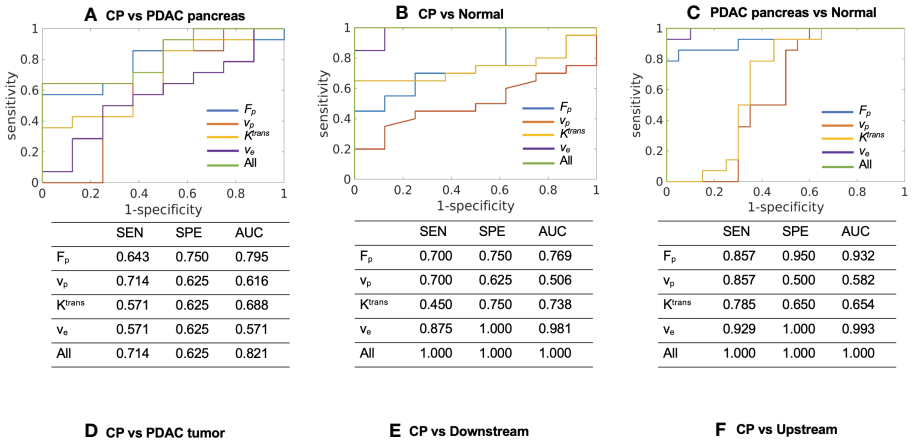

A	SEN	SPE	AUC
F_p	0.643	0.750	0.795
v_p	0.714	0.625	0.616
K^{trans}	0.571	0.625	0.688
v_e	0.571	0.625	0.571
All	0.714	0.625	0.821

B	SEN	SPE	AUC
F_p	0.700	0.750	0.769
v_p	0.700	0.625	0.506
K^{trans}	0.450	0.750	0.738
v_e	0.875	1.000	0.981
All	1.000	1.000	1.000

C	SEN	SPE	AUC
F_p	0.857	0.950	0.932
v_p	0.857	0.500	0.582
K^{trans}	0.785	0.650	0.654
v_e	0.929	1.000	0.993
All	1.000	1.000	1.000

D	SEN	SPE	AUC
F_p	0.786	0.750	0.929
v_p	0.571	0.750	0.723
K^{trans}	0.857	0.750	0.920
v_e	0.786	0.875	0.920
All	1.000	1.000	1.000

E	SEN	SPE	AUC
F_p	0.500	0.625	0.620
v_p	0.667	0.500	0.609
K^{trans}	0.750	0.625	0.640
v_e	0.833	0.625	0.781
All	0.917	0.750	0.917

F	SEN	SPE	AUC
F_p	0.778	0.625	0.792
v_p	0.667	0.500	0.556
K^{trans}	0.778	0.500	0.556
v_e	0.667	0.625	0.541
All	0.889	0.500	0.722

FIGURE 4
ROC curves and the sensitivity (SEN), specificity (SPE), and AUC to differentiate between **(A)** CP (N = 8) versus PDAC pancreas (N = 14), **(B)** CP (N = 8) versus normal control pancreas (N = 20), **(C)** PDAC pancreas (N = 14) versus normal control pancreas (N = 20), **(D)** CP (N = 8) versus PDAC tumor (N = 14), **(E)** CP (N = 8) versus PDAC downstream (N = 10), and **(F)** CP (N = 8) versus PDAC upstream (N = 9) using each single microcirculation parameter or the combination of all the four parameters. SEN, sensitivity; SPE, specificity; AUC, area under ROC curve.

single parameter; the combination of the four parameters can differentiate all the cases of current study cohort with AUC = 1.000 [1.000 – 1.000]. In the differentiation of PDAC pancreas and normal control pancreas (Figure 4C), v_e showed the highest AUC (0.993 [0.974 – 1.000]) for single parameter; the combination of the four parameters can differentiate all the cases with AUC = 1.000 [1.000 – 1.000]. For CP versus PDAC tumor (Figure 4D), F_p (0.929 [0.824 – 1.000]), K^{trans} (0.920 [0.806 – 1.000]), and v_e (0.920 [0.805 – 1.000]) showed excellent differentiation ability when using a single parameter; the combination of all the four parameters can differentiate all the cases with AUC = 1.000 [1.000 – 1.000]. For CP versus PDAC downstream (Figure 4E), v_e showed the highest AUC for single parameter (0.781 [0.569 – 0.994]), while the combination of the four parameters showed increased accuracy with excellent AUC (0.917 [0.795 – 1.000]). For CP versus upstream (Figure 4F), F_p showed the fair AUC for single parameter (0.792 [0.558 – 1.000]), and the combination of the four parameters showed slightly reduced but still fair accuracy (0.722 [0.465 – 0.980]).

Prediction of type of tissue using conventional TIC analysis

For TIC analysis, the number of cases in each category for each type of tissue are summarized in Table 4. CP demonstrated the TIC of type II (n = 2), type III (n = 5), and type IV (n = 1); the PDAC pancreas demonstrated type II (n = 3), type III (n = 4), and type IV (n = 7), which were within the same range of CP; PDAC tumor demonstrated type III (n = 3), type IV (n = 4), and type V (n = 7), representing a slower enhancement. Figure 5 displays the ROC plots to differentiate the CP versus PDAC pancreas (AUC [95% CI] = 0.629 [0.400 – 0.823], poor), CP versus normal control pancreas (0.984 [0.944 – 1.000], excellent), PDAC pancreas versus normal control pancreas (0.991 [0.968 – 1.000], excellent), CP versus PDAC tumor (0.915 [0.789 – 1.000], excellent), CP versus downstream (0.725 [0.468 – 0.905], fair), and CP versus upstream (0.625 [0.342 – 0.908], poor) with the sensitivity, specificity, and AUC listed under each plot.

TABLE 4 TIC category for each type of tissue.

Category	PDAC whole	CP	PDAC mass	Down-stream	Upstream	Control
I a	0	0	0	2	1	10
I b	0	0	0	0	0	5
II a	1	1	0	3	0	5
II b	2	1	0	0	1	0
III a	3	3	0	5	1	0
III b	1	2	3	0	2	0
IV a	4	0	3	0	4	0
IV b	3	1	1	0	0	0
V	0	0	7	0	0	0

TIC, time-signal intensity curve.

Comparison of quantitative DCE analysis and conventional TIC analysis

Table 5 lists the AUC from TIC, the highest AUC using a single microcirculation parameter from quantitative DCE, the AUC of combining all microcirculation parameters for the differentiation of each pair, and the P values using DeLong test to compare the performance of TIC analysis and quantitative DCE analysis. In most pairs, a single microcirculation parameter from quantitative DCE approach produced higher AUC than conventional TIC approach (except in the differentiation of CP versus normal control, where the AUC for TIC is 0.984 and the AUC from a single microcirculation parameter is 0.981). The combination of microcirculation parameters demonstrated higher AUC in all pairs when compared to the conventional TIC approach. The DeLong test indicated that quantitative DCE analysis performed significantly better in differentiating CP versus PDAC pancreas (P = 0.032) and CP versus PDAC downstream (P = 0.042).

Discussions

The differential diagnosis between PDAC and CP remains an unmet clinical need. In terms of clinical factors, both diseases

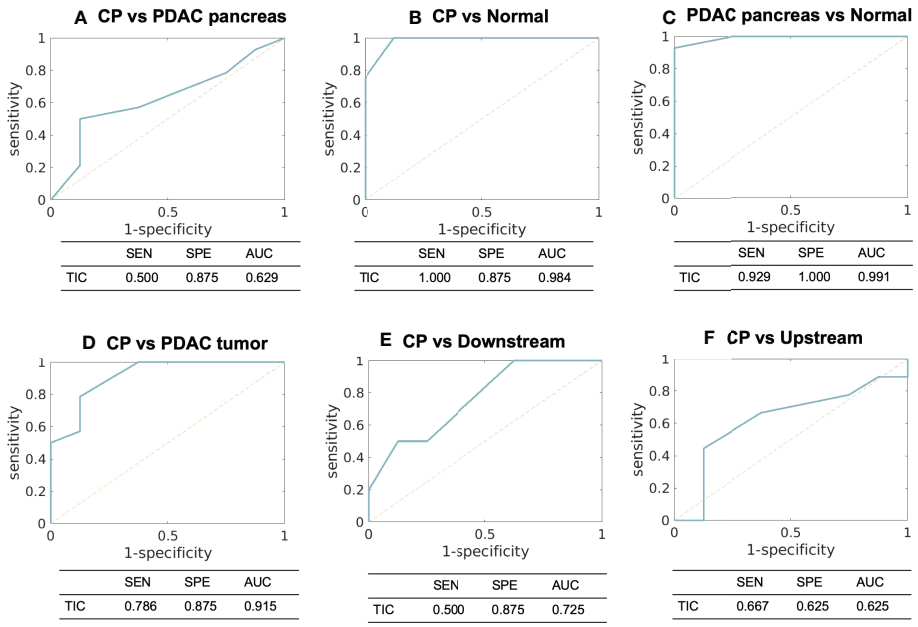

FIGURE 5
ROC curves and the sensitivity, specificity, and AUC using TIC analysis to differentiate between **(A)** CP versus PDAC pancreas, **(B)** CP versus normal control pancreas, **(C)** PDAC pancreas versus normal control pancreas, **(D)** CP versus PDAC tumor, **(E)** CP versus PDAC downstream, and **(F)** CP versus PDAC upstream. SEN, sensitivity; SPE, specificity; AUC, area under ROC curve; TIC, time-signal intensity curve.

TABLE 5 The comparison of the differentiation ability of TIC approach versus quantitative DCE approach.

Pairs		AUC of TIC	Highest AUC of a single microcirculation parameter	AUC of combined microcirculation parameters	P value
CP	PDAC pancreas	0.629	0.795	0.821	0.032*
CP	Normal control	0.984	0.981	1.000	0.353
PDAC pancreas	Normal control	0.991	0.993	1.000	0.353
CP	PDAC tumor	0.915	0.920	1.000	0.179
CP	Downstream	0.725	0.781	0.917	0.042*
CP	Upstream	0.625	0.792	0.722	0.380

For most pairs, the highest AUC produced by a single microcirculation parameter is higher than the AUC of TIC. The combination of the four microcirculation parameters outperforms the TIC analysis for all the pairs.
* indicates statistical significance.

can have similar background histories such a history of alcohol and tobacco use, and similar clinical signs such as weight loss, chronic abdominal pain, anorexia, and diabetes (8). For blood test, the best-established biomarker for PDAC diagnosis is carbohydrate antigen 19-9 (CA19-9), a Lewis antigen of the MUC1 protein class. Unfortunately, CA19-9 can also be elevated in patients with CP, yielding a distinction no better than 65% (35). Imaging is the most common approach to diagnose these diseases. Contrast-enhanced CT and multi-phasic contrast-enhanced MRI have shown high sensitivity and high specificity for the diagnosis of CP or PDAC solely (36, 37). However, the shared imaging findings make the differential diagnosis a complicated issue. The common imaging features include generalized parenchymal glandular atrophy, diffuse pancreatic calcifications, dilation of the main pancreatic duct, hypo-attenuation on contrast-enhanced CT (38), and hypo-enhancement on multi-phasic contrast-enhanced MRI. EUS and EUS-guided fine needle aspiration (FNA) have high sensitivity and specificity in the detection of PDAC and CP (39). However, studies have shown that the sensitivity drops significantly to only 50–75% in patients with chronic pancreatitis (40, 41) due to shared pathological features (17).

In recent years, advanced techniques have been developed to improve the diagnosis and differentiation of PDAC and CP. New blood biomarkers including plasma suPAR (42) and a bunch of metabolic markers (43) have shown promises in the differentiation of the two diseases. Perfusion CT has been used for the diagnosis and differentiation of PDAC (44) and CP (45, 46) with positive results, but remains in the research phase for pancreas due to higher radiation dose and limited field of view. In MRI, non-contrast techniques including diffusion-weighted imaging and T1 mapping, and contrast-enhanced techniques with more dynamic phases and TIC analysis (22) also show promising differential ability of the two diseases (12, 45). These new techniques are non-invasive approaches with clinical promises, but still need to be validated on larger cohorts of patients.

In this work, we investigated the differential ability of tissue microcirculation parameters estimated from Multitasking DCE technique. The microcirculation properties carry crucial information about disease characteristics, progression, and regression. The alteration of microcirculation properties usually precedes morphological changes (47–49), providing a pathway for early detection, staging, and treatment monitoring. DCE MRI has the potential to capture the microcirculation properties by tracking the contrast agent kinetics within the tissues, but has been limited by the demanding sampling requirements. The pathological lesions usually bear high-level heterogeneity within the structure, which requires adequate coverage and high spatial resolution to capture the spatial variation. On the other hand, high temporal resolution is required to accurately track the kinetics of contrast agent within the tissues. Previous studies have demonstrated that a temporal resolution of least 10 seconds is necessary to depict tumor enhancement dynamics (50), and 1-3 seconds to capture the dynamics of AIF (51, 52). Furthermore, respiratory motion remains a major challenge and can further degrade the image quality for pancreas imaging.

The recently-proposed Multitasking DCE technique is a promising solution to resolve the abovementioned limitations (28–31, 53–55). The technique is capable of resolving respiratory motion, achieving a free-breathing acquisition for 10-minutes to capture the contrast agent kinetics. It enables entire-abdomen coverage, clinical-sufficient spatial resolution, and 1-second temporal resolution simultaneously, allowing for the capture of spatial variation and temporal kinetics. Consequently, quantitative DCE analysis can be performed to estimate the microcirculation parameters. In this work, the two-compartment exchange model was used, and four independent microcirculation parameters were estimated: F_p, representing tissue blood flow, v_p, correlated with the microvascular density, K^{trans}, which has a joint effect of blood flow and permeability-surface area product, and v_e, which is correlated with fibrosis content. Compared with normal control pancreas, the PDAC

tumor, PDAC pancreas and CP all showed significantly lower F_p (P<0.001,<0.001, 0.012, respectively) and higher v_e (P<0.001, <0.001,<0.001, respectively), consistent with their pathological characteristics including reduced blood flow and high fibrosis replacement.

These microcirculation parameters showed strong ability in the differentiation of CP versus PDAC tumor. F_p, K^{trans}, and v_e demonstrated significant difference between CP and PDAC tumor (P<0.001, 0.012,<0.001, respectively); the AUC using these three parameters individually to differentiate CP versus PDAC tumor are all above 0.9 (0.929, 0.920, 0.920, respectively), representing excellent differential ability. The non-tumoral part of PDAC is frequently associated with secondary inflammatory changes (11, 56). This associated pancreatitis happens more frequently in the upstream of PDAC due to the obstruction of pancreatic duct (57, 58). The differential ability of the microcirculation parameter between CP and non-tumoral tissues in PDAC were also evaluated. For CP versus PDAC downstream, v_e showed significant difference (P = 0.024) and produced the highest AUC (0.781) with a single parameter; the combination of all the four parameters demonstrated excellent differential ability with an AUC of 0.971. For CP versus PDAC upstream, F_p showed a visible reduction in the upstream as displayed in Figure 3, but none of the microcirculation parameters had significant difference between the two tissues. A major reason could be the large standard deviation from the small sample size and varied diseases grade or severity. The ROC analysis showed a fair AUC of 0.792 using F_p and 0.722 when combining of all the four parameters. These results indicate that the microcirculation parameters, especially F_p, has a great potential to differentiate CP with PDAC upstream.

Furthermore, the evaluation of differential ability between CP and whole PDAC pancreas were performed. F_p was significantly different between CP and PDAC pancreas (P = 0.015) and showed a fair and close to good AUC of 0.795. Combing of all parameters presented a good differentiation with an AUC of 0.821. The ability to differentiate CP versus whole PDAC pancreas has great utility in clinical context. It provides the possibility to identify patients with PDAC without the accurate localization of tumor.

To demonstrate the advantages of the quantitative Multitasking DCE technique, the comparison with the conventional TIC approach was also performed. The TIC approach showed excellent accuracy to differentiate CP versus PDAC tumor (AUC = 0.915), CP versus normal control pancreas (AUC = 0.984), and PDAC pancreas versus normal control pancreas (AUC = 0.991). These results are comparable to the highest AUCs produced by a single microcirculation parameter but lower than the AUCs from the combination of all microcirculation parameters. For CP versus downstream, TIC produced fair accuracy with AUC of 0.725, while the microcirculation parameters showed excellent differential ability with AUC of 0.917. For CP versus upstream, TIC produced poor differentiation ability with AUC of 0.625, perhaps due to the similar enhancement pattern of CP and PDAC upstream with associated pancreatitis. The quantitative DCE approach, on the other hand, can capture more dynamic information and improve the differentiation ability to an AUC of 0.792. For CP versus PDAC pancreas, TIC performed poorly with AUC of 0.629. while quantitative DCE approach presented a good differentiation (AUC = 0.821) when using all microcirculation parameters. The comparison demonstrated that Multitasking DCE with quantitative DCE analysis outperformed the conventional TIC approach and can potentially improve the differentiation between CP versus PDAC.

Another intriguing potential of the quantitative Multitasking DCE technique is to evaluate and predict the treatment outcome of PDAC and CP (24, 59, 60). Most of the therapies affect tumor microvasculature and thus the microcirculation properties, altering tumor blood flow, microvascular density, and extravascular extracellular distribution. By identifying the changes in microcirculation properties with quantitative Multitasking DCE, there is a great potential to predict the treatment effect at early stage and individualize the therapy regimen.

Our study has several limitations. First, the sample sizes for all groups were relatively small, which may affect the statistical outcome. The ability to differentiate CP versus PDAC of Multitasking DCE need to be validated on larger patient cohort. Second, the PDAC and CP groups included a variety of tumor stages or disease severity. Sub-group analysis based on tumor grade or disease severity was not possible due to the small sample size. This variation can be a major factor contributing to the wide standard deviation of the microcirculation parameters. Third, all the PDAC patients had undergone neoadjuvant chemotherapy at the time of the study, which may change the tissues properties. Future studies on treatment-naïve PDAC patients will be performed. Finally, the resection specimens were not available in this pilot study. The correlation between the microcirculation parameters and the histological markers including the microvascular density and fibrosis were not accessible in this work. With the promising preliminary results, future studies with the correlation between pathological details and imaging parameters will be performed on untreated PDAC and CP patients.

Conclusion

A novel Multitasking DCE MRI technique with quantitative analysis of microcirculation parameters was performed to differentiate PDAC and CP. The combination of the microcirculation parameters showed strong ability to different CP from normal control pancreas, PDAC pancreas, PDAC tumor, PDAC downstream, and PDAC upstream, and superior

performance compared to conventional TIC analysis approach. Multitasking DCE appears to be a promising clinical tool for the differentiation of CP from PDAC on a quantitative and objective basis.

Data availability statement

The data will be available upon request with de-identification; the analytic methods are available upon request to the corresponding author.

Ethics statement

The studies involving human participants were reviewed and approved by Cedars-Sinai Medical Center. The patients/participants provided their written informed consent to participate in this study.

Author contributions

NW contributed to the data acquisition, analysis and interpretation, and article writing. SG, SP, SL, and AH contributed to the patient recruitment and study design. YX, AC, CW, SM, ZF, LW contributed to the data analysis and interpretation. DL contributed to the conception and study design. All authors contributed to the article and approved the submitted version.

Funding

This work was partially supported by NIH 1R01EB028146, and NIH 1R01EB032801.

Conflict of interest

The authors declare that the research was conducted in the absence of any commercial or financial relationships that could be construed as a potential conflict of interest.

Publisher's note

Supplementary material

The Supplementary Material for this article can be found online at: https://www.frontiersin.org/articles/10.3389/fonc.2022.1007134/full#supplementary-material

References

1. Siegel RL, Miller KD, Jemal A. Cancer statistics, 2020. *CA Cancer J Clin* (2020) 70:7–30. doi: 10.3322/caac.21590

2. Holzapfel K, Reiser-Erkan C, Fingerle AA, Erkan M, Eiber MJ, Rummeny EJ, et al. Comparison of diffusion-weighted MR imaging and multidetector-row CT in the detection of liver metastases in patients operated for pancreatic cancer. *Abdom Imaging* (2011) 36:179–84. doi: 10.1007/s00261-010-9633-5

3. Birgin E, Hablawetz P, Téoule P, Rückert F, Wilhelm TJ. Chronic pancreatitis and resectable synchronous pancreatic carcinoma: A survival analysis. *Pancreatology* (2018) 18:394–8. doi: 10.1016/j.pan.2018.04.009

4. Hao L, Zeng XP, Xin L, Wang D, Pan J, Bi YW, et al. Incidence of and risk factors for pancreatic cancer in chronic pancreatitis: A cohort of 1656 patients. *Digestive Liver Dis* (2017) 49:1249–56. doi: 10.1016/j.dld.2017.07.001

5. Kirkegård J, Mortensen FV, Cronin-Fenton D. Chronic pancreatitis and pancreatic cancer risk: a systematic review and meta-analysis. *Off J Am Coll Gastroenterol ACG* (2017) 112:1366–72. doi: 10.1038/ajg.2017.218

6. Gandhi S, de la Fuente J, Murad MH, Majumder S. Chronic pancreatitis is a risk factor for pancreatic cancer, and incidence increases with duration of disease: A systematic review and meta-analysis. *Clin Transl Gastroenterol* (2022) 13. doi: 10.14309/ctg.0000000000000463

7. Narkhede RA, Desai GS, Prasad PP, Wagle PK. Diagnosis and management of pancreatic adenocarcinoma in the background of chronic pancreatitis: Core issues. *Digestive Dis* (2019) 37:315–24. doi: 10.1159/000496507

8. Elsherif SB, Virarkar M, Javadi S, Ibarra-Rovira JJ, Tamm EP, Bhosale PR. Pancreatitis and PDAC: association and differentiation. *Abdominal Radiol* (2020) 45:1324–37. doi: 10.1007/s00261-019-02292-w

9. Li D, Xie K, Wolff R, Abbruzzese JL. Pancreatic cancer. *Lancet* (2004) 363:1049–57. doi: 10.1016/S0140-6736(04)15841-8

10. Choi SY, Kim SH, Kang TW, Song KD, Park HJ, Choi YH. Differentiating mass-forming autoimmune pancreatitis from pancreatic ductal adenocarcinoma on the basis of contrast-enhanced MRI and DWI findings. *Am J Roentgenol* (2016) 206:291–300. doi: 10.2214/AJR.15.14974

11. van Gulik TM, Moojen TM, Van Geenen R, Obertop H, Gouma DJ, Rauws EAJ. Differential diagnosis of focal pancreatitis and pancreatic cancer. *Ann Oncol* (1999) 10:S85–8. doi: 10.1093/annonc/10.suppl_4.S85

12. Wang L, Gaddam S, Wang N, Xie Y, Deng Z, Zhou Z, et al. Multiparametric mapping magnetic resonance imaging of pancreatic disease. *Front Physiol* (2020) 11:8. doi: 10.3389/fphys.2020.00008

13. Cruz-Monserrate Z, Gumpper K, Kaul S, Badi N, Terhorst S, Dubay K, et al. Delayed processing of secretin-induced pancreas fluid influences the quality and integrity of proteins and nucleic acids. *Pancreas* (2021) 50:17–28. doi: 10.1097/MPA.0000000000001717

14. Krishna NB, Mehra M, Reddy A. V & agarwal, b. EUS/EUS-FNA for suspected pancreatic cancer: influence of chronic pancreatitis and clinical presentation with or without obstructive jaundice on performance characteristics. *Gastrointest Endosc* (2009) 70:70–9. doi: 10.1016/j.gie.2008.10.030

15. Kim T, Murakami T, Takamura M, Hori M, Takahashi S, Nakamori S, et al. Pancreatic mass due to chronic pancreatitis: Correlation of CT and MR imaging features with pathologic findings. *Am J Roentgenol* (2001) 177:367–71. doi: 10.2214/ajr.177.2.1770367

16. Saraswat M, Joenväärä S, Seppänen H, Mustonen H, Haglund C, Renkonen R. Comparative proteomic profiling of the serum differentiates pancreatic cancer from chronic pancreatitis. *Cancer Med* (2017) 6:1738–51. doi: 10.1002/cam4.1107

17. Klöppel G, Adsay NV. Chronic pancreatitis and the differential diagnosis versus pancreatic cancer. *Arch Pathol Lab Med* (2009) 133:382–7. doi: 10.5858/133.3.382

18. Bang SJ, Kim MH, Kim DH, Lee TY, Kwon S, Oh HC, et al. Is pancreatic core biopsy sufficient to diagnose autoimmune chronic pancreatitis? *Pancreas* (2008) 36:84–9. doi: 10.1097/mpa.0b013e318135483d

19. Munigala S, Kanwal F, Xian H, Agarwal B. New diagnosis of chronic pancreatitis: Risk of missing an underlying pancreatic cancer. *Off J Am Coll Gastroenterol ACG* (2014) 109:1824–30. doi: 10.1038/ajg.2014.318

20. Coenegrachts K, Van Steenbergen W, De Keyzer F, Vanbeckevoort D, Bielen D, Chen F, et al. Dynamic contrast-enhanced MRI of the pancreas: initial results in healthy volunteers and patients with chronic pancreatitis. *J Magnetic Resonance Imaging: Off J Int Soc Magnetic Resonance Med* (2004) 20:990–7. doi: 10.1002/jmri.20212

21. Kim JK, Altun E, Elias Jr J, Pamuklar E, Rivero H, Semelka RC. Focal pancreatic mass: Distinction of pancreatic cancer from chronic pancreatitis using gadolinium-enhanced 3D-gradient-echo MRI. *J Magnetic Resonance Imaging: Off J Int Soc Magnetic Resonance Med* (2007) 26:313–22. doi: 10.1002/jmri.21010

22. Zhang TT, Wang L, Liu HH, Zhang CY, Li XM, Lu JP, et al. Differentiation of pancreatic carcinoma and mass-forming focal pancreatitis: qualitative and quantitative assessment by dynamic contrast-enhanced MRI combined with diffusion-weighted imaging. *Oncotarget* (2017) 8:1744. doi: 10.18632/oncotarget.12120

23. Kim JH, Lee JM, Park JH, Kim SC, Joo I, Han JK, et al. Solid pancreatic lesions: characterization by using timing bolus dynamic contrast-enhanced MR imaging assessment–a preliminary study. *Radiology* (2013) 266:185–96. doi: 10.1148/radiol.12120111

24. Akisik MF, Sandrasegaran K, Bu G, Lin C, Hutchins GD, Chiorean EG. Pancreatic cancer: utility of dynamic contrast-enhanced MR imaging in assessment of antiangiogenic therapy. *Radiology* (2010) 256:441–9. doi: 10.1148/radiol.10091733

25. Bali MA, Metens T, Denolin V, Delhaye M, Demetter P, Closset J, et al. Tumoral and nontumoral pancreas: Correlation between quantitative dynamic contrast-enhanced MR imaging and histopathologic parameters. *Radiology* (2011) 261:456–66. doi: 10.1148/radiol.11103515

26. Koelblinger C, Ba-Ssalamah A, Goetzinger P, Puchner S, Weber M, Sahora K, et al. Gadobenate dimeglumine–enhanced 3.0-T MR imaging versus multiphasic 64–detector row CT: prospective evaluation in patients suspected of having pancreatic cancer. *Radiology* (2011) 259:757–66. doi: 10.1148/radiol.11101189

27. Lee ES, Lee JM. Imaging diagnosis of pancreatic cancer: a state-of-the-art review. *World J gastroenterol: WJG* (2014) 20:7864. doi: 10.3748/wjg.v20.i24.7864

28. Christodoulou AG, Shaw JL, Nguyen C, Yang Q, Xie Y, Wang N, et al. Magnetic resonance multitasking for motion-resolved quantitative cardiovascular imaging. *Nat BioMed Eng* (2018) 2:215–26. doi: 10.1038/s41551-018-0217-y

29. Wang N, Christodoulou AG, Xie Y, Wang Z, Deng Z, Zhou B, et al. Quantitative 3D dynamic contrast-enhanced (DCE) MR imaging of carotid vessel wall by fast T1 mapping using multitasking. *Magn Reson Med* (2019) 81:2302–14. doi: 10.1002/mrm.27553

30. Wang N, Gaddam S, Wang L, Xie Y, Fan Z, Yang W, et al. Six-dimensional quantitative DCE MR multitasking of the entire abdomen: Method and application to pancreatic ductal adenocarcinoma. *Magn Reson Med* (2020) 84:928–48. doi: 10.1002/mrm.28167

31. Wang N, Xie Y, Fan Z, Ma S, Saouaf R, Guo Y, et al. Five-dimensional quantitative low-dose multitasking dynamic contrast-enhanced MRI: Preliminary study on breast cancer. *Magn Reson Med* (2021) 85:3096–111. doi: 10.1002/mrm.28633

32. Yadav D, Park WG, Fogel EL, Li L, Chari ST, Feng Z, et al. PROspective evaluation of chronic pancreatitis for EpidEmiologic and translational StuDies (PROCEED): Rationale and study design from the consortium for the study of chronic pancreatitis, diabetes, and pancreatic cancer. *Pancreas* (2018) 47:1229. doi: 10.1097/MPA.0000000000001170

33. Sourbron SP, Buckley DL. Classic models for dynamic contrast-enhanced MRI. *NMR BioMed* (2013) 26:1004–27. doi: 10.1002/nbm.2940

34. Mandrekar JN. Receiver operating characteristic curve in diagnostic test assessment. *J Thorac Oncol* (2010) 5:1315–6. doi: 10.1097/JTO.0b013e3181ec173d

35. Duffy MJ, Sturgeon C, Lamerz R, Haglund C, Holubec VL, Klapdor R, et al. Tumor markers in pancreatic cancer: a European group on tumor markers (EGTM) status report. *Ann Oncol* (2010) 21:441–7. doi: 10.1093/annonc/mdp332

36. Singh VK, Yadav D, Garg PK. Diagnosis and management of chronic pancreatitis: a review. *JAMA* (2019) 322:2422–34. doi: 10.1001/jama.2019.19411

37. Kichler A, Jang S. Chronic pancreatitis: epidemiology, diagnosis, and management updates. *Drugs* (2020) 80:1155–68. doi: 10.1007/s40265-020-01360-6

38. Eriksen RØ, Strauch LS, Sandgaard M, Kristensen TS, Nielsen MB, Lauridsen CA. Dynamic contrast-enhanced CT in patients with pancreatic cancer. *Diagnostics* (2016) 6:34. doi: 10.3390/diagnostics6030034

39. Kitano M, Yoshida T, Itonaga M, Tamura T, Hatamaru K, Yamashita Y. Impact of endoscopic ultrasonography on diagnosis of pancreatic cancer. *J Gastroenterol* (2019) 54:19–32. doi: 10.1007/s00535-018-1519-2

40. Dutta AK, Chacko A. Head mass in chronic pancreatitis: Inflammatory or malignant. *World J Gastrointest Endosc* (2015) 7:258–64. doi: 10.4253/wjge.v7.i3.258

41. Schima W, Böhm G, Rösch CS, Klaus A, Függer R, Kopf H. Mass-forming pancreatitis versus pancreatic ductal adenocarcinoma: CT and MR imaging for differentiation. *Cancer Imaging* (2020) 20:1–12. doi: 10.1186/s40644-020-00324-z

42. Aronen A, Aittoniemi J, Huttunen R, Nikkola A, Rinta-Kiikka I, Nikkola J, et al. Plasma suPAR may help to distinguish between chronic pancreatitis and pancreatic cancer. *Scand J Gastroenterol* (2021) 56:81–5. doi: 10.1080/00365521.2020.1849383

43. Mayerle J, Kalthoff H, Reszka R, Kamlage B, Peter E, Schniewind B, et al. Metabolic biomarker signature to differentiate pancreatic ductal adenocarcinoma from chronic pancreatitis. *Gut* (2018) 67:128–37. doi: 10.1136/gutjnl-2016-312432

44. Zaborienė I, Barauskas G, Gulbinas A, Ignatavičius P, Lukoševičius S, Žvinienė K. Dynamic perfusion CT–a promising tool to diagnose pancreatic ductal adenocarcinoma. *Open Med* (2021) 16:284–92. doi: 10.1515/med-2021-0228

45. Parakh A, Tirkes T. Advanced imaging techniques for chronic pancreatitis. *Abdominal Radiol* (2020) 45:1420–38. doi: 10.1007/s00261-019-02191-0

46. Yadav AK, Sharma R, Kandasamy D, Pradhan RK, Garg PK, Bhalla AS, et al. Perfusion CT–can it resolve the pancreatic carcinoma versus mass forming chronic pancreatitis conundrum? *Pancreatology* (2016) 16:979–87. doi: 10.1016/j.pan.2016.08.011

47. Mankoff DA, Dunnwald LK, Gralow JR, Ellis GK, Schubert EK, Tseng J, et al. Changes in blood flow and metabolism in locally advanced breast cancer treated with neoadjuvant chemotherapy. *J Nucl Med* (2003) 44:1806–14.

48. Jain RK, Duda DG, Willett CG, Sahani DV, Zhu AX, Loeffler JS, et al. Biomarkers of response and resistance to antiangiogenic therapy. *Nat Rev Clin Oncol* (2009) 6:327–38. doi: 10.1038/nrclinonc.2009.63

49. Othman AE, Falkner F, Weiss J, Kruck S, Grimm R, Martirosian P, et al. Effect of temporal resolution on diagnostic performance of dynamic contrast-enhanced magnetic resonance imaging of the prostate. *Invest Radiol* (2016) 51:290–6. doi: 10.1097/RLI.0000000000000234

50. Li KL, Buonaccorsi G, Thompson G, Cain JR, Watkins A, Russell D, et al. An improved coverage and spatial resolution–using dual injection dynamic contrast-enhanced (ICE-DICE) MRI: A novel dynamic contrast-enhanced technique for cerebral tumors. *Magn Reson Med* (2012) 68:452–62. doi: 10.1002/mrm.23252

51. Luypaert R, Sourbron S, de Mey J. Validity of perfusion parameters obtained using the modified tofts model: a simulation study. *Magn Reson Med* (2011) 65:1491–7. doi: 10.1002/mrm.22728

52. Shaw JL, Yang Q, Zhou Z, Deng Z, Nguyen C, Li D, et al. Free-breathing, non-ECG, continuous myocardial T1 mapping with cardiovascular magnetic resonance multitasking. *Magn Reson Med* (2019) 81:2450–63. doi: 10.1002/mrm.27574

53. Ma S, Nguyen CT, Han F, Wang N, Deng Z, Binesh N, et al. Three-dimensional simultaneous brain T1, T2, and ADC mapping with MR multitasking. *Magn Reson Med* (2020) 84:72–88. doi: 10.1002/mrm.28092

54. Ma S, Wang N, Fan Z, Kaisey M, Sicotte NL, Christodoulou AG, et al. Three-dimensional whole-brain simultaneous T1, T2, and T1ρ quantification using MR multitasking: Method and initial clinical experience in tissue characterization of multiple sclerosis. *Magn Reson Med* (2021) 85:1938–52. doi: 10.1002/mrm.28553

55. Baxi AC, Jiang Q, Hao J, Yang Z, Woods K, Keilin S, et al. The effect of solid pancreatic mass lesions on pancreatic duct diameter at endoscopic ultrasound. *Endosc Ultrasound* (2017) 6:103. doi: 10.4103/2303-9027.204812

56. Scialpi M, Cagini L, Pierotti L, De Santis F, Pusiol T, Piscioli I, et al. Detection of small (≤ 2 cm) pancreatic adenocarcinoma and surrounding parenchyma: correlations between enhancement patterns at triphasic MDCT and histologic features. *BMC Gastroenterol* (2014) 14:1–8. doi: 10.1186/1471-230X-14-16

57. Frampas E, Morla O, Regenet N, Eugene T, Dupas B, Meurette G. A solid pancreatic mass: Tumour or inflammation? *Diagn Interv Imaging* (2013) 94:741–55. doi: 10.1016/j.diii.2013.03.013

58. O'Flynn EAM, DeSouza NM. Functional magnetic resonance: biomarkers of response in breast cancer. *Breast Cancer Res* (2011) 13:1–10.

59. Georgiou L, Sharma N, Broadbent DA, Wilson DJ, Dall BJ, Gangi A, et al. Estimating breast tumor blood flow during neoadjuvant chemotherapy using interleaved high temporal and high spatial resolution MRI. *Magn Reson Med* (2018) 79:317–26. doi: 10.1002/mrm.26684

60. Johnson PT, Outwater EK. Pancreatic carcinoma versus chronic pancreatitis: dynamic MR imaging. *Radiology* (1999) 212:213–8. doi: 10.1148/radiology.212.1.r99jl16213

Frontiers in Oncology

Advances knowledge of carcinogenesis and tumor progression for better treatment and management

The third most-cited oncology journal, which highlights research in carcinogenesis and tumor progression, bridging the gap between basic research and applications to imrpove diagnosis, therapeutics and management strategies.

Discover the latest Research Topics

See more →

Frontiers

Avenue du Tribunal-Fédéral 34
1005 Lausanne, Switzerland
frontiersin.org

Contact us

+41 (0)21 510 17 00
frontiersin.org/about/contact